

MECHANICAL MODELS FOR  
INTERSEISMIC DEFORMATION IN  
SUBDUCTION ZONES

Thesis by

Ravi V. S. Kanda

In Partial Fulfillment of the Requirements for the  
degree of

Doctor of Philosophy



CALIFORNIA INSTITUTE OF TECHNOLOGY

Pasadena, California

2010

(Defended May 28<sup>th</sup>, 2010)

© 2010

Ravi V. S. Kanda

All Rights Reserved

## ACKNOWLEDGEMENTS

I want to thank Prof. Mark Simons for his patience, encouragement, and mentoring during the course of my PhD. I also want to thank my Committee Members, Prof. Jean-Philippe Avouac, Prof. Mike Gurnis, Prof. Jean-Paul Ampuero, and Prof. Robert Clayton for their guidance and mentoring throughout my stay at Caltech. I thank Prof. David Stevenson and Prof. Hiroo Kanamori for inspiring me to expect more from myself. I would not have embarked on my PhD without my wife, Liz, who inspired me to pursue my dreams and has been the “rock of stability” in our relationship. I want to thank my parents, who believed in my dreams enough to mortgage everything they had so I could come to the U.S.A. to pursue my dreams. I am also greatly indebted to my late grandfather, who inspired me through example – and made me realize that in life, the easy way out is not necessarily the most fulfilling. And lastly, I want to thank the Seismo Lab administrative staff, especially, Elisa Loeffen, Viola Carter, and Rosemary Miller, who went out of their way to make my stay here at Caltech very pleasant.

## ABSTRACT

Traditionally, interseismic deformation in subduction zones has been modeled using simple elastic dislocation models (EDMs). Such models have been extensively used over the past couple of decades as geodetic networks were being established around the world.

However, with the availability of 3D (vector) velocity data with dense spatio-temporal coverage during the past decade, it becomes possible to explore more complex models of deformation. Such models may allow us to infer higher-order properties of the megathrust interface or the subducting plate from the observed deformation field. For instance, we show that it may be possible to infer the elastic plate thickness of the subducting plate (over the seismic cycle timescale) under certain conditions, especially if ocean-bottom geodetic measurements become routinely available in the near future. The plate thickness can affect surface deformation on the overriding plate if only a small fraction of the flexural stresses at the trench are continuously released over the seismic cycle time-scale. Another problem we address here is how the rheology of the megathrust interface affects the evolution of slip over the seismic cycle, and therefore, the seismic hazard inferred from geodetic data. We model such slip evolution on a realistic 3D fault surface having a frictional rheology.

Assuming that seismic rupture zones (or “asperities”) persist across several seismic cycles, we test the hypothesis that mechanical coupling on such asperities alone is sufficient to explain currently available geodetic observations in northern Japan. We find that it is not necessary to lock large portions of the megathrust between ruptures – unlike recent EDM predictions for northern Japan – resulting in potentially large future earthquakes. Instead, post-seismic slip around asperities immediately following seismic rupture can result in large “stress-shadow” regions, which experience negligible slip late in the cycle. Such stress-shadow regions can mimic the long-wavelength “locked” zones inferred from EDMs for the interseismic period, and account for most of the present day GPS velocities in northern Japan. The approach developed here can be extended to more complex models of deformation that include heterogeneities in crustal properties, multiple fault surfaces, and perhaps, even multiple rheologies over a single fault.

## TABLE OF CONTENTS

<i>Chapter 1</i>	INTRODUCTION.....	1-1
	References.....	1-11
<i>Chapter 2</i>	AN ELASTIC PLATE MODEL FOR INTERSEISMIC DEFORMATION IN SUBDUCTION ZONES.....	2-1
2.1	Introduction .....	2-1
2.2	The Elastic Subducting Plate Model (ESPM).....	2-7
2.3	End-member models of the ESPM.....	2-11
2.4	Effect of plate flexure on the ESPM surface deformation field .....	2-15
2.5	Comparison of the ESPM and the BSM surface displacements.....	2-25
2.6	Elastic stresses and strains in the half-space .....	2-27
2.7	Discussion.....	2-29
2.8	Conclusions .....	2-33
	References.....	2-36
<i>Chapter 3</i>	A SENSITIVITY ANALYSIS OF ELASTIC DISLOCATION MODELS FOR INTERSEISMIC DEFORMATION IN SUBDUCTION ZONES.....	3-1
3.1	Introduction .....	3-1
3.2	Transition zones adjoining the locked megathrust .....	3-3
3.3	Inverting geodetic data using the ESPM vs. the BSM .....	3-8
3.4	Sensitivity of surface observables to parameterizing the BSM and the ESPM ....	3-13
3.5	Discussion.....	3-24
3.6	Conclusions .....	3-25
	References.....	28
<i>Chapter 4</i>	MODEL SETUP AND VALIDATION.....	4-1
4.1	Introduction .....	4-1
4.2	Model visualization .....	4-5
4.3	Megathrust interface geometry & discretization .....	4-6
4.4	Kernels .....	4-13
4.5	Rheology .....	4-22
4.6	Significant developments over the existing Matlab forward solver, <i>EvolveSlip</i> ....	4-24
4.7	Steps in running a model .....	4-26
4.8	Future directions for research and development .....	4-28
	References.....	4-30
<i>Chapter 5</i>	ASPERITY MODEL FOR INTERSEISMIC DEFORMATION IN NORTHEASTERN JAPAN.....	5-1
5.1	Introduction .....	5-1
5.2	Summary of the forward modeling approach.....	5-3
5.3	Asperity parameters for the Japan Trench megathrust.....	5-6
5.3.1	Fukuyshima-oki — ruptures of 1938 .....	5-7
5.3.2	Miyagi-oki — ruptures of 1936, 1978, and 2005.....	5-8
5.3.3	Sanriku-oki — ruptures of 1931, 1968, and 1994.....	5-9
5.3.4	Tokachi-oki — ruptures of 1952 and 2003.....	5-10
5.3.5	Nemuro-oki — rupture of 1973 .....	5-12
5.3.6	Summary .....	5-13
5.4	Simulating rupture-sequences for the northern Japan asperity configuration.....	5-14

5.4.1	Model Convergence for the Japan megathrust interface.....	5-15
5.4.2	Model spin-up using a synthetic rupture catalog.....	5-17
5.5	Station velocity predictions for northern Japan using a realistic fault rheology ...	5-21
5.6	Conclusions and future work.....	5-32
	References.....	5-34

## LIST OF FIGURES

- Figure 1-1. (a) Coseismic slip and (b) interseismic slip deficit (“backslip”) estimates for the megathrust interface off northeastern Japan. Adapted from Yamanaka and Kikuchi [2003; , 2004] and Suwa et al. [2006]. 1-8
- Figure 2-1 Comparison of the BSM, the pBSM, and the ESPM. The trench is defined by the intersection of the free-surface (horizontal solid line) and the (upper) dipping line; cross-sectional geometry is assumed to be identical along strike;  $D_{lock}$  is the depth to the downdip end of the locked megathrust;  $x_{lock}$  represents the surface projection of the downdip end of the locked megathrust;  $\theta$  is the dip of the plate interface;  $H$  is the plate thickness in the ESPM;  $x_G$  represents the typical range for the location of the nearest geodetic observation from the trench. The arrows represent relative motion at the plate boundary. 2-3
- Figure 2-2. Comparison of the velocity fields in the half-space for the BSM, the pBSM, and the ESPM. Top row illustrates the interseismic velocity fields predicted by the models (solid black line represents the locked zone), and the bottom row shows the imposed “geologic” steady state creep velocity field. All velocities are computed relative to the far-field of the overriding plate (and normalized relative to the plate convergence rate,  $V_p$ ). Velocity vectors are drawn to the same scale in all panels (yellow vector at bottom left in each panel), relative to the plate convergence rate. The steady state field for the BSM is only a schematic representation of “complex asthenospheric motions” assumed by Savage [1983], and not a computed field. 2-5
- Figure 2-3. Geometric comparison of the ESPM with planar (left column) and curved (right column) geometry. In each column, the top row is the ESPM in the limit of a very thick plate (the BFM); the bottom row is the ESPM in the limiting case of negligible plate thickness (the BSM). Note that the “dip” of the curved fault is defined at a point where the plate straightens out. The dip of the curved fault at the trench is assumed to be zero. Other notation and assumptions are identical to those in Figure 2-1. 2-12
- Figure 2-4. Appropriate application of the BSM to curved faults. Backslip must be applied to the curved interface geometry appropriate for a subduction zone, instead of to its tangent at the downdip end of the locked zone. The curved fault (solid gray line) resembles the subduction thrust interface geometry below the island of Nias, offshore of Sumatra ( $\theta_{top} = 3^\circ$ ,  $\theta_{bot} = 27^\circ$ [Hsu et al., 2006]). The tangent-approximation to the curved fault [Chlieh et al., 2004; Simoes et al., 2004; Chlieh et al., 2008] is represented by the dashed black line. The top panel presents the faults in cross-sectional view.  $x^*$  ( $= x/D_{Lock}$ ) is the dimensionless distance perpendicular to the trench;  $z^*$  ( $= z/D_{Lock}$ ) is the dimensionless depth. The origin of the dimensionless  $x^*-z^*$  system is at the location of the trench axis. Vertical surface velocity profile,  $V_z^*$  (middle panel), and horizontal surface velocity profile,  $V_x^*$  (bottom panel), are scaled by the uniform plate convergence velocity,  $V_p$ . 2-13
- Figure 2-5. Comparison of deformation for the BSM and the ESPM with plates of different thickness,  $H$ , for a realistic curved fault geometry. In all panels, the thick gray solid curves represent the BSM, and the extent of the locked zone is shaded in yellow. The blue solid curve coinciding with the BSM surface velocities is the ESPM with zero plate thickness. The thick light-blue curve is the surface velocity field due to the buried thrust downdip of the locked zone (i.e., the BFM). The thin dashed red curve coinciding with the BFM surface velocity field is the ESPM having an “infinite” plate thickness. In all cases, the imposed uniform slip rate is in the normal sense for the BSM (backslip), and reverse (thrust) sense for the ESPM. Panel organization and non-dimensionalization of the plot axes is identical to that in Figure 2-4. 2-16
- Figure 2-6. Kinematics of plate bending. (a) Bending of the plate at the trench for the ESPM with linear fault interface geometry; Motion of subducting material through the trench results in shearing as indicated by the shaded area. Axial hinges of folding can be kinematically represented by

dislocations, across which incoming material in the plate experiences a change in direction, but not in magnitude. (b) Bending of the plate at the trench for the ESPM with a non-planar (or curved) fault interface geometry. The curved interface is represented by a number of linear segments having different slopes, and the number of hinges corresponds to the number of planar segments representing the discretization. (c) Velocity vector diagram showing required slip rate on an axial hinge to kinematically restore strains due to bending at the hinge. 2-19

Figure 2-7. The surface deformation field for the ESPM for a planar plate geometry: (a) the ESPM with no locked zone is equivalent to the long-term, steady state plate motion (solid black line). The surface velocity field due to the axial hinge (thin dashed gray line) cancels the effect of plate flexure at the trench (thin solid black line), resulting in net zero long-term strain accumulation over the seismic cycle (thick solid black line). (b) Effect of a single axial hinge on the ESPM with a locked megathrust fault. Again, note that the ESPM predicts the correct sense of motion for the oceanic plate. The sum of the ESPM (thin solid black line) and axial hinge (thick dotted gray line) velocity fields — shown as the thick dashed black line — exactly equals that for the equivalent BSM (thick solid gray line). Panels and plot axes are as described in Figure 2-4. 2-22

Figure 2-8. Surface deformation field for the ESPM for curved plate geometry: (a) the ESPM with no locked zone is equivalent to the long-term, steady state plate motion (solid black line). The axial hinges or velocity gradient corrections are introduced at positions corresponding to the discretization resolution of the curved fault. The surface velocity field due to axial hinges or a velocity gradient (thin dashed gray line) cancels the effect of plate flexure at the trench (thin solid black line), resulting in net zero long-term strain accumulation over the seismic cycle (thick solid black line). Note that the peak uplift due to the bending of a curved plate is shifted arc-ward in comparison to the peak for the planar geometry (Figure 2-7). (b) Effect of the plate flexural field (axial hinges or velocity gradient corrections) on the ESPM with a locked megathrust fault. The sum of the ESPM (thin solid black line) and axial hinge (thick dotted gray line) velocity fields — shown as the thick dashed black line — exactly equals that for the equivalent BSM (thick solid gray line). Panels and plot axes are as described in Figure 2-4. 2-23

Figure 2-9. Comparison of predicted surface velocity profiles from the elastic plate bending flexural field [bottom panel, for plate thicknesses of 25 (dashed gray), 50 (gray), and 100 km (black)], with that of the long-term along-strike averaged trench-perpendicular topographic profile (middle panel, with error bars in blue) for the Sumatran subduction zone (top panel, and inset map). Note that the location of the peak uplift-rate is independent of plate thickness,  $H_{slab}$  (bottom panel). The trench profile in the map is from Bird [2003], and the rectangle indicates the zone of along-strike averaging of the plate geometry (top panel) as well as bathymetry (middle panel). The geometry of the mean plate interface profile (top panel, only  $H_{slab}=100$  km is shown) is similar to that assumed in [Hsu et al., 2006], and attains a dip of  $30^\circ$  at a depth of  $\sim 27$  km below the islands. Note the correspondence in the location of the peak values in the middle and bottom panels. See text for details. 2-32

Figure 3-1. Effect of doubling the width of the transition zones updip and downdip of the locked megathrust interface for the ESPM and the BSM.  $f_{tr}$  is the fractional length of the transition zone relative to the width of the locked megathrust,  $s_{trans}/s_{lock}$ . For updip transition zones (parts a and b), results are presented for  $f_{tr} = 0, 0.125,$  and  $0.25$ . For downdip transition zones (parts c and d), results are presented for  $f_{tr} = 0, 0.25, 0.5,$  and  $1$ . Axes are as described in text. 3-7

Figure 3-2. BSM inversions of ESPM synthetics. Each column represents results for a given plate-thickness to locking depth ratio:  $H/D_{lock} = 0.01$  (BSM), 1, and 3. (a) 1000 best-fit BSM in the  $s_{lock}-\theta$  parameter space that fit as many samples of ESPM-based noisy synthetic data for the specified  $H/D_{lock}$  ratio. Shown are the lowest misfit solutions satisfying only vertical data (top row), only horizontal data (middle row), and sum of the two datasets (bottom row). The corresponding  $1-\sigma$  error-ellipses are shown in red. (b) Misfit between the BSM at each point in the  $s_{lock}-\theta$  parameter space and one of the synthetic data samples in (a). (c) Best-fit backslip model (solid red line), satisfying both the horizontal and vertical synthetic data (solid gray lines) — corresponding to the yellow  $\otimes$  in the bottom row of (b). The best-fit BSMs are as follows:  $\theta = 25^\circ, D_{lock} = 40$  km

(identical to the ESPM, for column 1);  $\theta = 22.5^\circ$ ,  $D_{lock} = 38.3$  km (column 2); and  $\theta = 20^\circ$ ,  $D_{lock} = 39.3$  km (column 3). The BSM corresponding to  $\theta = 25^\circ$ , and  $D = 40$  km (dashed green line) is also shown. The top row shows the subduction zone geometry, the middle row shows vertical velocities, and the bottom row shows horizontal velocities. Dashed vertical lines mark the nearest geodetic observation point to the trench

3-11

Figure 3-3. Effect of curvature on the BSM surface velocity predictions. The curved fault (solid black line) resembles the subduction thrust interface geometry below the island of Nias, offshore of Sumatra ( $\theta_{top} = 3^\circ$ ,  $\theta_{bot} = 27^\circ$  [Hsu et al., 2006]). The gray solid line represents a planar fault having the same end-points as the curved fault, and the dashed gray line represents the tangent-approximation to the curved fault. The dotted line represents a shallow dipping fault that approximates the shallow part of the curved interface. See text for details. The top row presents the fault in cross-sectional view. In all cases, uniform normal slip was imposed on the fault patch. Plot axes are as described in text.

3-14

Figure 3-4. Schematic illustration of the relative locations of surface observables,  $x_{hinge}$ ,  $x_{lock}$ , and  $x_{max}$ , using the vertical velocity profile for the curved fault presented in Figure 3-6.

3-16

Figure 3-5. Location of the maximum vertical velocity ( $x_{max}$ ), zero vertical velocity ( $x_{hinge}$ ), the surface projection of the bottom of locked fault ( $x_{lock}$ ), and the differences between them, as a function of the length of the locked fault patch,  $s$ , and dip angle,  $\theta$ . Each parameter is plotted for  $s$  ranging from 25 to 200 km, in steps of 25 km. Thicker curves represent fault lengths of 50, 100, 150, and 200 km. (a) Planar faults: Blue curves (cutting across the  $s$ -curves from the top left to bottom right) are lines of constant locking depth (10 to 50 km, in steps of 10 km). Theoretical estimates are presented in dark yellow. (b) Curved faults: Red curves (cutting across the  $s$ -curves from the bottom right to top left) are lines of constant radii of curvature (100 to 300 km, in steps of 50 km). Blue curves are the same as in (a). Theoretical estimates for planar faults are presented in yellow in the bottom two panels for comparison to (a).

3-18

Figure 3-6. Dimensionless plots of the variation in the location of  $x_{max}$  and  $x_{hinge}$  as a function of fault dip in the BSM having a planar (a, c) or curved (b, d) plate interface geometry, with (c, d) or without (a, b) a transition zone (of fractional length,  $f_{tr} = 25\%$ ) downdip of the locked megathrust zone. See text for definitions of y-axis parameters. Top panels: Dimensionless relative distance between  $x_{max}$  and  $x_{lock}$  ( $\Delta x_m^*$ ) as a function of the dip of the BSM fault; Second-from-top panels: Dimensionless relative distances between  $x_{hinge}$  and  $x_{lock}$  ( $\Delta x_h^*$ ); Third-from-top panels: Mean value of plots in top two panels; Second-from-bottom panel: Difference between the top two panels; Bottom panels: ( $x_{hinge}/x_{max}$ ). Theoretical estimates for planar faults without any transition zone (thick gray lines from part(a)) are repeated for each panel in parts (b)-(d) for comparison purposes.

3-21

Figure 4-1. Workflow for the *Fslip* software developed to generate, simulate and visualize models of slip evolution on realistic fault surfaces. For simplicity, the exact long-from module names are not used for the lower level modules or Matlab pre-/post-processor scripts (e.g., *Fslip.Model.Out*, *FslipMATproc*, etc.). The matlab component, *EvolveSlip*, solves the forward problem, given the fault traction and surface displacement kernels, rheology, initial and boundary conditions for the 3D megathrust surface. The Matlab output is post-processed in two stages — in a Matlab and then in *Fslip* to generate VTK files and “dashboards” for visualization. See text for details.

4-5

Figure 4-2. An automatically generated Paraview dashboard showing fault traction components ( $\tau_S$ , top row;  $\tau_D$ , middle row;  $\tau_N$ , bottom row) due to dip-slip on all fault patches (column 1), slip on each asperity (column 2: the duller color is due to the use of transparency in Paraview to show all asperity contributions in a single panel), slip on the semi-infinite extensions of the fault (or backslip, column 3), and the residuals obtained from the superposition (Equation 1). For a planar fault, these residuals were found to be zero, as expected.

4-18

Figure 4-3. An automatically generated Paraview dashboard showing fault traction components ( $\tau_S$ , top row;  $\tau_D$ , middle row;  $\tau_N$ , bottom row) due to strike-slip on all fault patches (column 1), slip on each asperity (column 2: again, the duller color is due to the use of transparency in Paraview to show all asperity contributions in a single panel), slip on the semi-infinite extensions of the fault (or backslip,

column 3), and the residuals obtained from the superposition (Equation 1). For a planar fault, these residuals are zero, as expected. 4-19

Figure 4-4. An automatically generated Paraview quality control dashboard for unit dip-slip on the fault and asperities, showing the rheological parameter distribution (rightmost middle panel), initial slip distribution (bottom-right panel), tractions (top two rows of panels), and surface displacements. Such figures are automatically generated and used for visualizing model inputs before a run or for debugging after a run. All 3D plots are colored on a log-scale, to bring out any small-scale heterogeneities. 4-20

Figure 4-5. An automatically generated Paraview quality control dashboard for unit strike-slip on the fault and asperities, showing the rheological parameter distribution (rightmost middle panel), initial slip distribution (bottom-right panel), tractions (top two rows of panels), and surface displacements. Such figures are automatically generated and used for visualizing model inputs before a run or for debugging after a run. All 3D plots are colored on a log-scale, to bring out any small-scale heterogeneities. 4-21

Figure 4-6. (a) Strike-slip, and (b) dip-slip components of the non-dimensional backslip velocity field applied to the 3D fault surface. Color-scale indicates the same range of magnitudes in both figures as well as for the arrows. 4-27

Figure 5-1. Asperity configuration chosen for the northern Japan megathrust interface, and the epicentral locations of the last earthquake(s) prior to the year 2000 (blue stars, multiple around an asperity start indicate two ruptures within the same year). 5-14

Figure 5-2. Convergence of spun-up fault tractions over a full cycle with increasing mesh resolution (RES0 through RES2) around the asperity, for a JT2 mesh (see Section 4.7). Significant improvement is not observed between RES1 and RES2, even though the latter has three-times as many elements in the asperity transition zone compared to the former. 5-17

Figure 5-3. Spin-up of mean fault tractions, and their moving averages for a linear viscous fault rheology with  $\alpha' = 0.1$ . The gray curve represents the mean tractions at every time-step. The light blue curve at the bottom represents a single pick of the grey curve at the end of each cycle of duration equal to the reference time,  $T_0$ . The moving average window,  $T_{mov} = 8$  (dark blue) corresponds to  $T_{CRS}$ . See text for details. 5-19

Figure 5-4. Plot of slip-rate (left column) and cumulative fault slip (right-column) at the end of the first reference cycle ( $T_0$ ), post model spin-up, for the linear viscous rheology used in Figure 5-3. Top rows show the strike-slip component, bottom rows show the dip-slip component. As expected, the right column looks nearly identical to the input backslip velocities (Figure 4-6), except for the asperities themselves, which will match the surrounding fault only at the end of the  $T_{CRS}$ -cycle. See text for details. 5-21

Figure 5-5. Spin-up tractions for northern Japan megathrust, for a rate-strengthening frictional rheology, with  $\rho \approx 10$ , and  $\alpha \approx 10^5$  Pa ( $\alpha' \approx 1$ ) 5-23

Figure 5-6. Evolution of tractions over the “present” reference cycle of 75 yrs. Only the most recent events prior to the end-date of GPS velocity measurements (2000) are identified for each asperity. The two unlabeled events correspond to the 1968 “Tokachi-Oki” event off the Sanriku coast (but occurring in 1964 due to the approximate rupture interval chosen in Section 5.3), and the 2003 M8.2 Tokachi-oki 2003 event (here, occurring in 2002). 5-24

Figure 5-7. (a) Synthetic Tokachi-oki coseismic displacements and (b) actual coseismic displacements from 2003  $M_w$  8.2 Tokachi-oki earthquake [Koketsu *et al.*, 2004]. The synthetic displacements are scaled relative to the imposed mean coseismic slip of 6.4 m (Table 5-1). 5-25

Figure 5-8. Sample synthetic surface displacement time-series over the last 75 yr reference cycle for two stations (left: 960533; right: 950156; both located along the Sanriku coast). Blue dashed lines

indicate the observed and synthetic GPS velocity estimation window, and the slopes used to infer the velocities are indicated as grey lines within this window. 5-26

Figure 5-9. Observed (left), synthetic-backslip (middle), and residual (right) horizontal GPS velocity fields (relative to a fixed Okhotsk plate) for the period 1996-2000. Synthetics were computed assuming that the fault is locked only at the asperities late in the cycle, and the rest of the fault surface is frictionless. Asperities are shaded in light gray and off-shore of the northern Japan coastline. Thick black arrows indicate the plate convergence direction. Velocities are scaled relative to the plate velocity of 8.3 cm/yr for the Pacific Plate off Tohoku. The color intensity has the same scale in each plot. 5-28

Figure 5-10. Observed (left), synthetic-frictional (middle), and residual (right) horizontal GPS velocity fields (relative to a fixed Okhotsk plate) for the period 1996-2000. Synthetics were computed assuming that slip on the fault surface is governed by rate strengthening friction with  $\alpha' \approx 1$ . Asperities are shaded in light gray and off-shore of the northern Japan coastline. Thick black arrows indicate the plate convergence direction. Velocities are scaled relative to the plate velocity of 8.3 cm/yr for the Pacific Plate off Tohoku. The color intensity has the same scale in each plot. 5-28

Figure 5-11. Slip-rates at the end of the cycle, for a fault surface governed by rate strengthening friction with  $\alpha' \approx 1$ . Notice the much larger areas of near-zero slip-rates compared to the upper-left panel of Figure 5-4. 5-29

Figure 5-12. Observed (left), synthetic-frictional (middle), and residual (right) vertical GPS velocity fields (relative to a fixed Eurasian plate) for the period 1996-2000, for the same frictional rheology as in Figure 5-10. 5-31

## LIST OF TABLES

Table 2-1. Notation.....	2-35
Table 3-1 Theoretical Estimates for the horizontal distance between the trench and the surface projection of the downdip end of the locked zone, $x_{lock}$ , for planar and curved faults locked up to the trench. Notation: $\bar{X} = \left(\frac{X_{hinge} + X_{max}}{2}\right)$ , $X_h = X_{hinge}$ , $X_m = X_{max}$ .....	3-22
Table 3-2. Theoretical Estimates for the horizontal distance between the trench and the surface projection of the bottom of the locked patch, $x_{lock}$ , for planar and curved faults having transition segments immediately downdip of the locked zone. The following results are for transition zones having along-fault lengths of up to 25% of the length of the locked zone. Notation: $\bar{X} = \left(\frac{X_{hinge} + X_{max}}{2}\right)$ , $X_h = X_{hinge}$ , $X_m = X_{max}$ .....	3-22
Table 3-3. Notation.....	3-27
Table 4-1. Work-flow for generating fault patches from a geo-referenced subducting slab surface geometry. .....	4-10
Table 5-1. Summary of asperity parameters for Northern Japan. The last column represents the time from the present (here, the year 2000, which marks the end of the time-period over which the observed GPS velocities were computed in Hashimoto et al. [2009]) to the most recent earthquake for each asperity.....	5-13

## *Chapter 1*

### INTRODUCTION

Geodetic data collected since the 1990s from subduction zones have been interpreted using simple kinematic elastic dislocation models [Savage, 1983, 1995; Zweck *et al.*, 2002; Wang *et al.*, 2003; Chlieh *et al.*, 2008b]. However, over the last decade, a vast amount of geodetic data has become available from various subduction zones around the world, having not only good spatial coverage (using InSAR, see, e.g., Massonnet and Feigl [1998], Simons and Rosen [2007]), but also high temporal density and resolution (high-rate GPS, see for e.g., Larson *et al.* [2003]). Such dense datasets of velocity vectors provide an opportunity to explore more complex kinematic or quasi-dynamic mechanical models of the seismic cycle in subduction zones in order to estimate for instance, elastic thickness of the downgoing plate, or frictional properties on realistic 3D megathrust interface between the subducting and overriding plates. Eventually, such information will allow us to refine assessments of potential seismic hazard within different geographic regions of a plate boundary zone, thereby providing guidance on where to focus preventative measures (such as retrofitting buildings), and resources for emergency preparedness (such as evacuation plans and their facilitation).

Early theoretical attempts to model the kinematics of deformation during the entire seismic cycle were made in the late 1970s to mid 1980s, using 2D earth models having a single subduction interface embedded in (a) a fully elastic half-space [Savage, 1983], (b) an elastic layer (lithosphere) overlying a viscoelastic half-space (asthenosphere) [Thatcher and Rundle, 1979; Rundle, 1982; Thatcher and Rundle, 1984; Cohen, 1994], (c) an elastic layer (lithosphere) over a viscoelastic layer (asthenosphere), over an elastic half-space [Sato and Matsu'ura, 1988; Matsu'ura and Sato, 1989], or (d) a viscoelastic lithosphere over viscoelastic asthenosphere, over a viscoelastic half-space [Sato and Matsu'ura, 1992, 1993; Fukahata and Matsu'ura, 2006]. These models considered gravity and realistic subduction interface geometries. Models (a) and (b) assumed that there is no net accumulation of deformation in the overriding plate. Models (b) require two

parameters that have high uncertainties in addition to those in elastic dislocation models – the asthenospheric viscosity, and the recurrence time for seismic events. The key result from models (b) was that the surface velocity field was much larger than the corresponding elastic field [model (a)] right after a megathrust event, and much smaller than the elastic field just before the subsequent event. So, the integrated velocity field during the interseismic period exactly cancels the coseismic displacements after each cycle, resulting in zero net deformation of the overriding plate. Including gravity diminishes the magnitude of viscoelastic deformation in the model, which reaches steady state faster than in the zero-gravity case [Rundle, 1982]. Because the more complex physics included in these models introduces additional parameters, they can fit the coseismic, postseismic, and at least in some cases, the interseismic deformation fields well [Thatcher and Rundle, 1984]. Models (c) and (d) predict a net accumulation of deformation in the overriding plate after each seismic cycle, owing to the steady state motion at the rate of plate convergence along the curved fault interface within the upper elastic lithosphere — this conclusion is unaffected by the inclusion of gravity. As we will see in Chapter 1, this so-called permanent deformation is very similar to that required to support elastic stresses resulting from bending of the subducting plate at the trench. Although this runaway surface deformation can be modulated by parameterizing accretion, erosion and sedimentation during the seismic cycle [Sato and Matsu'ura, 1993; Cohen, 1999], such complexity introduces many more free parameters having high uncertainties. Furthermore, Savage [1995] argued that the coseismic, postseismic and interseismic fields can be fit equally well (given the data uncertainties) with a modified elastic dislocation model having a fault patch downdip of the locked zone that slips only post-seismically — and that it is hard to demonstrate that asthenospheric relaxation contributed to interseismic deformation on the surface of the overriding plate.

Going beyond these semi-analytical approaches, finite-element-method (FEM)-based models also do not do better than dislocation models, given the current spatial resolution and uncertainty limits of geodetic data. Quasi-static models that are computationally more challenging, and are driven by dynamically consistent boundary conditions have also been developed. It is illustrative to consider two representative studies that model

the two distinct types of plate compression zones — subduction and collision zones — using FEM models.

Williams and McCaffrey [2001] developed a 2D quasi-static, self-gravitating, purely elastic finite element model of the Cascadia subduction zone beneath Oregon and southwest Washington. The quasi-static deformation fields within the overriding plate are entirely determined by uniform and constant shear tractions along the locked subduction interface (a proxy for the effect of locking), as well as along its bottom surface (a proxy for upper mantle flow). Using that model, they attempted to constrain shear stresses acting along the fault interface and the bottom of the overriding plate using regional geodetic data. They compare the surface velocity and tilt-rate fields predicted by their preferred FEM with those of an equivalent elastic dislocation model having the same fault geometry, and find that both models fit the vertical velocities (at a single observation point) as well as the observed surface tilt rates equally well. Their main argument for preferring the FEM was its ability to better fit the location of the change in slope of the horizontal velocity profile, as well as a broad region of elevated horizontal velocities just beyond this slope change. As is well known, and also illustrated in Chapter 2, the location of the change in slope of the horizontal velocity profile predicted by an elastic dislocation model (with a locked zone extending all the way up to the trench) is sensitive to the abruptness of transition between zero to finite aseismic slip at the downdip end of the locked zone.

Vergne et al., [2001] compared the predictions of interseismic surface velocities and crustal stress concentrations from a realistic 2D finite element model of an intra-continental thrust fault — which is kinematically and dynamically similar to a subduction thrust interface — with an elastic dislocation model having the same fault geometry. The 2D finite element model incorporated a layered crust and mantle with temperature dependent rheology, topography, gravity, and surface processes, and fit all available constraints on interseismic and long-term surface displacements. Their main conclusion was that the dislocation model fit the data as well as the finite element model, including

predictions of micro-seismicity near the bottom of the locked patch during the interseismic period.

So, unless complexities such as poro-elasticity, material heterogeneity, anisotropy, or inelastic bulk rheology are included in modeling the subduction zone [e.g., Masterlark, 2003], simple elastic dislocation models would do as well as FEM in fitting current geodetic data. It seems reasonable, therefore, that such models — which can be essentially described with only two parameters, the extent of the locked fault interface, and the plate geometry — have been widely used in modeling interseismic period geodetic data in subduction zones, and have been used to successfully fit geodetic observations using realistic plate interface geometries [Savage, 1983, 1995; Zweck *et al.*, 2002; Wang *et al.*, 2003; Chlieh *et al.*, 2008b].

Here, we want to understand late post-seismic and interseismic deformation in subduction zones, and as such, only consider a purely elastic crust (represented by the half-space for the purpose of computing the surface deformation field). We do not seek to model the complex dynamics of rupture nucleation, interaction between asperities, or rupture propagation [see, e.g., Rice, 1993; Lapusta and Rice, 2003; Kato, 2008; Perfettini and Ampuero, 2008]. We also do not model topographic evolution on time-scales longer than the interseismic since we use purely linear elastic bulk rheology that, by definition, cannot accumulate net long-term (geologic) deformation while keeping the stresses bounded. Instead, we pursue kinematic and quasi-dynamic approaches to modeling slip (and its evolution) on the fault over the seismic-cycle. Throughout this work, we assume that crustal deformation is localized along fault zones, and the bulk of the crust is rigid, and perfectly elastic. We therefore ignore any bulk relaxation processes in the crust owing to viscous or poro-elastic effects. While this assumption may not hold true over the geologic time-scale, over the span of several seismic cycles ( $<10^4$  yrs) that we model here, it is reasonable to assume that crustal response to constant tectonic loading is elastic. This assumption is borne out by the ability of elastic dislocation models to fit much of the geodetic data collected over the past couple of decades. Further, elastic deformation fields can provide intuition about regions that could potentially experience

long-term deformation, where it may be more appropriate to use non-linear rheologies. Therefore, within the context of elastic crustal deformation, we want to ask the following questions:

### **Why does the backslip model fit geodetic observations so well?**

As a first step towards more complex models for interseismic deformation in subduction zones, we want to ask how the thickness of the downgoing plate influences the deformation field at the surface of the overriding plate. We also want to understand why the backslip model [Savage, 1983] works so well for interpreting interseismic geodetic data in subduction zones. In essence, how can one reconcile this half-space model with subduction of a downgoing plate? While standard textbooks discuss the elastic flexure of a subducting plate at the trench, the effect of this bending on overriding plate deformation has not been systematically analyzed so far. In Chapter 2, we introduce an elastic subducting plate model (ESPM), and compare its predictions with that of the backslip model (BSM), in order to address the above questions. The ESPM links elastic plate flexure processes to interseismic deformation, and helps clarify under what conditions the BSM is appropriate for fitting interseismic geodetic data at convergent margins. We show that the ESPM is identical to the BSM in the limiting case of zero plate thickness - thereby providing an alternative motivation for the BSM. The ESPM also provides a consistent convention for applying the BSM to any megathrust interface geometry. Even in the case of non-negligible plate thickness, the deformation field predicted by the ESPM reduces to that of the BSM if stresses related to plate flexure at the trench are released either continuously and completely at shallow depths during the interseismic period, or deep in the subduction zone (below  $\sim 100$  km). However, if at least a portion of these stresses are not continuously released in the shallow portion of the subduction zone (via seismic or aseismic events), then the predicted surface velocities of these two models can differ significantly at horizontal distances from the trench equivalent to a few times the effective interseismic locking depth. We also suggest potential geographic areas where the subduction zone geometry is favorable for testing the ESPM in the near future

— especially as onshore geodetic coverage improves in these areas, and ocean-bottom geodetic measurements become available.

**What are some practical surface observables that have immediate relevance to field-geologic studies or building intuition for numerical modeling?**

Surface observables — especially, the location of the zero-crossing (hinge-line) and peak value of uplift rates — can be useful tool in determining the approximate location (to within a horizontal distance of 50 km) of the location of the downdip end of the locked portion of a megathrust interface. These two uplift-rate values are important because gradients in the surface deformation field (strains) are strongest ocean-ward of this region, and highest right above the downdip end of the locked patch. Geodetic or field-geologic observations can be taken more cost-effectively by choosing to sample at a higher spatial resolution in the zone of peak strains (using either land-based or ocean-bottom stations), and more sparsely farther away. If a reasonable estimate for slab dip can be obtained, then the location of this high-strain region can be narrowed down to a zone as narrow as 10–15 km. So, while the relationship between the hinge-line and downdip end of the locked zone is not necessary for geodetic inversions per se, such information can be very helpful in optimally collecting the data for these inversions. The relationships between surface observables and ranges of fault dip, as well as the effect of fault curvature and subducting plate thickness are discussed in Chapter 3. We show that irrespective of the fault geometry, the mean of the location of zero-vertical surface velocities,  $x_{\text{hinge}}$ , and the peak surface vertical velocities,  $x_{\text{max}}$ , gives a good approximation for the surface projection of the locked zone,  $x_{\text{lock}}$ , for both the BSM and the ESPM with shallow dipping plate interfaces ( $< 30^\circ$ ). However, in the presence of a transition zone, or a large plate thickness,  $x_{\text{max}}$  gives a more reliable estimate for  $x_{\text{lock}}$ , and hence, the extent of the locked zone. Therefore, the common notion that the location of the peak in vertical velocities ( $x_{\text{max}}$ ) determines the extent of the locked megathrust ( $x_{\text{lock}}$ ), is valid only if a transition zone is assumed downdip of the locked interface.

**For a given subduction zone, what fraction of the current surface deformation field inferred from geodetic data can be explained by the stress-shadow effect of ruptures during the past century on known seismic asperities?**

During the past decade, with the availability of high-resolution spatio-temporal geodetic data as well as strong-motion seismic data, the characteristic asperity model for the seismic cycle [e.g., Ruff, 1992] has been shown to apply to the Sumatra [Chlieh *et al.*, 2008b; Sieh *et al.*, 2008; Konca *et al.*, 2009], Kurile [Nanayama *et al.*, 2003; Satake and Atwater, 2007], Chile [Cisternas *et al.*, 2005; Satake and Atwater, 2007], and northeastern Japan [Tanioka *et al.*, 1996; Nakayama and Takeo, 1997; Robinson and Cheung, 2003; Miyazaki *et al.*, 2004; Miura *et al.*, 2006; Umino *et al.*, 2006] subduction zones. For the Japan trench, for instance, it is thought that the ruptures off Miyagi [Miura *et al.*, 2006; Umino *et al.*, 2006], Sanriku [Tanioka *et al.*, 1996; Nakayama and Takeo, 1997], and Tokachi [Robinson and Cheung, 2003; Hamada and Suzuki, 2004; Miyazaki *et al.*, 2004; Satake *et al.*, 2006] occurred repeatedly over roughly the same region of the subduction megathrust. Owing to the fact that geodetic and seismic data resolution was much poorer during the earlier part of the last century — and good spatio-temporal coverage was lacking in most subduction zones excluding Japan even as recently as the 1990s — the exact details of coseismic slip distribution vary between each of these “repeating” sequence of ruptures. However, the picture that seems to be emerging is that, overall, coseismic slip tends to be restricted to only a small fraction of the shallow seismogenic megathrust interface — at “asperities” — while the rest of the interface slips aseismically during the postseismic or interseismic periods of the seismic cycle.

Inversions of geodetic data from interseismic periods, however, produce models that are locked (i.e., are modeled to have backslip) over spatially smooth and extensive region of the seismogenic megathrust [Bürgmann *et al.*, 2005; Suwa *et al.*, 2006; Chlieh *et al.*, 2008b], in contrast to the smaller discrete asperities estimated by the above earthquake source studies. Such smooth, broad regions may be a consequence of a lack of model resolution and the resulting need for regularization inherent to the use of onshore geodetic data. It is also possible that the inferred interseismically coupled regions are

larger than the collective asperity sizes for known earthquakes due to an incomplete earthquake catalogue, and may imply the potential for large earthquakes in the future. Hence, the different levels of apparent coupling implied by interseismic and seismic-source inversions (Figure 1-1) have very different implications for regional seismic hazard.

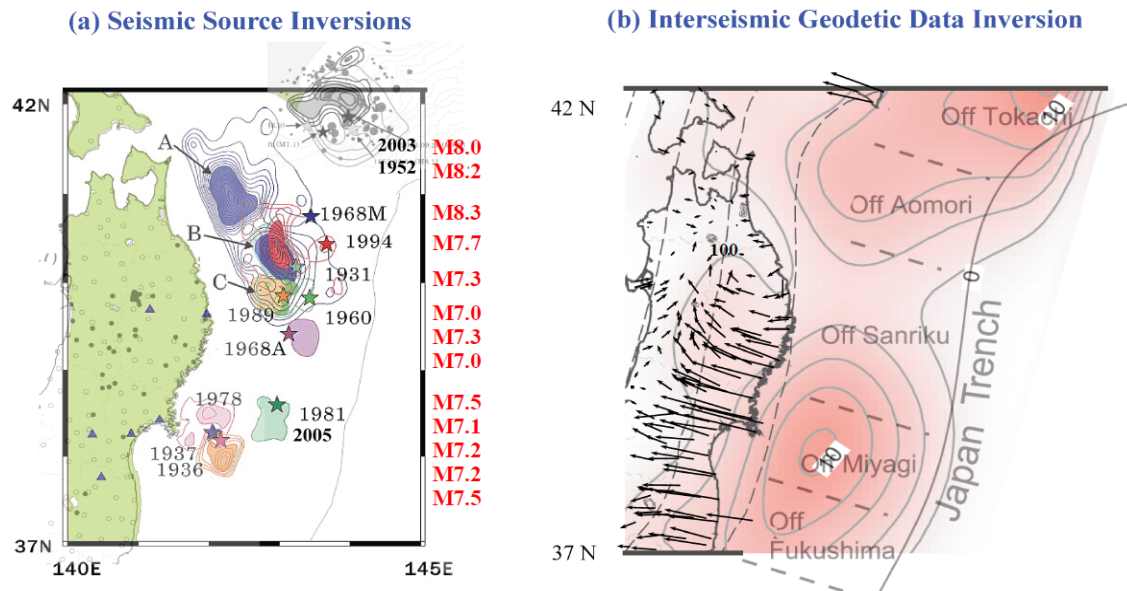


**Figure 1-1.** (a) Coseismic slip and (b) interseismic slip deficit (“backslip”) estimates for the megathrust interface off northeastern Japan. Adapted from Yamanaka and Kikuchi [2003; , 2004] and Suwa et al. [2006].

Bürgmann et al., [2005] tested several asperity models for the Kamchatka subduction zone, but assumed that all areas outside the asperities were freely slipping — so they did not model slip evolution around the asperities. Recently, Hetland et al. [2010] and Hetland and Simons [2010] developed a 3D mechanical model of stress-dependent interseismic creep along the megathrust, considering frictional rheologies. Their mechanical “toy”-models predict that late in the seismic cycle, there are relatively smooth, long wavelength regions of very low slip-rates on the megathrust interface surrounding these asperities, owing to the “stress-shadow” effect of seismic ruptures. The effect of such “physical” smoothing on surface velocity predictions may be

indistinguishable from the artificial smoothing produced by model regularization in inversions of interseismic geodetic data.

Here, assuming that (i) known asperities persist across multiple earthquake cycles, and (ii) ruptures are both time- and slip-predictable [see, e.g., Shimazaki and Nakata, 1980], we test the hypothesis that mechanical coupling on asperities inferred from the locations of past earthquakes alone is sufficient to explain currently available geodetic observations for Japan — or alternatively, that these data require additional regions of the Japan Trench megathrust to be coupled. Underlying our approach is the assumption that known asperities persist across multiple earthquake cycles. The modeling approach and setup are discussed in Chapter 4, and results presented in Chapter 5. The preliminary results presented here show that we can explain most of the horizontal interseismic GPS velocities in northern Japan, by assuming mechanical coupling only on the inferred asperities.

**As a corollary to the last question, can the late post-seismic and interseismic response in models incorporating these asperities tell us something about the rheology of the megathrust interface over the seismic-cycle timescale?**

Recently, several research groups have attempted to infer fault rheologies from inversions of post-seismic geodetic data at plate-boundary zones — for e.g., Sumatra [Hsu et al., 2006], California (Landers [Perfettini and Avouac, 2007], Parkfield [Johnson et al., 2005]), Taiwan [Perfettini and Avouac, 2004], and Japan (Tokachi-oki [Fukuda et al., 2009]). These have used either spring-slider type models [Perfettini and Avouac, 2004; Fukuda et al., 2009] or planar frictional faults made up of rectangular patches embedded in a half-space [quasi-static models, e.g., Johnson et al., 2005; Perfettini and Avouac, 2007]. The model introduced by Hetland et al. [2010] and Hetland and Simons [2010] (summarized in Sections 4.1 and 5.2) belongs to this class of quasi-static models. Spring-slider models have no spatial length-scale (or explicit fault geometry) associated with them, predictions using such models have only local applicability. On the other hand, fully heterogeneous fault frictional properties can be modeled by the latter class of

models. There is another class of forward models that consider the dynamic evolution of stresses and slip on a frictional fault surface due to non-uniform rheology [e.g., Hori, 2006; Kato, 2008]. Currently, such quasi-dynamic models focus on simulating seismic ruptures only, and are not constrained by surface geodetic observations. In contrast, the quasi-static models mentioned above are designed to be constrained by geodetic observations and allow us to ask an important question from a forward modeling standpoint: what is the effect of lateral and depth variations in rheological parameters on predictions for afterslip and postseismic/ interseismic deformation? Another important question is the practicality of considering different rheologies (and therefore, different evolution time-scales) over different regions of the megathrust interface. For the preliminary results presented in Chapter 5, we only consider uniform rheological properties over the entire fault surface.

## References

- Bürgmann, R., M. Kogan, V. Levin, G.E. Hilley, G. Steblov and E. Apel (2005), Interseismic coupling and asperity distribution along the Kamchatka subduction zone, *J. Geophys. Res.*, 110, B07405, doi:07410.01029/02005JB003648.
- Chlieh, M., J.P. Avouac, K. Sieh, D.H. Natawidjaja and J. Galetzka (2008), Heterogeneous coupling of the Sumatran megathrust constrained by geodetic and paleogeodetic measurements, *J. Geophys. Res.*, 113, B05305, doi:05310.01029/02007JB004981
- Cisternas, M., B.F. Atwater, F. Torrejn, Y. Sawai, G. Machuca, M. Lagos, A. Eipert, C. Youlton, I. Salgado, T. Kamataki, M. Shishikura, C.P. Rajendran, J.K. Malik, Y. Rizal and M. Husni (2005), Predecessors of the giant 1960 Chile earthquake, *Nature*, 437, 404-407.
- Cohen, S.C. (1994), Evaluation of the Importance of Model Features For Cyclic Deformation Due to Dip-Slip Faulting, *Geophys. J. Int.*, 119, 831-841.
- Cohen, S.C. (1999), Numerical Models of Crustal Deformation in Seismic Zones, *Adv. Geophys.*, 41, 133-231.
- Fukahata, Y. and M. Matsu'ura (2006), Quasi-static internal deformation due to a dislocation source in a multilayered elastic/viscoelastic half-space and an equivalence theorem, *Geophys. J. Int.*, 166, 418–434.
- Fukuda, J., K. Johnson, K.M. Larson and S. Miyazaki (2009), Friction parameters inferred from the early stages of afterslip following the 2003 Tokachi-oki earthquake, *J. Geophys. Res.*, 114, B04412, doi:04410.01029/02008JB006166.
- Hamada, N. and Y. Suzuki (2004), Re-examination of aftershocks of the 1952 Tokachi-oki earthquake and a comparison with those of the 2003 Tokachi-oki earthquake, *Earth Planets Space*, 56, 341–345.
- Hetland, E.A. and M. Simons (2010), Postseismic and interseismic deformation due to fault creep II: Transient creep and interseismic stress shadows on megathrusts. , *Geophys. J. Int.*, 181, 99–112, doi:110.1111/j.1365-1246X.2009.04482.x.
- Hetland, E.A., M. Simons and E.M. Dunham (2010), Postseismic and interseismic deformation due to fault creep I: Model description, *Geophys. J. Int.*, 181, 81–98, doi:10.1111/j.1365-1246X.2010.04522.x.
- Hori, T. (2006), Mechanisms of separation of rupture area and variation in time interval and size of great earthquakes along the Nankai Trough, southwest Japan, *J. Earth Simulator*, 8-19.

Hsu, Y.-J., M. Simons, J.-P. Avouac, J. Galetzka, K. Sieh, M. Chlieh, D. Natawidjaja, L. Prawirodirdjo and Y. Bock (2006), Frictional Afterslip Following the 2005 Nias-Simeulue Earthquake, Sumatra, *Science*, 312, 1921-1926.

Johnson, K.M., R. Burgmann and K. Larson (2005), Frictional Properties on the San Andreas Fault near Parkfield, California, Inferred from Models of Afterslip following the 2004 Earthquake, *Bull. Seism. Soc. Am.*, 96, S321-338.

Kato, N. (2008), Numerical simulation of recurrence of asperity rupture in the Sanriku region, northeastern Japan, *J. Geophys. Res.*, 113, B06302, doi:06310.01029/02007JB005515.

Konca, A.O., J.P. Avouac, A. Sladen, A.J. Meltzner, K. Sieh, P. Fang, Z.H. Li, J. Galetzka, J. Genrich, M. Chlieh, D.H. Natawidjaja, Y. Bock, E.J. Fielding, C. Ji and D.V. Helmberger (2009), Partial rupture of a locked patch of the Sumatra megathrust during the 2007 earthquake sequence, *Nature*, 456, 631-635.

Lapusta, N. and J. Rice (2003), Nucleation and early seismic propagation of small and large events in a crustal earthquake model, *J. Geophys. Res.*, 108, 2205, doi:2210.1029/2001JB000793.

Larson, K., P. Bodin and J. Gomberg (2003), Using 1 Hz GPS Data to Measure Permanent and Seismic Deformations Caused by the Denali Fault Earthquake, *Science*, 300, 1421-1424.

Massonnet, D. and K.L. Feigl (1998), Radar interferometry and its application to changes in the earth's surface, *Reviews Geophys.*, 36, 441-500

Masterlark, T. (2003), Finite element model predictions of static deformation from dislocation sources in a subduction zone: Sensitivities to homogeneous, isotropic, Poisson-solid, and half-space assumptions, *J. Geophys. Res.*, 108 2540.

Matsu'ura, M. and T. Sato (1989), A dislocation model for the earthquake cycle at convergent plate boundaries, *Geophys. J. Int.*, 96, 23-32.

Miura, S., I. Iinuma, S. Yui, N. Uchida, T. Sato, K. Tachibana and A. Hasegawa (2006), Co- and post-seismic slip associated with the 2005 Miyagi-oki earthquake (M7.2) as inferred from GPS data, *Earth Planets Space*, 58, 1567-1572.

Miyazaki, S., P. Segall, J. Fukuda and T. Kato, 2004. Space time distribution of afterslip following the 2003 Tokachi-oki earthquake: Implications for variations in fault zone frictional properties. in *Geophys. Res. Lett.*, pp. L06623.

Nakayama, W. and M. Takeo (1997), Slip history of the 1994 Sanriku-Haruka-Oki, Japan, earthquake deduced from strong-motion data, *B. Seismol. Soc. Am.*, 87, 918-931.

Nanayama, F., K. Satake, R. Furukawa, K. Shimokawa, B.F. Atwater, K. Shigeno and S. Yamaki (2003), Unusually large earthquakes inferred from tsunami deposits along the Kuril trench, *Nature*, 424, 660-663.

- Perfettini, H. and J.-P. Ampuero (2008), Dynamics of a velocity strengthening region: implications for slow earthquakes and postseismic slip, *J. Geophys. Res.*, 113, B09411, doi:09410.01029/02007JB005398.
- Perfettini, H. and J. Avouac (2004), Postseismic relaxation driven by brittle creep: A possible mechanism to reconcile geodetic measurements and the decay rate of aftershocks, application to the Chi-Chi earthquake, Taiwan, *J. Geophys. Res.*, 109, B02304.
- Perfettini, H. and J.P. Avouac (2007), Modeling afterslip and aftershocks following the 1992 Landers earthquake, *J. Geophys. Res.*, 112, B07409, doi: 07410.01029/02006JB004399.
- Rice, J. (1993), Spatio-temporal complexity of slip on a fault, *J. geophys. Res.* , 98, 9885–9907.
- Robinson, D.P. and L.T. Cheung (2003), Source process of the Mw 8.3, 2003 Tokachi-Oki, Japan earthquake and its aftershocks, *Geoph. J. Intl.*, 181, 334-342, DOI: 310.1111/j.1365-1246X.2010.04513.x.
- Ruff, L.J. (1992), Asperity distributions and large earthquake occurrence in subduction zones, *Tectonophysics*, 211, 61-83.
- Rundle, J.B. (1982), Viscoelastic-gravitational deformation by a rectangular thrust fault in a layered Earth, *J. Geophys. Res.*, 87, 7787-7796.
- Satake, K. and B.F. Atwater (2007), Long-term perspectives on giant earthquakes and tsunamis at subduction zones, *Annu. Rev. Earth Planet Sci.*, 35, 349-274.
- Satake, K., K. Hirata, S. Yamaki and Y. Tanioka (2006), Re-estimation of tsunami source of the 1952 Tokachi-oki earthquake, *Earth, Planets and Space*, 58, 535-542.
- Sato, T. and M. Matsu'ura (1988), A kinematic model for deformation of the lithosphere at subduction zones, *J. Geophys. Res.*, 93, 6410–6418.
- Sato, T. and M. Matsu'ura (1992), Cyclic crustal movement, steady uplift of marine terraces, and evolution of the island arc-trench system in southwest Japan, *Geophys. J. Intl.*, 111, 617–629.
- Sato, T. and M. Matsu'ura (1993), A kinematic model for evolution of island arc-trench systems, *Geophys. J. Intl.*, 114, 512-530.
- Savage, J.C. (1983), A dislocation model of strain accumulation and release at a subduction zone, *J. Geophys. Res.*, 88 4984-4996.
- Savage, J.C. (1995), Interseismic uplift at the Nankai subduction zone, Southwest Japan, 1951–1990, *J. Geophys. Res.*, 100, 6339–6350.
- Shimazaki, K. and T. Nakata (1980), Time-predictable recurrence model for large earthquakes, *Geophys. Res. Lett.*, 7, 279–282.

- Sieh, K., D.H. Natawidjaja, A.J. Meltzner, C.-C. Shen, H. Cheng, K.-S. Li, B.W. Suwargadi, J.G. Philiposian and R.L. Edwards (2008), Earthquake supercycles inferred from sea-level changes recorded in the corals of West Sumatra, *Science*, 322, 1674-1678, doi:1610.1126/science.1163589.
- Simons, M. and P. Rosen, 2007. Interferometric Synthetic Aperture Radar Geodesy. in *Treatise on Geophysics*, pp. 391-446, ed Schubert, G. Elsevier Press.
- Suwa, Y., S. Miura, A. Hasegawa, T. Sato and K. Tachibana (2006), Interplate coupling beneath NE Japan inferred from three-dimensional displacement field, *J. Geophys. Res.*, 111, B04402.
- Tanioka, Y., L. Ruff and K. Satake (1996), The Sanriku-Oki, Japan, Earthquake of December 28, 1994 (Mw 7.7): Rupture of a different asperity from a previous earthquake, *Geophys. Res. Lett.*, 23, 1465–1468.
- Thatcher, W. and J.B. Rundle (1979), A model for the earthquake cycle in underthrust zones, *J. Geophys. Res.*, 84, 5540-5556.
- Thatcher, W. and J.B. Rundle (1984), A viscoelastic coupling model for the cyclic deformation due to periodically repeated earthquakes at subduction zones, *J. Geophys. Res.*, 89, 7631-7640.
- Umino, N., T. Kono, T. Okada, J. Nakajima, T. Matsuzawa, N. Uchida, H. A., Y. Tamura and G. Aoki (2006), Revisiting the three Mw7 Miyagioki earthquakes in the 1930s: possible seismogenic slip on asperities that were re-ruptured during the 1978 M=7.4 Miyagi-oki earthquake, *Earth Planets Space*, 58, 1587-1592.
- Vergne, J., R. Cattin and J.P. Avouac (2001), On the use of Dislocations to Model Interseismic Strain and Stress Build-up at Intracontinental Thrust Faults, *Geophys. J. Int.*, 147, 155-162.
- Wang, K., R. Wells, S. Mazzotti, R.D. Hyndman and T. Sagiya (2003), A revised dislocation model of interseismic deformation of the Cascadia subduction zone, *J. Geophys. Res.*, 108, 2026.
- Williams, C.A. and R. McCaffrey (2001), Stress rates in the central Cascadia subduction zone inferred from an elastic plate model, *Geophys. Res. Lett.*, 28, 2125-2128.
- Yamanaka, Y. and M. Kikuchi (2003), Source processes of the recurrent Tokachi-oki earthquake on September 26, 2003, inferred from teleseismic body waves, *Earth Planet. Sci. Lett.*, 55, e21– e24.
- Yamanaka, Y. and M. Kikuchi (2004), Asperity map along the subduction zone in northeastern Japan inferred from regional seismic data, *J. Geophys. Res.*, 109, B07307, doi:07310.01029/02003JB002683.
- Zweck, C., J.T. Freymueller and S.C. Cohen (2002), Three-dimensional elastic dislocation modeling of the postseismic response to the 1964 Alaska earthquake, *J. Geophys. Res.*, 107, 2064.

## Chapter 2

# AN ELASTIC PLATE MODEL FOR INTERSEISMIC DEFORMATION IN SUBDUCTION ZONES<sup>1</sup>

### 2.1 Introduction

At subduction plate boundaries, geodetic data from the interseismic period — decades to centuries after a megathrust earthquake — help to delineate regions of the megathrust that are not presently slipping and can potentially produce large earthquakes. Due to both observational and theoretical considerations, such data are frequently interpreted using simple elastic dislocation models (EDMs). EDMs are in fact used for interpreting secular as well as transient deformation in subduction zones [e.g., Savage, 1983; 1995; Zweck et al., 2002; Miyazaki et al., 2004; Hsu et al., 2006]. The most common of the dislocation models used for interpreting surface deformation in subduction zones is the backslip model [Savage, 1983] (henceforth referred to as the BSM, and depicted schematically in the left column of Figure 2-1). The BSM was originally motivated by the recognition that the overriding plate apparently experiences little permanent inelastic deformation on the time scales relevant to the seismic cycle (several hundred years) [see, Savage, 1983]. The BSM accomplishes this zero net strain in the overriding plate by parameterizing interseismic fault slip as normal slip, i.e., backslip, on the same patch that also slips in the reverse sense during great earthquakes [Savage, 1983]. Therefore, the seismic cycle is completely described by two equal and opposite perturbations — abrupt coseismic reverse slip cancels cumulative interseismic normal slip (or “backslip”) at the plate convergence rate. Thus, to first order, the interseismic strain field and the sum of coseismic and postseismic (afterslip) strain fields must cancel each other, and asthenospheric relaxation does not significantly contribute to the interseismic deformation field [Savage, 1983, 1995]. Further, it has been shown that the predictions of interseismic surface velocities for a two-layered elastic halfspace model (e.g., elastic-

---

<sup>1</sup> Published in JGR-Solid Earth: Kanda, R. V. S., and M. Simons (2010), An elastic plate model for interseismic deformation in subduction zones, *J. Geophys. Res.*, 115, B03405, doi:10.1029/2009JB006611.

layer-over-elastic-halfspace) differ by less than 5% from those for a homogeneous elastic-halfspace model [Savage, 1998]. Similarly, the effect of gravity on the elastic field is also very small (< 2%, see [Wang, 2005]). In the case of linear elastic-layer-over-viscoelastic-halfspace models, data for the interseismic period do not require asthenospheric relaxation, and can be fit equally well by afterslip downdip of the locked zone in an equivalent homogeneous elastic-halfspace model [Savage, 1995].

Thus, the BSM provides a first-order description of the subduction process on the time-scale of several seismic cycles (on the order of  $10^3$  yrs) using only two parameters — the extent of the locked fault interface and the plate geometry (constant or depth—dependent fault dip). To be precise, the BSM as intended by Savage [1983], assumed a mature subduction zone — where plate bending and local isostatic effects on the overriding plate are compensated by unspecified “complex asthenospheric motions” [Savage, 1983, page 4985]. These asthenospheric motions are assumed not to play a role in surface deformation, and there is no net vertical motion between the two plates at the trench. Thus, the BSM as intended by Savage [1983] is purely a perturbation superimposed over steady state subduction, with the deformation fields due to coseismic slip (thrust sense) and cumulative post-/interseismic-slip (backslip) on the locked portion of the fault canceling each other (left column of Figure 2-1 and Figure 2-2). Therefore, the BSM does not include block motion [Savage, 1983, page 4985; and J.C. Savage (personal communication, 2009)]. Henceforth, we use BSM to refer to this original model, as intended by Savage [1983]. However, subsequent authors have interpreted the relative steady state motion illustrated in Figure 1 of Savage [1983] literally, assuming that steady state motion implies block-motion (e.g., Yoshioka et al. [1993], Zhao and Takemoto [2000]; Vergne et al. [2001]; Iio et al. [2002; , 2004]; Nishimura et al. [2004]; Chlieh et al. [2008a]). Henceforth, we use pBSM to refer to this popular (mis-) interpretation of the BSM with block-motion (middle column of Figure 2-1 and Figure 2-2). In the pBSM, the interseismic backslip perturbation applied to the locked zone is viewed as the difference between two elastic solutions: (a) continuous steady state rigid-block motion along the plate interface, and (b) continuous aseismic slip along the plate interface

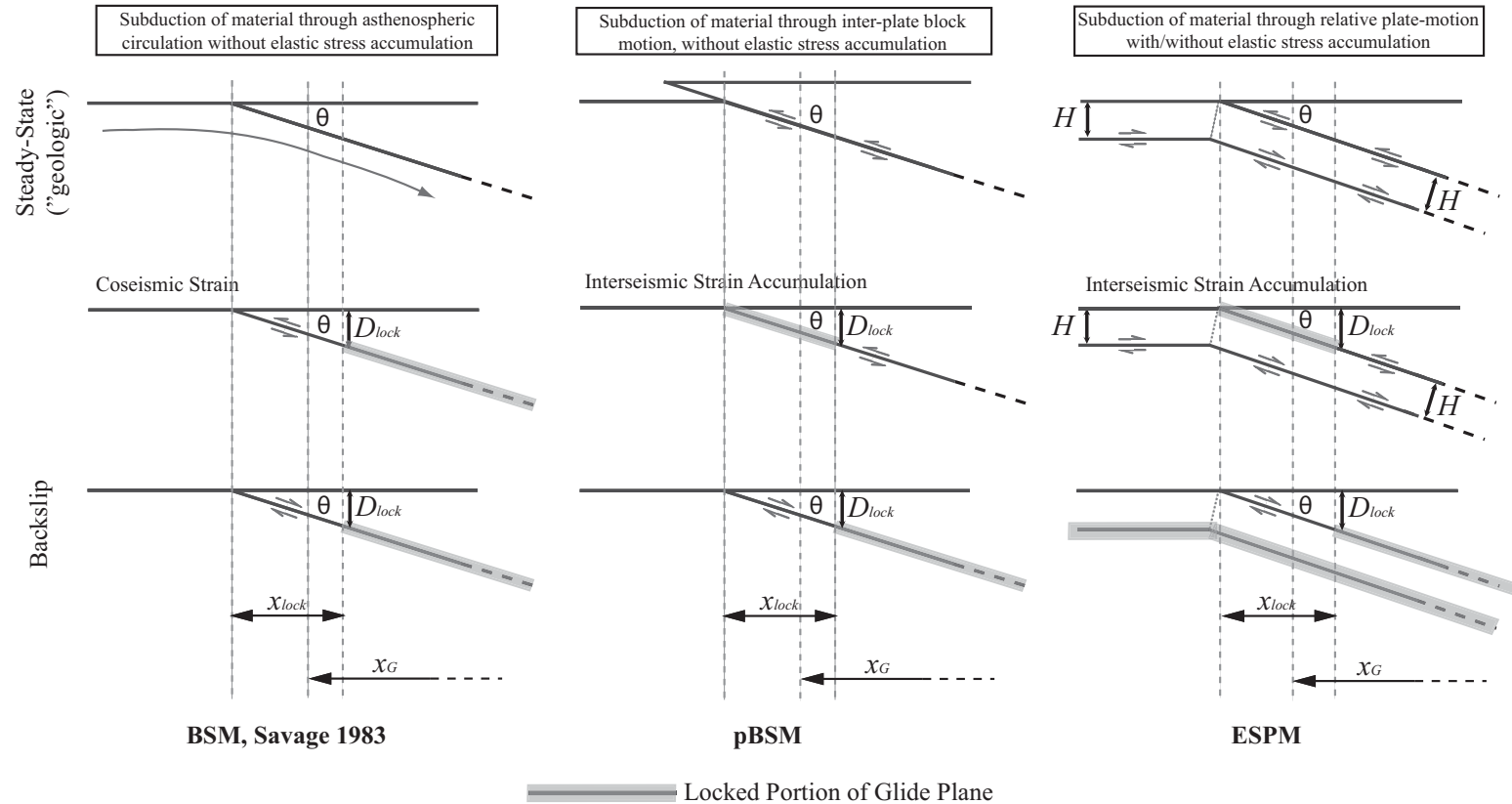


**Figure 2-1** Comparison of the BSM, the pBSM, and the ESPM. The trench is defined by the intersection of the free-surface (horizontal solid line) and the (upper) dipping line; cross-sectional geometry is assumed to be identical along strike;  $D_{lock}$  is the depth to the downdip end of the locked megathrust;  $x_{lock}$  represents the surface projection of the downdip end of the locked megathrust;  $\theta$  is the dip of the plate interface;  $H$  is the plate thickness in the ESPM;  $x_G$  represents the typical range for the location of the nearest geodetic observation from the trench. The arrows represent relative motion at the plate boundary.

downdip of the locked zone, representing the interseismic strain accumulation process. Thus, in the pBSM, the asthenosphere is primarily represented as two rigid fault blocks, and strain accumulation is assumed to occur only at the upper boundary of the subducting plate, specifically, as steady-slip downdip of the locked zone. The pBSM is unphysical in that on longer time scales, the steady state block motion along the megathrust interface between the two converging plates results in net long-term uplift of the overriding plate, as well as an unrealistic prediction of zero net strain in the downgoing plate. *Ad hoc* arguments have been used to simply ignore the vertical component of block motion, while including its horizontal component to account for plate convergence. From the perspective of implementation and interpretation, the pBSM is also ambiguous when considering non-planar faults — i.e., where one should one impose backslip. Even though the original BSM envisaged by Savage [1983] postulates application of backslip directly to the locked interface, irrespective of its geometry, this ambiguity arises in the pBSM because assuming block motion along a non-planar interface leads to net deformation in the overriding plate over the seismic cycle (upper middle panel of Figure 2-2), violating the original BSM's assumption of zero-net deformation there. As a result, several authors have either used a fictitious planar fault tangent to the downdip end of the locked zone to apply interseismic backslip [e.g., Simoes et al., 2004; Chlieh et al., 2008], or have argued against the use of the BSM for curved fault geometries [e.g., Chlieh et al., 2004].

In order to reconcile a plate view of subduction with observed deformation over the seismic cycle, we propose here a plate-like EDM for subduction zones, the ESPM, that essentially differs from the BSM as well as the pBSM in the form of the steady state solution (right column of Figure 2-1 and Figure 2-2). The steady state “plate” solution in the ESPM is simply the superposition of two parallel dislocation glide surfaces in the half-space, representing the top and bottom of the plate. The ESPM is intended to be a kinematic proxy for slab driven subduction [e.g., Forsyth and Uyeda, 1975; Hager, 1984], where the shear strains between the bottom of the downgoing plate and the surrounding mantle are approximated by the bottom dislocation glide surface. So, the

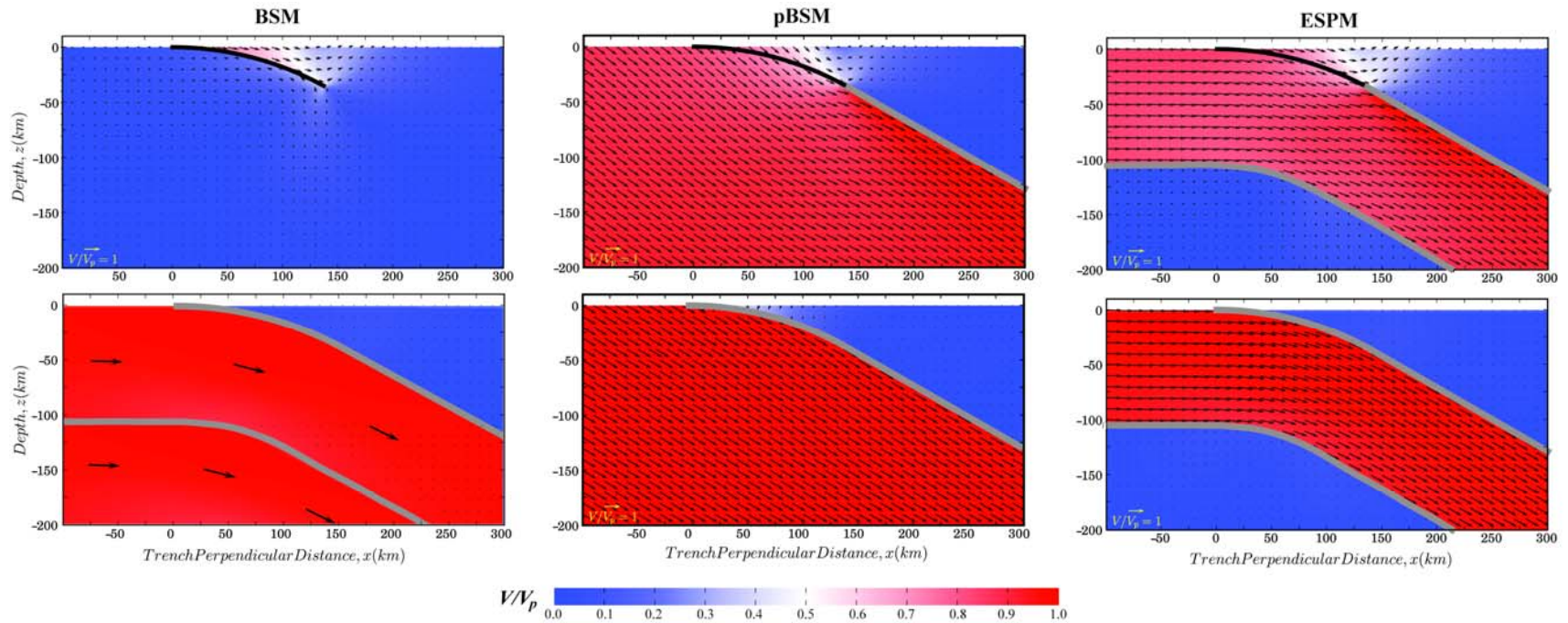


**Figure 2-2.** Comparison of the velocity fields in the half-space for the BSM, the pBSM, and the ESPM. Top row illustrates the interseismic velocity fields predicted by the models (solid black line represents the locked zone), and the bottom row shows the imposed “geologic” steady state creep velocity field. All velocities are computed relative to the far-field of the overriding plate (and normalized relative to the plate convergence rate,  $V_p$ ). Velocity vectors are drawn to the same scale in all panels (yellow vector at bottom left in each panel), relative to the plate convergence rate. The steady state field for the BSM is only a schematic representation of “complex asthenospheric motions” assumed by Savage [1983], and not a computed field.

ESPM retains the BSM's mathematical simplicity, while providing more intuition regarding the plate bending process. Because bending is explicitly included in the ESPM, the fraction of flexural stresses released continuously over the seismic cycle,  $f_{\sigma}$ , as well as plate thickness,  $H$ , are two additional parameters in this model. Our goals here are to (a) understand the contribution of flexure to such short-term surface deformation, (b) quantify the criteria under which flexural contribution to surface deformation can be ignored, as originally postulated by Savage [1983] for the BSM; and (c) obviate the need for many of the ambiguities inherent in the pBSM, the popular (mis-) interpretation of the BSM. We will show that the ESPM may not fit currently available geodetic data any better than the BSM, but its importance lies in providing additional physical insight into the complete elastic deformation field owing to plate flexure at the trench, and why a fault interface perturbation model has been so successful in approximating a more complicated geodynamic process like plate subduction over the seismic cycle timescale.

The simplicity of EDMs allows parameters such as the slip distribution on the subduction interface during different phases of the seismic cycle to be easily estimated from inversions of geodetic data. It is therefore not surprising that the BSM has been used to successfully fit geodetic observations using realistic plate interface geometries [e.g., Zweck et al., 2002; Khazaradze and Klotz, 2003; Wang et al., 2003; Suwa et al., 2006]. Clearly, as the quality of geodetic data as well as our knowledge of the 3D elastic structure improves, EDMs can be used to constrain more complicated models [e.g. Masterlark, 2003]. However, in spite of their success in fitting geodetic observations, it is important to remember that kinematic EDMs such as the ones discussed here fit the geodetic data by assuming that all of the observed deformation is due to current fault motion, ignoring any bulk relaxation processes [see Wang and Hu, 2006; see review by Wang, 2007]. Another disadvantage of purely elastic models is that they cannot model topographic evolution on time-scales longer than a few seismic cycles since they cannot accommodate monotonically increasing displacements (over geologic time) while keeping the stresses bounded. To the extent that such elastic deformation may provide the driving stresses for building permanent topography on the overriding plate, however, EDMs could be useful in guiding our intuition for models with inelastic rheologies. Using

the ESPM, we demonstrate below the potential for such net surface topographic evolution owing to elastic flexure of the subducting plate at the trench.

## 2.2 The Elastic Subducting Plate Model (ESPM)

If the negative buoyancy of subducting plates plays a significant role in mantle convection [as suggested originally by Forsyth and Uyeda, 1975; and explored for example, in Hager, 1984], then there must be shear tractions and associated shear strain between the downgoing slab (“plate”, or “lithosphere”) and the surrounding mantle (“asthenosphere”). We want to encapsulate the effect of such plate-driven subduction on the deformation at the surface of the overriding plate during the interseismic time period. In order to reconcile the BSM view of subduction along a single fault interface with that of subduction of a finite thickness plate at the trench, we propose a more physically intuitive and generalized kinematic model – the elastic subducting plate model (ESPM, right column of Figure 2-1 and Figure 2-2). The ESPM is constructed by the superposition of solutions for two edge dislocation glide surfaces in an elastic half-space that delineate the subducting plate, having a uniform plate thickness that remains unchanged as it subducts at the trench (right column of Figure 2-1). The lower dislocation glide surface is a kinematic proxy for the shear strains related to plate-buoyancy driven subduction. In fact, such a surface is the simplest way to explicitly account for Savage [1983]’s assumption of asthenospheric motions compensating for overriding plate deformation — especially for subduction zones that may not be mature, and therefore affected by plate flexure at the trench. By construction, the relative slip across the upper and lower plate surfaces of the ESPM is equal in magnitude, but opposite in sign. The principal effect of the lower glide surface (i.e., surface along which the lower edge dislocation moves) is to channel material in the “oceanic plate” into the “mantle”, relative to a reference frame that is fixed with respect to both the sub-oceanic mantle as well as the far-field of the overriding plate (right column of Figure 2-2). In contrast, while the pBSM considers steady state subduction of material down the trench via block motion (lower-middle panel of Figure 2-2), usually *ad hoc* arguments are used

to ignore the vertical component of block-motion – resulting in no net subduction of material into the mantle. The BSM does not explicitly model asthenospheric motions causing material subduction (left panel of Figure 2-1 and Figure 2-2).

There are two significant assumptions implicit in the construction of the ESPM. The first assumption is that the lithosphere-asthenosphere boundary is sharp (rather than diffuse), contrary to expectations from seismic, thermal, and rheological data. This simplification of a sharp lithosphere-asthenosphere boundary may be justified here because over the short timescales being considered here relative to mantle convection, surface deformation on the overriding plate is relatively insensitive to whether there is a gradient or step-jump in velocities across the lower boundary, as long as the same volume of material undergoes subduction. In addition to this kinematic role, the bottom dislocation glide also serves to decouple the shallow depths of the half-space (“lithosphere”) from mantle depths, so that there are negligible elastic stresses in the region of the half-space that would normally be considered to be viscous mantle. Further, such a sharp lower lithospheric boundary is commonly assumed in the parameterization of the flexural strength of oceanic lithosphere with an elastic plate thickness,  $T_e$  [Turcotte and Schubert, 2001], as well as in viscous plate models for analyzing long-term flexural stresses and dissipation in the subducting slab [Buffett, 2006]. Thus, the plate thickness defined in the ESPM could also be viewed as a way to parameterize the fraction of volumetric flexural stresses that may persist in the subducting lithosphere over the duration of a seismic cycle.

The second assumption is that over a single seismic cycle, the underlying “mantle” in the ESPM does not undergo significant motion relative to the far-field boundary of the overriding plate. The BSM as motivated by Savage [1983] assumes such motion as being part of the “complex asthenospheric motions” not included in that model. In contrast, by including block subsidence of the footwall (or block uplift of the hanging-wall), the pBSM predicts net relative vertical motion between the entire “oceanic” block (which includes the downgoing plate as well as the mantle) and the “continental” block (lower-middle panel of Figure 2-2), which is unrealistic. However, if this net relative uplift were

eliminated by an *ad hoc* correction to only the vertical velocity field of the overriding plate, then the pBSM would predict only net horizontal convergence between the footwall and the hanging-wall, but with a velocity equal to only the horizontal component of block motion. In addition, given that the pBSM assumes no net deformation in the overriding plate over the seismic cycle, there is no “sink” for this converging material — thus leading to a physically irreconcilable model that violates mass balance. In contrast, the ESPM satisfies continuity by allowing material to “subduct”, in addition to predicting the expected sense and magnitude of relative motion between the two plates to be at the plate convergence velocity. The ESPM can be viewed as the elastic component of lithospheric response over the seismic cycle timescale, and does not preclude the existence of viscous stresses at mantle depths (in a visco-elastic sense). In fact, one could add a (linear-) viscous mantle convection deformation field to the ESPM field below the subducting plate (similar to the layered models mentioned in the previous section), in order to introduce a gradient in the deformation field at the bottom boundary of that plate, as well as introduce relative motion between the sub-oceanic mantle and the overriding plate when integrated over several seismic cycles. Superposing such a field is no different from the asthenospheric motions envisaged by Savage [1983], because while such a field introduces long-term relative motion in the mantle underlying both plates, it does not affect the short-wavelength deformation field in the vicinity of the trench (upper-left panel of Figure 2-2), thereby not changing the predictions of the ESPM over the seismic cycle.

Thus, the ESPM adds only two extra degrees of freedom relative to the BSM — the plate thickness,  $H$ , and the fraction of flexural stresses released continuously,  $f_\sigma$  — while still retaining the BSM’s advantages (small number of parameters) for geodetic data inversion. The additional complexity of the ESPM due to these extra parameters is compensated by the elimination of ambiguities related to the implementation of the pBSM. By separating the subduction zone into distinct regions that undergo coseismic slip (locked megathrust along the upper surface) and interseismic slip (remainder of the plate surfaces), the ESPM unambiguously accounts for (a) the expected horizontal convergence at the plate-rate between the subducting and overriding plates, (b) a net zero

steady state vertical offset between the subducting and overriding plate (integrated over many seismic cycles), and (c) deformation due to slip along non-planar megathrust interfaces. As we will show in the next section, the ESPM can also be thought of as a more general model that reduces to the BSM under special conditions.

EDMs similar to the ESPM have been adopted in earlier papers on modeling interseismic surface deformation in subduction zones. For instance, Sieh et al. [1999] consider a tapered “bird-beak” shaped subducting plate whose thickness reduces to a point at its downdip end. Such a tapered geometry violates mass conservation within the subducting plate, given the purely elastic and homogeneous rheology assumed. Zhao and Takemoto [2000] propose a dislocation model for the subduction zone using a superposition of steady slip along a planar thrust fault downdip of the locked zone, and reverse slip along two lower glide surfaces representing the bottom of the subducting plate before and after the trench. However, they assume that the lower glide surfaces have interseismic velocities that are twice that of the upper surface and that the subducting plate thickness decreases with depth — both of which are again inconsistent with the conservation of mass within the subducting plate. In contrast, the simpler ESPM assumes a constant, depth invariant plate thickness for the downgoing plate,  $H$ , as well as identical slip velocity magnitudes along both glide surfaces at all times.

We use the 2D elastic dislocation solutions for a dip-slip fault embedded in an elastic half-space given by Freund and Barnett [1976], as corrected by Rani and Singh [1992] (see also, Tomar and Dhiman [2003] and Cohen [1999]) for computing surface velocities. To verify our code, we compared surface velocity predictions using the above formulation with those predicted by Okada [1992]’s compilation, for identical plate geometries. We choose the origin to be at the trench, the  $x$ -axis to be positive “landward” of the trench, and the  $z$ -axis to be positive upwards (so depths within the half-space are negative). Dips are positive clockwise from the positive  $x$ -axis. For the vertical surface deformation field, uplift is considered positive, and for the horizontal field, arc-ward motion is assumed positive. Although we only consider the plane strain problem here, the ESPM can be extended to 3D problems with along-strike geometry variations;

however, in this case, flexure associated with along-strike plate-interface curvature (e.g., Japan trench between northern Honshu and Hokkaido, or the Arica bend of the Peruvian/Chilean trench) may cause additional elastic deformation in the overriding plate.

### 2.3 End-member models of the ESPM

For the ESPM, subtracting the steady plate-subduction solution (top-right panel of Figure 2-1) from that for strain-accumulation during the interseismic (middle-right panel of Figure 2-1), we obtain a mathematically equivalent model for the interseismic — the BSM (bottom-right panel of Figure 2-1). Thus, the ESPM provides an alternate but kinematically more intuitive framework for deriving the BSM. Further, in the limiting case of the ESPM with zero plate thickness ( $H=0$ ), the edge dislocation representing the horizontal section of the bottom surface of the plate vanishes. Also, slip along the creeping sections of the top and bottom dipping surfaces cancel each other — except along the locked megathrust zone, where normal slip (or “backslip”) ensues, irrespective of fault geometry (bottom panels of Figure 2-3). Thus, backslip along the locked megathrust can also be understood as the slip prescribed along the bottom surface of a “thin” subducting plate, and in this limit, the ESPM is identical to the BSM as motivated by Figure 1 of *Savage* [1983] (left column of Figure 2-1). In this zero plate thickness limit, there is no net deformation in the overriding plate over the seismic cycle, irrespective of the plate interface geometry. In contrast, for the pBSM with a non-planar plate interface, since no lower plate boundary is assumed, net deformation in the overriding plate is unavoidable owing to steady state slip along a curved interface [e.g., Sato and Matsu'ura, 1988; Matsu'ura and Sato, 1989; Sato and Matsu'ura, 1992; 1993; Fukahata and Matsu'ura, 2006]). Thus, when using the BSM (or the pBSM) to invert for geodetic data in subduction zones, one is inherently assuming negligible thickness for the subducting plate, or continuous relaxation of stresses resulting from plate flexure. In this limit, kinematic consistency requires not only that the two glide surfaces (plate surfaces) in the ESPM have the same magnitude of slip, but also identical geometries.

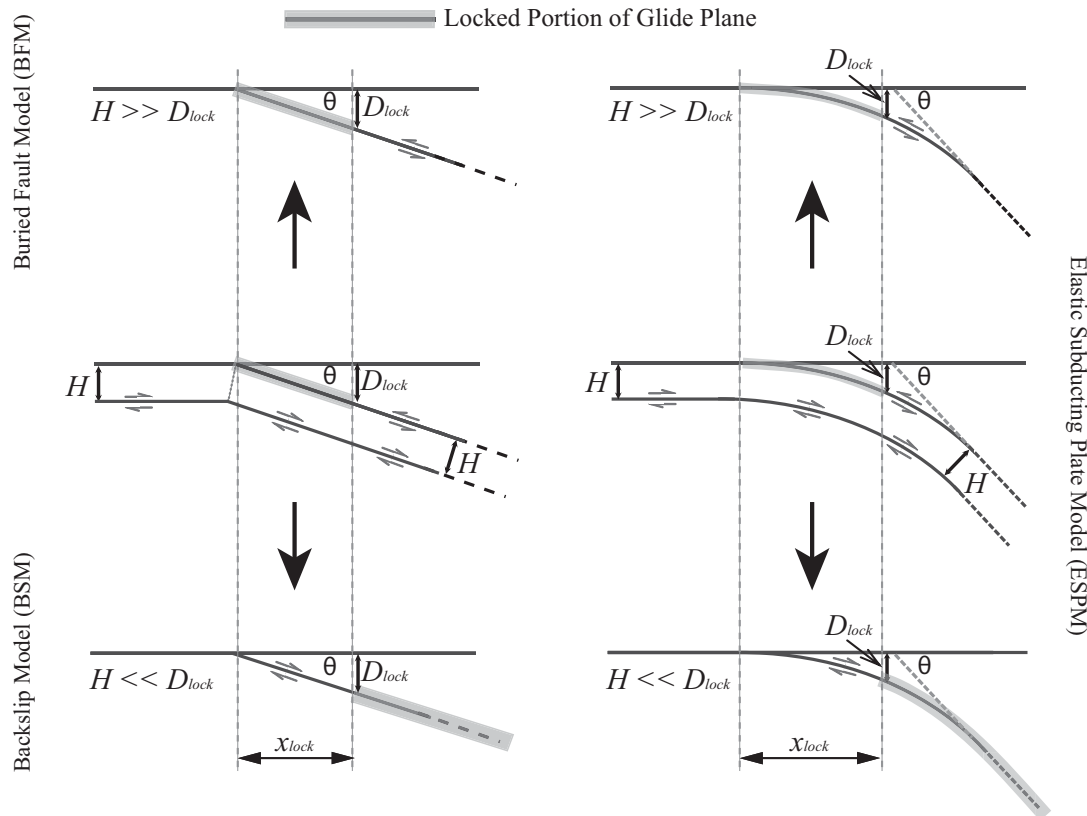


**Figure 2-3.** Geometric comparison of the ESPM with planar (left column) and curved (right column) geometry. In each column, the top row is the ESPM in the limit of a very thick plate (the BFM); the bottom row is the ESPM in the limiting case of negligible plate thickness (the BSM). Note that the “dip” of the curved fault is defined at a point where the plate straightens out. The dip of the curved fault at the trench is assumed to be zero. Other notation and assumptions are identical to those in Figure 2-1.

Therefore, when applying the pBSM to subduction zones where the downgoing slab is inferred to have a non-planar geometry, the locked megathrust interface — where backslip is imposed — should be modeled with the same geometry as that of the bottom surface of the downgoing plate directly beneath it (lower-right panel of Figure 2-3).

While there are several examples of papers that use the actual non-planar interface geometry for the BSM [e.g., Zweck et al., 2002; Khazaradze and Klotz, 2003; Wang et al., 2003; Suwa et al., 2006], some confusion has been created by the use of a planar extension of the deeper portion of a curved subduction interface for modeling backslip [e.g., Simoes et al., 2004; Chlieh et al., 2008]. Such a planar fault tangential to the interface at the downdip end of the locked zone intersects the free surface arc-ward of the

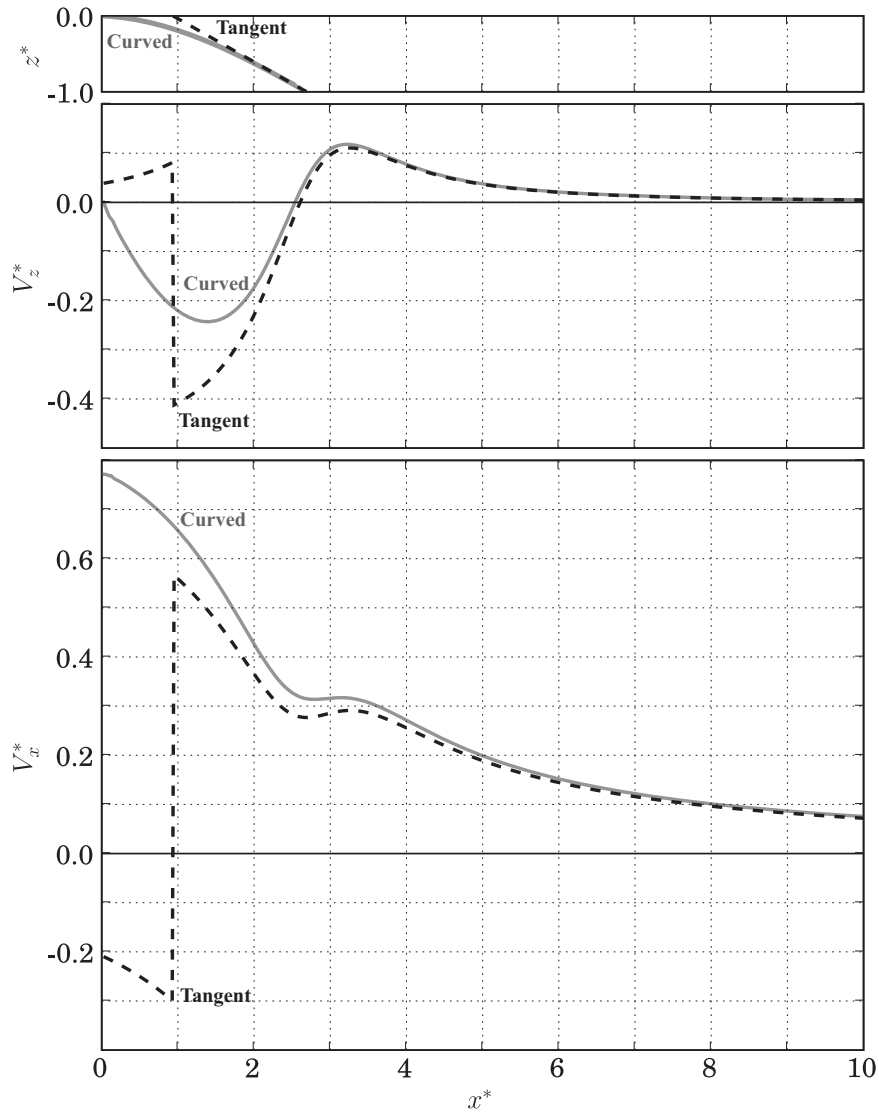


**Figure 2-4.** Appropriate application of the BSM to curved faults. Backslip must be applied to the curved interface geometry appropriate for a subduction zone, instead of to its tangent at the downdip end of the locked zone. The curved fault (solid gray line) resembles the subduction thrust interface geometry below the island of Nias, offshore of Sumatra ( $\theta_{top} = 3^\circ$ ,  $\theta_{bot} = 27^\circ$  [Hsu et al., 2006]). The tangent-approximation to the curved fault [Chlieh et al., 2004; Simoes et al., 2004; Chlieh et al., 2008] is represented by the dashed black line. The top panel presents the faults in cross-sectional view.  $x^*$  ( $= x/D_{Lock}$ ) is the dimensionless distance perpendicular to the trench;  $z^*$  ( $= z/D_{Lock}$ ) is the dimensionless depth. The origin of the dimensionless  $x^*$ - $z^*$  system is at the location of the trench axis. Vertical surface velocity profile,  $V_z^*$  (middle panel), and horizontal surface velocity profile,  $V_x^*$  (bottom panel), are scaled by the uniform plate convergence velocity,  $V_p$ .

trench (“pseudo-trench”, top panel of Figure 2-4). The surface velocity predictions in the far-field due to slip on a curved fault and its tangent planar approximation are nearly indistinguishable. But because of the artificial arc-ward shift in the tangent approximation’s “trench”, its predictions of surface deformation differ significantly from those for the curved megathrust right above the locked interface (middle and bottom panels of Figure 2-4). An additional concern is the use of entirely different faults for coseismic and interseismic displacements. Savage [1983] explicitly states this notion of applying backslip to the megathrust interface, irrespective of its shape. But as discussed earlier, that model’s application by subsequent researchers – possibly arising from the pBSM notion of block-motion - have created an apparent ambiguity in the implementation of the BSM to non-planar fault geometries.

In the limiting case of the ESPM with very large plate thickness ( $H \rightarrow \infty$ ), the lower glide surface is at a large depth below the upper plane, and for a fixed radius of curvature (typically a few hundred km), the plate behaves like a planar slab with a sharp kink at the trench (left panels of Figure 2-3). So, the contribution of the bottom glide surface reduces to a single dislocation at this kink that is deeply embedded within the half-space. Consequently, the contribution of the bottom glide surface has almost negligible amplitude and a very broad wavelength, its contribution to the total ESPM surface deformation field becomes negligible. The only contribution to the surface ESPM deformation field in this “infinite-thickness” limit comes from the buried thrust fault downdip of the locked zone. Thus, in this limit of “infinite” plate thickness (i.e., for very thick plates, as in plate collision zones), the ESPM mathematically reduces to the buried fault model (the BFM, top panels of Figure 2-3), which is typically used for modeling interseismic surface deformation in continental collision zones [e.g., Vergne et al., 2001]. The ESPM can therefore be viewed as a more general model for plate convergence zones, which reduces to previously developed models for subduction (the BSM or pBSM) or collision zones (the BFM) for limiting values of plate thickness (zero and infinity, respectively).

## 2.4 Effect of plate flexure on the ESPM surface deformation field

When the plate has non-negligible thickness,  $H$ , the ESPM and the BSM differ significantly close to the trench due to strains induced by plate flexure. The differences in the predictions of the ESPM and the BSM arise from having the same magnitude of relative slip along both surfaces of the downgoing plate, as it subducts at the trench. As a consequence, material at any cross-section of the downgoing plate moves with a uniform velocity equal to the plate-convergence rate, resulting in permanent shearing of the subducting material passing through the trench. Henceforth, we use “flexural strain” to refer to this shear-dominated strain within the elastic subducting plate as it passes through the trench. The associated “flexural stresses” cause net deformation in the overriding plate at the end of each seismic cycle. So, unless these flexural stresses (a) have negligible magnitudes (as when  $H = 0$ ), or (b) are continuously released in their entirety in the shallow portions of subduction zones, the surface velocity predictions of the ESPM differ significantly from those of the BSM above the locked megathrust interface (Figure 2-5). One might argue that this region of discrepancy in these models’ predictions lies over the forearc wedge, and therefore cannot be modeled by a purely elastic model like the ESPM. However, any excess elastic deformation predicted for this zone by the ESPM (compared to that of the BSM) can provide insight into the localization of incremental inelastic strain accumulation over multiple seismic cycles. Also, to the extent that such net seismic-cycle deformation can contribute to the long-term evolution of surface topography in the real Earth, we expect inelastic processes (such as erosion, accretion and/or sedimentation) to counter any “runaway” topographic evolution resulting from the discrepancy in these models’ predictions. In addition, the ESPM can still be used to infer the short-term elastic component of wedge deformation over the duration of a single seismic cycle, especially as ocean-bottom geodetic data become available in the near future.

To understand the strain accumulation arising from our assumption of uniform velocity for the two ESPM glide surfaces, we need only consider the steady state motion of the subducting plate (i.e., without any locked patch). Such steady state motion results in a

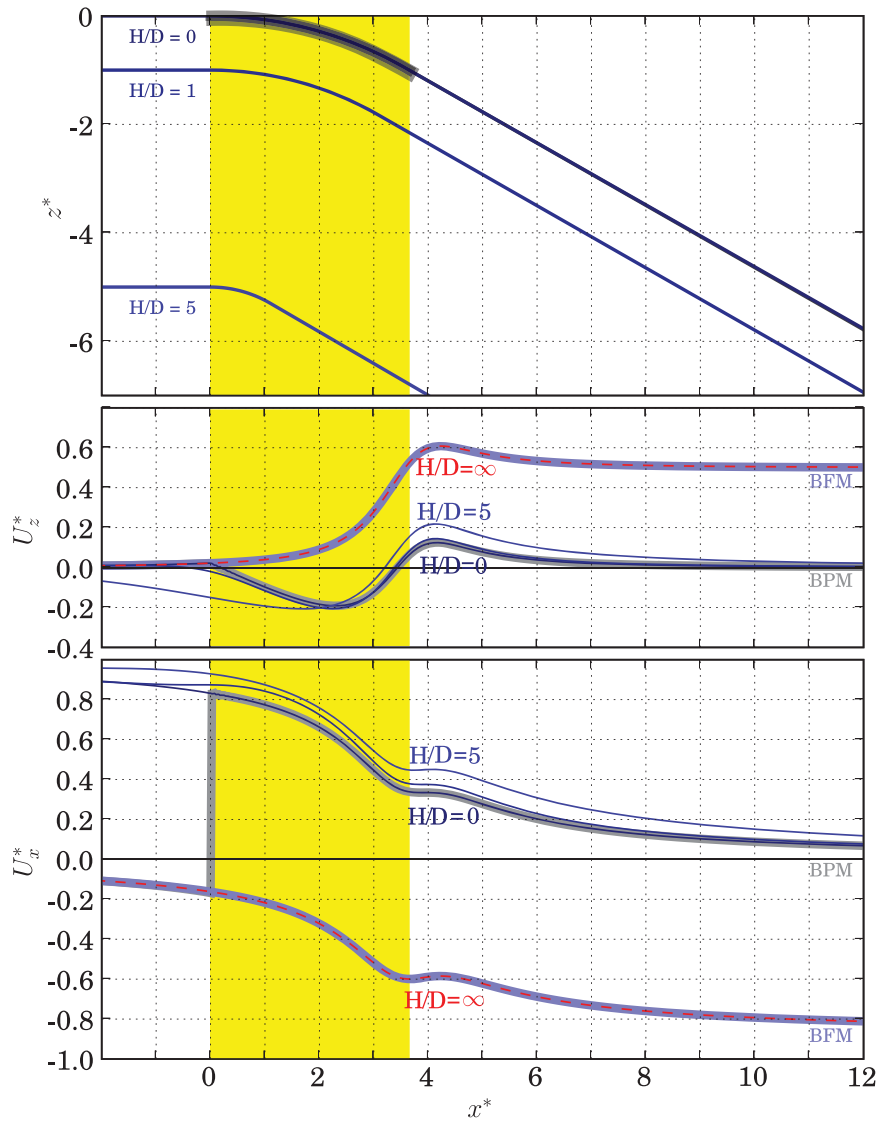


**Figure 2-5.** Comparison of deformation for the BSM and the ESPM with plates of different thickness,  $H$ , for a realistic curved fault geometry. In all panels, the thick gray solid curves represent the BSM, and the extent of the locked zone is shaded in yellow. The blue solid curve coinciding with the BSM surface velocities is the ESPM with zero plate thickness. The thick light-blue curve is the surface velocity field due to the buried thrust down-dip of the locked zone (i.e., the BFM). The thin dashed red curve coinciding with the BFM surface velocity field is the ESPM having an “infinite” plate thickness. In all cases, the imposed uniform slip rate is in the normal sense for the BSM (backslip), and reverse (thrust) sense for the ESPM. Panel organization and non-dimensionalization of the plot axes is identical to that in Figure 2-4.

uniform cross-sectional velocity for material being transported within the subducting plate, and is identical to flexural shear folding, where individual layers within the plate do not undergo changes in either their thickness or length (similar to folding a deck of cards [see Suppe, 1985; Twiss and Moores, 1992]). Material moving through each layer undergoes only a change in direction as it bends through the trench during the interseismic time period (bottom-right panel of Figure 2-2). This kinematic, volume-conserving assumption leads to runaway deformation of the plate beyond the trench.

Within the framework of dislocations embedded in an elastic half-space, there are two equivalent approaches to simulating flexural stress release as the plate subducts at the trench:

- a) Applying an additional uniform velocity gradient within the plate — whose magnitude varies continuously along its length depending on the local curvature — that extends material near the top surface of the plate, and compresses material near the bottom surface as the plate subducts at the trench. This gradient is therefore zero for the planar sections of the plate before the trench and after straightening out in the upper mantle.
- b) Allowing slip at the axial hinges across which the plate successively bends as it subducts, so as to rotate planes that were perpendicular to the top and bottom surface of plate before subduction remain so after subduction.

We first consider releasing the flexural stresses in the ESPM by superimposing a velocity gradient within the plate — which is equivalent to assuming that the subducting slab behaves as a thin viscous or elastic plate in flexure [Turcotte and Schubert, 2001]. This approach is a bit arbitrary when applied to a planar interface geometry as its curvature is infinite at the trench and zero otherwise. So, we illustrate this approach using a curved plate geometry. We want plane sections that are normal to the top and bottom surface of the incoming plate to remain so as it bends through the trench and straightens out in the upper mantle. We assume that the material at the centerline (or the neutral-axis) of the incoming plate passes through the trench without a change in speed,  $V_p$ . Material above

the centerline accelerates as it passes through the trench relative to  $V_p$ , in proportion to its “radial” distance from this centerline:

$$V = \frac{V_p}{R_p} r, \quad (1)$$

where,  $R_p$  is the radius of curvature of the centerline as it passes through the bend, and  $r$  is the distance normal to the centerline profile. This would ensure that the rectangular patch in Figure 2-6(a) remains rectangular as it passes through the trench. So, the speeds for the top and bottom surfaces of the plate would be:

$$\begin{aligned} V_{top} &= \frac{V_p}{R_p} R_{top} = \frac{V_p}{R_p} \left( R_p + \frac{H}{2} \right) = V_p \left( 1 + \frac{HC_p}{2} \right) = V_p \left( 1 + \frac{\delta V}{V_p} \right) \text{ and} \\ V_{bot} &= \frac{V_p}{R_p} R_{bot} = \frac{V_p}{R_p} \left( R_p - \frac{H}{2} \right) = V_p \left( 1 - \frac{HC_p}{2} \right) = V_p \left( 1 - \frac{\delta V}{V_p} \right) \end{aligned} \quad (2)$$

where  $R_{top}$  and  $R_{bot}$  refer to the local radii of curvature for the top and bottom surfaces of the plate,  $H$  is the plate thickness, and  $C_p$  is the plate curvature.  $C_p$  is equal to zero for the straight sections in the ESPM. So, the velocity corrections apply only to the curved section of the subducting plate. For radius of curvature,  $C_p$ , equal to 250 km (which is roughly the value used for all the curved profiles in this paper), and an elastic plate thickness,  $H$ , of 50 km for the subducting lithosphere, the velocity correction,  $(\delta V/V_p)$ , equals 10%. We verified that the surface velocity field predicted by the ESPM with these velocity corrections is identical to that predicted by the BSM. Therefore, as long as the plate geometry has finite curvature, adding velocity corrections to the finite thickness ESPM ( $H > 0$ ) generates a model with no net deformation of the overriding plate (the BSM). Since the resulting surface deformation field due to this visco-elastic approximation looks identical to that for the kinematically equivalent plastic approximation (discussed next), we do not show separate plots for this approach here.

We next consider releasing flexural stresses via slip along planar axial hinges of folding as the plate subducts through the trench (the “plastic” formulation of flexure), which is equivalent to adding localized plastic deformation within the subducting plate. In order to conserve the thickness of the plate as it bends at the trench, the hinge must bisect the angle between the horizontal and bent sections of a planar subduction interface, or

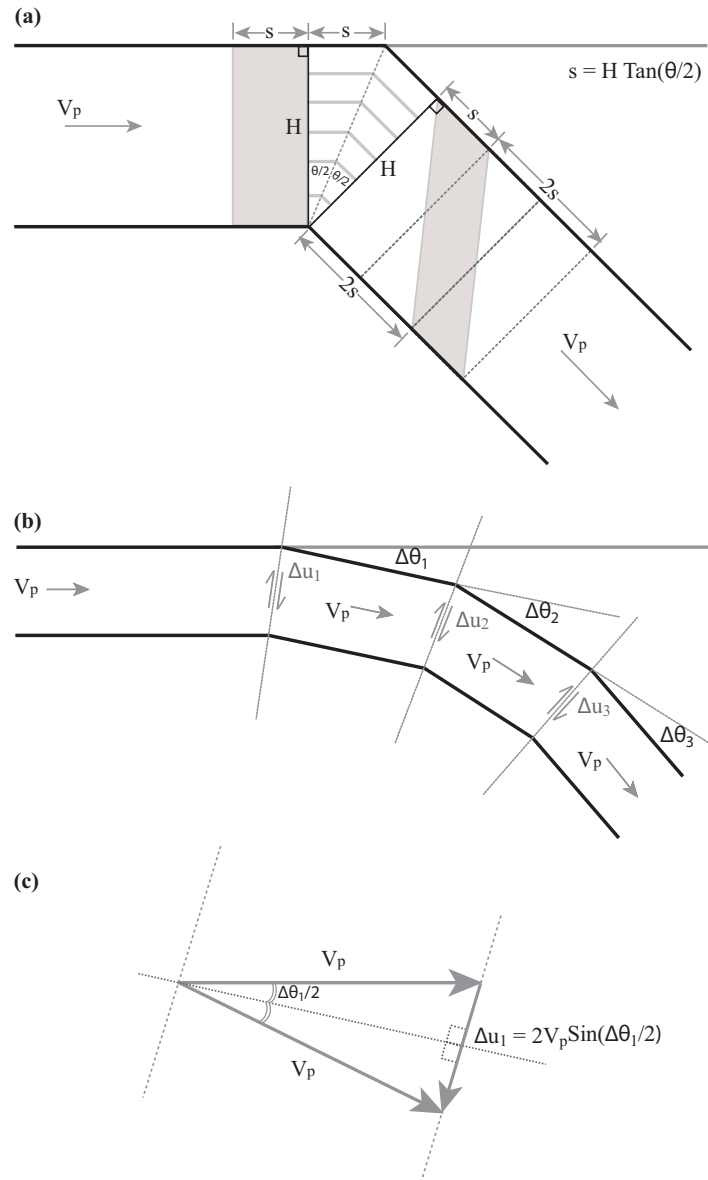


**Figure 2-6.** Kinematics of plate bending. (a) Bending of the plate at the trench for the ESPM with linear fault interface geometry; Motion of subducting material through the trench results in shearing as indicated by the shaded area. Axial hinges of folding can be kinematically represented by dislocations, across which incoming material in the plate experiences a change in direction, but not in magnitude. (b) Bending of the plate at the trench for the ESPM with a non-planar (or curved) fault interface geometry. The curved interface is represented by a number of linear segments having different slopes, and the number of hinges corresponds to the number of planar segments representing the discretization. (c) Velocity vector diagram showing required slip rate on an axial hinge to kinematically restore strains due to bending at the hinge.

between adjacent sections of a non-planar interface, whose dip changes with increasing depth (Figure 2-6(a) and (b)). Although the axial hinge plane does not experience relative displacement across itself, it can be shown that the deformation gradient tensor associated with this plane is identical to that of a fault experiencing relative displacement across that plane, especially at distances larger than the radius of curvature of the fold hinge [Souter and Hager, 1997]. A curved fault can be thought of as bending along a set of such axial hinge planes, whose number depends on the discretization of the non-planar fault profile (Figure 2-6(b)). As the discretization of the fault profile becomes finer, correspondingly more hinges are required to accurately model flexural strains. Axial hinges help relax the accumulated flexural stresses by allowing the transport of material from the vicinity of the trench down the subducting plate in a kinematically consistent way (Figure 2-6(c)) – resulting in a thrust sense of slip across each axial hinge with the magnitude,

$$\Delta v = 2V_p \sin\left(\frac{\Delta\theta}{2}\right), \quad (3)$$

where,  $\Delta v$  is the relative slip required to exactly compensate for plate flexural strains at the hinge, and  $\Delta\theta$  is the same as in Equation 1. Again, in the limiting case of a curved fault, this reduces to,

$$\Delta v \approx V_p \Delta\theta. \quad (4)$$

Figure 2-6(a) geometrically illustrates this flexural strain for a planar fault interface characterized by a single discrete bend in the subduction plate. Since the two glide surfaces have the same slip rate, the gray rectangular volume in that figure is sheared into a parallelogram after completely passing through the trench. The accumulated shear strain due to bending (represented by the hachured zone in Figure 2-6(a)) is proportional to the difference in path lengths for the top and bottom edges of the rectangle at the upper and lower dislocations (Figure 2-6(a)):

$$\varepsilon_{xz} = \frac{2H \tan(\frac{\Delta\theta}{2})}{H} = 2 \tan(\frac{\Delta\theta}{2}), \quad (5)$$

where  $\varepsilon_{xz}$  is the shear strain, and  $\Delta\theta$  is the change in dip angle at the trench. Similarly, a curved geometry can be thought of as a series of infinitesimally small bends in the plate (Figure 2-6(b)). In this case, the incremental strain due to each such bend can be calculated from Equation 1, in the limit of infinitesimally small  $\Delta\theta$ .

$$\Delta\varepsilon_{xz} \approx 2(\frac{\Delta\theta}{2}) = \Delta\theta, \quad (6)$$

which is identical to pure shear. In this case, the local rate of strain accumulation along the curved plate is given by:

$$\frac{d\varepsilon_{xz}}{dt} = V_p \left. \frac{\Delta\varepsilon_{xz}}{\Delta s} \right|_{\Delta s \rightarrow 0} = V_p \left. \frac{\Delta\theta}{\Delta s} \right|_{\Delta s \rightarrow 0} = V_p C_p, \quad (7)$$

where  $V_p$  is the long-term plate convergence velocity,  $t$  is time,  $s$  is the arc-length along the curved profile, and  $C_p$  is the local curvature of the profile, as in Equation 2. So, the strain rate in the slab is proportional to the convergence velocity and curvature in this purely kinematic model. Because this derivation was based on fixing the geometry of the plate, the strain rate obtained above is equivalent to that derived for viscous plates by Buffett [2006], or bending of thin plates by Turcotte and Schubert [2001], except for a factor of distance from neutral axis (since we have assumed uniform velocity here).

Henceforth, we use “flexural field” to denote the deformation field resulting from either the velocity corrections or the axial hinges for a steadily slipping plate with no locked zone on the subduction thrust interface (Figure 2-7(a) and Figure 2-8(a)). Subtracting the surface velocity field due to either of the flexural fields from that for the ESPM having a locked zone results in the BSM surface velocity field (Figure 2-7(b) and Figure 2-8(b)). It is important to note that the plate interface geometry has a very strong effect on the shapes of the surface velocity profiles of the flexural field. For the planar interface, both the horizontal and vertical surface velocity profiles indicate that the frontal wedge of the

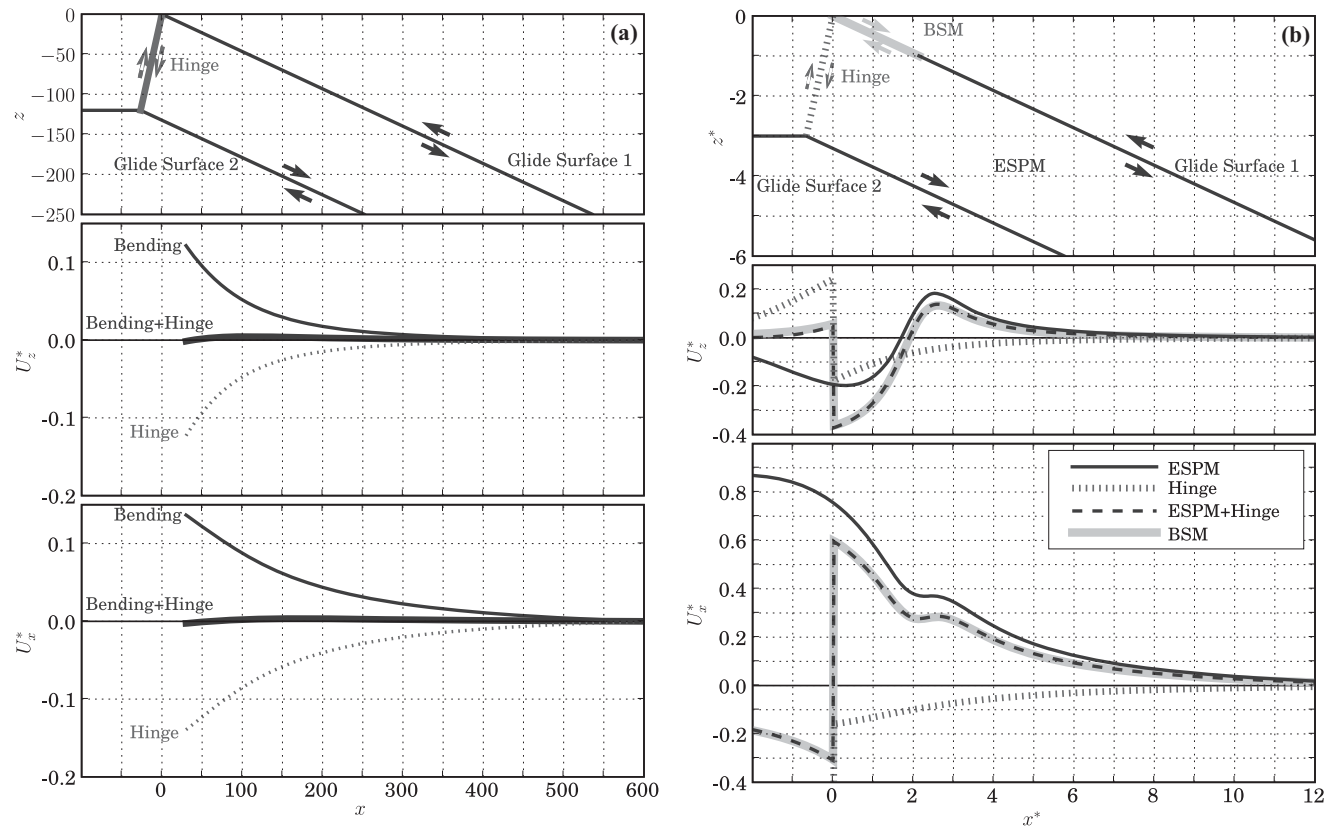


**Figure 2-7.** The surface deformation field for the ESPM for a planar plate geometry: (a) the ESPM with no locked zone is equivalent to the long-term, steady state plate motion (solid black line). The surface velocity field due to the axial hinge (thin dashed gray line) cancels the effect of plate flexure at the trench (thin solid black line), resulting in net zero long-term strain accumulation over the seismic cycle (thick solid black line). (b) Effect of a single axial hinge on the ESPM with a locked megathrust fault. Again, note that the ESPM predicts the correct sense of motion for the oceanic plate. The sum of the ESPM (thin solid black line) and axial hinge (thick dotted gray line) velocity fields — shown as the thick dashed black line — exactly equals that for the equivalent BSM (thick solid gray line). Panels and plot axes are as described in Figure 2-4.

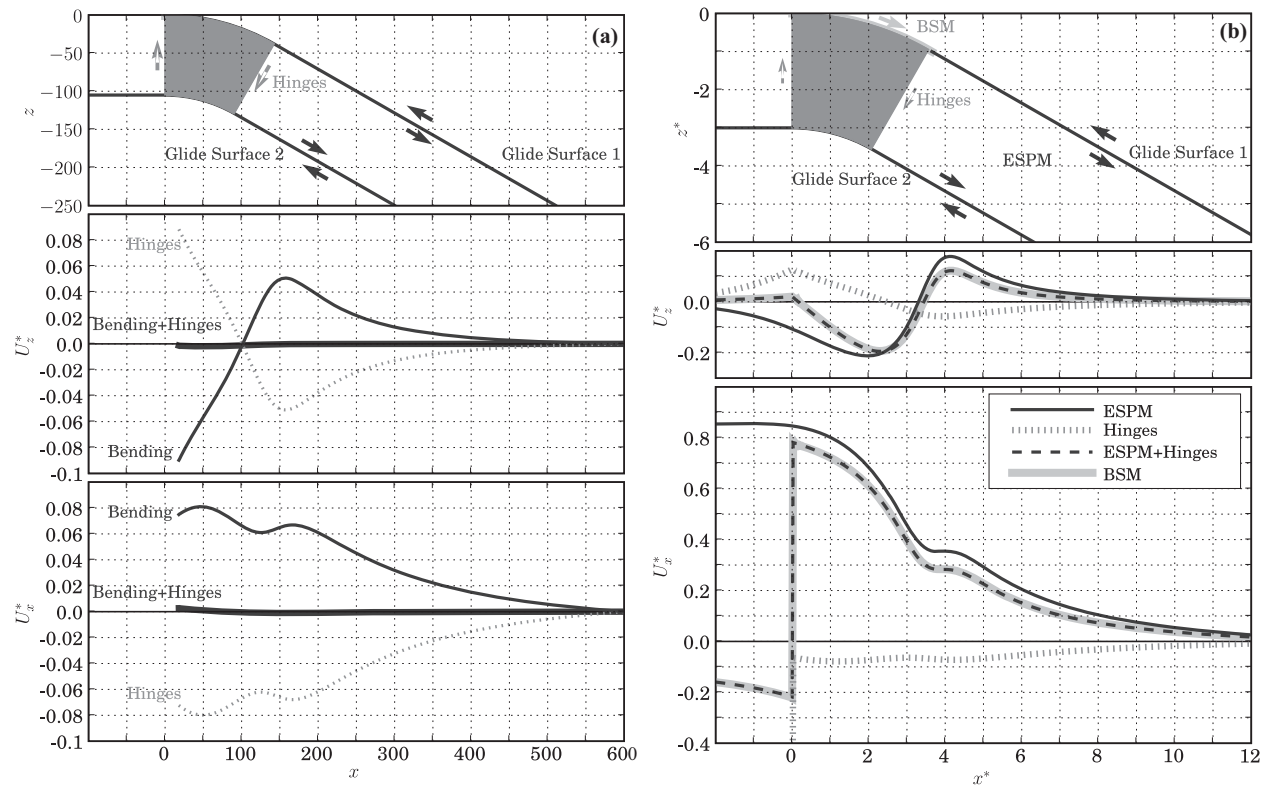


**Figure 2-8.** Surface deformation field for the ESPM for curved plate geometry: (a) the ESPM with no locked zone is equivalent to the long-term, steady state plate motion (solid black line). The axial hinges or velocity gradient corrections are introduced at positions corresponding to the discretization resolution of the curved fault. The surface velocity field due to axial hinges or a velocity gradient (thin dashed gray line) cancels the effect of plate flexure at the trench (thin solid black line), resulting in net zero long-term strain accumulation over the seismic cycle (thick solid black line). Note that the peak uplift due to the bending of a curved plate is shifted arc-ward in comparison to the peak for the planar geometry (Figure 2-7). (b) Effect of the plate flexural field (axial hinges or velocity gradient corrections) on the ESPM with a locked megathrust fault. The sum of the ESPM (thin solid black line) and axial hinge (thick dotted gray line) velocity fields — shown as the thick dashed black line — exactly equals that for the equivalent BSM (thick solid gray line). Panels and plot axes are as described in Figure 2-4.

overriding plate — immediately adjacent to the trench — undergoes net compression (bottom two panels of Figure 2-7(a)). The horizontal surface velocity profile for the curved interface is “ramp-like” — but shows more subdued strain rates (flatter slope) near the trench compared to the planar case (bottom panel of Figure 2-8(a)). In contrast, the vertical surface velocity profile for the curved interface predicts subsidence adjacent to the trench, strains having the opposite sense to those for the planar case (middle panel of Figure 2-8(a)), and attains a maximum value directly above the straightening of the plate interface at depth (compare the top and middle panels of Figure 2-8(a)).

Thus, irrespective of the geometry of the downgoing plate, adding either flexural deformation field to that for the finite thickness ESPM ( $H > 0$ , and having a locked zone) yields predictions identical to that for the ESPM with  $H = 0$  (i.e., the BSM). This equivalence between the ESPM having a finite plate thickness ( $H \neq 0$ ) and the BSM implies that if the “volumetric” flexural stresses are released continuously and aseismically in the shallow parts of the subduction zone during the interseismic period, then the surface deformation due to both BSM and the ESPM are identical for any plate thickness and shape (curvature). If these stresses are released in the deeper parts of the subduction zone (depth  $\gg H$ ) — episodically or continuously — we expect net surface topography to persist after each cycle. But in the real Earth, we would expect such topographic buildup to be modulated by gravity and limited by processes like accretion, sedimentation, and/or erosion in the frontal wedge of the overriding plate. In this equilibrium scenario, the support for near-trench flexural stresses would eventually generate surface topography that is stable after each seismic cycle. So, even when flexural stresses are released at depths ( $> 100$  km), the interseismic velocity fields from the ESPM and the BSM should be nearly identical. In all the above cases, it is appropriate to use the BSM as a simple mathematical approximation to the ESPM. However, within the context of an elastic Earth, the ESPM is still the kinematically more realistic model to interpret the pBSM. The only scenario where the ESPM and the BSM (or pBSM) surface velocity predictions differ would be when part or all of the flexural stresses not released continuously in the shallow parts of the subduction zone (e.g.,

normal faulting in the forebulge of the subducting plate) — and in this case, it is more appropriate to adopt the ESPM.

## 2.5 Comparison of the ESPM and the BSM surface displacements

As noted in the previous section, Flexural stresses near the trench cause the ESPM field to be more compressive than the BSM stress field — resulting in larger surface uplift rates above the downdip end of the locked megathrust interface. This compression is enhanced with either increasing plate thickness or plate curvature. For typical  $H/D_{lock}$  ratios and curvatures found in most subduction zones, a measurable difference exists between the BSM and the ESPM surface velocity fields ( $> 5$  mm/yr, for a typical subducting plate velocity of 5 cm/yr) up to a distance of approximately five to six times the locking depth (Figure 2-5). Intuitively, we expect that in the real Earth, the tip of the frontal wedge adjacent to the trench may not deform in a purely elastic manner. But even in this region, deformation predicted by the ESPM can be considered as the purely elastic component of the total deformation field within the overriding plate during a seismic cycle, and as the driving force for inelastic deformation — and the discrepancy between the ESPM and the BSM (or the pBSM) at a horizontal distance of one interseismic locking depth from the trench can still be as large as  $\sim 100\%$  in the verticals and  $\sim 15\%$  in the horizontals.

As plate thickness increases, this zone of significant difference between these two models broadens for both horizontals and verticals. The location of the zero vertical velocity (commonly referred to as the “hingeline”) for a thick plate shifts trenchward by as much as 20% from its location for the BSM (middle panel of Figure 2-5). However, the locations of the peak in vertical velocity profile or the break in slope of the horizontal velocity profile show negligible dependence on plate thickness. Increasing plate thickness results in a nearly uniform increase in the horizontal strain-rate profile, resulting in a long-wavelength upward tilt of the horizontal surface velocity field relative to the far-field boundary of the overriding plate (middle and bottom panels of Figure

2-5). Thus, a larger plate thickness enhances the non-uniform differences between the vertical surface velocity profiles of the ESPM and the BSM, in contrast to causing only a subtle change in slope between their horizontal surface velocity profiles. Therefore, vertical surface velocities are the key to differentiating between the ESPM and the BSM — i.e., for estimating the minimum elastic plate thickness for a given subduction interface geometry. Owing to the sensitivity of hingeline location to plate thickness, vertical velocities are clearly important in constraining the arc-ward extent of the locked megathrust.

Hence, to characterize both the degree of coupling and minimum elastic plate thickness, it is best to use both horizontal and vertical velocity data for geodetic inversions. Perhaps most importantly, the uncertainties in the measured vertical velocities on land must be small ( $< 1$  cm/yr) — which is possible with current processing methods for regions having good geodetic data coverage over long periods of time (e.g.,  $> 13$  years of continuous GPS coverage in Japan) — and/or ocean bottom geodetic surveys are required. Of course, we must also be confident that these vertical velocities are only due to elastic processes, and not due to inelastic effects like subduction erosion [Heki, 2004]. Therefore, given the current uncertainty of geodetic data and their location with respect to the trench, unless a thick lithosphere or a shallow locking depth can be inferred from other kinds of data (e.g. seismicity, gravity signature associated with plate flexure, seismic reflection, etc.), the BSM is as good a model as the ESPM. But the ESPM still provides not only a generalized framework for deriving, implementing, and interpreting the BSM, but also a fundamental understanding of why the BSM (or pBSM) has been so successful in interpreting interseismic geodetic data in subduction zones. This generality is an important feature of the ESPM, regardless of whether geodetic data can, at present, distinguish the predictions of this model from that of either the BSM or the BFM.

## 2.6 Elastic stresses and strains in the half-space

Subduction is ultimately governed by the negative buoyancy of the downgoing slab [e.g., Elsasser, 1971; Forsyth and Uyeda, 1975]. The kinematic assumptions used here assume that the dynamics of subduction do not change significantly during time-scales relevant to seismic cycles ( $< 10^4$  yr), and therefore the convergence velocity between the subducting and overriding plates, and the geometry of the subduction interface are relatively constant over this time period.

Viewing the BSM (or pBSM) as an end-member model of the ESPM clarifies some of the concerns of Douglass and Buffett [1995; 1996] regarding the former model. By definition, all glide surfaces in the ESPM creep aseismically (at a steady rate) during the interseismic period, continuously loading the locked megathrust as well as surrounding regions in the overriding plate. The burgers vector — which is the displacement of the edge-dislocation representing the bottom of the locked fault over one seismic cycle — accumulates steadily over the glide surfaces bounding the plate until a megathrust event. Therefore, the ESPM provides a natural explanation for the slip-rate dependence of stress along the locked zone even though there is no relative slip across that portion of the interface. It must be noted that both the BSM and the pBSM also consider the locked zone to be at rest during the entire inter-seismic period because of the superposition of steady-creep and backslip on the fault. In fact, as noted earlier, in the ESPM view of the BSM, “backslip” is actually the creep along the bottom surface of the plate, as well as equal to the creep directly downdip of the locked zone.

Another concern of Douglass and Buffett [1995; 1996] was that given the boundaries of the half-space are at infinite distance in EDMs, the tractions along the bottom of the overriding plate (“hanging-wall”) are equal but opposite in sense, on either side of the dislocation tip (i.e., the downdip end of the locked zone). Within the kinematic context of EDMs, we can make a rough estimate of the strain (and stress) perturbations introduced by BSM during a seismic cycle. Typical plate convergence rates are of the order of cm/yr with the maximum convergence having a value of the order of 10 cm/yr

( $10^{-1}$  m/yr). This long-term slip velocity divided by the typical width of the locked patch of the order of 100 km ( $10^5$  m) should give us an estimate of the magnitude of strains and stresses in the elastic half-space owing to the presence of the edge dislocation representing the locked patch. The above calculations yield a typical strain-rate of several  $\mu$ -strain/yr, which, when multiplied by a typical value of shear modulus for crustal rocks (10s of GPa), gives stress rates of the order of 10 kPa/yr. Thus, over a typical megathrust earthquake recurrence interval of 300 yrs, the accumulated stress on the locked patch reaches 3 MPa, equivalent to the average stress drop in inter-plate earthquakes [Kanamori and Anderson, 1975]. In addition to the BSM strain field, the ESPM introduces additional strains associated with material transport down the subducting plate. Observations and theoretical estimates constrain the radius of curvature for subducting plates to  $\sim 200$  km [Conrad and Hager, 1999, and references therein]. From Equation 3, we can calculate the additional flexural strain rate introduced by the ESPM to be of the order of  $0.1 \mu$ -strain/yr, ( $1/10^{\text{th}}$  of the BSM's interseismic strain accumulation rate) which causes a mean surface velocity perturbation of roughly 10% of the BSM's field (Figure 2-5, Figure 2-7, and Figure 2-8). In contrast, both plate flexure theory [Turcotte and Schubert, 2001] and thin-plate finite-strain theory [e.g., Seth, 1935] predict plate bending stresses that are of the order of several 100 MPa — 1 GPa over mantle-convection time-scales. Therefore, the ESPM (as well as the BSM) introduces stress perturbations during the seismic cycle that are much smaller than the long-term stress field associated with plate tectonics. Thus, as Savage [1996] argued for the BSM, when this plate-tectonic stress field is added back to that for the BSM, the correct sense of absolute stress is restored all along the bottom of the overriding plate.

The flexural fields discussed in the previous sections help counter the bending strain perturbation from the ESPM, either partially or in full. The key to estimating the ESPM plate thickness,  $H$ , then is identifying what fraction of the flexural stresses associated with the above perturbation is released episodically in the shallow part of the subduction zone. If we can estimate a plate thickness from interseismic geodetic data ignoring this fraction — that is, assume that all of the flexural stresses are only released episodically in the shallow portion of the subduction zone — then we will end up with the minimum

effective plate thickness required by such data. Otherwise, this fraction can also be estimated as an additional ESPM parameter during inversion. Thus, depending on whether other kinds of data warrant the determination of a fractional flexural stress release ( $f_\sigma$ ), the ESPM can be used for inverting interseismic geodetic data with only one ( $H$ ), or two ( $H$ , and  $f_\sigma$ ) additional parameters compared to the BSM.

## 2.7 Discussion

Our capacity to resolve between the BSM and the ESPM, and therefore, the characteristics of plate flexural stress relaxation, depends on whether there are geodetic observations close to the trench [ $x_{GPS} < x_{lock}$ , see Figure 2-1]. Typically, GPS stations are on the overriding plate at distances much larger than  $x_{lock}$  from the trench, where both the ESPM and the BSM predict nearly identical velocities. However, if highly accurate vertical geodetic data are available on the surface of the overriding plate, at distances less than  $x_{lock}$  from the trench — and if we are confident that this data reflects elastic processes — then we would be able to discriminate between the surface deformation fields predicted by these two models if: (a) subducting plate thickness in the ESPM is large, and/or (b) the plate geometry has a large curvature near the trench, and (c) if the volumetric strain associated with plate bending is released episodically in the shallow portions of the subduction zone (< 100 km depth). Even in this case, there will be a trade-off between the actual plate thickness and the fraction of flexural stresses released episodically in the shallow portion of the subduction zone. Therefore, we will only be able to estimate a minimum plate thickness from even a very accurate and dense network of geodetic observation stations. However, if the flexural strain is released continuously in the shallow parts of the subduction zone, or released at larger than  $\sim 100$  km depth — in which case the release occurs too deep to have an effect on the surface deformation of the overriding plate — then the surface velocity fields predicted by the ESPM and the BSM are nearly identical to each other and the latter may be a better model to use because it has two fewer parameters to estimate.

Potential areas where the subduction zone geometry is favorable for testing the ESPM include: Nankai Trough underneath Kii Peninsula [e.g., Hacker et al., 2003 (Figure 3)], Costa Rica Trench, south of the Nicoya peninsula [e.g., Hacker et al., 2003 (Figure 4)], Peru-Chile Trench from Ecuador through Peru [e.g., Gutscher et al., 2000 (Figures 3, 5, and 10)], northern Chile [e.g., ANCORP Working Group, 2003 (Figure 7)], and perhaps, Sumatra [e.g., Chlieh et al., 2008a].

Based on the typical radius of curvature of most subducting slabs, the current distribution of geodetic observations as well as their accuracy, and the surface velocity field predictions above, the ESPM is a relevant model for subduction zones wherever  $H/D_{lock} \geq 2$  — that is, either the locked zone is constrained to be shallow (for instance, from thermal modeling [Oleskevich et al., 1999]) or the downgoing slab can be inferred to be thick (say  $> 50$  km) based on sea-floor age at the trench [e.g., Fowler, 1990; Turcotte and Schubert, 2001]. In contrast, the ESPM with  $H/D_{lock} \leq 1$  is indistinguishable from the BSM, even though the latter may over-predict the extent of the locked zone by roughly 10 km (leading to similar discrepancies in  $x_{lock}$ ); in this case, the BSM may be a better model to use because of its simplicity. These requirements immediately exclude the following: Nankai Trough (because of the small curvature of the Phillipine Sea plate, with shallow dip  $< 15^\circ$  [Park et al., 2002]), Tohoku, Japan Trench (inferred to have very deep locking depth [Suwa et al., 2006]); and Sumatra (because the inferred locking depth is not shallow (30–55 km [Subarya et al., 2006])). The most promising of the above subduction zones for future investigations to discriminate the ESPM from the BSM (or the pBSM) are: Nicoya peninsula, Costa Rica (shallow seismogenic zone and strong slab curvature [DeShon et al., 2006]); and Northern Chile in the vicinity of the Mejillones peninsula (possibly shallow locking depth, and strong plate curvature [ANCORP Working Group, 2003; Brudzinski and Chen, 2005]). Of course if ocean bottom geodetic stations are successfully installed in the future [see for instance, Gagnon et al., 2005], then many of the above subduction zones might be more amenable to application of the ESPM.

To the extent that net deformation remaining after a seismic cycle may contribute incrementally to the long term surface topography of the overriding plate, Figure 2-8(a) (middle panel) points to another important consequence of elastic plate flexure. For a realistic curved subduction megathrust interface, the peak in the vertical surface velocity field due to plate flexure has a magnitude of  $< 5\%$  of the long-term plate convergence rate (for plate thickness of  $< 100$  km), and occurs at distances of approximately 75–150 km arcward of the trench. The location of the peak uplift rate is independent of the plate thickness, but depends strongly on plate curvature. The purely elastic ESPM cannot accumulate such long-term inelastic strain, but it can still provide a measure of where such deformation could occur in the overriding plate over several seismic cycles. In the real Earth, we expect such runaway elastic deformation to be continuously modulated by gravity, inelasticity, accretion, sedimentation, and erosion, resulting in near-equilibrium surface topography. So, if even a small fraction of this peak surface uplift rate arising from elastic flexure promotes inelastic deformation in the real earth, then stable islands, or coastal uplift [e.g., Klotz et al., 2006] could occur at such distances over the long-term. We illustrate this flexural effect for the Sumatran subduction zone (Figure 2-9, with interface geometry as described in [Hsu et al., 2006]). The location of the peak uplift rate is at a distance of  $\sim 100$  km, irrespective of plate thickness (bottom panel of Figure 2-9), and corresponds roughly to the location of the islands in the forearc — as discerned by the along-strike averaged, trench perpendicular bathymetric profile (middle panel of Figure 2-9).

Thus, plate bending could be a plausible driving mechanism for forearc uplift phenomena — such as the presence of forearc islands or coastal uplift — in young, evolving subduction zones, even if only a fraction of the flexural strain after each seismic cycle is inelastic. While such forearc uplift phenomena have been predicted by layered elastic-over viscoelastic models [e.g., Sato and Matsu'ura, 1988; Matsu'ura and Sato, 1989; Sato and Matsu'ura, 1992; 1993; Fukahata and Matsu'ura, 2006], they include many more parameters related to erosion, accretion, and sedimentation, with much larger uncertainties. In addition, the long-term deformation in these models was shown by the above authors to be entirely attributable to only the portion of the fault interface

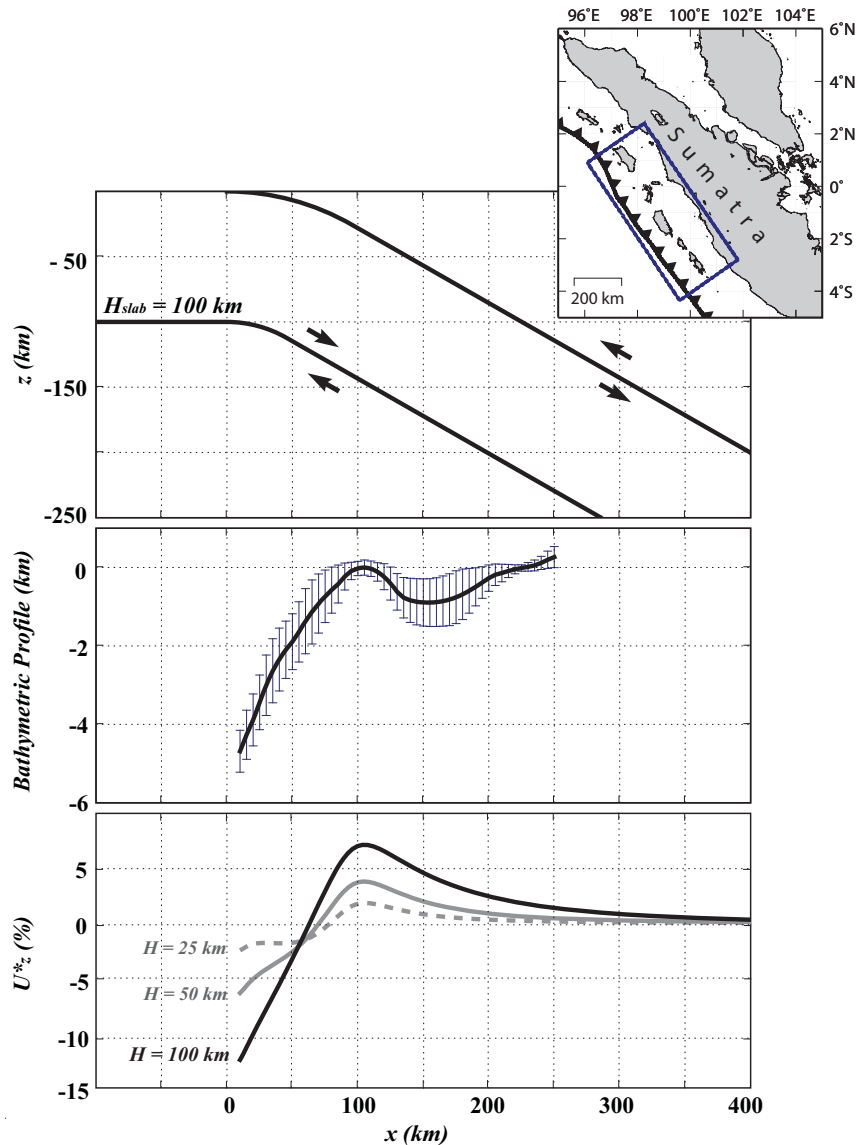


**Figure 2-9.** Comparison of predicted surface velocity profiles from the elastic plate bending flexural field [bottom panel, for plate thicknesses of 25 (dashed gray), 50 (gray), and 100 km (black)], with that of the long-term along-strike averaged trench-perpendicular topographic profile (middle panel, with error bars in blue) for the Sumatran subduction zone (top panel, and inset map). Note that the location of the peak uplift-rate is independent of plate thickness,  $H_{slab}$  (bottom panel). The trench profile in the map is from Bird [2003], and the rectangle indicates the zone of along-strike averaging of the plate geometry (top panel) as well as bathymetry (middle panel). The geometry of the mean plate interface profile (top panel, only  $H_{slab}=100$  km is shown) is similar to that assumed in [Hsu et al., 2006], and attains a dip of  $30^\circ$  at a depth of  $\sim 27$  km below the islands. Note the correspondence in the location of the peak values in the middle and bottom panels. See text for details.

embedded in the upper elastic layer (of thickness  $H$ ), which results in a surface deformation field that is qualitatively similar to that of the steady state component of the ESPM with plate thickness,  $H$ . The advantage of the ESPM is that only a single parameter ( $f_\sigma$ ) is required to determine the potential locations of permanent deformation, and therefore much more conducive to geodetic inversions.

## 2.8 Conclusions

The ESPM can be thought of as a kinematic proxy for slab-buoyancy-driven subduction. The derivation of the ESPM provides a kinematically consistent and physically more intuitive rationale for why the BSM works so well for interpreting current interseismic geodetic data, especially for young, evolving subduction zones. The BSM can be viewed as an end-member model of the ESPM, in the limiting case of zero plate thickness. The BSM is also an end-member model of the ESPM having a finite plate thickness, if all of the stresses associated with these plate flexural strains are either released continuously in the shallow portion of the subduction zone, or released deeper in the subduction zone ( $> 100$  km depth). So, the current practice of fitting available interseismic geodetic data using the BSM is in effect using the ESPM, but assuming either (a) a negligible elastic plate thickness, or (b) that all flexural stresses are released continuously during bending or at depth. Only in the case where these plate flexural stresses are not released continuously in the shallow parts of the subduction zone, can the deformation field of the ESPM be distinguished from that of the BSM. In this case, the differences between the surface velocity fields predicted by the two models is measurable within a few locking depths of the trench, and our ability to discriminate between them is limited by lack of geodetic observations above the locked patch in most subduction zones.

Unlike the pBSM, the ESPM, by definition, yields the correct sense and magnitude of horizontal velocities on the surface of the downgoing plate before it subducts into the trench, as well as zero net steady state block uplift of the overriding plate — primarily because volume conservation is integral to its formulation. Therefore, unlike the pBSM,

the ESPM does not require *ad hoc* steady state velocity corrections. The ESPM eliminates ambiguities associated with the application of the pBSM to non-planar geometries by providing a kinematically consistent framework in which to do so. For plates with curved geometry, the equivalent BSM should have backslip applied along the corresponding curved subduction interface (Figure 2-3, and as explicitly stated by Savage [1983]), and not along the tangent plane to this curved interface at depth.

Characterizing the ESPM requires the estimation of at most two additional parameters (plate thickness, and fraction of flexural stresses released), which can potentially be inverted for in subduction zones that have an  $H/D_{lock}$  ratio equal to 2 or greater. If we assume all flexural stresses are only released episodically in the shallow part of the subduction zone, then this elastic thickness is a minimum plate thickness over the seismic-cycle timescale — as seen by geodetic data. If the BSM is used for the inversion instead of the ESPM, it would predict a wider locked zone compared to the ESPM, assuming that the fault geometry is well constrained. In order to discriminate between the ESPM and the BSM, we must use both the horizontal and vertical surface velocity fields. As the data quality, duration, and coverage improve in the future — especially station density near the trench, say with the deployment of GPS stations on islands or peninsulas close to the trench or on the ocean bottom — inversion for the ESPM parameters can provide an independent estimate for a minimum elastic thickness of the subducting plate, and perhaps even its along-strike variation.

**Table 2-1.** Notation

$\epsilon_{xz}$	Shear-strain
$d\epsilon_{xz}/dt$	Shear strain rate
$\theta, \theta_{dip}$	Planar fault/plate interface dip
$\theta_{bot}$	Dip at the bottom of the locked zone for a curved plate interface
$\Delta\theta$	Change in interface dip from one curved segment to the next
$D_{lock}, d_{lock}$	Depth of locking along the megathrust interface
$C_p$	Local curvature of the centerline of the plate
$f_\sigma$	Fraction of flexural stresses released episodically at shallow depths
$H$	Thickness of the subducting plate in the ESPM
$R_{bot}$	Local radius of curvature for the bottom surface of the plate
$R_p$	Local radius of curvature for the centerline of the plate
$R_{top}$	Local radius of curvature for the top surface of the plate
$s$	Arc-length along the plate interface, or fault-width
$s_{lock}$	Width of locked plate interface
$T_e$	Elastic plate thickness in plate flexure models
$\delta V$	Velocity perturbation to be added to (subtracted from) the centerline plate velocity
$V_{bot}$	Velocity at the bottom surface of the plate
$V_p$	Plate convergence velocity
$V_{top}$	Velocity at the top surface of the plate
$V_x^*$	Horizontal surface velocity normalized by plate rate
$V_z^*$	Vertical surface velocity normalized by plate rate
$x$	Horizontal coordinate, positive landward, or away from the trench
$x^*$	Horizontal coordinate, normalized w.r.t. locking depth
$x_{GPS, (min/max)}$	Distance range from the trench to the nearest geodetic observation
$x_{hinge}$	Distance from the trench to the location of zero vertical surface velocity
$x_{lock}$	Distance between trench and surface projection of the downdip end of the locked zone
$x_{max}$	Distance from trench to the location of the peak in the vertical surface velocity field
$z$	Vertical coordinate, positive upward (depths are therefore, negative)
$z^*$	Vertical coordinate, normalized w.r.t. locking depth

## References

- ANCORP-Working-Group (2003), Seismic Imaging of a convergent continental margin and plateau in the central Andes (Andean Continental Research Project 1996 (ANCORP'96)), *J. Geophys. Res.*, 108, B7, 10.1029/2002JB001771.
- Bird, P. (2003), An updated digital model of plate boundaries, *Geochem Geophys Geosy*, 4, 3, 1027, doi:10.1029/2001GC000252.
- Brudzinski, M. R., and Chen, W.-P. (2005), Earthquakes and strain in subhorizontal slabs, *J. Geophys. Res.*, 110, B08303, 10.1029/2004JB003470.
- Buffett, B. A. (2006), Plate force due to bending at subduction zones, *J. Geophys. Res.*, 111, B9, B09405, [10:1029/2006JB004295](https://doi.org/10.1029/2006JB004295).
- Chlieh, M., Avouac, J.-P., Sieh, K., Natawidjaja, D. H., and Galetzka, J. (2008), Heterogeneous coupling on the Sumatra megathrust constrained from geodetic and paleogeodetic measurements, *J. Geophys. Res.*, 113, B05305.
- Chlieh, M., Chabalier, J. B. d., Ruegg, J. C., Armijo, R., Dmowska, R., Campos, J., and Feigl, K. L. (2004), Crustal deformation and fault slip during the seismic cycle in the North Chile subduction zone, from GPS and InSAR observations, *Geophys. J. Int.*, 158, 2, 695-711, 10.1111/j.1365-246X.2004.02326.x
- Cohen, S. C. (1999), Numerical Models of Crustal Deformation in Seismic Zones, *Adv. Geophys.*, 41, 133-231.
- Conrad, C. P., and Hager, B. H. (1999), Effects of plate bending and fault strength at subduction zones on plate dynamics, *J. Geophys. Res.*, 104, 17551-17571.
- DeShon, H. R., Schwartz, S. Y., Newman, A. V., González, V., Protti, M., Dorman, L. M., Dixon, T. H., Sampson, D. E., and Flueh, E. R. (2006), Seismogenic zone structure beneath the Nicoya Peninsula, Costa Rica, from three-dimensional local earthquake P- and S-wave tomography, *Geophys. J. Int.*, 164, 1, 109–124.
- Elsasser, W. M. (1971), Sea-floor spreading as thermal convection, *J. Geophys. Res.*, 76, 1101-1112.
- Forsyth, D. W., and Uyeda, s. (1975), On the relative importance of the driving forces of plate motion, *Geophys. J. R. Astron. Soc.*, 43, 163-200.
- Fowler, C. M. R. (1990), *The solid earth*, 472 pp., Cambridge University Press, Cambridge.

- Freund, L. B., and Barnett, D. M. (1976), A Two-Dimensional Analysis of Surface Deformation due to Dip-slip Faulting, *Bull. Seismol. Soc. Am.*, 66, 3, 667-675.
- Gagnon, K., Chadwell, C. D., and Norabuena, E. (2005), Measuring the onset of locking in the Peru–Chile trench with GPS and acoustic measurements, *Nature*, 434, 205–208.
- Gutscher, M.-A., Spakman, W., Bijwaard, H., and Engdahl, E. R. (2000), Geodynamics of at subduction: Seismicity and tomographic constraints from the Andean margin, *Tectonics*, 19, 5, 814-833.
- Hacker, B. R., Peacock, S. M., Abers, G. A., and Holloway, S. D. (2003), Subduction Factory, 2: Are intermediate-depth earthquakes in subducting slabs linked to metamorphic dehydration reactions?, *J. Geophys. Res.*, 108, B1, 2030, 10.1029/2001JB001129.
- Hager, B. H. (1984), Subducted slabs and the geoid: constraints on mantle rheology and flow. , *J. Geophys. Res.*, 89, 6003-6015.
- Heki, K. (2004), Space Geodetic Observation of Deep Basal Subduction Erosion in Northeastern Japan, *Earth Planet. Sci. Lett.*, 219, 13-20.
- Hsu, Y.-J., Simons, M., Avouac, J.-P., Galetzka, J., Sieh, K., Chlieh, M., Natawidjaja, D., Prawirodirdjo, L., and Bock, Y. (2006), Frictional Afterslip Following the 2005 Nias-Simeulue Earthquake, Sumatra, *Science*, 312, 5782, 1921-1926, 10.1126/science.1126960.
- Iio, Y., Sagiya, T., and Kobayashi, Y. (2004), Origin of the Concentrated Deformation Zone in the Japanese Islands and Stress Accumulation Process of Intraplate earthquakes, *Earth Planets Space*, 56, 831-842.
- Iio, Y., Sagiya, T., Kobayashi, Y., and Shiozaki, I. (2002), Water-weakened lower crust and its role in the concentrated deformation in the Japanese Islands, *Earth Planet. Sci. Lett.*, 203, 245-253.
- Kanamori, H., and Anderson, D. L. (1975), Theoretical basis of some empirical relations in seismology, *Bull. Seism. Soc. Am.*, 65, 1073-1095.
- Klotz, J., Abolghasem, A., Khazaradze, G., Heinze, B., Vietor, T., Hackney, R., Bataille, K., Maturana, R., Viramonte, J., and Perdomo, R. (2006), Long-term signals in the present-day deformation field of the Central and Southern Andes and Constraints on the viscosity of the Earth's Upper Mantle. , in *The Andes: Active Subduction Orogeny*, *Frontiers in Earth Sciences*, edited by O. Oncken, G. Chong, G. Franz, P. Giese, H. Goetze, V. A. Ramos, M. R. Strecker and P. Wigger, pp. 65–89, Springer Berlin.
- Masterlark, T. (2003), Finite element model predictions of static deformation from dislocation sources in a subduction zone: Sensitivities to homogeneous, isotropic, Poisson-solid, and half-space assumptions, *J. Geophys. Res.*, 108 B11, 2540, 10.1029/2002JB002296.

- Nishimura, T., Hirasawa, T., Miyazaki, S., Sagiya, T., Tada, T., Miura, S., and Tanaka, K. (2004), Temporal change of interplate coupling in northeastern Japan during 1995-2002 estimated from continuous GPS observations, *Geophys. J. Int.*, 157, 901-916.
- Okada, Y. (1992), Internal deformation due to shear and tensile faults in a half-space, *Bull. Seismol. Soc. Am.*, 82, 2, 1018-1040.
- Oleskevich, D. A., Hyndman, R. D., and Wang, K. (1999), The updip and downdip limits to great subduction earthquakes: thermal and structural models of Cascadia, south Alaska, SW Japan, and Chile, *J. Geophys. Res.*, 104, 14965–14991.
- Park, J.-O., Tsuru, T., Kodaira, S., Cummins, P. R., and Kaneda, Y. (2002), Splay Fault Branching Along the Nankai Subduction Zone, *Science*, 297, 1157-1160.
- Rani, S., and Singh, S. J. (1992), Static Deformation of a Uniform Half-space due to a Long Dip-slip Fault, *Geophys. J. Int.*, 109, 469-476.
- Savage, J. C. (1983), A dislocation model of strain accumulation and release at a subduction zone, *J. Geophys. Res.*, 88 4984-4996.
- Savage, J. C. (1995), Interseismic uplift at the Nankai subduction zone, Southwest Japan, 1951–1990, *J. Geophys. Res.*, 100, 6339–6350.
- Savage, J. C. (1996), Comment on "The stress state implied by dislocation models of subduction deformation" by J. J. Douglass and B. A. Buffett, *Geophys. Res. Lett.*, 23, 19, 2709-2710.
- Savage, J. C. (1998), Displacement field for an edge dislocation in a layered half-space, *J. Geophys. Res.*, 103, 2439-2446.
- Seth, B. R. (1935), Finite Strain in Elastic Problems, *Philosophical Transactions of the Royal Society of London*, 234, 738, 231-264.
- Sieh, K., Ward, S. N., Natawidjaja, D., and Suwargadi, B. W. (1999), Crustal deformation at the Sumatran subduction zone revealed by coral rings, *Geophys. Res. Lett.*, 26, 3141-3144.
- Souter, B. J., and Hager, B. H. (1997), Fault propagation fold growth during the 1994 Northridge, California, earthquake?, *J. Geophys. Res.*, 102, B6, 11,931–911,942.
- Subarya, C., Chlieh, M., Prawirodirdjo, L., Avouac, J. P., Bock, Y., Sieh, K., Meltzner, A., Natawidjaja, D., and McCaffrey, R. (2006), Plate-boundary deformation of the great Aceh-Andaman earthquake, *Nature*, 440, 46–51.
- Suppe, J. (1985), *Principles of Structural Geology*, 537 pp., Prentice-Hall.

- Suwa, Y., Miura, S., Hasegawa, A., Sato, T., and Tachibana, K. (2006), Interplate coupling beneath NE Japan inferred from three-dimensional displacement field, *J. Geophys. Res.*, 111, B4, B04402, 10.1029/2004JB003203.
- Tomar, S., and Dhiman, N. K. (2003), 2D Deformation Analysis of a Half-space due to a Long Dip-slip Fault at Finite Depth, *Proc. Indian Acad. Sci. (Earth Planet. Sci.)*, 112, 4, 587-596.
- Turcotte, D. L., and Schubert, G. (2001), *Geodynamics*, 2 ed., 456 pp., Cambridge University Press, New York.
- Twiss, R. J., and Moores, E. M. (1992), *Structural Geology*, 1st ed., 532 pp., W. H. Freeman and Company, New York.
- Vergne, J., Cattin, R., and Avouac, J. P. (2001), On the use of Dislocations to Model Interseismic Strain and Stress Build-up at Intracontinental Thrust Faults, *Geophys. J. Int.*, 147, 1, 155-162, 10.1046/j.1365-246X.2001.00524.x.
- Wang, K. (2007), Elastic and viscoelastic models of crustal deformation in subduction earthquake cycles, in *The Seismogenic Zone of Subduction Thrust Faults*, edited by T. Dixon and J. C. Moore, pp. 540-575, Columbia University Press, New York.
- Wang, K., and Hu, Y. (2006), Accretionary Prisms in Subduction Earthquake Cycles: The Theory of Dynamic Coulomb Wedge, *J. Geophys. Res.*, 111, B06410, 10.1029/2005JB004094.
- Wang, R. (2005), The dislocation theory: a consistent way for including the gravity effect in (visco)elastic plane-earth models, *Geophys. J. Int.*, 161, 191-196.
- Yoshioka, S., Yabuki, T., Sagiya, T., Tada, T., and Matsu'ura, M. (1993), Interplate coupling and relative plate motion in the Tokai district, central Japan, deduced from geodetic data inversion using ABIC, *Geophys. J. Int.*, 113, 607-621.
- Zhao, S., and Takemoto, S. (2000), Deformation and stress change associated with plate interaction at subduction zones: a kinematic modeling, *Geophys. J. Int.*, 142, 300-318.

## *Chapter 3*

### A SENSITIVITY ANALYSIS OF ELASTIC DISLOCATION MODELS FOR INTERSEISMIC DEFORMATION IN SUBDUCTION ZONES

#### **3.1 Introduction**

At subduction plate boundaries, geodetic data from the interseismic period — decades to centuries after a megathrust earthquake — help to delineate regions of the megathrust that are not presently slipping and can potentially produce large earthquakes. Due to both observational and theoretical considerations, such data are frequently interpreted using simple elastic dislocation models (EDMs). The simplest of these EDMs, the backslip model [the BSM, see Savage, 1983], can be essentially described with only two parameters — the extent of the locked fault interface, and the plate geometry. The BSM has been widely used in modeling interseismic period geodetic data in subduction zones, and to successfully fit geodetic observations using realistic plate interface geometries [Zweck et al., 2002; Khazaradze and Klotz, 2003; Wang et al., 2003; Suwa et al., 2006]. Even when nonlinear rheologies (e.g., elasto-plastic) are assumed for modeling plate deformation, strains tend to localize in narrow zones. The far-field deformation due such shear zones can be hard to distinguish from the field resulting from slip along a single fault, assuming purely elastic rheology [Souter and Hager, 1997]. Also, as the quality of geodetic data improves, they can be used to constrain more complicated 3D models [e.g., Masterlark, 2003].

Owing to the simplicity of EDMs, and their success in fitting current geodetic observations, the analysis presented here is entirely based on such models — specifically, on the BSM. The BSM is motivated by the recognition that the overriding plate apparently experiences little permanent inelastic deformation on the time scales relevant to the seismic cycle (less than a few thousand years) [see, Savage, 1983; Wang and Hu, 2006]. To first order, the interseismic and coseismic strain fields must cancel each other

and asthenospheric relaxation does not significantly contribute to the interseismic deformation field [Savage, 1983, 1995]. In a previous paper [see Chapter 2, and Kanda and Simons, 2010], we showed the equivalence between a subducting plate model (the ESPM) and the BSM, and concluded that owing to practical considerations, the BSM would fit currently available geodetic data as well as the ESPM. For reasons described there, the small effects associated with layering as well as gravity are typically ignored when applying the BSM, a homogeneous elastic half-space is assumed for estimating the first-order features of the interseismic surface deformation field..

Owing to the rich variety of behavior that can be simulated, as well as their computational speed, such simple EDMs warrant serious consideration when inverting interseismic geodetic data in subduction zones. Even though geometry has a first-order effect on EDM predictions, geometric parameters (and sensitivity to variations in these parameters) are seldom included in slip-inversions because inverting for geometry at the same time as slip distribution can become prohibitively expensive (since Greens functions/kernels have to be re-computed each time fault discretization changes significantly). So, this paper is a purely theoretical effort to systematically analyze, and quantitatively estimate the sensitivity of surface velocity predictions to parameterizations of (i) megathrust interface geometry, and (ii) presence of slip-transition zones along the megathrust interface. By allowing quantitative estimation of uncertainties due to geometrical parameterization, we obtain more accurate constraints on the actual slip deficit along the megathrust interface during the interseismic period.

In the following analysis, the definition of the locked zone during the interseismic period includes both coseismic and postseismic slip zones on the subduction interface.

Throughout this paper, we assume Volterra edge-dislocations, i.e., the burger's vector is uniform and constant over the glide-plane of the dislocations — except for the section of the glide surface that is locked ( $V_p = 0$ ) or lies within a slip transition zone ( $V_p$  is a linear function) immediately above or below the locked section. We use the 2D elastic dislocation solutions for a dip-slip fault embedded in an elastic half-space given by Freund and Barnett [1976], as corrected by Rani and Singh [1992] (see also, Tomar and

Dhiman [2003] and Cohen [1999]) for computing surface velocities. We quantify the sensitivity of key surface observables — the locations of the hinge-line ( $x_{hinge}$ , where the vertical velocities switch from subsidence to uplift during the interseismic, i.e., where  $U_z = 0$ ) and maximum uplift rates in the vertical velocity field ( $x_{max}$ , where  $U_z$  is a maximum) — to EDM parameters: subduction thrust geometry, the extent of the locked zone,  $s_{lock}$ , and the width of a transition zone,  $s_{trans}$ , downdip of  $s_{lock}$ . We assume that the origin is at the trench, the  $x$ -axis is positive “landward” of the trench, and the  $z$ -axis is positive upwards (so depths within the half-space are negative). Dips are positive clockwise from the positive  $x$ -axis. For the vertical surface deformation field, uplift is considered positive, and for the horizontal field, “landward” motion is assumed positive. If the fault geometry is linear (straight line), a circular arc (constant curvature), or a parabolic profile (decreasing curvature with depth) — all passing through the origin (the trench) — it is straightforward to relate  $s_{lock}$  to either  $D_{lock}$ , or  $x_{lock}$ . Using faults having the same lengths and same dips at the downdip end of the locked zone allows us to compare predictions of surface observables like  $x_{hinge}$  and  $x_{max}$  for different fault geometries. Although we only consider the 2D problem (the fault is assumed to extend to infinity along strike, in-and-out of the plane of this paper) the analysis here can be easily extended to 3D problems with geometry varying along the strike of the trench axis.

### 3.2 Transition zones adjoining the locked megathrust

In reality, it is physically implausible for an abrupt transition from locked to creeping at the downdip end of the locked zone, as a dislocation model would imply. Stress concentrations would be too high for the material to behave elastically [e.g., Scholz, 1990]. In addition, the downdip end of the locked zone as well as the surrounding overriding plate is thought to be thermally controlled [Hyndman and Wang, 1993] and experience time-dependent anelastic deformation. So, we make use of a kinematically imposed transition zone along the plate interface downdip of the locked zone as a proxy for the integrated effects of anelastic deformation during the seismic cycle [e.g., Wang et al., 2003]. The width of this transition zone is thought to be controlled by the  $350^\circ$  and

450° isotherms [Hyndman and Wang, 1993], and its location along the subduction interface strongly depends both on the interface geometry as well as the thermal structure for the subduction zone. For instance, Wang et al. [2003] assume a transition zone whose width is as large as the locked zone, governed by different tapered slip distribution profiles at different times during the seismic cycle. Here, in our intuition building toy models, we consider a transition zone whose width is 25% of that of the locked zone ( $f_{tz}=0.25$ ), along which slip increases linearly from zero to the long-term plate convergence rate during the interseismic period. Such a tapered slip zone is only partially slipping (creeping) during the interseismic period, but also partially ruptures coseismically. Although  $f_{tz}$  was arbitrarily chosen here, our purpose is to demonstrate its significant effect of tapered slip zones on the predictions of elastic dislocation models – even when they have such a small extent. For a subducting plate having a finite thickness, as represented in the ESPM, the steady motion of its bottom surface can result in interseismic slip — at velocities less than or equal to the plate convergence rate — along the shallow portion of the plate interface (between the trench and depths of 5–10 km). Such shallow slip is plausible in view of the fact that the frontal wedge of the overriding plate is made up of unconsolidated sediments that do not have significant internal strength. However, slip along the shallow interface must transition from a finite value to zero at the updip limit of the locked zone. As will be shown later, such shallow updip transition zones do not significantly affect the vertical velocities (and hence, surface observables like the locations of the hinge-line and maximum vertical velocity), but strongly affect horizontal velocities within a few locking depths of the trench (~ by as much as 100% of the plate convergence rate). In this study, we use an updip transition zone extending from the trench (where, slip velocity is assigned the plate rate) to the updip limit of the locked zone (where slip is zero during the interseismic), to illustrate the effects of varying its extent. Here, we consider a lower transition zone having a width,  $s_{trans}$ , along the plate interface downdip of the locked zone, as well as a shallow transition zone of width  $\leq s_{trans}$  along the plate interface between the trench and the updip limit of the locked zone.

We explore the effect of fractional transition zone widths,  $f_{tr} (= s_{trans}/s_{lock})$  in Figure 3-1 (a) through (d). The effect of adding a downdip transition zone is the same as that of increasing  $s_{lock}$ , and slightly reducing the effective uniform convergence velocity (averaged over both the fully and partially locked interface) for the interseismic period (Figure 3-1 (a) and (b)). In other words, the velocity profiles from dislocation models having a transition zone are of a longer wavelength (or broader) than those for the case having no transition zone. Also, a transition zone of the same length affects the surface velocity predictions for both the ESPM and the BSM (having the same geometry and convergence velocity), by roughly the same fractional amount. Because the locations of the change in slope of the horizontal velocity profiles follow the effective  $x_{lock}$ , it occurs farther than that for the no-transition-zone case. Furthermore, the horizontal velocity profile is broader beyond this change in slope when there is a transition zone. To facilitate comparison, the geometry considered in Figure 3-1 is identical to that considered for the Cascadia subduction zone by Williams and McCaffrey [2001]. The broadening of horizontal velocity profiles due to a downdip transition zone (Figure 3-1 a and b – for the ESPM or the BSM) can help explain the discrepancy between their EDM-predicted and observed horizontal GPS velocities [Figure 3a, Williams and McCaffrey, 2001]. Again, the shapes of the vertical velocity profiles are much more sensitive to the extent of the transition zone (Figure 3-1 (a) and (b) middle), compared to those of the horizontal velocity profiles (Figure 3-1 (a) and (b) bottom).

On the other hand, the vertical surface velocity profiles predicted by either the ESPM or the BSM are not significantly affected by the presence of an updip transition zone (Figure 3-1 (c) and (d)), owing to the typically shallow dip of the plate interface near the trench (which is typical of most subduction interfaces). An updip transition zone causes a large gradient in horizontal surface velocities near the trench, without significantly affecting these velocities landward of  $x_{lock}$ . As before, the shapes of the horizontal surface velocity predictions of the ESPM and the BSM are nearly identical, making it hard to use this

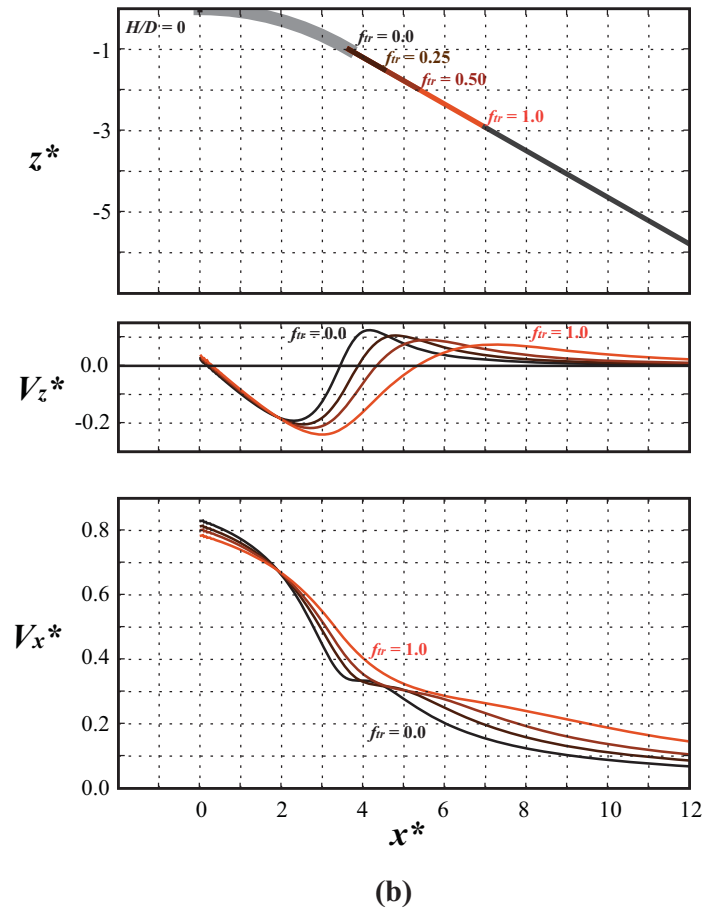
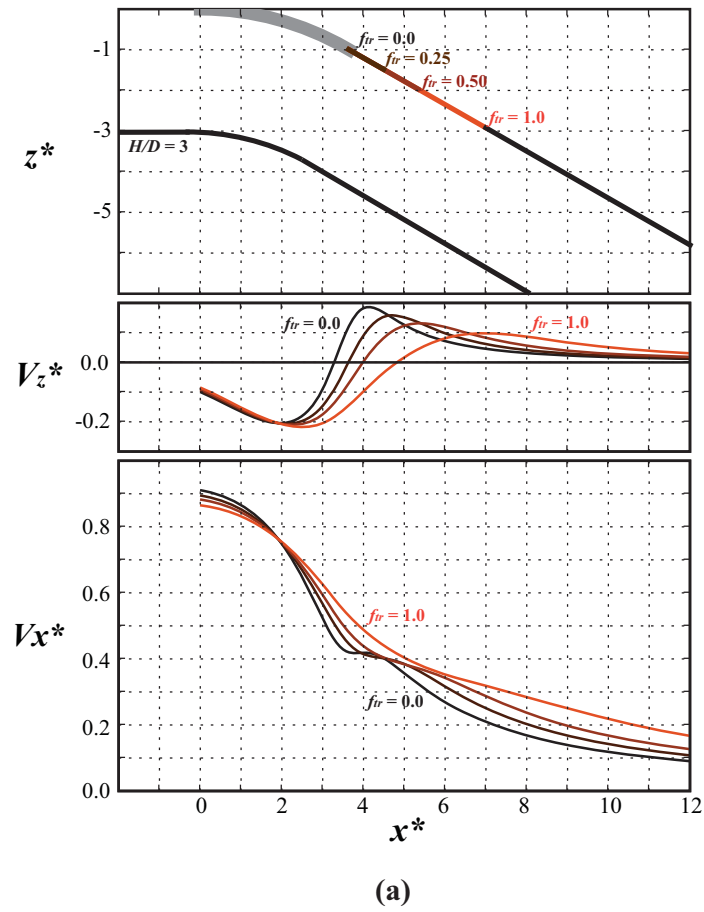
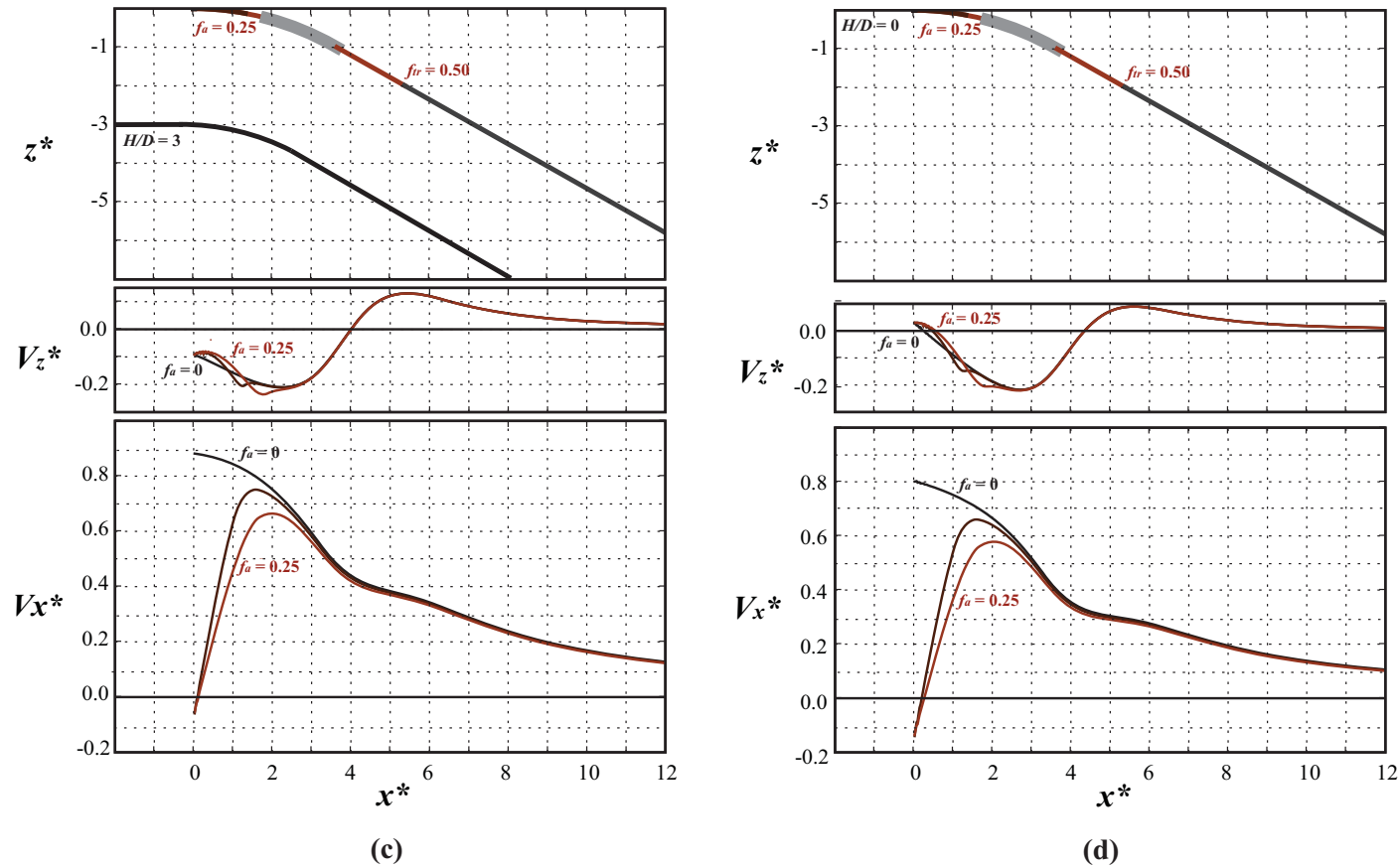


Figure 3-1.



**Figure 3-1.** Effect of doubling the width of the transition zones up dip and down dip of the locked megathrust interface for the ESPM and the BSM.  $f_{tr}$  is the fractional length of the transition zone relative to the width of the locked megathrust,  $s_{trans}/s_{lock}$ . For up dip transition zones (parts a and b), results are presented for  $f_{tr} = 0, 0.125,$  and  $0.25$ . For down dip transition zones (parts c and d), results are presented for  $f_{tr} = 0, 0.25, 0.5,$  and  $1$ . Axes are as described in text.

component to distinguish between the two models. The vertical surface velocity profiles can still discriminate between the two models, owing to the strong dependence of their shape on both the plate thickness as well as the extent of the downdip transition zone (Figure 3-1 (c) and (d)). Therefore, vertical surface velocities are the key to not only differentiating between the ESPM and the BSM (i.e., for estimating the minimum elastic plate thickness for a given subduction interface geometry), but also the location of the effective  $x_{lock}$ . However, the uncertainties in horizontal velocities are smaller than those for the verticals (sometimes by a factor of two), and for most subduction zones or thrust faults (which typically have dips  $< 30^\circ$  near their surface trace), surface horizontal velocities are much larger than the verticals, and therefore have a much better signal-to-noise ratio compared to the verticals. The relative importance of horizontal and vertical velocity data in inverting geodetic data is investigated next, using an idealized distribution of noisy, “synthetic” observations derived from the ESPM having different plate thicknesses.

### 3.3 Inverting geodetic data using the ESPM vs. the BSM

We performed a general Monte Carlo simulation to determine the potential error incurred in inverting geodetic data using the BSM as opposed to the ESPM. We generate synthetic data (horizontal and vertical surface velocities) assuming that subduction zones in the real Earth are represented by ESPMs having different plate thicknesses. The ESPM is characterized by three independent parameters of practical interest — fault dip,  $\theta$ , length of the locked megathrust (extending downdip from the trench along the plate interface),  $s_{lock}$ , and the plate thickness,  $H$  ( $H/D_{lock} = 0.01$  (nearly identical to the BSM), 1, and 3 are presented in the respective columns of Figure 3-2 (a), (b) and (c)). For simplicity, we use a planar megathrust interface geometry having a dip,  $\theta = 25^\circ$ , and depth of locking,  $D_{lock} = 40$  km, corresponding to a fault width,  $s_{lock}$ , of  $\sim 95$  km). Our principal conclusions here would not differ qualitatively for curved plate geometry. Although typical geodetic inversions do not invert for geometry, we include the sensitivity of the misfits to variations in dip, in order to emphasize the importance of

tightly constraining this parameter at the outset. We show that the minimum BSM misfits become biased — that is, the best fit BSM would predict a wider fault with a shallower dip — with increasing subducting plate thickness. If dip were tightly constrained (using seismic data, for instance), then the extent of the locked zone along the megathrust can be better constrained. The generalized Monte Carlo approach used here consists of the following steps:

- a) We assume a Gaussian distribution for noise, having zero means and standard-deviations of  $0.02V_p$  for the horizontals and  $0.03 V_p$  for the verticals — or 2 and 3 mm/yr, respectively, if  $V_p = 10$  cm/yr.
- b) Next, one thousand samples of the noise in vertical and horizontal data are generated from the above distributions for the ESPM having a given  $H$  (perturbations:  $\delta V_x, \delta V_z$ ). These perturbations are then added to the respective ESPM surface velocity fields (synthetics:  $V_x, V_z$ ) to generate “noisy” datasets ( $V_x + \delta V_x, V_z + \delta V_z$ ).
- c) Finally, the BSM with the smallest misfit to each noisy (synthetic) dataset — consisting of only the vertical velocities, only the horizontal velocities, or verticals-plus-horizontals (presented in respective rows of a, b and c) — is estimated via a grid-search in the  $\theta$ - $s_{lock}$  parameter space for a given  $H$ .

The closest geodetic observation on the overriding plate was assumed to be 100 km landward from the trench — a typical distance for most subduction zones — and observations were assumed to be uniformly spaced at 5 km intervals. Increasing observation station spacing, or using a different set of ESPM parameters for generating the synthetic surface velocity data would not qualitatively change our conclusions. With such uniform and dense spacing, we are assuming that we have a high-resolution dataset (e.g., GPS and InSAR imagery) to understand the model-based limitations of the inversion process, given the “best-case scenario” data. Here, we use the arc-length of the locked zone,  $s_{lock}$ , for parameterization. Had we chosen either  $D_{lock}$  ( $= s_{lock} \sin(\theta)$ ) or  $x_{lock}$  ( $= s_{lock} \cos(\theta)$ ) instead, we would have observed positive and negative correlations (respectively) between these parameters and fault dip, since the steeper the best-fit BSM fault, the deeper its  $D_{lock}$ , and smaller its  $x_{lock}$ . By using  $s_{lock}$ , we avoid these obvious

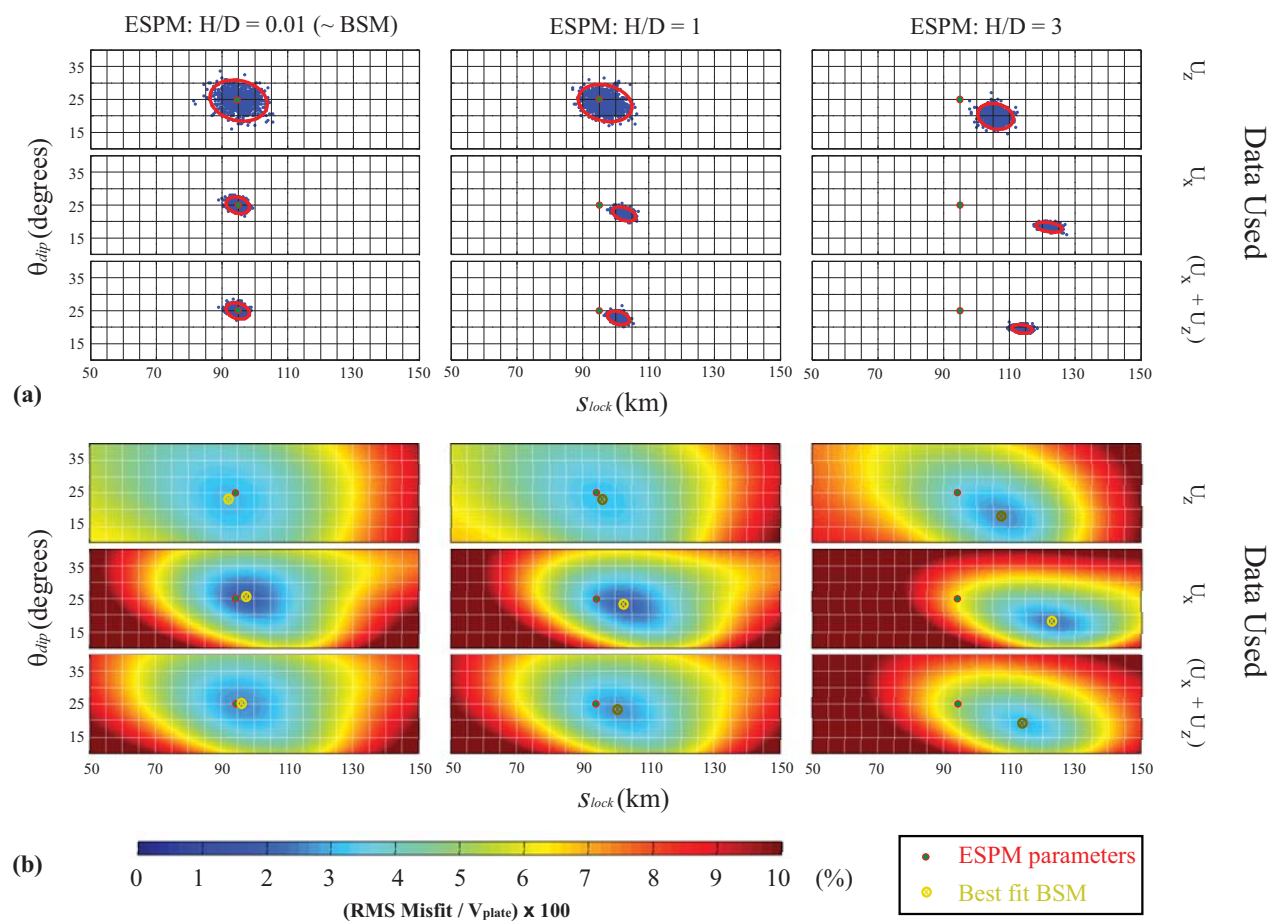
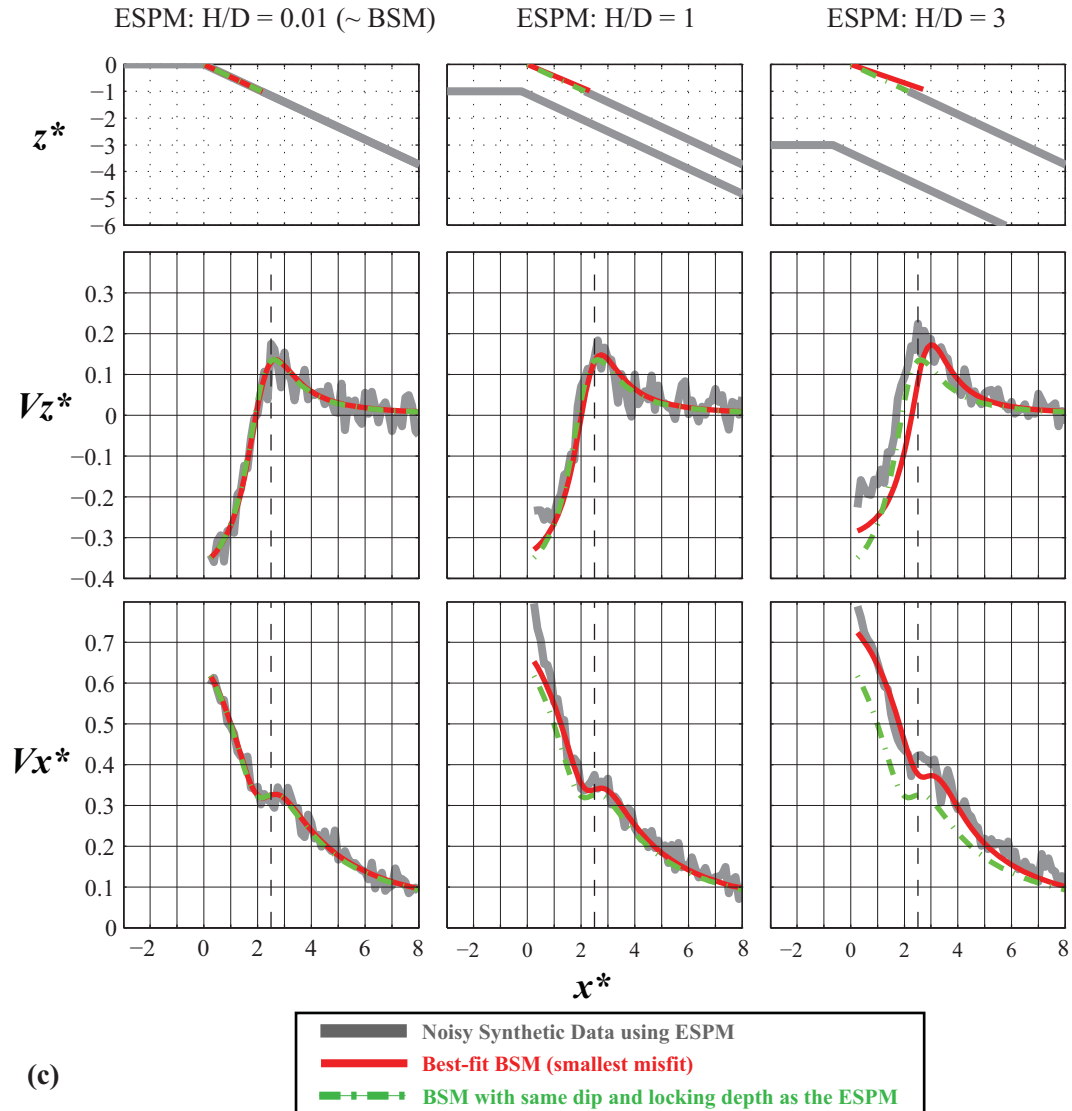


Figure 3-2.



**Figure 3-2.** BSM inversions of ESPM synthetics. Each column represents results for a given plate-thickness to locking depth ratio:  $H/D_{lock} = 0.01$  (BSM), 1, and 3. (a) 1000 best-fit BSM in the  $s_{lock}-\theta$  parameter space that fit as many samples of ESPM-based noisy synthetic data for the specified  $H/D_{lock}$  ratio. Shown are the lowest misfit solutions satisfying only vertical data (top row), only horizontal data (middle row), and sum of the two datasets (bottom row). The corresponding  $1-\sigma$  error-ellipses are shown in red. (b) Misfit between the BSM at each point in the  $s_{lock}-\theta$  parameter space and one of the synthetic data samples in (a). (c) Best-fit backslip model (solid red line), satisfying both the horizontal and vertical synthetic data (solid gray lines) — corresponding to the yellow  $\otimes$  in the bottom row of (b). The best-fit BSMs are as follows:  $\theta = 25^\circ$ ,  $D_{lock} = 40$  km (identical to the ESPM, for column 1);  $\theta = 22.5^\circ$ ,  $D_{lock} = 38.3$  km (column 2); and  $\theta = 20^\circ$ ,  $D_{lock} = 39.3$  km (column 3). The BSM corresponding to  $\theta = 25^\circ$ , and  $D = 40$  km (dashed green line) is also shown. The top row shows the subduction zone geometry, the middle row shows vertical velocities, and the bottom row shows horizontal velocities. Dashed vertical lines mark the nearest geodetic observation point to the trench

correlations. The best fitting BSM was found by computing the  $L_2$ -norm of the misfit at every point of the discretized  $s_{lock}$ - $\theta$  parameter space — having limits of 0-200 km, and 0-45°, respectively — and discretized at a resolution of 0.5 km x 0.5° for each  $H/D_{lock}$  ratio.

Owing to their larger signal-to-noise ratio, the best-fit BSM for the combined (horizontal-plus-vertical) datasets are controlled by the errors in horizontal velocities (note the similarity of the misfit surface for the bottom two rows in Figure 3-2(a)). In the limit of small plate thickness, the geometry of the best-fit BSM corresponds to that of the thin plate ESPM, and the centroids of the error ellipses (which give the most likely model parameter estimates) are nearly the same as the original parameters used to generate the ESPM synthetic data, irrespective of the velocity component(s) considered. This similarity implies that given a dense dataset with randomly distributed data errors, if we repeatedly sample a subset of the data for inverting a BSM, after a sufficient number of samples, we will be able to obtain the “true” model parameters. However, a given sample in this distribution of models can be off by as much as 10% in estimating the extent of the locked zone,  $s_{lock}$ , which translates into  $\sim 5\%$  error in estimating the locking depth,  $d_{lock}$ , for typical dips found in subduction zones. Furthermore, as the plate thickness increases, and stresses are released episodically in the shallow portions of the subduction zone, the best-fit models collapse into an error-ellipse having much smaller dimensions and a biased centroid, indicating that the region of small misfits both shifts and shrinks as  $H$  increases.

We would expect the minimum misfit region of the parameter space to shrink because the synthetic data (from the ESPM) have a variability (plate thickness,  $H$ ) that the forward model (the BSM) cannot capture and therefore, the overall misfits would become larger, shrinking the regions of low misfit in the parameter space. The minimum misfit region would shift because the effect of increasing  $H$  is larger for larger  $s_{lock}$  and  $\theta$ . By taking the  $L_2$ -norm misfit surface as well as the minimum misfit model for one of the data-sets randomly chosen from each panel of Figure 3-2(a), we obtain Figure 3-2(b) – in which this shrinking of the low misfit regions can be clearly seen going from the right to the left columns. If a different data-set were chosen, the misfit surface would look slightly different with a different best fit model, but clearly, the error ellipses (Figure 3-2(a))

reside in the corresponding minimum misfit troughs, which also shrink in size with increasing plate thickness (Figure 3-2(b)). If the dip of the fault-segment undergoing rupture is tightly constrained from teleseismic studies, then the minimum misfit lies along a horizontal line corresponding to that dip ( $25^\circ$  in this case), thus constraining  $s_{lock}$  (and hence,  $x_{lock}$  and  $D_{lock}$ ) more tightly.

Therefore, if the BSM is used to fit interseismic geodetic data, the mean of the best-fit models (the centroids of the ellipses in Figure 3-2(a)) always underestimates  $\theta$  or overestimates  $s_{lock}$ , if plate thickness is non-negligible — that is, the BSM typically predicts a wider-deeper fault, if dip were well constrained. The overestimation of locking depth stems from the main effect of plate thickness on the ESPM predicted surface velocities — above the locked zone, both the horizontal and vertical velocity profiles landward of  $x_{hinge}$  are higher (as well as broader) than those for the corresponding BSM. The BSM with a wider fault (or shallower dip) has exactly the same amplification effect above the locked zone (Figure 3-2(c), which presents the best fit models for inversions based on the vertical-plus-horizontal data-set). When the observing stations are located sufficiently far from the trench, as is frequently the case, the error associated with the underestimation of  $\theta$  or overestimation of  $s_{lock}$  is small, and the BSM does a good job of fitting the observations.

### 3.4 Sensitivity of surface observables to parameterizing the BSM and the ESPM

In view of the wide applicability of the BSM, it is important to understand the sensitivity of surface observables to parameterization of the BSM, especially interface geometry. It has long been known that the geometry of the plate interface has a first-order effect on the surface velocity predictions of dislocation models.

Figure 3-3 presents the effect of fault curvature on the BSM surface velocity predictions. The geometry presented in the figure is similar to that inferred for the Sumatran

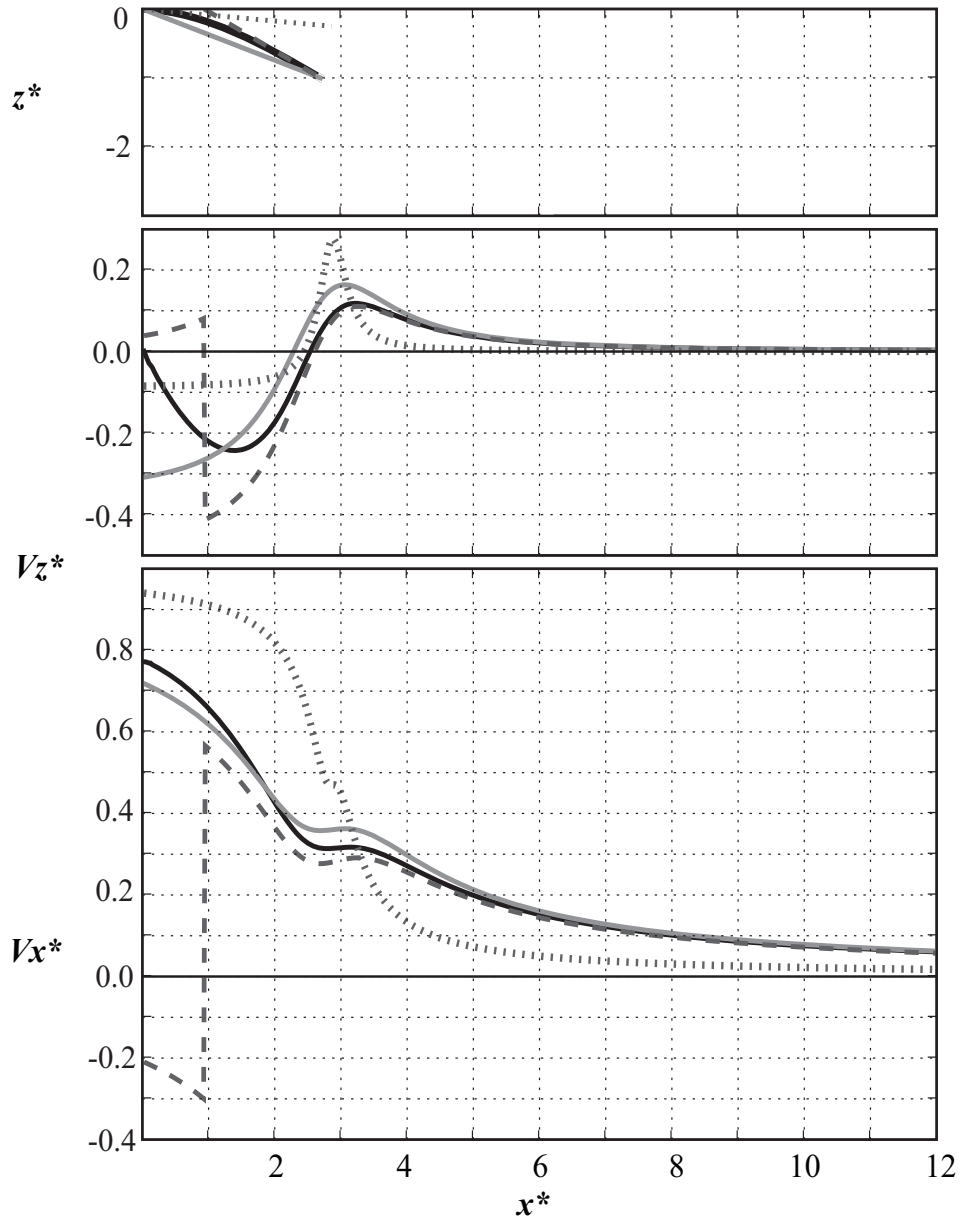


**Figure 3-3.** Effect of curvature on the BSM surface velocity predictions. The curved fault (solid black line) resembles the subduction thrust interface geometry below the island of Nias, offshore of Sumatra ( $\theta_{top} = 3^\circ$ ,  $\theta_{bot} = 27^\circ$  [Hsu et al., 2006]). The gray solid line represents a planar fault having the same end-points as the curved fault, and the dashed gray line represents the tangent-approximation to the curved fault. The dotted line represents a shallow dipping fault that approximates the shallow part of the curved interface. See text for details. The top row presents the fault in cross-sectional view. In all cases, uniform normal slip was imposed on the fault patch. Plot axes are as described in text.

subduction zone in the area of the 28 March 2005, ( $M_w$  8.7) Nias-Simeulue rupture [Engdahl et al., 2007]. The effect of curvature is to stretch the velocity profiles non-linearly near either end. Compared to the velocity field of the planar fault having the same end-points, the curved fault behaves like a shallower dipping planar fault with a smaller locking depth near the trench; the curved geometry predicts a shorter-wavelength velocity profile, with a smaller subsidence (Figure 3-3 middle) but larger horizontal compression (Figure 3-3 bottom) near the trench. But away from the trench, the curved fault velocity profiles resemble the broader fields characteristic of a planar fault having a steeper dip (lower peak amplitude of vertical and horizontal velocities above the bottom of the locked patch). Also, above the bottom of the locked zone (and farther landward), the curved fault velocities are nearly identical to those of a steeper but shorter planar fault extending tangentially to the surface (dashed gray line).

Given that geodetic data in subduction zones are typically available starting at distances comparable to  $x_{lock}$  from the trench, and the surface velocity profiles at these distances for a curved fault and its downdip tangential approximation are nearly indistinguishable, it may be reasonable to use this tangential fault approximation for modeling far-field landward surface velocities [Chlieh *et al.*, 2004; Simoes *et al.*, 2004; Chlieh *et al.*, 2008b]. However, the tangential fault intersects the free surface landward of the trench, while the location and slope of the tangent fault is highly sensitive to the width of the locked zone,  $s_{lock}$ . Also, in this case, interseismic deformation is modeled to be due to slip on the tangent fault, while coseismic deformation is due to slip on the curved (or any non-planar) fault — which is kinematically inconsistent. Therefore, as Savage [1983] originally asserted, if the geometry of the seismogenic zone of the megathrust is known to be curved, then this surface should be used for the BSM as well. Figure 3-3, therefore, demonstrates the significant effect of fault geometry on interpreting geodetic data where data above the locked patch and/or in the vicinity of the trench may become available in the near future.

We next consider the sensitivity of surface observables  $x_{hinge}$  and  $x_{max}$  to the BSM parameterization — specifically, we explore the values for these observables relative to  $x_{lock}$  (Figure 3-4). Although  $x_{lock}$  can be directly inverted from geodetic data (especially

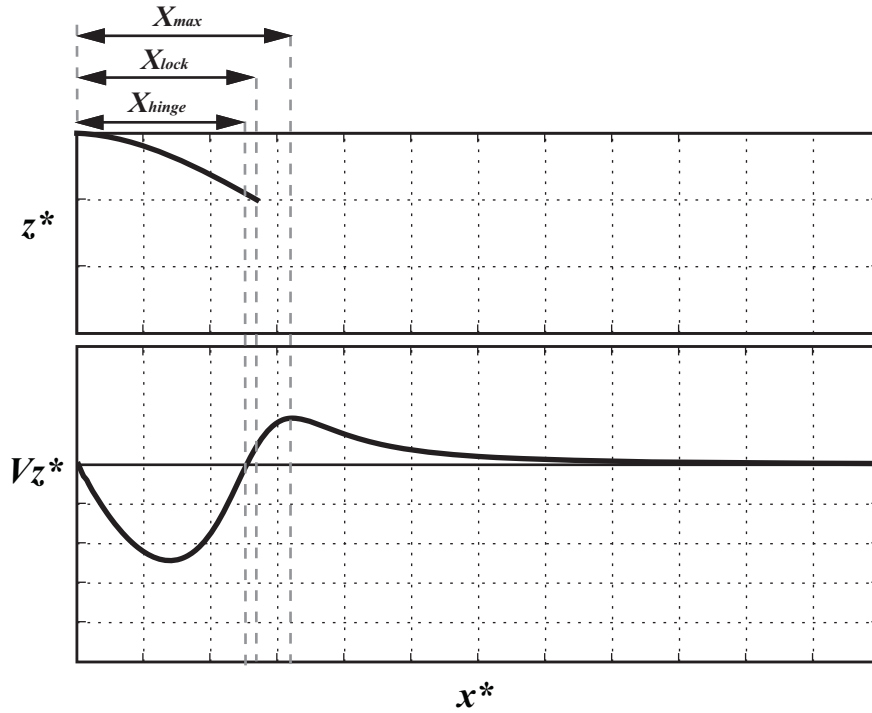


**Figure 3-4.** Schematic illustration of the relative locations of surface observables,  $x_{hinge}$ ,  $x_{lock}$ , and  $x_{max}$ , using the vertical velocity profile for the curved fault presented in Figure 3-6.

from the vertical velocity field), being able to constrain that parameter using  $x_{hinge}$  or  $x_{max}$  (or both) — in addition to constraining dip from teleseismic observations — can allow us to better constrain the remaining BSM parameter,  $f_{tr}$  ( $= s_{trans}/s_{lock}$ ). So, here we quantify how the dimensionless distances between  $x_{lock}$ , and  $x_{hinge}$ ,  $x_{max}$ , their mean, or their difference, vary with fault dip,  $\theta$  for generalized fault geometries. By normalizing these distances with  $x_{lock}$ , our results can be made independent of  $s_{lock}$ . We start with the analytical expression for the surface vertical velocity due to an edge-dislocation in a half-space, normalized by the geologic plate convergence rate,  $V_p$ ,  $v_y^*$ , as a function of trench perpendicular distance,  $x$ , dip,  $\theta$ , and fault width,  $s$  (corrected version of Freund and Barnett [1976] — see Savage [1983], and Rani and Singh [1992]):

$$v_y^* = \frac{v_y}{V_p} = \frac{\sin(\theta)}{\pi} \left[ \left( \frac{xs \cdot \sin(\theta)}{x^2 + s^2 + 2xs \cdot \cos(\theta)} \right) + \tan^{-1} \left( \frac{x - s \cos(\theta)}{s \cdot \sin(\theta)} \right) - \frac{\pi}{2} \right]. \quad (1)$$

To find the hinge-line location,  $x_{hinge}$ , we set the above equation to zero, and solve the resulting transcendental equation numerically using a non-linear root-finding algorithm. Although not obvious from the above equation, for nearly vertical faults (as  $\theta$  tends to  $90^\circ$ ),  $x_{hinge}$  tends to infinity, and as  $\theta$  tends to  $0^\circ$ ,  $x_{hinge}$  tends to a value close to (but less than)  $s$ . As Savage [1983] has already shown, the location of the maximum velocity,  $x_{max}$ , can be obtained by differentiating (1), setting the result to zero, and solving for  $x$ . The final result is:

$$x_{max} = \frac{s}{\cos(\theta)} = s \cdot \sec(\theta) . \quad (2)$$

For nearly vertical faults, (as  $\theta$  tends to  $90^\circ$ ),  $x_{max}$  tends to infinity (but at a faster rate than  $x_{hinge}$ ) and as  $\theta$  tends to  $0^\circ$ ,  $x_{max}$  tends to  $s$ . As discussed previously, the depth of locking,  $D_{lock}$ , equals  $s \cdot \sin(\theta)$ ; the surface projection of the bottom of locked fault is given by,

$$x_{lock} = s \cdot \cos(\theta) . \quad (3)$$

For nearly vertical faults ( $\theta$  tends to  $90^\circ$ ),  $x_{lock}$  tends to zero, but at a much slower rate than either  $x_{max}$  or  $x_{hinge}$  blow up; as  $\theta$  tends to  $0^\circ$ ,  $x_{lock}$  tends to  $s$ . For the analysis here, we choose as our independent parameters, the locked fault width,  $s$ , and fault dip,  $\theta$ , which naturally fall out of the analytical solution (1). The theoretical solutions shown in the last three equations are plotted as yellow curves, wherever they appear in Figure 3-5 (a) and (b). For curved faults, faults with downdip transition zones, as well as the ESPM, we first compute the vertical surface velocity field ( $U_z$ ), for every combination of  $\theta$  and  $s$ , at a resolution of  $0.5^\circ \times 50$  km. We then search for the locations of both the hinge-line ( $U_z = 0$ ) and maximum vertical velocity ( $U_z' = 0$ ). To verify our code, we compute these locations for the planar fault case and check that they plot right on top of the theoretical solutions (Figure 3-5(a)).

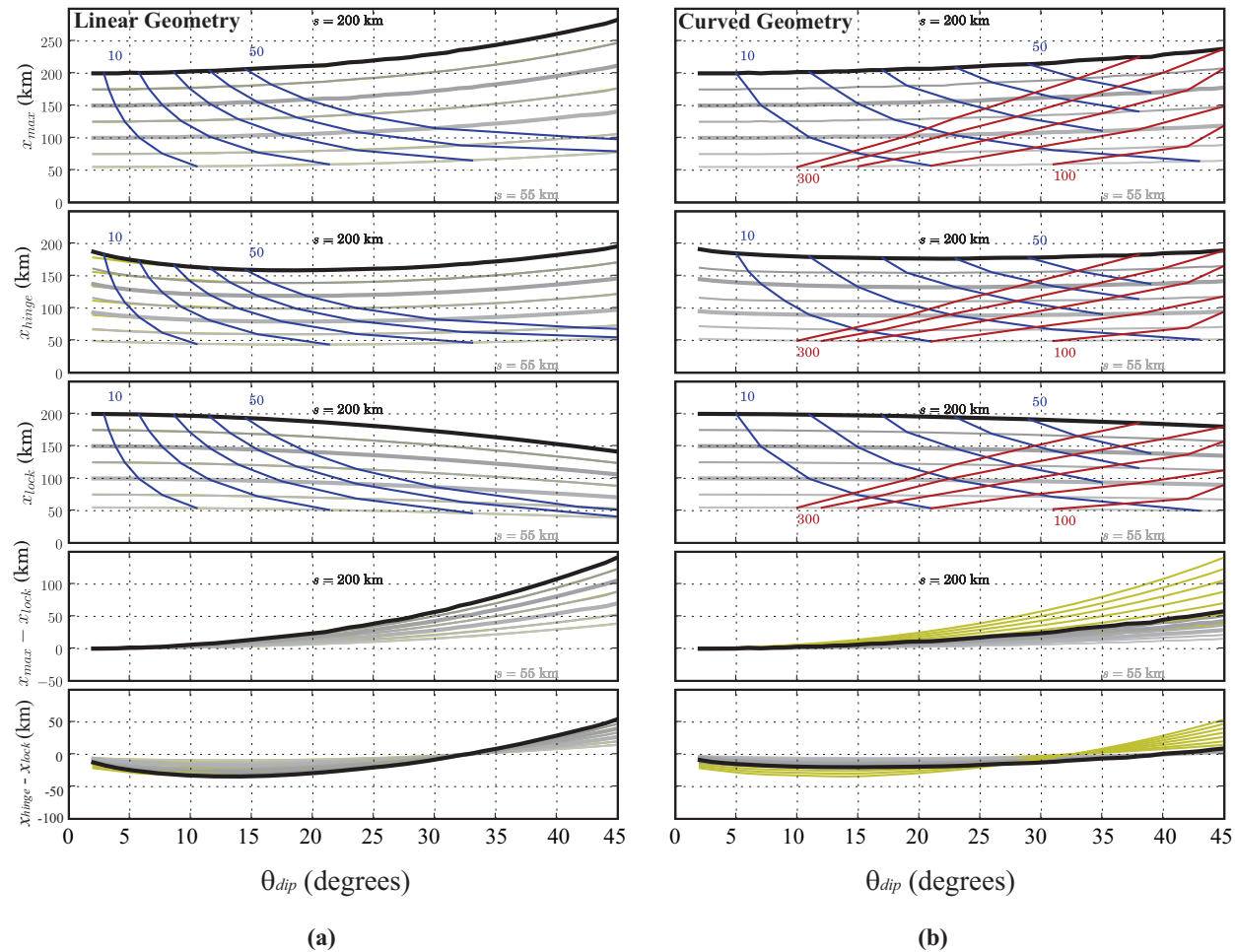


**Figure 3-5.** Location of the maximum vertical velocity ( $x_{max}$ ), zero vertical velocity ( $x_{hinge}$ ), the surface projection of the bottom of locked fault ( $x_{lock}$ ), and the differences between them, as a function of the length of the locked fault patch,  $s$ , and dip angle,  $\theta$ . Each parameter is plotted for  $s$  ranging from 25 to 200 km, in steps of 25 km. Thicker curves represent fault lengths of 50, 100, 150, and 200 km. (a) Planar faults: Blue curves (cutting across the  $s$ -curves from the top left to bottom right) are lines of constant locking depth (10 to 50 km, in steps of 10 km). Theoretical estimates are presented in dark yellow. (b) Curved faults: Red curves (cutting across the  $s$ -curves from the bottom right to top left) are lines of constant radii of curvature (100 to 300 km, in steps of 50 km). Blue curves are the same as in (a). Theoretical estimates for planar faults are presented in yellow in the bottom two panels for comparison to (a).

Owing to the simple geometrical parameterizations used to generate linear or curved subduction profiles here,  $x_{hinge}$ ,  $x_{max}$ , and  $x_{lock}$  are directly proportional to the fault width,  $s_{lock}$ . Therefore, dividing by  $x_{lock}$  removes any dependence on fault width, and curves for different  $s_{lock}$  collapse into a single curve (Figure 3-6). Figure 3-6 presents the variation of  $x_{hinge}$  and  $x_{max}$  as a function of  $\theta$  (for any  $s_{lock}$ ) for planar faults without a downdip transition zone (Figure 3-6(a)), curved faults without a downdip transition zone (Figure 3-6(b)), planar faults having a downdip transition zone (Figure 3-6(c)), and curved faults having a downdip transition zone (Figure 3-6(d)). Within each part, the first (top) panel presents the dimensionless distance between  $x_{max}$  and  $x_{lock}$ , relative to  $x_{lock}$ :

$$\Delta x_m^* = (x_{max} - x_{lock}) / x_{lock} . \quad (4)$$

The second panel presents the dimensionless distance between  $x_{hinge}$  and  $x_{lock}$ , relative to  $x_{lock}$ :

$$\Delta x_h^* = (x_{hinge} - x_{lock}) / x_{lock} . \quad (5)$$

The third panel presents the mean of (4) and (5), i.e., the dimensionless mean of  $x_{hinge}$  and  $x_{max}$ ,  $\Delta X_M^* = (\Delta x_m^* + \Delta x_h^*) / 2$ . The fourth panel presents the difference between Equations 4 and 5, i.e., the distance between  $x_{hinge}$  and  $x_{max}$ ,  $\Delta X_D^* = (\Delta x_m^* - \Delta x_h^*)$ . Finally, the fifth (bottom) panel presents the ratio of  $x_{hinge}$  and  $x_{max}$  (which is always less than 1.0). Ranges of  $\theta$  within which  $x_{hinge}$ ,  $x_{max}$ , or some combination of the two is a good predictor for the location of  $x_{lock}$  for the BSM are highlighted by gray boxes in Figure 3-6 and encapsulated in Table 3-1 (for faults without a downdip transition zone) and Table 3-2 (for faults with a downdip transition zone,  $f_{tr} = 25\%$ ). As noted previously, updip transition zones do not significantly affect vertical velocities, and therefore, do not influence the values of these surface observables significantly. For the ESPM (not shown), the variation of these dimensionless parameters with dip angle is qualitatively similar to that for the corresponding BSM, but with wider uncertainty relative to  $x_{lock}$ .

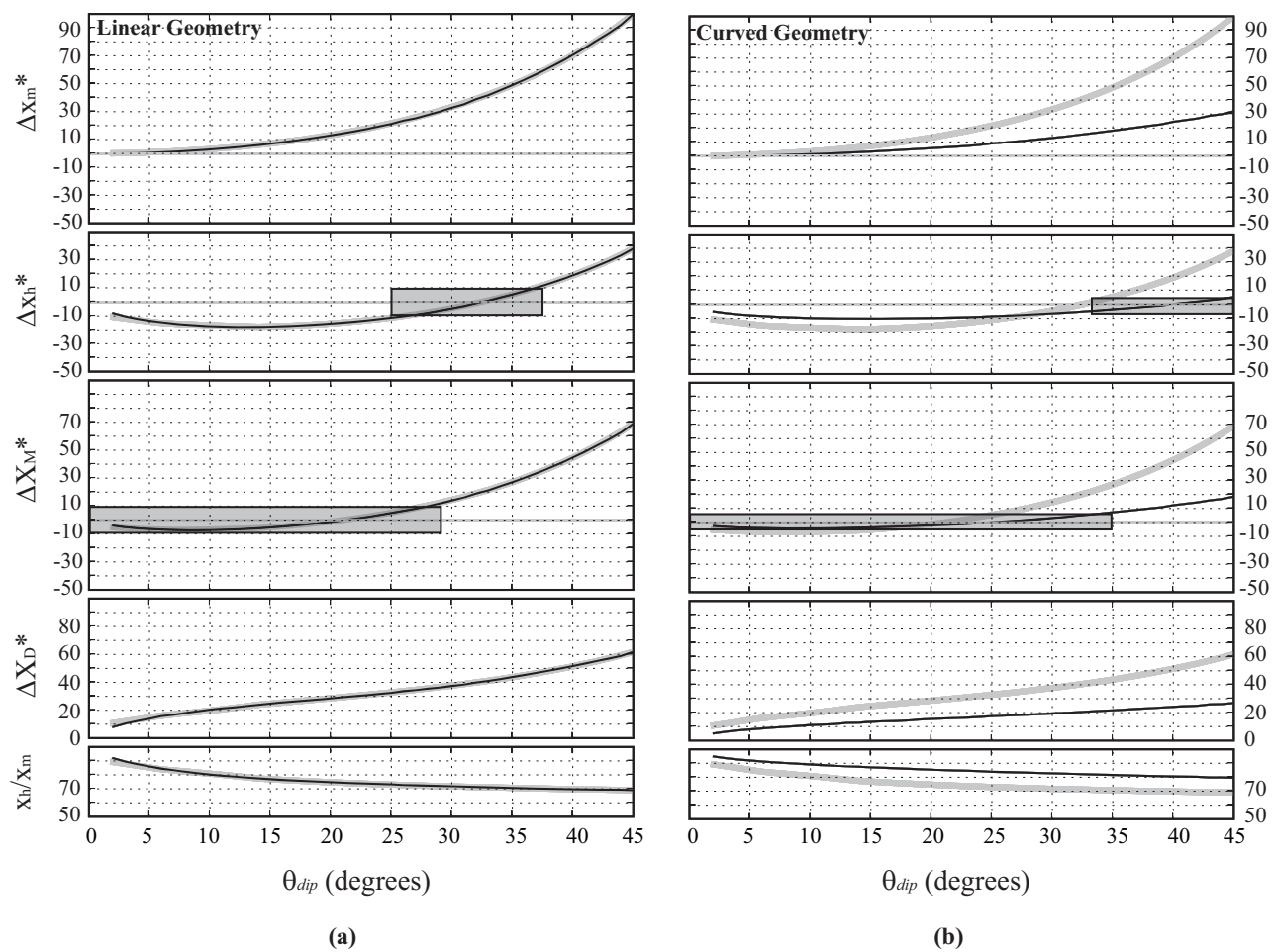
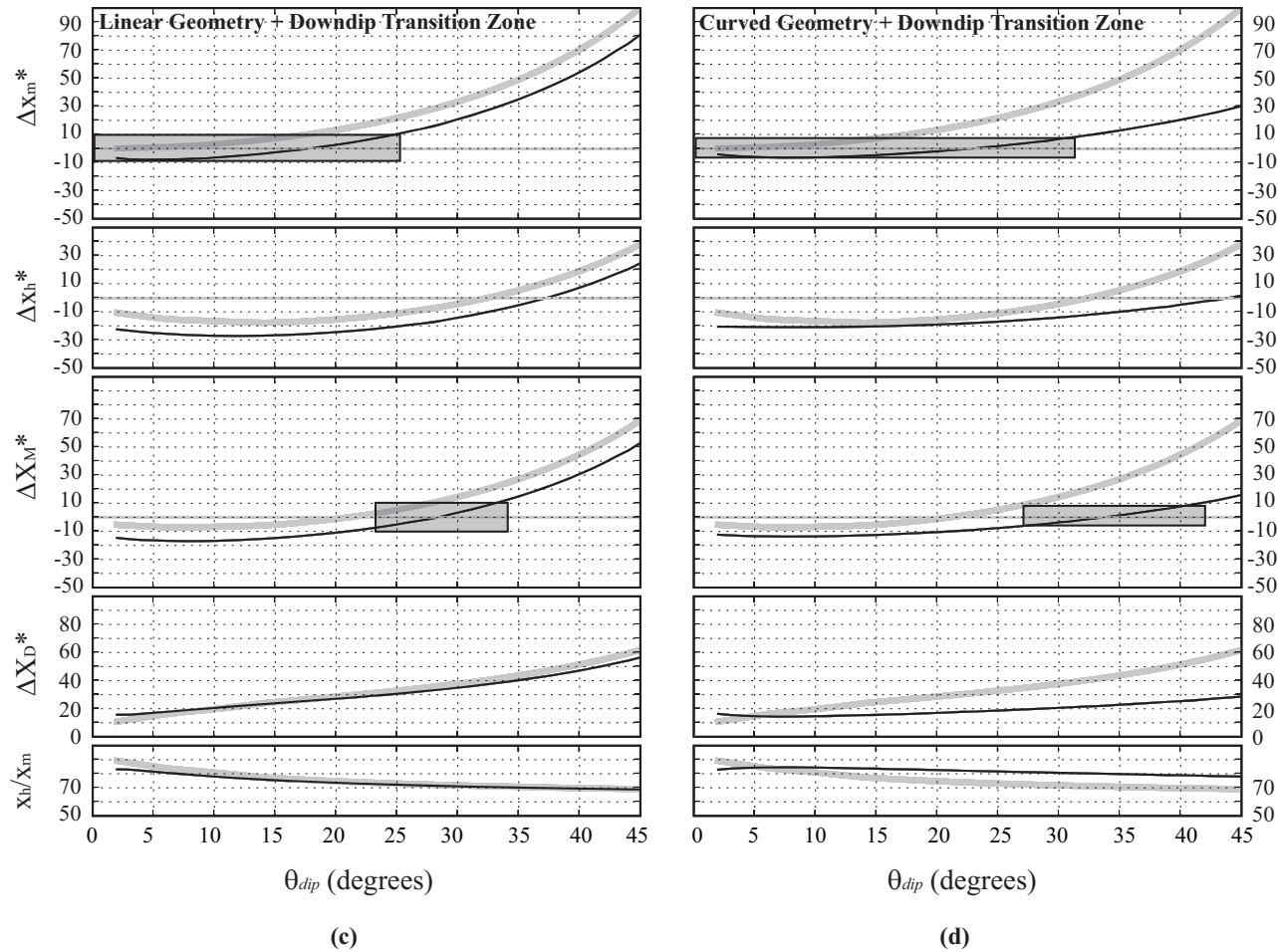


Figure 3-6.



**Figure 3-6.** Dimensionless plots of the variation in the location of  $x_{max}$  and  $x_{hinge}$  as a function of fault dip in the BSM having a planar (a, c) or curved (b, d) plate interface geometry, with (c, d) or without (a, b) a transition zone (of fractional length,  $f_{tr} = 25\%$ ) downdip of the locked megathrust zone. See text for definitions of y-axis parameters. Top panels: Dimensionless relative distance between  $x_{max}$  and  $x_{lock}$  ( $\Delta x_m^*$ ) as a function of the dip of the BSM fault; Second-from-top panels: Dimensionless relative distances between  $x_{hinge}$  and  $x_{lock}$  ( $\Delta x_h^*$ ); Third-from-top panels: Mean value of plots in top two panels; Second-from-bottom panel: Difference between the top two panels; Bottom panels:  $(x_{hinge}/x_{max})$ . Theoretical estimates for planar faults without any transition zone (thick gray lines from part(a)) are repeated for each panel in parts (b)-(d) for comparison purposes.

**Table 3-1** Theoretical Estimates for the horizontal distance between the trench and the surface projection of the downdip end of the locked zone,  $x_{lock}$ , for planar and curved faults locked up to the trench. Notation:  $\bar{X} = \left(\frac{X_{hinge} + X_{max}}{2}\right)$ ,  $X_h = X_{hinge}$ ,  $X_m = X_{max}$ .

Fault Type	$0^\circ < \theta_{Dip} \leq 25^\circ$	$25^\circ < \theta_{Dip} \leq 35^\circ$	$35^\circ < \theta_{Dip} \leq 45^\circ$
Planar fault	$1.1 \bar{X} > X_{lock} > 0.9 \bar{X}$	$1.1 X_h > X_{lock} > 0.9 X_h$	$1.0 X_h > X_{lock} > 0.7 X_h$
Curved fault (Circular/ Parabolic arc)	$1.05 \bar{X} > X_{lock} > 0.95 \bar{X}$	$1.0 \bar{X} > X_{lock} > 0.9 \bar{X}$	$1.1 X_h > X_{lock} > 0.9 X_h$

**Table 3-2.** Theoretical Estimates for the horizontal distance between the trench and the surface projection of the bottom of the locked patch,  $x_{lock}$ , for planar and curved faults having transition segments immediately downdip of the locked zone. The following results are for transition zones having along-fault lengths of up to 25% of the length of the locked zone. Notation:  $\bar{X} = \left(\frac{X_{hinge} + X_{max}}{2}\right)$ ,  $X_h = X_{hinge}$ ,  $X_m = X_{max}$ .

Fault Type	$0^\circ < \theta_{Dip} \leq 25^\circ$	$25^\circ < \theta_{Dip} \leq 35^\circ$	$35^\circ < \theta_{Dip} \leq 45^\circ$
Planar fault	$1.1 X_m > X_{lock} > 0.9 X_m$	$1.1 \bar{X} > X_{lock} > 0.9 \bar{X}$	$1.0 X_h > X_{lock} > 0.7 X_h$
Curved fault (Circular arc)	$1.1 X_m > X_{lock} > 1.0 X_m$	$1.0 X_m > X_{lock} > 0.9 X_m$	$1.1 X_h > X_{lock} > 1.0 X_h$
Curved fault (Parabolic arc)	$1.1 X_m > X_{lock} > 1.0 X_m$	$1.1 \bar{X} > X_{lock} > 0.9 \bar{X}$	$1.1 X_h > X_{lock} > 0.9 X_h$

From the theoretical solutions for planar faults (Figure 3-5(a)), we note that the location of peak vertical uplift rates,  $X_{max}$ , changes significantly (by as much as 50% as  $\theta$  varies from  $0^\circ$  to  $45^\circ$ , as expected from Equation 2. Also,  $x_{max} \geq x_{lock}$  always, because comparing (2) and (3),  $\sec(\theta) \geq \cos(\theta)$  (Figure 3-6(a) top and middle). We also plot curves of constant locking depth,  $D_{lock}$ , for every 10 km, in the range, 10-50 km (Figure 3-6(a), blue curves). This allows for quantifying  $x_{max}$ ,  $x_{hinge}$ , and  $x_{lock}$  for any combination of independent parameters defining the planar BSM ( $s$ ,  $\theta$  or  $D_{lock}$ ). Using the non-dimensionalization discussed above for the dependent variables in Figure 3-5(a), all curves for different fault dimensions,  $s$ , collapse into a single curve (Figure 3-6(a)). Dimensional plots for a curved fault are presented in Figure 3-5(b)). In addition to the curves of constant locking depth (blue), another set is included in the upper three panels of this figure for curves of constant radius of curvature,  $R_p$  (red), for every 50 km, in the

range, 100–300 km. This allows for quantifying  $x_{max}$ ,  $x_{hinge}$ , and  $x_{lock}$  for any combination of independent parameters defining the curved BSM ( $s$ , curvature,  $\theta_{bot}$  or  $D_{lock}$ ).

Theoretical plots for planar faults (yellow curves) are also presented in the bottom two panels of this figure for comparison.

For shallow dips characteristic of most subduction zones ( $\theta \leq 30^\circ$  irrespective of geometry, Figure 3-5(a) and (b)),  $x_{hinge}$  lies trenchward of  $x_{lock}$  (so,  $\Delta x_h^*$  is negative), while  $x_{max}$  lies landward of it ( $\Delta x_m^*$  is always positive), but almost equally distant - irrespective of the extent of  $s_{lock}$ . We would therefore expect that  $\Delta X_M^*$  would be a good estimator of  $x_{lock}$  for shallow dipping interfaces (third panel of Figure 3-6(a) and (b)) — in fact, this parameter can estimate  $x_{lock}$  to within 5 % for planar faults and 2.5 % for curved faults (i.e., with half the uncertainty of using either  $x_{hinge}$  or  $x_{max}$  alone). To get a feel for the maximum possible difference between these two distances, for  $s_{lock} \sim 200$  km, the difference between  $x_{hinge}$  and  $x_{lock}$  can vary between 20–40 km for such shallow dipping interfaces. For steeper dips ( $30^\circ < \theta \leq 45^\circ$ ), both  $x_{hinge}$  and  $x_{max}$  lie on the same side of  $x_{lock}$ , with the former being much closer to it (Figure 3-5). So, we would expect  $x_{hinge}$  to be a better estimator of  $x_{lock}$  compared to  $x_{max}$  for steeper plate interfaces (second panel of Figure 3-6(a) and (b)).

In the presence of a transition zone along the plate interface, downdip end of the locked fault — in which slip transitions gradually from zero to the full plate convergence rate — both  $\Delta x_h^*$  and  $\Delta x_m^*$  are negative for dips as high as  $40^\circ$  (Figure 3-6(c) and (d), top). Also, owing to the parameterization of the profile geometries — and given that the effective  $s_{lock}$  increases in the presence of a transition zone (Figure 3-1(a) and (b)) —  $x_{lock}$  also increases by a factor equal to  $f_{tz}$ , irrespective of the fault geometry. Furthermore,  $x_{max}$  now becomes much closer to  $x_{lock}$  than  $x_{hinge}$ . So, in the presence of a downdip transition zone, we would expect  $x_{max}$  to be a better estimator of  $x_{lock}$  compared to either  $x_{hinge}$ , or the mean of  $x_{hinge}$  and  $x_{max}$  (top panel of Figure 3-6(c) and (d)). However, the uncertainties are almost quadruple the values for faults without any transition zone — that is,  $x_{max}$  can be used to estimate  $x_{lock}$  to within 20% for planar fault interfaces, and to within 10% for curved interfaces. The ratio  $x_{hinge}/x_{max}$  varies between 70 and 90 % for a wide range of

realistic dips of the subduction interface irrespective of both the geometry as well as the presence of a transition zone.

The effect of including the bottom glide surface of the ESPM is to move  $x_{hinge}$  trenchward (Figure 2-5; and Kanda and Simons [2010]). For shallow dips ( $\theta < 20^\circ$ ), the effect of bending is small, and the dimensionless parameter curves  $x_{hinge}$  are nearly identical to those for the corresponding geometry in Figure 3-6. For steeper dips,  $x_{hinge}$  is located trenchward relative to that for the BSM having the same  $s_{lock}$  and  $\theta$ . Therefore, the distance between  $x_{hinge}$  and  $x_{lock}$  will be negative over a wider range of  $\theta$ , compared to the corresponding BSM. Also,  $x_{max}$  for the ESPM with a finite plate thickness changes little from its value for the ESPM having zero plate thickness (that is, the BSM) [Owen, 2006]. The above results were confirmed for the ESPM having planar or curved interface geometry and different plate thicknesses. In general, we find that  $x_{lock}$  for the ESPM can be constrained using the same dimensionless parameter ranges as those for the BSM (Table 3-1 and Table 3-2), for shallow dips ( $< 20^\circ$ ). Even for the range,  $20^\circ < \theta < 30^\circ$ , the uncertainty in estimating  $x_{lock}$  using these tables is only double that for the corresponding BSM. However, for steeper dips, the uncertainty in estimating  $x_{lock}$  from the above surface observables increases significantly.

### 3.5 Discussion

For megathrust interfaces dipping at an angle of  $15^\circ$  or greater, the distance between  $x_{hinge}$  (or  $x_{max}$ ) and  $x_{lock}$  for planar fault geometry is roughly twice that for a curved geometry having the same dip at the downdip end of the locked zone. Also, the location of  $x_{lock}$  for a planar fault is much more sensitive to fault dip than for a curved fault (see Figure 3-5, Figure 3-6, and Table 3-1). If geodetic stations are located right above the locked zone (as in Sumatra, for example), then ignoring curvature of the megathrust interface may overpredict vertical uplift rates in that region by as much as 50% (Figure 3-3). Therefore, it is important to constrain fault geometry as tightly as possible before inverting geodetic data. If fault geometry cannot be tightly constrained, then the above uncertainties due to fault geometry should be incorporated into any Bayesian (or Monte-Carlo type) inversion

procedure. Accounting for geometry uncertainties prior to inversion modeling will lead to more realistic families of best-fitting slip-deficit distributions for the megathrust interface. For the ESPM, a tighter *a priori* estimate for interface geometry and  $s_{lock}$  also allows better constraints to be placed on the minimum elastic plate thickness [2001].

There is a strong trade-off between including subducting plate thickness and including a transition zone downdip of the locked megathrust (compare Figure 3-1(a) and (b)), especially for horizontal velocities, which have the best signal-to-noise ratio amongst surface velocity components. The horizontal velocity profile for  $f_{tr}=0$  for finite plate-thickness (black, Figure 3-1(a), bottom) may be indistinguishable in real life from the  $f_{tr}=0.25$  horizontal velocity profile for the BSM (or zero plate thickness case, red in Figure 3-1(b), bottom). This similarity will be more pronounced for subduction zones where plate thickness to locking depth ratio ( $H/D_{lock}$ ) is 2 or greater (e.g., northeastern Japan, Cascadia, Nicoya Peninsula in Costa-Rica, Peru-Chile trench between Ecuador and northern Chile, and perhaps Sumatra [see Figure 2-9, and Kanda and Simons, 2010]). As demonstrated with the Monte-Carlo analysis, a similar trade-off exists between the ESPM and a BSM having a wider (and deeper) locked zone (Figure 3-2(c)).

### 3.6 Conclusions

Here, we quantified the effects of using a more realistic curved plate interface profile, as opposed to a linear fault tangent to it at the downdip end of the locked zone. We note that where the megathrust is not planar, one should still assign backslip onto the actual plate interface (as [1983] originally intended), instead of to a planar fault tangent to the bottom of the locked zone. Irrespective of the fault geometry, we can estimate the surface projection of the downdip end of the locked zone ( $x_{lock}$ ) from the mean of the locations of  $x_{hinge}$  and  $x_{max}$ , for most realistic fault dips.

The presence of transition zones broadens the surface velocity profiles landward of the surface projection of the downdip end of the locked zone, and the zone of “broadening” increases with increasing transition zone width. A transition zone can thus smooth the

stresses associated with dislocations while increasing the effective depth of locking. Surface velocities for the curved fault geometry trenchward of  $x_{max}$  — the location of the maximum vertical velocities — differ significantly from those due to a planar fault tangent to it at the bottom of the locked zone. However, velocities due to the curved fault landward of  $x_{max}$  are nearly identical to those due to the tangent fault. We showed that irrespective of the fault geometry, the mean of  $x_{hinge}$  and  $x_{max}$  gives a good approximation for  $x_{lock}$  for both the BSM and the ESPM with shallow dipping plate interfaces ( $< 30^\circ$ ). However, in the presence of a transition zone, or a large plate thickness,  $x_{max}$  gives a more reliable estimate for  $x_{lock}$ , and hence, the extent of the locked zone. Therefore, the common notion that the location of the peak in vertical velocities ( $x_{max}$ ) determines the extent of the locked megathrust ( $x_{lock}$ ), is valid only if a transition zone is assumed downdip of the locked interface. Using the BSM instead of the ESPM (having a finite plate thickness,  $H$ ) for inverting interseismic geodetic data would result in the prediction of a wider (and hence, deeper) locked zone, assuming that the fault geometry is well constrained.

**Table 3-3.** Notation

$\theta, \theta_{dip}$	Planar fault/plate interface dip
$\theta_{bot}$	Dip at the bottom of the locked zone for a curved plate interface
$\Delta\theta$	Change in interface dip from one curved segment to the next
$D_{lock}, d_{lock}$	Depth of locking along the megathrust interface
$d_a$	Depth to bottom of updip transition zone, or to the updip limit of locked zone
$C_p$	Local curvature of the centerline of the plate
$f_{tr}$	Fractional length of transition zone downdip of locked plate interface, $s_{trans}/s_{lock}$ .
$f_a$	Fractional depth of updip transition zone w.r.t. locking depth, $d_a/d_{lock}$ .
$H$	Thickness of the subducting plate in the ESPM
$R_p$	Local radius of curvature for the centerline of the plate
$S$	Arc-length along the plate interface, or fault-width
$s_{lock}$	Width of locked plate interface
$s_{trans}$	Width of the transition zone downdip of the locked plate interface
$\Delta v$	Change in velocity from one plate segment to the next
$V_x^*$	Horizontal surface velocity normalized by plate rate
$V_z^*$	Vertical surface velocity normalized by plate rate
$\Delta X_D^*$	Dimensionless distance between $x_{max}$ and $x_{hinge}$ , $(\Delta x_m^* - \Delta x_h^*)$
$\Delta X_M^*$	Mean of dimensionless $x_{lock}$ and $x_{max}$ , $(\Delta x_m^* + \Delta x_h^*)/2$
$\Delta x_h^*$	Dimensionless distance between $x_{hinge}$ and $x_{lock}$ , $(x_{hinge} - x_{lock})/x_{lock}$
$\Delta x_m^*$	Dimensionless distance between $x_{max}$ and $x_{lock}$ , $(x_{max} - x_{lock})/x_{lock}$
$x$	Horizontal coordinate, positive landward, or away from the trench
$x^*$	Horizontal coordinate, normalized w.r.t. locking depth
$x_{GPS}$	Distance from the trench to the nearest geodetic observation
$x_{hinge}$	Distance from the trench to the location location of zero vertical surface velocity
$x_{lock}$	Distance between trench and surface projection of the downdip end of the locked zone
$x_{max}$	Distance from trench to the location of the peak in the vertical surface velocity field
$z$	Vertical coordinate, positive upward (depths are therefore, negative)
$z^*$	Vertical coordinate, normalized w.r.t. locking depth

## References

- Chlieh, M., J.P. Avouac, K. Sieh, D.H. Natawidjaja and J. Galetzka (2008), Heterogeneous coupling of the Sumatran megathrust constrained by geodetic and paleogeodetic measurements, *J. Geophys. Res.*, 113, B05305, doi:05310.01029/02007JB004981
- Chlieh, M., J.B.d. Chabalier, J.C. Ruegg, R. Armijo, R. Dmowska, J. Campos and K.L. Feigl (2004), Crustal deformation and fault slip during the seismic cycle in the North Chile subduction zone, from GPS and InSAR observations, *Geophys. J. Int.*, 158, 695-711.
- Cohen, S.C. (1999), Numerical Models of Crustal Deformation in Seismic Zones, *Adv. Geophys.*, 41, 133-231.
- Engdahl, E.R., A. Villasenor, H.R. DeShon and C. Thurber (2007), Teleseismic relocation and assessment of seismicity (1918-2005) in the region of the 2004 Mw 9 Sumatra-Andaman and 2005 M 8.7 Nias great earthquakes, *Bull. Seismol. Soc. Am.*, 97 S43-S61.
- Freund, L.B. and D.M. Barnett (1976), A Two-Dimensional Analysis of Surface Deformation due to Dip-slip Faulting, *Bull. Seismol. Soc. Am.*, 66, 667-675.
- Hsu, Y.-J., M. Simons, J.-P. Avouac, J. Galetzka, K. Sieh, M. Chlieh, D. Natawidjaja, L. Prawirodirdjo and Y. Bock (2006), Frictional Afterslip Following the 2005 Nias-Simeulue Earthquake, Sumatra, *Science*, 312, 1921-1926.
- Hyndman, R.D. and K. Wang (1993), Thermal constraints on the zone of major thrust earthquake failure: The Cascadia subduction zone, *J. Geophys. Res.*, 98, 2039-2060.
- Iwasaki, T., W. Kato, T. Moriya, A. Hasemi, N. Umino, T. Okada, K. Miyashita, T. Mizogami, T. Takeda, S. Seikine, T. Matsushima, K. Tashiro and H. Miyamachi (2001), Extensional structure in northern Honshu arc as inferred from seismic refraction/wide-angle reflection profiling, *Geophys. Res. Lett.*, 28, 2329-2332.
- Kanda, R.V.S. and M. Simons (2010), An elastic plate model for interseismic deformation in subduction zones, *J. Geophys. Res.*, 115, B03405.
- Khazaradze, G. and J. Klotz (2003), Short and long-term effects of GPS measured crustal deformation rates along the South-Central Andes, *J. Geophys. Res.*, 108, 2289.
- Masterlark, T. (2003), Finite element model predictions of static deformation from dislocation sources in a subduction zone: Sensitivities to homogeneous, isotropic, Poisson-solid, and half-space assumptions, *J. Geophys. Res.*, 108 2540.
- Owen, S.J., 2006. CUBIT 10.2 Documentation, pp. 532, Sandia National Laboratories, Albuquerque, NM, U.S.A.
- Rani, S. and S.J. Singh (1992), Static Deformation of a Uniform Half-space due to a Long Dip-slip Fault, *Geophys. J. Int.*, 109, 469-476.
- Savage, J.C. (1983), A dislocation model of strain accumulation and release at a subduction zone, *J. Geophys. Res.*, 88 4984-4996.

- Savage, J.C. (1995), Interseismic uplift at the Nankai subduction zone, Southwest Japan, 1951–1990, *J. Geophys. Res.*, 100, 6339–6350.
- Scholz, C.H. (1990), *The Mechanics of Earthquakes and Faulting*, edn, vol., pp. 439, Cambridge University Press, New York.
- Simoes, M., J.-P. Avouac, R. Cattin and P. Henry (2004), The Sumatra Subduction Zone: A Case for a Locked Fault Zone Extending into the Mantle, *J. Geophys. Res.*, 109, B10402.
- Souter, B.J. and B.H. Hager (1997), Fault propagation fold growth during the 1994 Northridge, California, earthquake?, *J. Geophys. Res.*, 102, 11,931–911,942.
- Suwa, Y., S. Miura, A. Hasegawa, T. Sato and K. Tachibana (2006), Interplate coupling beneath NE Japan inferred from three-dimensional displacement field, *J. Geophys. Res.*, 111, B04402.
- Tomar, S. and N.K. Dhiman (2003), 2-D Deformation Analysis of a Half-space due to a Long Dip-slip Fault at Finite Depth, *Proc. Indian Acad. Sci. (Earth Planet. Sci.)*, 112, 587-596.
- Wang, K. and Y. Hu (2006), Accretionary Prisms in Subduction Earthquake Cycles: The Theory of Dynamic Coulomb Wedge, *J. Geophys. Res.*, 111, B06410.
- Wang, K., R. Wells, S. Mazzotti, R.D. Hyndman and T. Sagiya (2003), A revised dislocation model of interseismic deformation of the Cascadia subduction zone, *J. Geophys. Res.*, 108, 2026.
- Williams, C.A. and R. McCaffrey (2001), Stress rates in the central Cascadia subduction zone inferred from an elastic plate model, *Geophys. Res. Lett.*, 28, 2125-2128.
- Zweck, C., J.T. Freymueller and S.C. Cohen (2002), Three-dimensional elastic dislocation modeling of the postseismic response to the 1964 Alaska earthquake, *J. Geophys. Res.*, 107, 2064.

## *Chapter 4*

### MODEL SETUP AND VALIDATION

#### **4.1 Introduction**

Hetland et al. [2010] (referred to as HSD10, henceforth), and Hetland and Simons [2010] (referred to as HS10, henceforth) developed a procedure for simulating slip evolution on a planar fault surface resulting from kinematically imposed ruptures on pre-defined portions of the fault (“asperities”) that are otherwise locked during a seismic cycle. Slip evolves on the fault surface because as the stress perturbation around an asperity resulting from the imposed seismic rupture decays. The rate of this decay is determined by the induced slip-rates, which in turn, are determined by the fault rheology. A fundamental feature of this model is that the mean stress on the fault surface evolves to a steady state because the imposed ruptures and far-field loading are identical over multiple cycles. This “spin-up” results in self-consistent background stresses that depend only on the history of past ruptures. The above formulation supports a variety of rheological relationships (linear/non-linear viscous, purely rate dependent, or Dieterich-Ruina rate and state friction).

The work presented here extends the procedure developed above to not only handle 3D fault geometry and actual rupture history for a given megathrust interface, but also the complex visualization required for the analysis of fault surface parameters, surface velocity field, as well as routine quality control checks. Several major developments were required in order to achieve the above goals:

- HSD10 and HS10 use a planar fault discretized into rectangular patches. However, it is nearly impossible to discretize an arbitrary 3D surface using rectangles without developing surface discontinuities (“kinks”) in regions having even moderate curvature, unless extremely high resolution is used over the entire fault surface. For the problem to be tractable, we require a mesh that is fine only near the asperities,

where the gradients in the stress and strain fields are extreme. For such an “adaptive” mesh, kinks are unavoidable, unless extra elements are added wherever there is non-negligible curvature along the fault surface. Since we are dealing with the decay of coseismic stress “pulses” along the fault surface, the stress-singularities resulting from such kinks would not only dominate the simulation, but also make it very unstable. Here, we choose to avoid such kinks by discretizing with triangular patches. We use a comprehensive geometry and meshing package developed by Sandia National Laboratory, Cubit [Owen, 2006], for this purpose.

- The discretization above is a four-stage process: First, the geometry needs to be generated in a CAD package such as the widely used commercial package for geologic applications, Gocad [2010]. Such a base model was put together by Eric Hetland. Next, this geometry needs to be imported into a meshing package like Cubit, cut and smoothed into an orthogonal edged curved surface. Then, the smoothed fault surface is discretized using an optimal adaptive mesh (different for every configuration of asperities) designed to focus most elements (“patches”) around the asperities. Finally, the numerical quality of the mesh and its smoothness are improved through an iterative process involving the computation of fault traction kernels at the centroids of all patches (see below).
- Before this project, the only openly available triangular dislocation solutions [Meade, 2007] were in Matlab and much slower than the Okada [1992] solutions available for rectangular patches. So, effort was put into improving the efficiency of the triangular solutions (by 250X), building a common interface for both types of solutions for benchmarking purposes, so they can directly process the discrete patch information from unstructured surface meshes output from Cubit. Fault traction kernels at the centroids of all patches are used to determine the local mesh resolution, and hence, the quality of the mesh (as described in the previous bullet-point).
- HSD10 and HS10 use Matlab for visualizing the simple planar faults tested in those papers. Since here, we are dealing with unstructured meshes for 3D fault surfaces,

arbitrarily oriented surface grid for computing synthetic observations, and a “point-cloud” of stations at the surface where actual data is available, a visualization system is needed that can handle such complex tasks on-the-fly. For that purpose, we use a comprehensive, open-source, 3D visualization package, the Visualization ToolKit [Schroeder et al., 2006], VTK, that allows easy visualization of multiple types of 3D spatial datasets such as those mentioned above, as well as their temporal evolution. Such visualization is an essential part of both the analysis of simulation output as well as routine quality control tasks such as checking and validating model input parameters.

- HSD10 and HS10 do not consider surface displacement/velocity fields, but instead focus on the stress shadow effect on the fault surface due to different configurations and shapes of asperities. Here, we want to compare the surface velocity predictions from the model to actual GPS data. In order to facilitate this, we needed to not only make sure the model is properly geo-referenced, so correct station locations can be used, but also develop a way to view maps and geographical locations (e.g., epicenters) for visualization in both a meshing package like CUBIT as well as VTK-based visualization packages (e.g., Paraview, and Mayavi). Without such geo-referencing, it is hard to make sure the locations of asperities are consistent with the epicentral coordinates, and their extents are consistent with say, topographic features on the overriding plate (e.g., locations of long-term geologic uplift, locations of coastlines, undersea canyons, etc.).
- HSD10 and HS10 use one or two asperities with relatively simple rupture sequences with specified rupture intervals on each asperity. Model spin-up was a straightforward point measure — namely, the mean value of tractions along the fault surface at the last time-step of every cycle. Here, we are dealing with a real subduction zone, where the rupture sequence for a given set of asperities is quite arbitrary, and the rupture interval has to be estimated from the best known near-field seismic and geodetic data. Also, in such cases, the definition of a “cycle” for a single characteristic earthquake has to be changed to that of a “cycle” for a characteristic

sequence of earthquakes — a characteristic rupture sequence time, or CRS-time. Instead of a single point in time, spin-up has to be tested over a span of at least a single CRS duration. In order to check for spin-up of solutions, the simulated tractions are averaged over several moving average “windows” and the smallest window (typically, the CRS-time) that shows stable spin-up is chosen to determine which cycle to use for finally computing synthetic GPS velocities to compare to data.

- HSD10 and HS10 use all asperity patches in their forward calculations. Here, by predefining the asperities during meshing, we compute fault parameters only on fault patches during forward modeling. Given that a large fraction of the total number of patches lie within asperities, we end up with up to 50% smaller kernel matrix sizes for a given mesh resolution (see below), or use 50% more elements for modeling stress/slip evolution on a given fault surface.

This chapter details the framework of pre-processors, elastic-dislocation codes, and post-processors that were developed to handle simulations with realistic 3D fault surfaces. In what follows, the general codes we developed for generating a smooth megathrust interface, its discretization into patches for kernel and model parameter generation, and major developments to the existing forward model solver to handle the complexities of 3D faults as well as realistic rupture patterns, as well as some key post-processing steps are discussed. While each of the above steps is “automated”, the underlying code was built so that the results from each stage can be extracted, visualized, and validated independently. All newly developed codes use open-source and/or free programming languages/packages. All lower-level (and stable) code is built as a python package (“Fslip”) which is installable, so it can be invoked from any python script or dynamically, in the python interpreter.

Figure 4-1 illustrates the workflow involving the *Fslip* package and external packages used for the analysis here. Currently, there are two components to running a model using *Fslip*: The python pre- and post-processors developed here, and the forward model solver

in Matlab (*EvolveSlip*, written by Eric Hetland, and modified for more general application to real faults here).

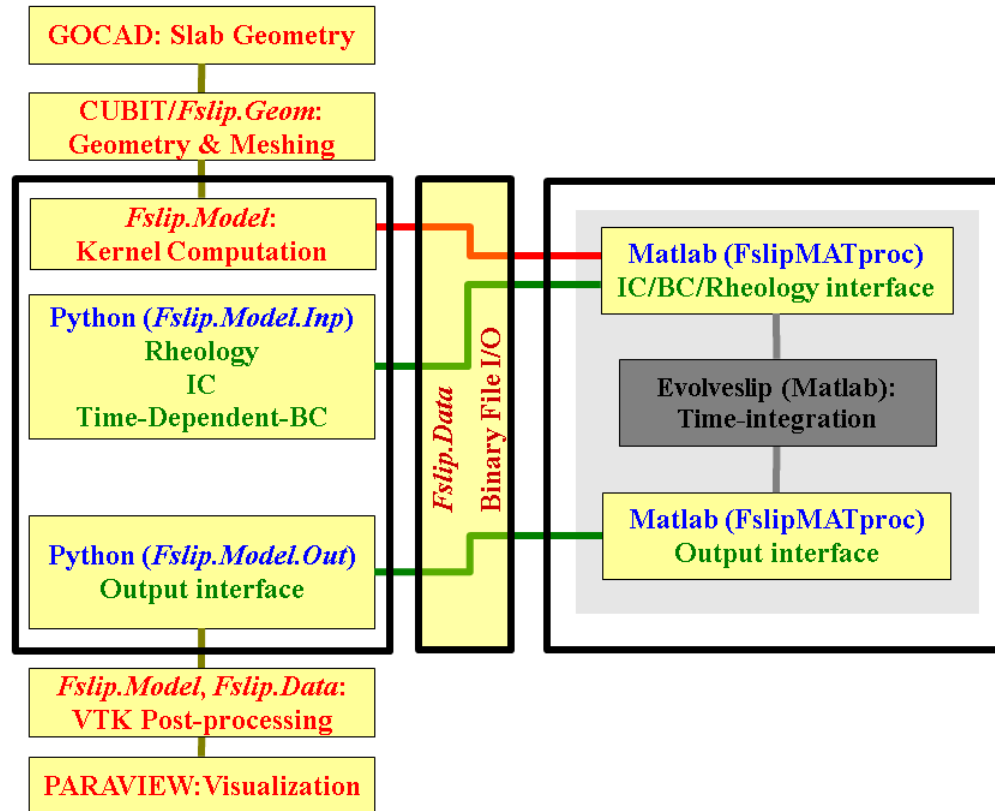


**Figure 4-1.** Workflow for the *Fslip* software developed to generate, simulate and visualize models of slip evolution on realistic fault surfaces. For simplicity, the exact long-form module names are not used for the lower level modules or Matlab pre-/post-processor scripts (e.g., *Fslip.Model.Out*, *FslipMATproc*, etc.). The matlab component, *EvolveSlip*, solves the forward problem, given the fault traction and surface displacement kernels, rheology, initial and boundary conditions for the 3D megathrust surface. The Matlab output is post-processed in two stages — in a Matlab and then in *Fslip* to generate VTK files and “dashboards” for visualization. See text for details.

## 4.2 Model visualization

Given the complex nature of real fault/station geometries, it is important to have the ability to probe both input and output data “on-the-fly”. As mentioned previously, we use VTK, as it is an extensive 3D data visualization package having well-defined native input file formats for different data types (e.g., structured/unstructured grids, and point

clouds). For example, while the fault is discretized as an unstructured mesh, the structured mesh is used to define a surface grid of observation points to sample surface deformation more densely than station locations allow. Stations are treated as surface point clouds. The XYZ-Cartesian system in which the 3D fault interface is defined in a CAD package such as Gocad [2010], becomes the “geographic” reference frame for all the forward models: i.e., all hypocenters, stations, and seismic asperities on the megathrust interface are now defined relative to this reference frame in the VTK format. Coastal boundaries and trench location are also defined in this frame for visually locating the extents of seismic asperities on the megathrust interface. These legacy or XML-based VTK files can then be visualized using several open-source or free software packages (Mayavi, Paraview, etc). Such “on-the-fly” visualization is extremely helpful in debugging model inputs as well as outputs by making it possible to quickly probe the quality of a 3D model or simulation statistically, point-wise, along line-profiles, cross-sections, as well as from different angles. The tremendous flexibility in visualization, however, comes at the cost of extensive bookkeeping, and file I/O required for keeping track of the multiple types of data-sets being handled here. So, both pre- and post-processing steps are more involved and much slower than the Matlab based plotting used in HSD10 or HS10. While VTK follows a relatively simple protocol for mesh numbering (e.g., nodes are numbered in the order they appear in element connectivity), translators are required to convert unstructured mesh nodal IDs (which are typically output in arbitrary order by Cubit) into the ordering expected by VTK. All this functionality is built into the input and output modules under *Fslip.Model*. The actual file I/O is performed under the *Fslip.Data* module.

### 4.3 Megathrust interface geometry & discretization

Since triangular patches can represent a 3D surface with higher accuracy than quadrilateral patches, we choose unstructured triangular meshing to divide the megathrust interface into discrete patches. All model parameters (i.e., rheological parameters, stresses, slip, slip-rate, any state-variables, etc.) are defined or computed at the centroids

of these triangular patches. The procedures adopted for creating and analyzing the megathrust geometry and subsequent triangulation into patches are discussed here.

Table 4-1 illustrates our workflow for generating an optimal discretization of the fault. The geometry for the upper surface of the subducting slab for the whole of Japan was generated by Eric Hetland, by fitting hypocentral locations, and published seismic reflection surveys in the commercial geological CAD package, Gocad (Table 4-1.1). These discrete patches (“facets”) are then exported to the geometry and meshing package, Cubit [Owen, 2006] (Table 4-1.2). All stages in the geometry/mesh generation process are fully automated using python scripts within CUBIT, using separate input files for model geometry and meshing. These functions are available under the module *Fslip.Geom*. However, at the present time, access to Cubit without the GUI interface (“Claro”) is not straightforward (since CUBIT is not open-source, the version of python packaged in the binary release might conflict with the local system python), so the default assumption behind these geometry/mesh scripts is that they will be run from inside Cubit’s python command line interpreter.

In CUBIT, the geometry is first cut along a vertical surface defined by the trench profile. The same profile is shifted down-dip (by  $\sim 400$  km), to make a parallel cut defining the bottom of the “active” megathrust boundary, or “fault”. Two vertical surfaces, locally orthogonal to the trench-profile then cut the interface, completing the basic fault geometry generation. The resulting orthogonal-edged fault surface is extended to the surface ( $z=0$ ), then smoothed to remove any along-dip kinks in the fault surface, owing to the fact that the amount of updip extension required to get to the free-surface varies along strike. Next, the fault surface is extended along the local trench strike at both ends, so its boundaries are far-enough from the outermost asperities ( $\sim 4$ – $5$  times the characteristic asperity size,  $D_{asp}$ ). The surface is smoothed once more after this extension to remove any kinks along strike (Table 4-1.3). This two-stage smoothing of the fault surface was found to be necessary in order for the tractions computed from any triangulation (or mesh, see below) to be relatively smooth over the curved fault surface. Next, the fault surface is subdivided into six orthogonal edged surfaces (three along strike, times two

down-dip), such that the upper middle surface [“Fsurf”, the yellow patch in (Table 4-1.4a)] contains all asperities. “Fsurf” enables tighter control over transitioning of the mesh from coarser resolution near the fault boundaries to very fine resolution around the asperities (patch sizes vary over two orders of magnitude). The asperities are then cut out of “Fsurf” and locally smoothed around each “cut”, to remove any discontinuities. The megathrust interface is now ready to be meshed (Table 4-1.4b).

The first step in the meshing process is setting interval sizes for its bounding curves and/or surfaces. The interval size used directly affects not only the quantity, but also the quality of elements in the mesh. We set the mesh interval size for the asperity-region bounding curves, as well as all asperity boundaries, to  $\sim 0.3-0.5$  of the interval size for rest of the fault. This ratio of interval sizes depends on the aspect ratio of “Fsurf” relative to that of the fault surface, as well as the circumference of the smallest asperity relative to the edge-lengths of “Fsurf”. We use “QTri” patches (quads divided into constituent triangles) outside the asperity region, as these were found to result in much faster convergence of the forward model (as opposed to fully unstructured triangular patches). Meshing within “Fsurf” as well as inside the asperities is done by an automatic paving algorithm built into Cubit.

The mesh is first refined (each triangular patch is split into three triangles formed by its edge-bisectors) around to asperity, to improve its resolution at a coarse level. So, it is important to obtain good quality elements around the asperities in the lowest resolution mesh because any poor quality element yields poorer quality “child” elements during such refinement. The whole of “Fsurf” is now refined once, transitioning into the coarse “QTri” elements outside this asperity region. This forms the base resolution mesh ( $\sim 3500$  fault elements, and  $\sim 500$  asperity elements, for the mesh presented here), “RES0” (Table 4-1.5(a)). The mesh itself is smoothed after every refinement step, to eliminate any abrupt element-size changes as well as better represent the original geometry. Since our model is driven by near singular tractions due to ruptures on asperities, most of the driving stress is concentrated right around the asperity. Therefore, further refinement is intended to better resolve the stresses around the asperity, and

results in a transition zone of high mesh density between the asperity and the surrounding fault surface. The upper limit on the number of elements is placed by 64-bit Matlab's restriction of  $10^4 \times 10^4$  elements. This limitation can be overcome when the forward model code, *EvolveSlip*, is eventually ported out of Matlab into Python. Given this restriction on the maximum number of fault patches, there are tradeoffs between the dimension of the smallest asperity, the fractional area of "Fsurf" that all asperities constitute, the size of "Fsurf", and the number of elements in the transition zone between the asperity and "Fsurf" – "Ftrans". For the coarse "RES0" mesh, roughly one-fourth of the fault patches (that is, excluding asperity patches) lie within a distance from asperity centers equal to the respective asperity dimensions ("Ftrans"). For the highest resolution mesh tested here ("RES2", with ~9,500 fault elements, and 4000 asperity elements), nearly 70% of the fault elements lie within this same distance (Table 4-1.5(b)). Thus, virtually all of the increase in resolution (~ 6000 elements) occurs right around the asperities, leaving the rest of the mesh relatively untouched. One could generate meshes that conform to the fault surface outside of "Fsurf" even better, by adaptively focusing on regions of higher curvature. In our case, the added expense due to refined elements far from the asperities did not allow for the use of such meshes. However, this form of mesh refinement can be explored in the future.

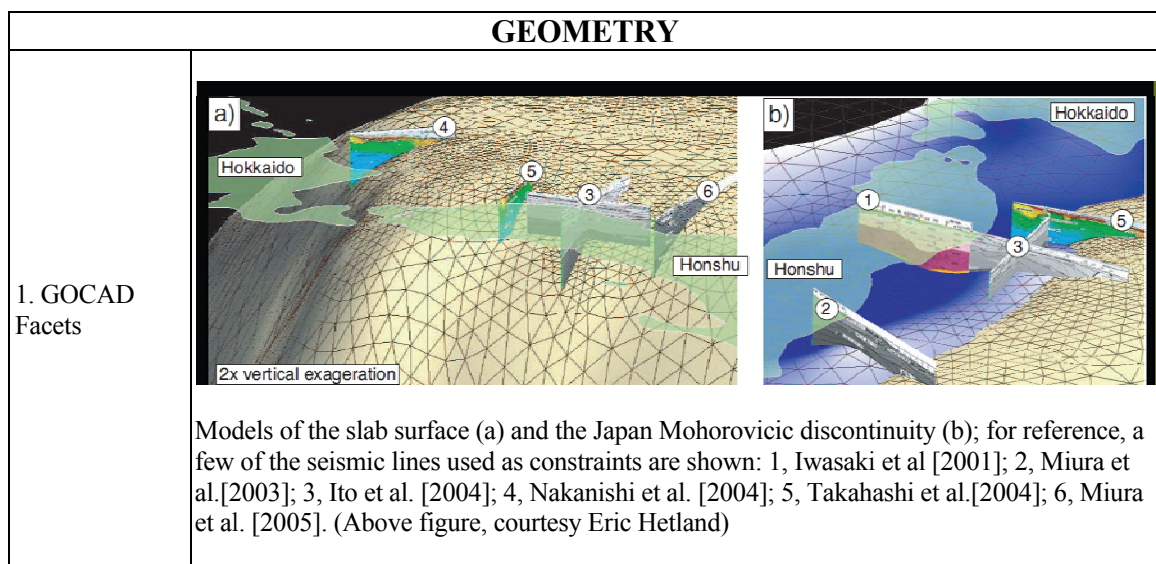
The ultimate check for a mesh is the smoothness of the traction kernels computed from that mesh. For every mesh used in benchmarking and simulations, several iterations were required to remove any subtle kinks from the fault surface. The goal was to preserve the large scale 3D structure of the fault, without introducing numerical perturbations of the traction field (at least in the predominant slip direction). Knowledge gained from these iterations were directly incorporated into making the geometry and meshing modules, *Fslip.Geom*, more effective. Benchmarking with kernels is discussed in more detail below.

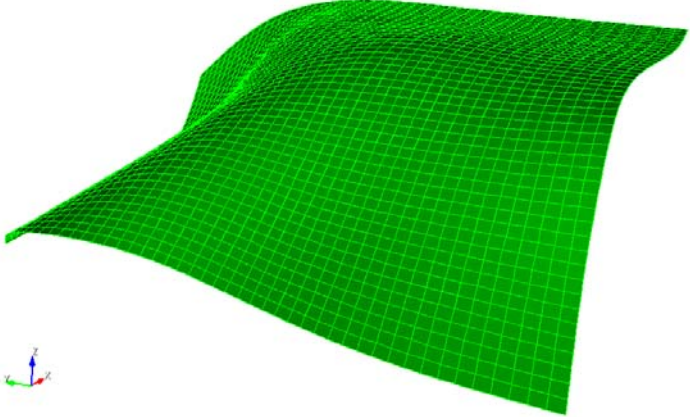
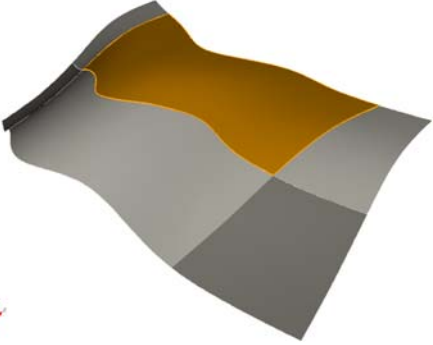
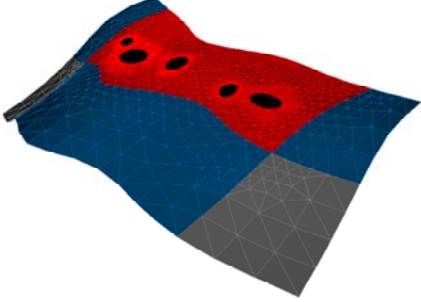
In order to improve the accuracy of locating asperities relative to the geographical region, a set of scripts were written to import a coastline map into the meshing package, Cubit. This not only aids in visualizing where the asperities are relative to surface stations, but

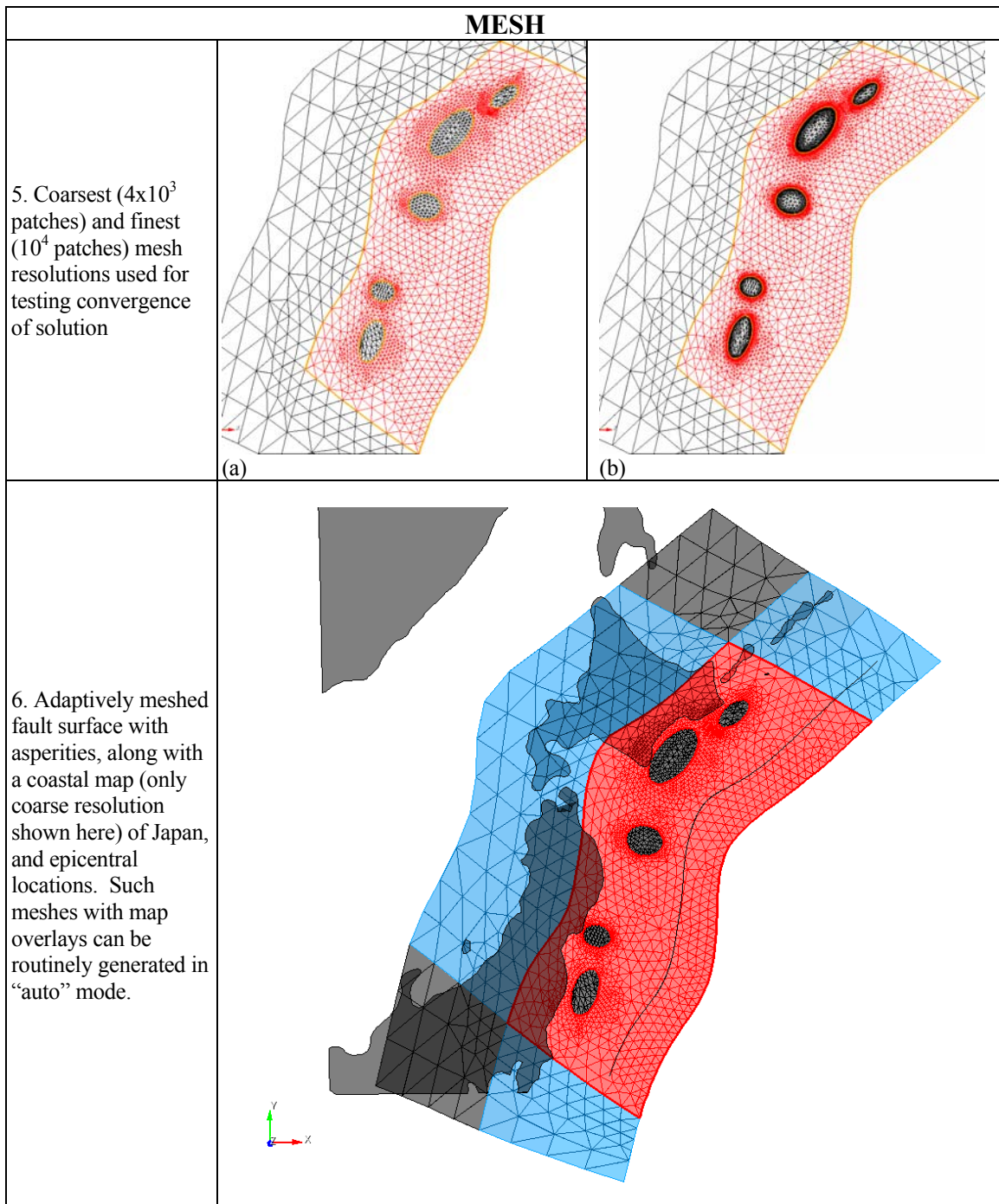
also provides a scale for quickly checking their extent, as well as their location relative to seismic epicenters (Table 4-1.6).

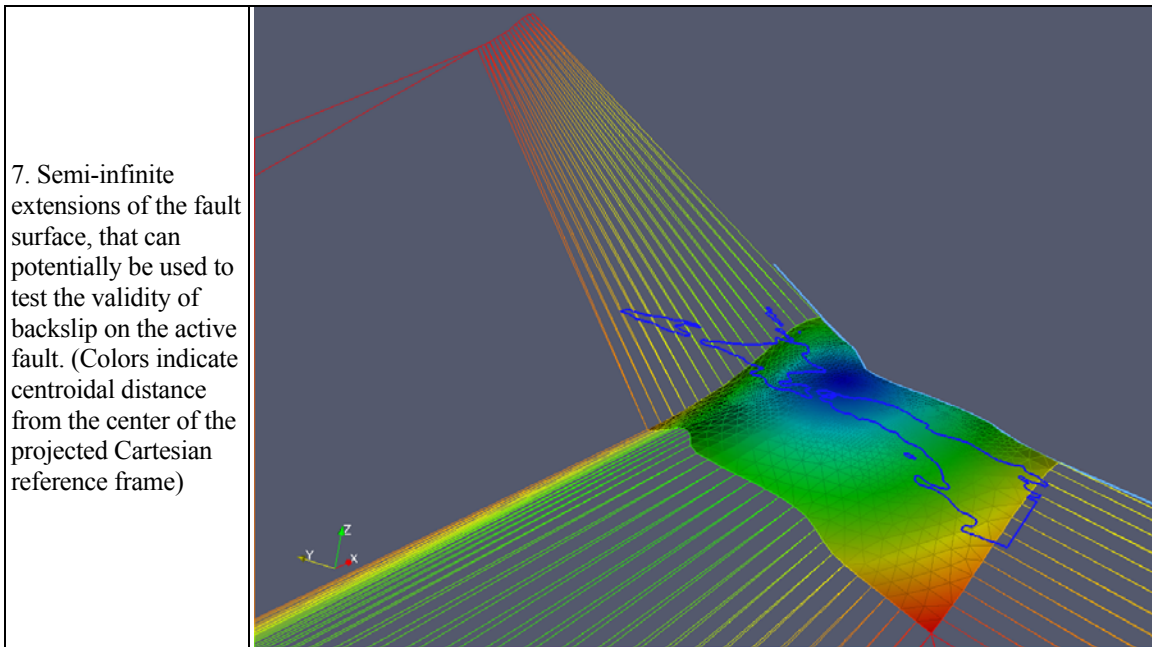
Finally, the mesh is output in Abaqus as well as ExodusII (for the sake of generality) formats. An Abaqus parser module (within *Fslip.Data*) and a comprehensive mesh post-processor module (within *Fslip.Geom*) were written to then extract patch data for Kernel computation. Such patch data include the nodal coordinates, area, aspect-ratio, strike, and dip of each element. Given we are dealing with unstructured meshes here, the mesh post-processor also includes several advanced utility functions to generate semi-infinite extensions of the curved fault surface (for imposing far-field boundary conditions), finding neighboring elements based on several criteria, e.g., shared edges, or element IDs, are included in this module. In addition, the mesh post-processor is general enough (and tested) to handle both triangular and quadrilateral meshes. The output from the Mesh post-processor is directly used by *Fslip.Kernel* module, to compute any type or combination of Kernels, as discussed in the next section.

**Table 4-1.** Work-flow for generating fault patches from a geo-referenced subducting slab surface geometry.



<p>2. Cubit ACIS net-surface approximation to Gocad facets</p>		
<p>3. Smoothed, orthogonally cut fault surface generated from the above mesh</p>		
<p>4. Subdivided fault surface (a) creating an upper-central area for locating asperities, “Fsurf” [yellow region in (a), red in (b)]</p>	 <p>(a)</p>	 <p>(b)</p>





#### 4.4 Kernels

The term “Kernel” is used here to denote the matrix of impulse-response functions that define the tractions or displacements at each observation point due to a unit slip along each of the constituent source patches of the fault. Considerable effort was expended in generating and testing the source code for the kernels. The existing half-space solutions for rectangles [summarized in Okada, 1992] and triangles [summarized in Meade, 2007] have different sign conventions. The Okada [1992] solutions were originally written in F77, but their most common form is a Matlab-MEX file, which needs to be recompiled and/or modified with each Matlab upgrade. The Meade [2007] solutions were entirely cast in Matlab, but very inefficient because the bulk of the calculations were “cut-and-pasted” from Matlab’s symbolic language toolbox. The Meade [2007] approach resulted in typical arithmetic expressions that were thousands of elements long, with nearly as many repetitions of function evaluations. Significant improvements in efficiency could be achieved by simplifying these symbolic language expressions. Here, triangular patches are used to accurately represent a real (curved) megathrust interface, and the much widely used rectangular patch solutions were used to benchmark these triangular solutions.

In order to overcome (a) the lack of a common interface for defining real-world faults for either the Okada [1992] or Meade [2007] solutions (the existence of which would be useful for benchmarking), (b) improve the computational efficiency of the triangular-dislocation solutions, and (c) make these solutions available in open-source format, two distinct but architecturally similar python-wrapped packages (*OkadaWrap*, and *TriWrap*) were developed, having identical functional interfaces that could be called from the same driver script using identical input data (a set of fault patches and observation points). These packages were extensively benchmarked using a suite of tens of 2D and 3D test problems — not only against each other (“peer-to-peer”), but also against the original Matlab versions (“parent-to-peer”). For *OkadaWrap*, the original F77 code was converted into F90 syntax, while for *TriWrap*, the original code was entirely re-written as optimized F90 modules. For *TriWrap*, special python scripts were written to automatically parse and translate the hundreds of Matlab expressions (output from the symbolic toolbox) into F90 syntax, as well as subsequently simplifying the resulting expressions to eliminate any repeating expressions or intrinsic function calls. As a result, *TriWrap* was found to be roughly 250 times faster than the original Matlab code [Meade, 2007] during benchmarking. The core dislocation codes in both packages are supported by several common F90 modules. The respective F90 driver routines for each package take care of the different input parameter conventions for these two solutions, and assemble kernels for a specified combination of patch and observation stations. These F90 driver routines are finally wrapped into python functions using the *F2py* package within *Numpy*. Installing and using either of these packages require both python/numpy as well as one of the free F90/95 compilers (Intel Fortran, or GFortran), but scripts for compiling with *F2py* are included with the packages. Beyond this basic requirement, the end-user can simply use these solutions as a “black-box” with a common interface. The packages also provide sample “well-commented” python driver scripts that can be a good starting point.

While space does not permit presenting the tests done in ensuring the accuracy of the kernels, it is worth mentioning the kinds of tests that were carried out in comparing the two sets of kernels. In all tests, fault orientation (strike and dip) were varied to get four

different combinations (positive or negative values for each angle). 2D tests included comparison of both free-surface and along fault displacement and traction vectors, as well as the full stresses tensor, for different fault and observation profile resolutions. The profile along the free-surface or fault was varied to compare both near- and far-field predictions. 3D tests involved comparing surface and fault deformation fields due to slip on a planar fault, discretized using rectangular patches, with a planar fault discretized using different triangular subdivisions of these same rectangles (from two to seven triangles per rectangle).

For the Japan megathrust interface used in the simulations here, the computed traction kernels were checked for both internal consistency and smoothness. In the context of half-space models, if a fault surface were to rupture the entire half-space, the relative motion between the hanging-wall and foot-wall can be described by rigid blocks sliding past each other. There is no net strain accumulation anywhere in the half-space owing to such rigid-body sliding. Say, we divide this fault surface into three regions: (a) small patches that slip only episodically (“asperities”) during seismic ruptures, (b) a region surrounding these asperities that slips in response to these ruptures (“fault”), and (c) the semi-infinite extension of the fault both along strike and dip (“loading”). The basic idea here is that over the course of an appropriately defined seismic “cycle”, all three regions of the fault would experience the same slip (albeit at different times), so that the net motion is equivalent to rigid-block motion. Let us now define at every point on the fault surface (in practice, at the centroid of every triangle on the discretized fault), (a) tractions resulting from slip on all fault patches (excluding asperities),  $\tau_{FF}$ , (b) tractions resulting from slip on all asperity patches,  $\tau_{FA}$ , and (c) those resulting from slip of the semi-infinite loading patches that continuously slip at the plate convergence rate,  $\tau_{FL}$ . If all three regions slip the same amount, then the resulting rigid-body motion implies that at every point on the semi-infinite fault surface within the half-space,

$$\tau_{FF} + \tau_{FA} + \tau_{FL} = 0 . \tag{1}$$

For realistic 3D meshes, however, discretization of the fault surface results in not all components of Equation 1 exactly cancelling each other. This consistency check is carried out every time kernels are computed for a given asperity configuration.

“Dashboards” containing 3D views of the above fault tractions are automatically generated for viewing in the open-source parallel VTK visualization package, *Paraview* [e.g., Henderson, 2004]. This consistency check (Equation 1) is presented for each traction component (strike-slip, dip-slip, and normal), for dip-slip over the fault, asperity, and loading patches in Figure 4-2, and for strike-slip along these patches in Figure 4-3. In these figures, each row of panels represents the contributions for one traction component, while each column represents  $\tau_{FF}$ ,  $\tau_{FA}$ ,  $\tau_{FL}$ , and the residual  $\Delta\tau$  (the right-hand side of Equation 1), respectively.

Since coseismic tractions are the principal driver of the models presented here, both the 3D fault geometry and the mesh were iteratively smoothed until the tractions along the principal slip-component directions (e.g.,  $\tau_{dip}$  due to dip-slip, and  $\tau_{strike}$  due to strike-slip) exhibited local fluctuations of  $< 0.1\%$  of the main coseismic signal around the asperities. However, for the “cross”-component directions (e.g.,  $\tau_{strike}$  due to dip-slip, and  $\tau_{dip}$  due to strike-slip), these fluctuations cannot be entirely eliminated owing to the fact that these tractions (which are mathematically the difference of two large numbers) are small over most of the fault surface, and due to the inherent discontinuities from the discretization of the fault surface (see upper-right and lower-right panels of Figure 4-2 and Figure 4-3). It was checked that such fluctuations did not exist for a planar fault surface, which yielded zero residuals everywhere on the fault surface from Equation 1. These fluctuations for the 3D fault geometry can, however, be minimized if curvature-based adaptive meshing is used everywhere on the fault surface, but the current limit on the maximum mesh size did not allow the use of meshes having high resolutions far from the asperities. Once kernels have been computed, they are stored and used for multiple simulation scenarios (or “runs”). In order to check model inputs going into the Matlab forward solver, *EvolveSlip*, another “dashboard” of model inputs is automatically generated for Paraview after generating all inputs for a run (see Figure 4-4 for dip-slip motion and Figure 4-5 for strike-slip motion), including (a) the tractions on the fault surface due to slip on fault and

asperity patches, (b) surface displacement field due to unit asperity slip for every asperity, (c) rheological parameter distribution, and (d) the initial slip, or slip all over the fault surface immediately after each asperity ruptures.

To be more realistic, a narrow slip transition zone is included around each asperity over which coseismic slip drops to zero (see bottom right panel of Figure 4-4 and Figure 4-5). The effect of different parameterizations for the slip distribution in this transition zone (or slip-”tapering”) are discussed in Hetland et al. [2010]. Several tapering functions are available in *Fslip.ModelInp* module for estimating this transitional slip. Typically, a fraction (0.25–0.5) of the asperity dimension is chosen to be the (arbitrary) width of this transition zone. As noted above, during meshing, this transition zone is where much of the refinement occurs to resolve coseismic tractions, and routine checks are carried out for each mesh to make sure that most of the coseismic stress pulse lies within this well-resolved transition zone, as far as practically possible.

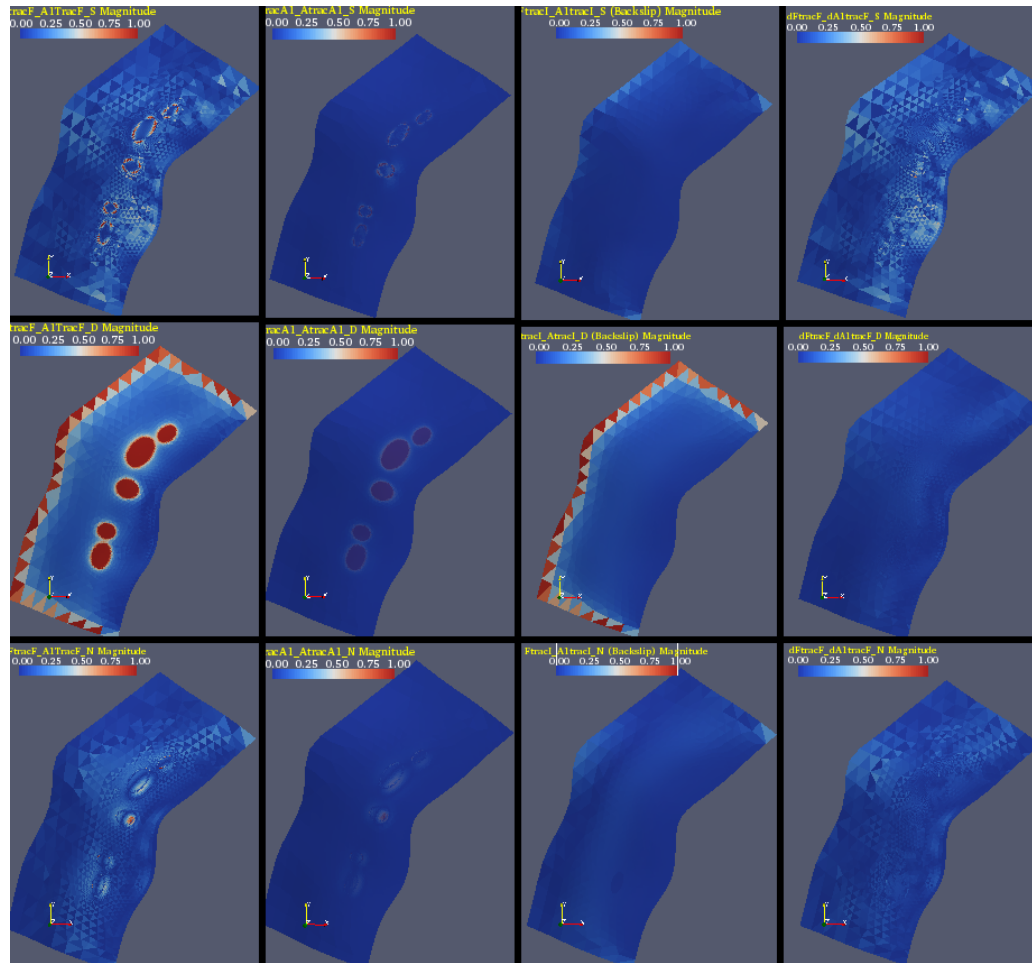


**Figure 4-2.** An automatically generated Paraview dashboard showing fault traction components ( $\tau_S$ , top row;  $\tau_D$ , middle row;  $\tau_N$ , bottom row) due to dip-slip on all fault patches (column 1), slip on each asperity (column 2: the duller color is due to the use of transparency in Paraview to show all asperity contributions in a single panel), slip on the semi-infinite extensions of the fault (or backslip, column 3), and the residuals obtained from the superposition (Equation 1). For a planar fault, these residuals were found to be zero, as expected.

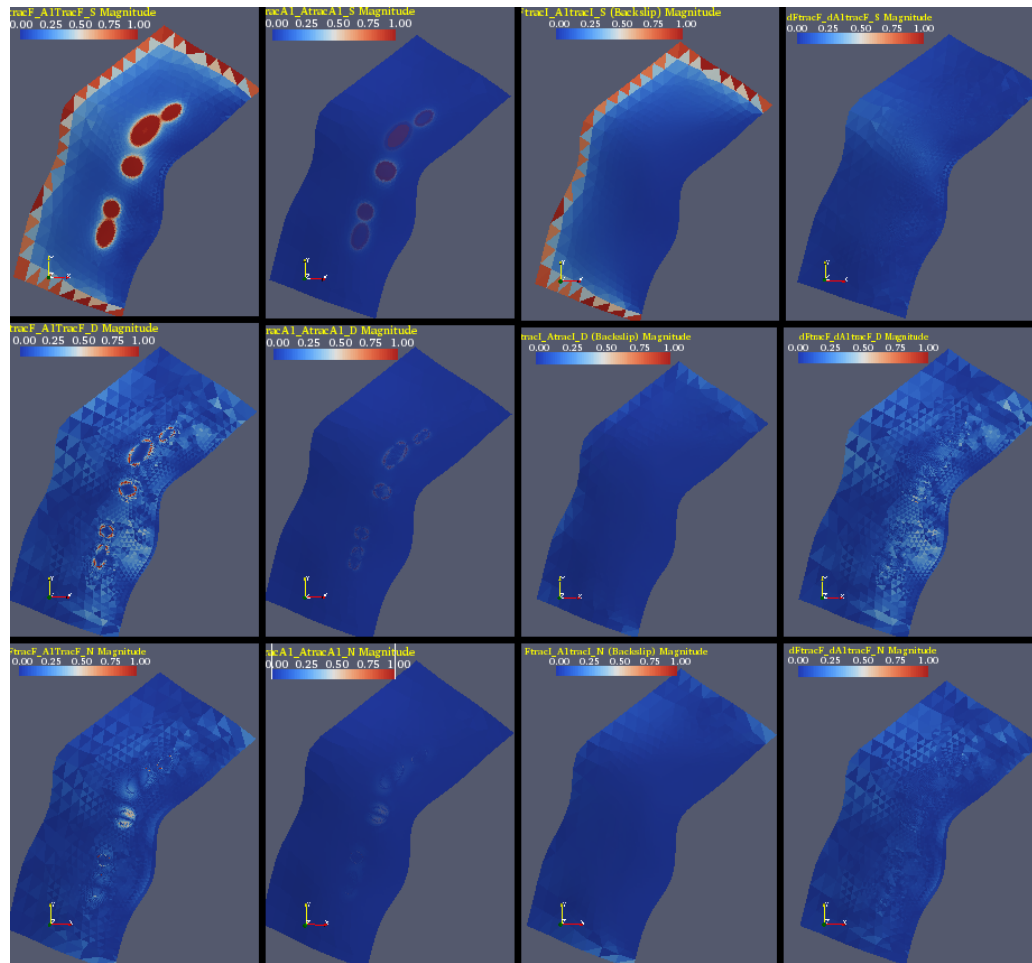


**Figure 4-3.** An automatically generated Paraview dashboard showing fault traction components ( $\tau_S$ , top row;  $\tau_D$ , middle row;  $\tau_N$ , bottom row) due to strike-slip on all fault patches (column 1), slip on each asperity (column 2: again, the duller color is due to the use of transparency in Paraview to show all asperity contributions in a single panel), slip on the semi-infinite extensions of the fault (or backslip, column 3), and the residuals obtained from the superposition (Equation 1). For a planar fault, these residuals are zero, as expected.

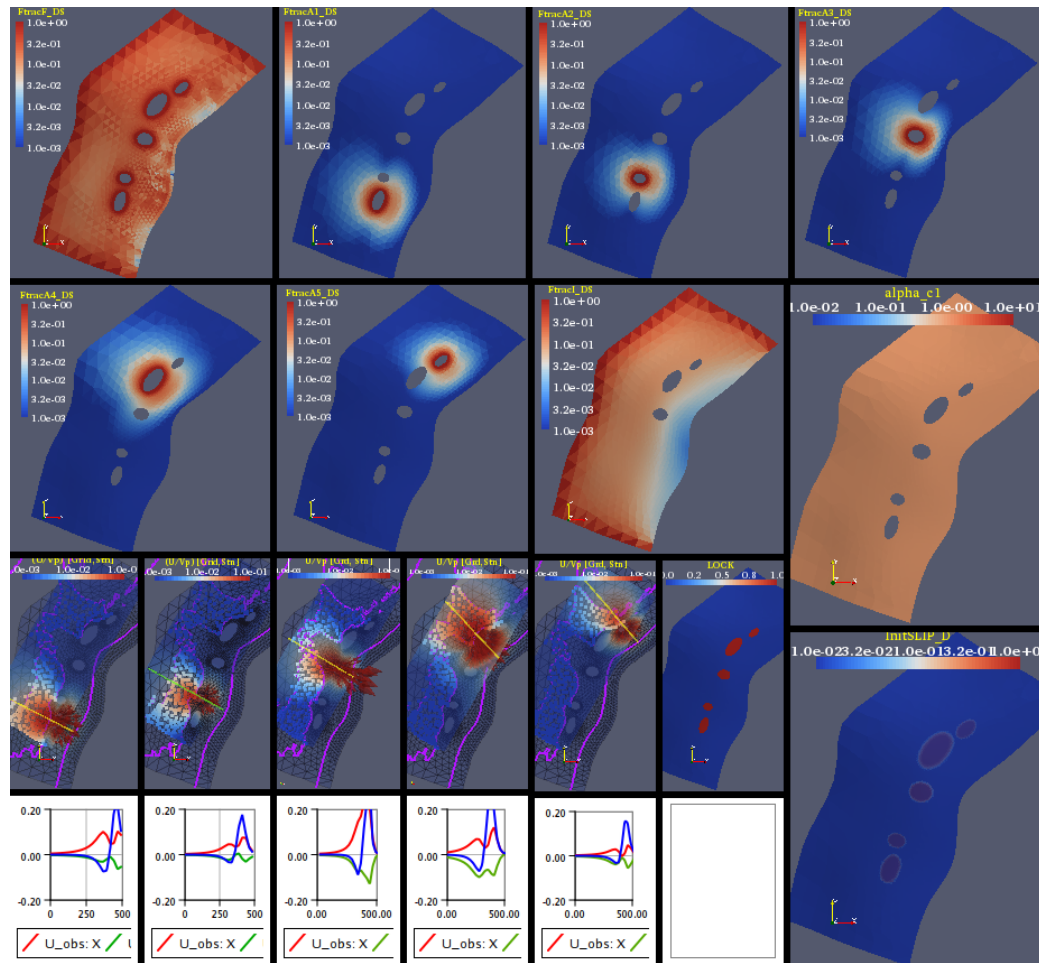


**Figure 4-4.** An automatically generated Paraview quality control dashboard for unit dip-slip on the fault and asperities, showing the rheological parameter distribution (rightmost middle panel), initial slip distribution (bottom-right panel), tractions (top two rows of panels), and surface displacements. Such figures are automatically generated and used for visualizing model inputs before a run or for debugging after a run. All 3D plots are colored on a log-scale, to bring out any small-scale heterogeneities.

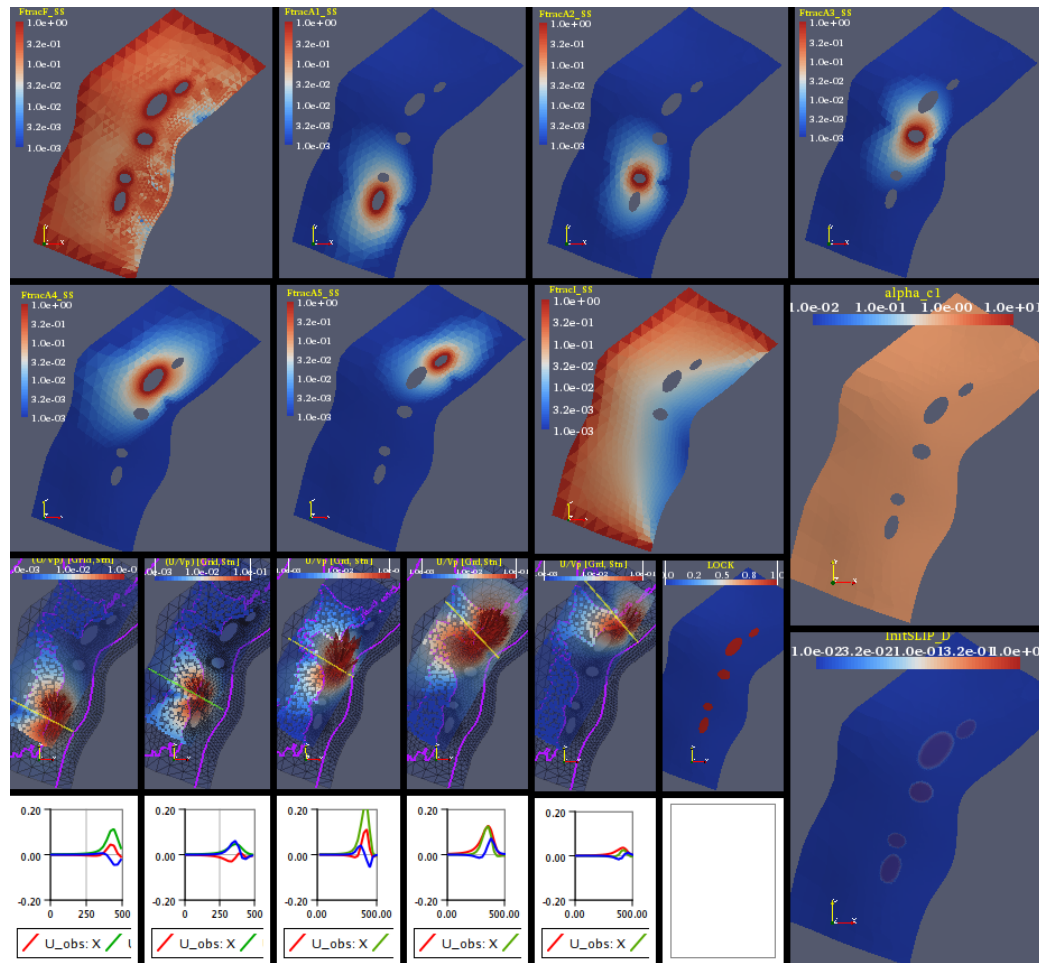


**Figure 4-5.** An automatically generated Paraview quality control dashboard for unit strike-slip on the fault and asperities, showing the rheological parameter distribution (rightmost middle panel), initial slip distribution (bottom-right panel), tractions (top two rows of panels), and surface displacements. Such figures are automatically generated and used for visualizing model inputs before a run or for debugging after a run. All 3D plots are colored on a log-scale, to bring out any small-scale heterogeneities.

## 4.5 Rheology

The Matlab forward solver, *EvolveSlip*, models linear-viscous, non-linear viscous, purely rate-dependent and Dietrich-Ruina rate-state rheologies. Hetland et al. [2010] showed that late in the seismic cycle, which is what we are attempting to simulate here, both purely rate-dependent as well as rate-state rheologies give very similar fault slip rates. In our simulations presented here, we use only purely rate-dependent rheology. However, for the purposes of intuition building in terms of the effects of strong vs. weak faults, we use a linear viscous rheology. For linear viscous rheology, slip-rate depends linearly on fault loading tractions, as opposed to the exponential dependence in typical rate-dependent rheologies. Therefore, simulations with linear viscous rheology can be used as a starting point in understanding the “strength” of the fault required to match surface velocity predictions to the observed velocities. While *EvolveSlip* can theoretically handle heterogeneous fault zone rheology, in this initial work, we only explore constant rheological properties, ignoring any lateral or depth dependence. In order to compare runs for different rheologies, all simulations are carried out with non-dimensional parameterizations. Hetland et al. [2010] cast the relationship between slip-rate and fault tractions for various rheologies in the form:

$$\dot{s} = f(\tau, \alpha) \quad (2)$$

where,  $\alpha$  is a strength parameter that depends on the rheology.

For linear viscous rheology,

$$\dot{s} = f(\tau, \alpha) = \frac{\tau}{\alpha} \quad (3)$$

and  $\alpha$  depends only on the characteristic viscosity,  $\eta$ , and width,  $h$ , of the fault zone:

$$\alpha = \frac{\eta}{h} . \quad (4)$$

The viscosity can be computed as the product of the shear-modulus,  $\mu$ , and a relaxation time (in the case of Maxwell viscoelasticity),  $T_R$ . The non-dimensional scaling for the strength parameter is simply,

$$\alpha_0 = \frac{\tau_0}{V_0} = \frac{\mu S_0}{V_0 D_0} \quad (5)$$

where,  $V_0$  is the loading rate (plate velocity),  $S_0$  is the characteristic slip on the asperity, and  $D_0$  is the characteristic asperity dimension. So, from (4) and (5), a dimensionless strength parameter for viscous rheology is:

$$\alpha' = \frac{\alpha}{\alpha_0} = \frac{\mu T_R}{h} \frac{V_0 D_0}{\mu S_0} = \frac{V_0 T_R}{S_0} \frac{D_0}{h} \quad (6)$$

Non-dimensionalizing (3) using  $\alpha_0$ ,  $\tau_0$ , and  $V_0$ , and rearranging, we obtain,

$$\tau' = \frac{\tau}{\tau_0} = \frac{\alpha \dot{s}}{\alpha_0 V_0} = \alpha' V' \quad (7)$$

Thus, late in the cycle, when most of the fault is slipping at the loading rate, the mean dimensionless shear tractions along the fault surface will equal the dimensionless strength parameter,  $\alpha'$ . Typical values for the above parameters are:  $V_0 \approx 10^{-2}$  m/yr,  $S_0 \approx 1$  m,  $D_0 \approx 10^4$  m,  $h \approx 1$  m, and  $T_R \approx 10^{-3}$ – $10^{-1}$  yr. Substituting these into (6) yields the range of values for  $\alpha'$  as 0.1 to 10.

For rate-dependent rheology,

$$\dot{s} = f(\tau, \alpha) = V_0 e^{\left(\frac{-f_0}{(a-b)}\right)} \sinh\left(\frac{\tau}{(a-b)\sigma_0}\right) \quad (8)$$

where,  $f_0$  is the static friction coefficient,  $a$  and  $b$  are the coefficients of the direct and indirect (state-dependent) dynamic frictional effects, and  $\sigma_0$  is the effective normal traction on the fault surface. In our model,  $\sigma_0$  can be both time-dependent (e.g., in response to slip evolution on the fault surface), as well as spatially heterogeneous (e.g., due to pore-pressure variations). In the demonstrative results presented in Chapter 5, we choose a constant  $\sigma_0$  over the entire fault surface. The implications of such an assumption are discussed in more detail in Section 5.2. Therefore, there are two non-dimensional rheological parameters in this case [Hetland et al., 2010]:

$$V' = \frac{\dot{s}}{V_0} = e^{(-\rho)} \sinh\left(\frac{\tau'}{\alpha'}\right) \quad (9)$$

where,  $\rho = f_0/(a-b)$ , and  $\alpha = (a-b)\sigma_0$ . Thus, late in the cycle, when most of the fault is slipping at the loading rate, the mean dimensionless shear tractions along the fault surface

will equal  $\rho$  times the dimensionless strength parameter,  $\alpha'$ . Typical values of  $(a-b) \approx 10^{-2}$  [Blanpied et al., 1991; Marone et al., 1991],  $f_0 \approx 0.1-1$ ,  $\sigma_0 \approx 10-10^2$  MPa [Rice, 1993; Lapusta and Rice, 2003]. Thus, typical range of values for  $\rho \approx 10-100$ , and  $\alpha \approx 10^5-10^6$  Pa. Assuming the same values as before for the non-dimensionalization of stresses, and  $\mu \approx 10^{10}$  Pa,  $\alpha' \approx 10^{-2}-10^{-1}$ .

#### 4.6 Significant developments over the existing Matlab forward solver, *EvolveSlip*

In addition to the general codes discussed above, several developments needed to be made to the existing Matlab forward solver, *EvolveSlip*, and its dependencies, in order to handle models with real fault surfaces. Here, we discuss the most significant changes. As before, we refer to Hetland et al. [2010], and Hetland and Simons [2010] as HSD10, and HS10, respectively.

**Size of the problem:** In HSD10 and HS10, a set rectangular region surrounding the asperities is always discretized at a fine resolution. This fine rectangular mesh around the asperities transitions into coarser rectangles towards the edges of the fault. In their implementation, asperities are defined at the time of running the model by designating patches lying within a specified region of the planar fault to be locked (“asperity”). Here, we use a different approach, whereby the asperities are defined at the time of meshing the megathrust interface, and fault parameter evolution is simulated only over the region of the fault outside these asperities. Driving coseismic stresses (and hence, the largest gradients in the modeled field parameters) occur along a narrow band surrounding the asperities. Therefore, as discussed in the meshing section, a very fine mesh resolution is applied over a narrow transition zone around the asperities. By not storing model parameter evolution over asperities during forward model calculations, the size of the Kernel array can be reduced by a factor of 40–50%, which can be significant when there are thousands of patches within the asperities. Also, a much higher patch size contrast is achieved between the fault edges and asperity boundaries, because a large fraction of the finer mesh residing within the asperities is ignored. In addition, the above references did

not consider surface deformation at observation stations (which can number in the several 100s to 1000, for a place like Japan). So, excluding the evolution of model parameters over asperity surfaces allows us to not only resolve the driving tractions after each rupture at a much finer scale than in the scheme implemented in Hetland et al. (by roughly an order of magnitude), but also to include thousands of surface observation points (actual stations as well as a surface observation grid for visualizing surface deformation).

**Rupture sequence and timing of rupture:** Since HSD10 and HS10 were trying to demonstrate a method for simulating postseismic fault slip, they did not consider realistic rupture sequences. In reality, the rupture interval for each asperity may not be related to that of another asperity by whole fractions (because rupture timing offset, or rupture intervals, or both). In this case, the concept of a characteristic rupture sequence time (or CRS cycle) — which is arithmetically equivalent to the least common multiple of all asperity rupture intervals — is utilized. Essentially, after each CRS cycle, ruptures on all asperities repeat in the same sequence, and rupture-time offsets as the previous CRS cycle. Therefore, a different convergence criterion had to be developed for the case of an arbitrary sequence of ruptures on multiple asperities. The convergence criterion used in Hetland et al. was designed for relatively uniform meshes with small gradients in mesh size (arithmetic mean of tractions measured at a single time — just before a subsequent rupture). When using unstructured grids having a large range of mesh element sizes (as is the case here), it is more appropriate to use an area-weighted mean for checking convergence. In addition, when using realistic rupture sequences, the mean tractions vary significantly between the individual constituent earthquakes in each CRS-cycle, thus making it inappropriate to use only a single point in time to measure convergence. Here, we use moving averages taken over different time-spans to determine an appropriate time-scale over which the model is deemed to have converged. Not surprisingly, the smallest moving average window beyond which convergence is stable turns out to be the CRS-cycle time. Therefore, the first complete CRS-cycle after convergence gives the simulated earthquake sequence for the given set of asperities. Synthetic surface velocities are extracted from this cycle for comparison to surface geodetic data.

### **Application of backslip with varying rake over an arbitrary fault surface in 3D:**

HSD10 and HS10 considered only planar faults. For a given relative plate velocity orientation, the rake (angle between slip vector and down-dip vector along the fault plane) is constant across the fault surface. However, for an arbitrary dipping fault surface in 3D, rake is a spatially varying quantity, whose local rate of variation depends on the degree of smoothing applied to that surface (as discussed in the meshing and kernels sections above). As originally postulated by Savage [1983], and demonstrated by Kanda and Simons [2010], backslip over a curved megathrust interface must be applied only along the local tangent to the fault surface. So, an additional feature was introduced whereby backslip is prescribed locally, over every patch depending on its orientation (strike and dip) relative to that of the plate velocity vector. Also, depending on the relation between the plate velocity vector direction and trench strike along the megathrust interface, it is possible to have strike-slip component of the plate velocity having both “up-strike” and “down-strike” directions along the same mega-thrust interface. In order to handle both positive and negative slip-rates in a given slip-direction, Kernel pre-multipliers computed from the local backslip unit vector were used to determine their correct response. Using a local backslip distribution results in significant strike-parallel fault slip partitioning (Figure 4-6) along the northern Japan-Kurile trench, with negligible along-strike slip for the southern Japan-Trench. This is consistent with slip inferred from observed surface geodetic measurements [see for example, DeMets, 1992; Loveless and Meade, 2010].

#### **4.7 Steps in running a model**

All model parameters (numbering about 150 for a typical run) are input into a comprehensively documented Input file, *ModelData.py*, consisting of three python data-classes — *Global Data*, *Kernel Data*, and *Run Data*. Given the number of inputs, and for

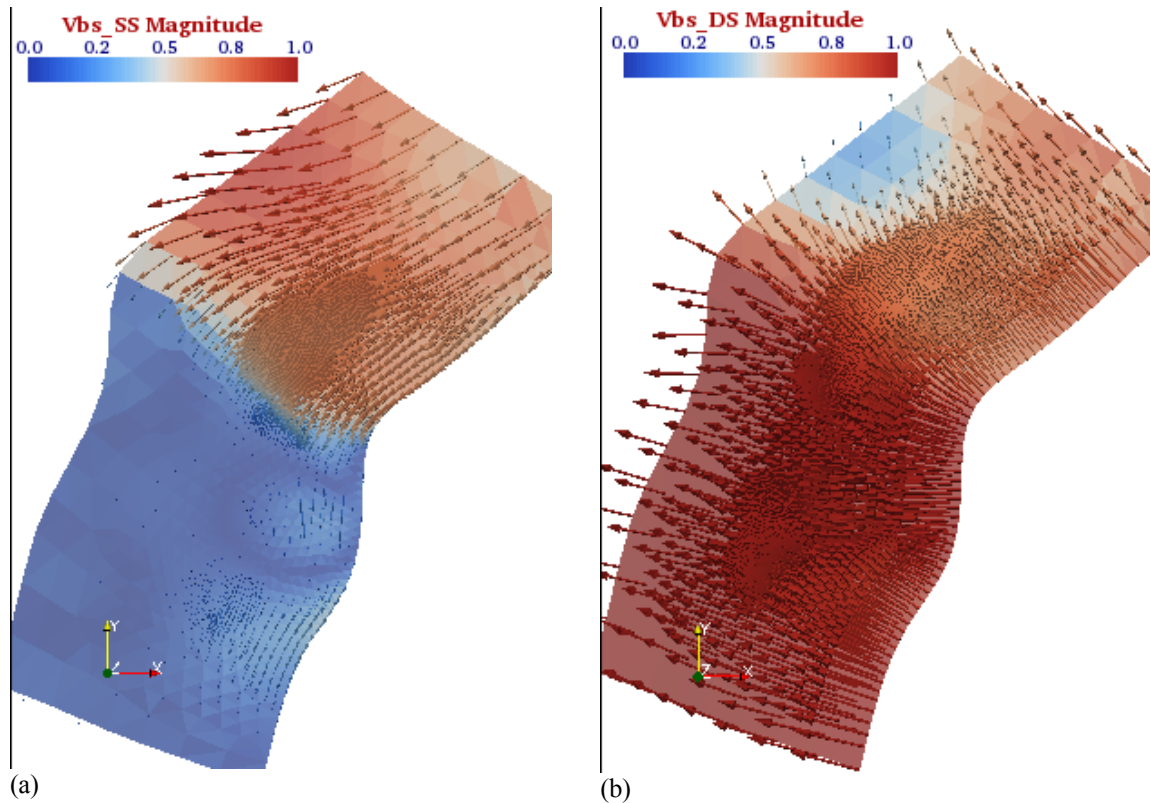


**Figure 4-6.** (a) Strike-slip, and (b) dip-slip components of the non-dimensional backslip velocity field applied to the 3D fault surface. Color-scale indicates the same range of magnitudes in both figures as well as for the arrows.

tight quality control, this same input file is read by all the python drivers in *Fslip*, as well as the Matlab driver for *EvolveSlip*. A parser/translator was written in Matlab (and extensively tested) that can understand simple python assignment statements, including: lists, tuples, 1D and 2D arrays, concatenated strings, intrinsic functions and simple arithmetic expressions.

Currently, there are three python driver scripts and one matlab driver script for carrying out the different components of a simulation: (1) *Mesh2Kernels.py*: Mesh data extraction and kernel generation (typically, a one-time process for a given mesh resolution), (2) *ModelPar.py*: Python pre-processing run to generate model input parameters (Coseismic slip components, rupture history, Initial slip and rheological parameters distributions, locked fault patches — for every run), (3) *RunPyModel.m*: Forward model calculations,

using a Matlab driver that parses the input file, *ModelData.py*, extracts the kernels as well as model parameters from binary files, assembles the kernel matrix, sets additional run-time parameters, and finally, runs *EvolveSlip*, and (4) *Matbin2Vtk.py*: Post-processing to probe and extract binary Matlab output for further processing as well as VTK files for visualization.

In order to aid in debugging and check for any run-time issues, the drivers currently output a large amount of screen output to indicate different stages of activity. In the future a verbosity flag will be added to suppress this output when not required. Also, as part of validating the code, we tested a series of runs for both spin-up and consistency of surface velocity predictions. Different fault-asperity configurations were used along with either linear viscous (for benchmarking) or rate strengthening rheology: (a) single asperity on a planar fault approximating the Tohoku section of the Japan Trench (TL), (b) entire 3D fault along the Japan Trench, with one (JT1) and two (JT2) asperities, (c) entire 3D fault along the Japan Trench, with the five major asperities (discussed in the next chapter), both without (JT5) and with variable backslip rake (JT5vb). Due to space constraints only the results from the last run (JT5vb) are presented in the next chapter.

#### **4.8 Future directions for research and development**

More sophisticated scientific questions can be addressed with extensions to the software developed here, for instance:

- The effect of lateral and depth variations in fault rheology.
- As the spatio-temporal resolution of geodetic data gets better, and crustal structure gets better resolved using seismic data, we could also use kernels generated accounting for local 3D crustal heterogeneities. Such 3D kernels would have to be computed numerically, using for example, a Finite Element Method (FEM) code, but are straightforward to compute at the present time.
- A long-term challenge is to attain the ability to simultaneously model multiple rheologies on the fault surface, which result in slip evolution over multiple length and

time-scales on the fault surface. This will involve a thorough re-formulation of the meshing schemes, as well as the forward model solver, taking into account any potential numerical instabilities resulting from such multi-scale evolution.

Thus, future software development can proceed in several directions. First, we want to migrate all the forward modeling functionality (currently in the Matlab scripts *EvolveSlip*) to python in order to avoid the array size limitations imposed by Matlab — so higher resolution discretizations and/or larger fault areas can be handled. The current code can also be speeded by simple changes such as eliminating verbose screen output and further optimization of file-I/O. However, in order to make it feasible to routinely carry out inversions of geodetic data for fault rheological properties, significant speed improvements are needed. Such improvements are possible by recognizing that the elastic fields due to slip on a fault patch have an inherent length-scale (roughly a few times the characteristic patch size). So, at the present, the kernel matrix is very “sparse” in a numerical sense. Therefore, by introducing scale-dependent kernels, a kernel matrix with a much smaller band-width can be used for the forward model. However, given that we are testing non-linear rheologies, the inherent time-stepping (even if adaptive) limits the ultimate speed improvement that is possible for this problem, irrespective of the numerical integration scheme used. However, even now, simulations can be run and processed within a couple of days using an “embarrassingly-parallel” approach — that is, by simultaneously launching jobs on thousands of processors. In this sense, even now, a limited Bayesian type inversion is currently feasible within a reasonable time-frame. However, with increasing computing power (e.g., use of Graphical Processing Units, or GPUs) and cluster sizes, inverting for fault rheological properties in a fully Bayesian sense will become even more tractable in the coming years.

## References

- Blanpied, M., D. Lockner and D. Byerlee (1991), Fault stability at hydrothermal conditions, *Geophys. Res. Lett.*, 18, 609–612.
- DeMets, C. (1992), Oblique Convergence and Deformation Along the Kuril and Japan Trenches, *J. Geophys. Res.*, 97, 17,615–617,625, doi:610.1029/1092JB01306.
- Gocad, 2010. (<http://www.gocad.org/www/gocad/index.shtml>) Gocad Research Group.
- Henderson, A. (2004), *The Paraview Guide*, 1st edn, vol., Kitware Inc.
- Hetland, E.A. and M. Simons (2010), Postseismic and interseismic deformation due to fault creep II: Transient creep and interseismic stress shadows on megathrusts. , *Geophys. J. Int.*, 181, 99–112, doi:110.1111/j.1365-1246X.2009.04482.x.
- Hetland, E.A., M. Simons and E.M. Dunham (2010), Postseismic and interseismic deformation due to fault creep I: Model description. , *Geophys. J. Int.*, 181, 81–98, doi:10.1111/j.1365-1246X.2010.04522.x.
- Ito, A., G. Fujie, T. Tsuru, S. Kodaira, A. Nakanishi and Y. Kaneda (2004), Fault plane geometry in the source region of the 1994 Sanriku-oki earthquake *Earth Planet. Sci. Lett.*, 223, 163-175.
- Iwasaki, T., W. Kato, T. Moriya, A. Hasemi, N. Umino, T. Okada, K. Miyashita, T. Mizogami, T. Takeda, S. Seikine, T. Matsushima, K. Tashiro and H. Miyamachi (2001), Extensional structure in northern Honshu arc as inferred from seismic refraction/wide-angle reflection profiling, *Geophys. Res. Lett.*, 28, 2329–2332.
- Kanda, R.V.S. and M. Simons (2010), An elastic plate model for interseismic deformation in subduction zones, *J. Geophys. Res.*, 115, B03405.
- Lapusta, N. and J. Rice (2003), Nucleation and early seismic propagation of small and large events in a crustal earthquake model, *J. geophys. Res.*, 108, 2205, doi:2210.1029/2001JB000793.
- Loveless, J.P. and B.J. Meade (2010), Geodetic imaging of plate motions, slip rates, and partitioning of deformation in Japan, *J. Geophys. Res.*, 115, B02410, doi:02410.01029/02008JB006248.
- Marone, C., C. Scholz and R. Bilham (1991), On the mechanics of earthquake afterslip, *J. geophys. Res.*, 96, 8441–8452.
- Meade, B.J. (2007), Algorithms for the calculation of exact displacements, strains, and stresses for triangular dislocation elements in a uniform elastic half space. , *Comp. Geosci.*, 33, 1064-1075, doi:1010.1016/j.cageo.2006.1012.1003.
- Miura, S., S. Kodaira, A. Nakanishi and T. Tsuru (2003), Structural characteristics controlling the seismicity of southern Japan Trench fore- arc region, revealed by ocean bottom seismographic data, *Tectonophysics*, 363, 79-102.
- Miura, S., N. Takahashi, A. Nakanishi, T. Tsuru, S. Kodaira and Y. Kaneda (2005), Structural characteristics off Miyagi forearc region, the Japan Trench seismogenic zone, deduced from a wide-angle reflection and refraction study, *Tectonophysics*, 407, 165-188.

- Nakanishi, A., A.J. Smith, S. Miura, T. Tsuru, S. Kodaira, K. Obana, N. Takahashi, P.R. Cummins and Y. Kaneda (2004), Structural factors controlling the coseismic rupture zone of the 1973 Nemuro-Oki earthquake, the southern Kuril Trench seismogenic zone, *J. Geophys. Res.*, 109, B05305, doi: 05310.01029/02003JB002574.
- Okada, Y. (1992), Internal deformation due to shear and tensile faults in a half-space, *Bull. Seismol. Soc. Am.*, 82, 1018-1040.
- Owen, S.J., 2006. CUBIT 10.2 Documentation, pp. 532, Sandia National Laboratories, Albuquerque, NM, U.S.A.
- Rice, J. (1993), Spatio-temporal complexity of slip on a fault, *J. geophys. Res.* , 98, 9885–9907.
- Savage, J.C. (1983), A dislocation model of strain accumulation and release at a subduction zone, *J. Geophys. Res.*, 88 4984-4996.
- Schroeder, W., K. Martin and B. Lorensen (2006), *The Visualization Toolkit An Object-Oriented Approach To 3D Graphics*, 4th edn, vol., Kitware Inc. .
- Takahashi, N., S. Kodaira, T. Tsuru, J.-O. Park, Y. Kaneda, K. Suyehiro, H. Kinoshita, S. Abe, M. Nishino and R. Hino (2004), Seismic structure and seismogenesis off Sanriku region, northeastern Japan, *Geophys. J. Int.*, 159, 129-145.

## *Chapter 5*

### ASPERITY MODEL FOR INTERSEISMIC DEFORMATION IN NORTHEASTERN JAPAN

#### **5.1 Introduction**

In the last century, several large ( $M > 7$ ) earthquakes have occurred on the megathrust interface along the Japan Trench, offshore of Japan's Tohoku region. Published earthquake source inversions based on seismological and high-rate GPS data suggest that the earthquakes off Miyagi [Miura et al., 2006; Umino et al., 2006], Sanriku [Tanioka et al., 1996; Nakayama and Takeo, 1997], and Tokachi [Robinson and Cheung, 2003; Hamada and Suzuki, 2004; Miyazaki et al., 2004; Satake et al., 2006] occurred repeatedly over roughly the same region of the subduction megathrust. In contrast, inversions of geodetic data from interseismic periods produce models that are locked over more spatially extensive regions [e.g., Bürgmann et al., 2005; Suwa et al., 2006; Chlieh et al., 2008b]. These broad and smooth regions are in contrast to the smaller discrete asperities indicated by earthquake source studies, and may be a consequence of lack of model resolution and a resulting need for regularization that is inherent to the use of onshore geodetic data. Alternatively, the differences may imply the potential for a large earthquake in the future. Thus, the different levels of apparent coupling implied by these two classes of models have very different implications for regional seismic hazard (Figure 1-1). Here, we explore whether post-seismic slip resulting from mechanical coupling of the inferred seismic asperities alone can reconcile this apparent difference in seismic hazard estimates. We do not seek to model the complex dynamics of rupture nucleation, interaction between asperities, or rupture propagation [see for e.g., Rice, 1993; Lapusta and Rice, 2003; Hori, 2006; Kato, 2008; Perfettini and Ampuero, 2008].

Several studies have recently attempted to constrain post-seismic creep on faults from inversions of high-rate geodetic data. These studies either tested the inferred postseismic creep for consistency with specific fault rheologies [e.g., Miyazaki et al., 2004; Hsu et al., 2006], or by modeling this inferred creep as a response of the fault to coseismic tractions, inferred its rheological properties [e.g., Johnson et al., 2005; Perfettini and Avouac, 2007]. However, the latter modeling studies were restricted to planar faults with rate-state frictional rheologies, and used ad hoc, but physically based initial conditions — for example, both studies assume that the entire fault slips at the plate convergence rate just before an earthquake. Below, we show that this assumption is not true, especially within the “stress-shadow” regions surrounding the asperities. While Perfettini and Avouac [2007] assumed that fault behavior was partitioned between an upper seismogenic zone and a lower brittle creep zone, Johnson et al. [2005] allowed coseismic and post-seismic slip to occur along the entire modeled fault surface.

Using a Boundary Element Method (BEM) model, Bürgmann et al., [2005] tested the effect of stress-shadows from “pinned” asperities on horizontal velocity predictions for the subduction zone off Kamchatka for several asperity models. They assumed that all areas outside the asperities slip freely (i.e., with zero driving shear stress, which is unphysical), resulting in a stress-shadow that is primarily located up-dip from each asperity. Since they ignore fault friction, they cannot model slip evolution around the asperities over the seismic cycle — especially down-dip of, and laterally (along strike) from, the asperity. Recently, Hetland et al. [2010] and Hetland and Simons [2010] developed an internally consistent 3D mechanical model of stress-dependent interseismic creep along the megathrust, considering both frictional and viscous fault rheologies. The stresses in this model evolve as a consequence of long-term deformation of the system (“spin-up”), and are determined by cumulative slip on the fault over this evolutionary period. Further, their model allows localized regions (“asperities”) of the fault surface to only slip coseismically at pre-assigned rupture times, thus allowing them to model the known spatio-temporal distribution of large earthquakes (similar to Bürgmann et al., [2005]). Unlike Bürgmann et al., [2005], however, slip in the regions surrounding these asperities is controlled by the specific fault rheology being assumed. They used “toy”

models to show that asperities are surrounded by a “halo” of very low creep-rates (a “stress-shadow” effect) late in the seismic cycle, which can potentially result in a relatively smooth and long wavelength surface velocity field.

As described in detail in the previous chapter, we extend this approach to an arbitrary 3D fault surface experiencing an arbitrary sequence of ruptures. We apply this extended model to northern Japan, to investigate whether this “physical” smoothing preserves any signature of the original asperities, in comparison to the artificial smoothing produced by model regularization in inversions of interseismic geodetic data. Here, we test the hypothesis that on inferred asperities along the Japan Trench megathrust, mechanical coupling alone is sufficient to explain available geodetic observations or alternatively, that these data require additional regions on the megathrust to be coupled. Underlying our analysis is the assumption that known asperities persist across multiple earthquake cycles.

In the following sections, we briefly review the forward modeling approach (see Hetland et al. [2010] for details), discuss the criteria used to determine the extent and rupture interval of each asperity chosen, present model “spin-up” and “convergence”, and finally, present results of our hypothesis test. The results presented here are meant to demonstrate the applicability of our approach for simulating realistic 3D fault surfaces. More thorough parameter-space searches are planned to be carried out in the near future to refine the analysis presented here.

## 5.2 Summary of the forward modeling approach

As discussed in Chapter 4, Hetland et al. [2010] cast the relationship between slip-rate and fault tractions for various rheologies in the following dimensionless form:

$$\dot{s}' = f(\tau', \alpha') \quad (1)$$

where,  $\alpha'$  is a strength parameter that depends on the rheology. For linear viscous rheology,

$$\dot{s}' = f(\tau', \alpha') = \frac{\tau'}{\alpha'}. \quad (2)$$

Thus, late in the cycle, when most of the fault is slipping at the loading rate, the mean dimensionless shear tractions along the fault surface will equal the dimensionless strength parameter,  $\alpha'$ . In Chapter 4, we estimated a typical range of values for  $\alpha'$  as 0.1 to 10.

For rate-dependent rheology,

$$\dot{s}' = e^{(-\rho)} \sinh\left(\frac{\tau'}{\alpha'}\right) \quad (3)$$

where,  $\rho = f_0/(a-b)$ , and  $\alpha = (a-b)\sigma_0^*$ . For the results presented below, we assume a uniform  $\sigma_0^*$ . Hetland and Simons [2010] demonstrated that the effect of including variable normal tractions (that is, normal tractions due to the evolving slip distribution over the fault surface) was negligible, unless the static strength of the fault is assumed to be large (cf. Figure 3 of Hetland and Simons [2010]). Even in the case where the fault is statically strong, the effect of variable tractions is significant only updip of the asperity, far from typical geodetic observations. However, they consider an effective (or reference) stress,  $\sigma_0^*$ , that is much higher than the imposed coseismic traction perturbation. If  $\sigma_0^*$  is small, as is thought to be typical of most subduction zones (owing to pore-pressure effects [e.g., Kanamori, 1971; Hyndman and Wang, 1993]), then variable normal tractions will significantly influence slip-evolution over the fault surface. But their effect will be pronounced in the vicinity of the asperities and especially during the period immediately following a rupture.

From Equation 3 we can deduce that late in the cycle, when most of the fault is slipping at the loading rate, the mean dimensionless shear tractions along the fault surface will equal the product of  $\rho$  and the dimensionless strength parameter,  $\alpha'$  — that is,

$$\tau_{ss}' = \rho \alpha' \quad (4)$$

Plate loading and frictional stresses are then in equilibrium over most of the “active” fault surface (over which slip evolves), except around the regularly rupturing asperities. This

product is nothing but  $f_0\sigma_0^*/\tau_0$ , where the denominator is the characteristic rupture stress,  $\mu S_0/D_0$ , the mean frictional resistance over the fault surface (see Chapter 4). So,  $\alpha'$  determines the relative static strength of the fault surface relative to the induced coseismic stresses. In Chapter 4, we estimated a typical range of values for  $\rho \approx 10-100$ , and  $\alpha \approx 10^5-10^6$  Pa. Assuming the same values as before for the non-dimensionalization of stresses, and  $\mu \approx 10^{10}$  Pa,  $\alpha' \approx 0.01-0.1$ . At the lower end, we have a fault that is “weak” ( $f_0\sigma_0^* \ll \tau_0$ ) compared to the imposed coseismic tractions, and the model spins up quickly. On the other hand, a fault that is “strong” in comparison to the imposed coseismic tractions results in slow spin-up of fault tractions. For  $\alpha' \approx 1$ , and the fault strength is comparable to the imposed coseismic stress pulses. For realistic values of the “damping-parameter”,  $\rho$ , noted above, the effect of the first factor on the right hand side of equation (3) has only a minor influence on the evolution of post-seismic slip compared to that of the second factor. However, tractions late in the seismic cycle (i.e., when the mean fault slip-rate is close to the imposed plate velocity) are strongly dependent on both  $\rho$  and  $\alpha'$  (Equation 4, also see Figure 14 of Hetland et al. [2010]). Thus, changing these two parameters allows us to explore the effect of background stresses on slip-evolution over a spun-up seismic cycle.

In order to solve for slip evolution on the fault surface, the tractions,  $\tau'$ , everywhere on the fault surface at any given time have to be related to coseismic slip, the far-field plate loading rate, and any ongoing post-seismic slip along the fault itself. This is accomplished by a discretized traction evolution equation, that can be represented in indicial notation as,

$$\tau'_i = (s'_j - t'V'_j)K'_{ji} + \sum_a S'_{ja} K'_{ji} \quad (5)$$

where,  $K'_{ji}$  are the traction kernels (i.e., tractions at patch  $i$  due to slip on patch  $j$ ), and traction ( $\tau'$ ), and slip ( $s'$ ) vary both in space and in time. Also, as discussed extensively in Chapter 2, in order to be kinematically consistent, we use a backslip rate distribution that is everywhere tangential to the 3D fault surface (i.e., backslip with spatially varying rake; Figure 4-6). The first term in Equation 5 accounts for ongoing fault slip and continuous far-field plate loading, while the second term is the cumulative effect of

co-seismic slip ( $S'$ ) on all asperities. Due to the kinematic nature of the imposed ruptures, we cannot consistently model the effect of coseismic tractions due to the rupture of one asperity on subsequent coseismic slip on an adjacent asperity. A relationship similar to Equation 5 defines surface displacement evolution. Using indicial notation,

$$u'_k = (s'_j - t'V'_j)G'_{jk} + \sum_a S'_{ja} G'_{jk} \quad (5)$$

where,  $G'_{jk}$  are the surface displacement kernels (or Green's functions, i.e., displacements at observation station  $k$  due to slip on patch  $j$ ).

As discussed in Chapter 4, we use the triangular dislocation solutions [as compiled in Meade, 2007] to compute K and G for a spatially discretized 3D fault in a homogeneous Poisson half-space. The traction evolution Equation 5 is solved together with the appropriate constitutive relation (e.g., Equation 3), by marching in time using adaptive time-stepping. The time-step at any given time in such an adaptive scheme is controlled by the slip rate at that time, with larger slip rates resulting in smaller time-steps.

### 5.3 Asperity parameters for the Japan Trench megathrust

In this section, we discuss in detail the methodology used to estimate the location and extent of each inferred characteristic asperity on the Japan Trench megathrust surface, as well as its characteristic rupture interval. We are inherently assuming there is no variability between individual ruptures on each asperity (that is, the rupture sequence is both time- and slip-predictable), and therefore there is a characteristic rupture dimension, characteristic coseismic slip, and hence, a characteristic rupture interval. In determining these parameters, we try to honor, at a minimum, the latest significant ( $M_w > 7.5$ ) ruptures inferred to have occurred on these asperities during the past century. Depending on the characteristic rupture interval determined for each asperity, some of the previous ruptures may not occur exactly at the same time as historical events. However, usually, they occur within 5 years of their actual date – the effect of such small shifts in earlier ruptures was

not found to have a significant impact on surface displacement predictions, especially because of the much stronger influence of the more recent event. We proceed from the southernmost asperity of our modeling domain (Fukushima) to the northernmost (Nemuro). A summary of estimated parameters is presented in Table 5-1.

### 5.3.1 *Fukuyshima-oki — ruptures of 1938*

In the megathrust interface off Fukushima, three large events -  $M_w$ 7.4 (May, 1938),  $M_w$  7.7 and  $M_w$  7.8 (both in Nov 1938) — occurred in close succession. On the scale of simulating an whole seismic cycle ( $\sim 100$  yrs), the moment release from these three events can be considered “instantaneous”. So, combining the moment release from these three events (estimated from long-period surface waves [Abe, 1977]) yields a moment,  $M_0$ , of  $1.6 \times 10^{21}$  N.m, equivalent to a moment-magnitude,  $M_w$ , of 8.1. Using only the locally high-slip patches, Abe [1977] estimated stress-drop,  $\Delta\sigma$ , to be in the range  $\sim 2.8$ – $5.6$  MPa. However, if we assume an equivalent single characteristic elliptical asperity (assuming for purposes of mesh-quality, an aspect-ratio,  $f = (r_{min}/r_{maj}) = 0.8$ ), with  $\Delta\sigma_{mean} \sim 1$  MPa (10 bar), then the characteristic semi-major axis dimension can be estimated as:

$$r_{maj} = \Theta(1) \cdot \left( \frac{M_0}{f \Delta\sigma} \right)^{\frac{1}{3}} \approx 1.26 \times 10^5 \text{ m} = 126 \text{ km} \quad (6)$$

resulting in a characteristic asperity area ( $= \pi r_{maj} r_{min} = \pi f r_{maj}^2$ )  $\sim 4 \times 10^4 \text{ km}^2$ . In comparison, Abe [1977] estimated the combined total area for these three events (based on first-motion data) to be  $\sim 1.5 \times 10^4 \text{ km}^2$ . However, the corresponding rupture interval turns out to be:

$$\Delta T_R = \left( \frac{M_0}{\mu \pi f (r_{maj})^2 V_p} \right) \approx 16 \text{ yrs (!)} \quad (7)$$

because we are assuming the same characteristic slip for every rupture event on this asperity. Since there hasn't been a  $M_w > 7$  earthquake off Fukushima since 1938, we assume a recurrence interval of  $\sim 75$  yrs for a characteristic earthquake similar to the value assumed for the Tokachi-Oki region [Yamanaka and Kikuchi, 2003]. With this assumption, the characteristic semi-major axis dimension becomes:

$$r_{maj} = \left( \frac{M_0}{\mu \pi f V_P (\Delta T_R)} \right)^{\frac{1}{2}} \approx 6 \times 10^4 \text{ m} = 60 \text{ km} \quad (8)$$

implying a stress drop of:

$$\Delta \sigma = \Theta(1) \cdot \left( \frac{M_0}{f (r_{maj})^3} \right) \approx 1.0 \times 10^7 \text{ Pa} = 10 \text{ MPa}, \quad (9)$$

which is at the upper-bound of observed seismic stress-drops [Kanamori and Anderson, 1975]. To get a feel for the sensitivity of the above estimates to the exact value of the plate velocity vector (which has been assumed to be between 8 and 9 cm/yr by different researchers), we find that:

$$\frac{\partial r_{maj}}{\partial V_P} = -\frac{1}{2V_P} \left( \frac{M_0}{\mu \pi f V_P \Delta T_R} \right)^{\frac{1}{2}} = -\frac{r_{maj}}{2V_P} \Rightarrow \frac{\Delta r_{maj}}{r_{maj}} = -\frac{\Delta V_P}{2V_P} \quad (10)$$

and,

$$\frac{\partial r_{maj}}{\partial (\Delta \sigma)} = -\frac{1}{3(\Delta \sigma)} \left( \frac{M_0}{f \Delta \sigma} \right)^{\frac{1}{3}} = -\frac{r_{maj}}{3(\Delta \sigma)} \Rightarrow \frac{\Delta r_{maj}}{r_{maj}} = -\frac{\Delta (\Delta \sigma)}{3(\Delta \sigma)} \quad (11)$$

so, for a  $\sim 10\%$  larger  $V_P$  (9.2 cm/yr),  $r_{maj}$  will be 5% (or  $\sim 3$  km) smaller, slip 10% (or  $\sim 0.6$  m) larger, and stress-drop, 15% (1.5 MPa) higher.

### 5.3.2 Miyagi-oki — ruptures of 1936, 1978, and 2005

Umino et al. [2006] infer that three ruptures on this asperity that occurred in the mid 1930s — in 1933, 1936, and 1937 (with a combined moment release of  $2.6 \times 10^{20}$  N.m, equivalent to  $M_w 7.5$ ) overlapped with the western, central and eastern portions of the  $M_w 7.5$  1978 rupture area, but with a moment of only a third of the latter event [Tanioka, 2003b]. The 2005 rupture also partially overlapped with the updip (southeastern) portion of the 1978 rupture area [Miura et al., 2006]. We assume the 1978  $M_w 7.4-7.5$  event as the characteristic earthquake for this region ( $M_0 = 1.7-3 \times 10^{20}$  N.m estimated from tsunami data [Tanioka, 2003b], and long-period surface waves [Seno et al., 1980]). The stress drop,  $\Delta \sigma$ , based on localized high-slip patches was estimated to be 10 - 15 MPa. As before, assuming a characteristic elliptical asperity having a mean stress drop,  $\Delta \sigma_{mean} \sim 1$  MPa, the semi-major asperity dimension is:

$$r_{maj} = \Theta(1) \cdot \left( \frac{M_0}{f \Delta \sigma} \right)^{\frac{1}{3}} \approx 7 \times 10^4 m = 70 km \quad (12)$$

resulting in a recurrence interval for the characteristic earthquake

$$\Delta T_R = \left( \frac{M_0}{\mu \pi f (r_{maj})^2 V_P} \right) \approx 9 yrs (!) \quad (13)$$

Since the next major event after the 1933–37 sequence did not occur until the 1978 event, we estimate a semi-major asperity dimension, instead, assuming a rupture interval of ~40 years (the 2005 event may be consistent with the 1933–37 sequence in that it ruptured only one part of the characteristic asperity, and subsequent events may follow to rupture the rest of the characteristic asperity) to be

$$r_{maj} = \left( \frac{M_0}{\mu \pi f V_P (\Delta T_R)} \right)^{\frac{1}{2}} \approx 3.5 \times 10^4 m = 35 km \quad (14)$$

implying a mean stress drop

$$\Delta \sigma = \Theta(1) \cdot \left( \frac{M_0}{f (r_{maj})^3} \right) \approx 9 \times 10^6 Pa = 9 MPa, \quad (15)$$

which is, again, near the upper-bound of observed seismic stress-drops [Kanamori and Anderson, 1975]. Another way to estimate the characteristic asperity dimension in this case is by assuming that the mean stress-drops and asperity shapes in the 2005 and 1978 events are similar. In this case, an estimate can be made of the 1978 (characteristic) asperity size relative to the well-determined asperity size for the 2005  $M_w 7.2$  event ( $M_0 = 1.7 \cdot 7 \times 10^{19}$  N.m estimated from GPS and seismic data [Miura et al., 2006]):

$$\begin{aligned} \Delta \sigma_{1978} = \Delta \sigma_{2005} &= \Theta(1) \cdot \left( \frac{M_0^{(1978)}}{f (r_{maj,1978})^3} \right) = \Theta(1) \cdot \left( \frac{M_0^{(2005)}}{f (r_{maj,2005})^3} \right) \\ \Rightarrow r_{maj,1978} &= r_{maj,2005} \left( \frac{M_0^{(1978)}}{M_0^{(2005)}} \right)^{\frac{1}{3}} \approx 35 km \end{aligned} \quad (16)$$

which agrees almost exactly with that from the assumed recurrence interval.

### 5.3.3 Sanriku-oki — ruptures of 1931, 1968, and 1994

The 1994  $M_w 7.8$  event off Sanriku ( $M_0 = 3 \cdot 4 \times 10^{20}$  N.m) [Nishimura et al., 1996; Tanioka et al., 1996; Nakayama and Takeo, 1997] coincided with the shallow portion of the 1968

$M_w$ 8.2 event (based on source inversion for the former event using strong-motion [Nakayama and Takeo, 1997], and broad-band [Nishimura et al., 1996] data; and for the 1968 event, using P-wave first motions as well as long-period surface waves [Kanamori, 1971]). We consider only the 1994 even rupture area as the characteristic asperity because the deeper part of the 1968 event may not even be on the subduction megathrust (based on focal mechanisms — Hiroo Kanamori, personal communication). Again, if we assume a characteristic elliptical asperity having a mean stress drop,  $\Delta\sigma_{mean} \sim 1$  MPa, the maximum semi-major asperity dimension is

$$r_{maj} = \Theta(1) \cdot \left( \frac{M_0}{f\Delta\sigma} \right)^{\frac{1}{3}} \approx 8 \times 10^4 \text{ m} = 80 \text{ km} \quad (17)$$

with an estimated recurrence interval for the characteristic earthquake as,

$$\Delta T_R = \left( \frac{M_0}{\mu\pi f (r_{maj})^2 V_P} \right) \approx 12 \text{ yrs (!)} \quad (18)$$

Again, since the next “major” rupture after the 1968 one was not until 1994, we instead estimate a semi-major asperity dimension assuming a rupture interval of  $\sim 30$  years (approximate mean value of rupture intervals between 1931, 1968, and 1994 events):

$$r_{maj} = \left( \frac{M_0}{\mu\pi f V_P (\Delta T_R)} \right)^{\frac{1}{2}} \approx 4.5 \times 10^4 \text{ m} = 45 \text{ km} \quad (19)$$

implying a mean stress drop of

$$\Delta\sigma = \Theta(1) \cdot \left( \frac{M_0}{f (r_{maj})^3} \right) \approx 5 \times 10^6 \text{ Pa} = 5 \text{ MPa}, \quad (20)$$

in the middle of the range of observed seismic stress-drops [Kanamori and Anderson, 1975].

### 5.3.4 Tokachi-oki — ruptures of 1952 and 2003

The 2003 rupture off Tokachi was determined to be either slightly smaller than the 1952 event ( $M_w$ 8.0, from tsunami waveform modeling [Satake et al., 2006], and re-estimation of 1952 aftershock pattern [Hamada and Suzuki, 2004]), or roughly equal in size to the 1952 rupture ( $M_w$ 8.2, from broad-band SH & long-period mantle phases [Robinson and Cheung, 2003], as well as joint inversion using strong-motion and GPS [Koketsu et

al., 2004]), with nearly coincident rupture areas. Using the better constrained and more recent estimates, the characteristic moment release,  $M_0$ , for Tokachi-Oki is  $\sim 2 \times 10^{21}$  N.m. Robinson and Cheung [2003] estimated stress drop,  $\Delta\sigma$ , between 10–25 MPa, using localized high-slip regions, but a mean stress-drop,  $\Delta\sigma_{mean} \sim 0.5$  MPa. They also estimated the mean slip to be  $\sim 2.2$  m. If we assume that the 1952 and 2003 events ruptured the same characteristic elliptical asperity having a mean stress drop,  $\Delta\sigma_{mean} = 1$  MPa (10 bar), then the semi-major asperity dimension is

$$r_{maj} = \Theta(1) \cdot \left( \frac{M_0}{f \Delta\sigma} \right)^{\frac{1}{3}} \approx 1.4 \times 10^5 \text{ m} = 140 \text{ km} \quad (21)$$

resulting in a characteristic earthquake recurrence interval of

$$\Delta T_R = \left( \frac{M_0}{\mu \pi^2 (r_{maj})^2 V_P} \right) = \left( \frac{2 \times 10^{21}}{(3 \times 10^{10})(0.8\pi)(1.36 \times 10^5)^2 (8.3 \times 10^{-2})} \right) \approx 17 \text{ yrs (!)} \quad (22)$$

Therefore, we assume that the 2003 event is the characteristic repeat event of the 1952 event, for a rupture interval of  $\sim 50$  years, implying a characteristic semi-major asperity dimension

$$r_{maj} = \left( \frac{M_0}{\mu \pi^2 V_P (\Delta T_R)} \right)^{\frac{1}{2}} = \left( \frac{2 \times 10^{21}}{(3 \times 10^{10})(0.8\pi)(8.3 \times 10^{-2})(50)} \right)^{\frac{1}{2}} \approx 8 \times 10^4 \text{ m} = 80 \text{ km} \quad (23)$$

resulting in a mean stress drop of

$$\Delta\sigma = \Theta(1) \cdot \left( \frac{M_0}{f (r_{maj})^3} \right) \approx 5 \times 10^6 \text{ Pa} = 5 \text{ MPa}, \quad (24)$$

which is within the observed range of seismic stress-drops [Kanamori and Anderson, 1975]. Again, as with the Miyagi-oki asperity, if we assume that the mean stress-drops and asperity shapes in the 2003 and 1952 events are similar, then the last equation can be used to compute yet another estimate of the characteristic semi-major asperity dimension relative to the well determined coseismic asperity for the 2003 event:

$$\begin{aligned} \Delta\sigma_{1952} = \Delta\sigma_{2003} &= \Theta(1) \cdot \left( \frac{M_0^{(1952)}}{f (r_{maj,1952})^3} \right) = \Theta(1) \cdot \left( \frac{M_0^{(2003)}}{f (r_{maj,2003})^3} \right) \\ \Rightarrow r_{maj,1952} &= r_{maj,2003} \left( \frac{M_0^{(1952)}}{M_0^{(2003)}} \right)^{\frac{1}{3}} \approx 75 \text{ km} \end{aligned} \quad (25)$$

which agrees well with that estimated from the assumed recurrence interval. The along-strike dimension of the asperity,  $D (=2 \times r_{maj})$ , of  $\sim 150$  km, also agrees well with the width between two subduction zone geologic features that seem to bound this rupture

area: Koshiro canyon to the east, and the plate bend with deepening of continental shelf to the west [Hamada and Suzuki, 2004].

### 5.3.5 Nemuro-oki — rupture of 1973

Great earthquakes occurred off Nemuro in 1894 and 1973, but the latter event is estimated to have been much smaller than the 1894 event. It is conjectured that the 1894 event ruptured the source areas of both the 1973 Nemuro-oki and 1952 Tokachi-oki events [Tanioka, 2003a]. The 1973 event has been estimated to be between  $M_w7.8$  [Tanioka, 2003a] (from tsunami waveforms, with  $M_0 \sim 5 \times 10^{20}$  N.m), and  $M_w7.9$  [Shimazaki, 1974] ( $M_0 \sim 6.7 \times 10^{20}$  N.m). We adopt the more recent estimate from Tanioka [2003a], who estimated mean fault slip to be  $\sim 2$  m. In contrast, Shimazaki [1974] estimated a slip of 1.6 m, and mean stress drop of 35 bars (3.5 MPa). As before, assuming a characteristic elliptical asperity having a mean stress drop,  $\Delta\sigma_{mean} \sim 1$  MPa, the semi-major asperity dimension is

$$r_{maj} = \Theta(1) \cdot \left( \frac{M_0}{f\Delta\sigma} \right)^{\frac{1}{3}} \approx 8.5 \times 10^4 \text{ m} = 85 \text{ km} \quad (26)$$

implying a recurrence interval for the characteristic earthquake of,

$$\Delta T_R = \left( \frac{M_0}{\mu\pi f (r_{maj})^2 V_P} \right) \approx 11 \text{ yrs (!)} \quad (27)$$

So, we instead assume a recurrence interval of  $\sim 75$  yrs for a characteristic earthquake as in the Tokachi-Oki region [Yamanaka and Kikuchi, 2003] (which is not unreasonable, given that the 1894 event must have completely ruptured the 1973 asperity), obtaining a semi-major asperity dimension of

$$r_{maj} = \left( \frac{M_0}{\mu\pi f V_P (\Delta T_R)} \right)^{\frac{1}{3}} \approx 3 \times 10^4 \text{ m} = 30 \text{ km} \quad (28)$$

implying a mean stress drop of

$$\Delta\sigma = \Theta(1) \cdot \left( \frac{M_0}{f (r_{maj})^3} \right) \approx 2 \times 10^7 \text{ Pa} \approx 20 \text{ MPa}, \quad (29)$$

which is beyond the upper bound for the range of observed seismic stress-drops [Kanamori and Anderson, 1975]. However, given there hasn't been a rupture off Nemuro

since 1973, if we assume a characteristic rupture interval of  $\sim 40$  years (similar to the Miyagi-oki region adjacent to the Fukushima asperity), we obtain a semi-major asperity dimension of

$$r_{maj} = \left( \frac{M_0}{\mu \pi V_P (\Delta T_R)} \right)^{\frac{1}{2}} \approx 4.5 \times 10^4 \text{ m} = 45 \text{ km} \quad (30)$$

This latter estimate of  $r_{maj}$  implies a mean stress drop of:

$$\Delta \sigma = \Theta(1) \cdot \left( \frac{M_0}{f (r_{maj})^3} \right) \approx 7 \times 10^6 \text{ Pa} = 7 \text{ MPa}, \quad (31)$$

which is within the range of observed seismic stress-drops [Kanamori and Anderson, 1975].

### 5.3.6 Summary

A summary of the final asperity parameters chosen for the northern Japan megathrust is presented in Table 5-1, and the resulting asperity configuration is illustrated in Figure 5-1.

**Table 5-1.** Summary of asperity parameters for Northern Japan. The last column represents the time from the present (here, the year 2000, which marks the end of the time-period over which the observed GPS velocities were computed in Hashimoto et al. [2009]) to the most recent earthquake for each asperity.

Region	$D$ (km)	$f (=r_{min}/r_{max})$ (non-dim)	$s_0^*$ (m)	$\Delta T_R^1$ (yr)	$\Delta \sigma_{mean}^{2,3}$ (MPa)	$T_R$ [yrs(date)]
Fukushima-oki	120	0.8	6.4	75	10	62 (1938)
Miyagi-oki	70	0.8	3.3	40	9	22 (1978)
Sanriku-oki	90	0.8	2.5	30	5	6 (1994)
Tokachi-oki	160	0.8	4.2	50	5	48 (1952)
Nemuro-oki	90	0.8	3.3	40	7	27 (1973)

\*  $V_P = 8.3 \times 10^{-2}$  m/yr;

<sup>1</sup>  $\Delta T_R \propto (1/A) \propto (1/r^2)$

<sup>2</sup>  $\Delta \sigma \propto s_0 = V_P \times \Delta T_R$

<sup>3</sup>  $\Delta \sigma \propto (1/AD) \propto (1/r^3)$ , and,  $\Delta \sigma \propto (\Delta T_R)^{1.5}$

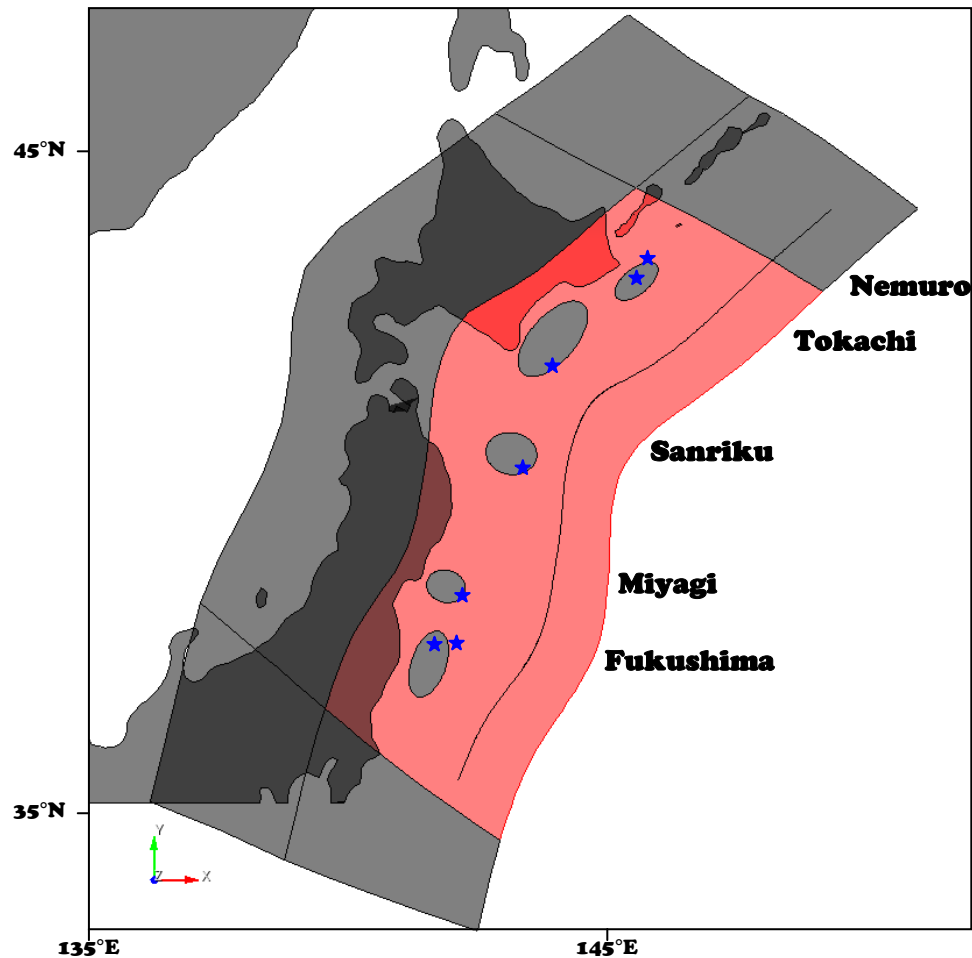


**Figure 5-1.** Asperity configuration chosen for the northern Japan megathrust interface, and the epicentral locations of the last earthquake(s) prior to the year 2000 (blue stars, multiple around an asperity start indicate two ruptures within the same year).

#### 5.4 Simulating rupture-sequences for the northern Japan asperity configuration

In section 4.7, we briefly mentioned the hierarchy of basic, but general benchmark tests done to test the physicality of our simulations. Here, we discuss the issue of numerical convergence specifically for the Japanese megathrust problem, and then explore the analysis of model spin-up for the full five-asperity problem. The first tests with any model were carried out with a linear viscous fault rheology (even if it may not be a realistic rheology for modeling slip evolution on fault surfaces). Since the strain-rate and stress are linearly dependent, this rheology is more straightforward for testing model behavior (benchmarking, convergence, spin-up), and for developing some intuition about

the interaction between asperities and their relationship to the predicted surface velocity field.

#### ***5.4.1 Model Convergence for the Japan megathrust interface***

An important issue for determining the accuracy of model predictions is whether the coseismic signal is accurately resolved by a given mesh resolution. From the meshing convention described in Chapter 4, a higher resolution mesh has essentially the same number of elements as the coarse mesh outside the asperity transition zone, but may have significantly more elements within this transition zone. The goal of such refinement was to better resolve the coseismic tractions that drive fault slip, which ultimately determines the predicted surface velocities. However, increasing the mesh resolution beyond a certain point does not significantly improve the spun-up fault tractions.

Exact convergence tests for the full five-asperity problem (JT5, of Section 4.7) will be carried out in the near future. Such tests are time-consuming, especially for the JT5 problem with frictional rheologies. During the hierarchical tests mentioned in Section 4.7, we found that even though frictional faults were spun-up in fewer rupture-cycles than linear viscous faults, each cycle had a lot more time-steps owing to the exponential dependence of strain-rates on imposed coseismic stresses. However, such tests are worth the “cost” because they allow us to test whether further mesh resolution improvement (which could be still more expensive computationally) is necessary.

Here, we present the results from such test for the two-asperity case (JT2, of Section 4.7, containing only the Miyagi & Sanriku asperities). Since the strategy used in both cases is identical, as long as the kernels are computed from nearly identical sources around two common asperities in both models (i.e., having roughly the same element size, or resolution, in the transition zone), it is reasonable to qualitatively extrapolate convergence of spun-up solutions for the JT2 mesh to the JT5 mesh. Such extrapolation through intuition can be helpful in figuring out whether the time spent generating the

mesh, computing kernels, and subsequent iterations for smoothing (discussed in Chapter 4) would be worth it.

Figure 5-2 shows the spun-up tractions for a benchmark linear-viscous run for three different transition zone mesh resolutions for JT2. The number of elements in the asperity transition zone increases threefold between “RES1” (blue) and “RES2” (red) runs, but the spun-up solution appears to have “converged”, because no significant improvement is seen for the added cost of a high-resolution mesh – especially late in each rupture cycle (i.e., just before each rupture). So, compared to the lowest resolution JT5 mesh, the next level (“RES1”, with nearly 6000 fault patches) can be expected to improve our solution, but the next higher resolution (“RES2”, with nearly 9700 fault patches) may not be worth its significantly larger computational time relative to the improvement in the solution. But it is perhaps good practice to compute the “RES2” solution for one case, and if significant improvement is not seen, then ignore this resolution for the rest of the suite of runs. Further, the surface displacement field is much smoother (i.e., of longer wavelength) than the stress-perturbation on the fault surface, and therefore affected much less by the small improvement in tractions from “RES1” to “RES2”.

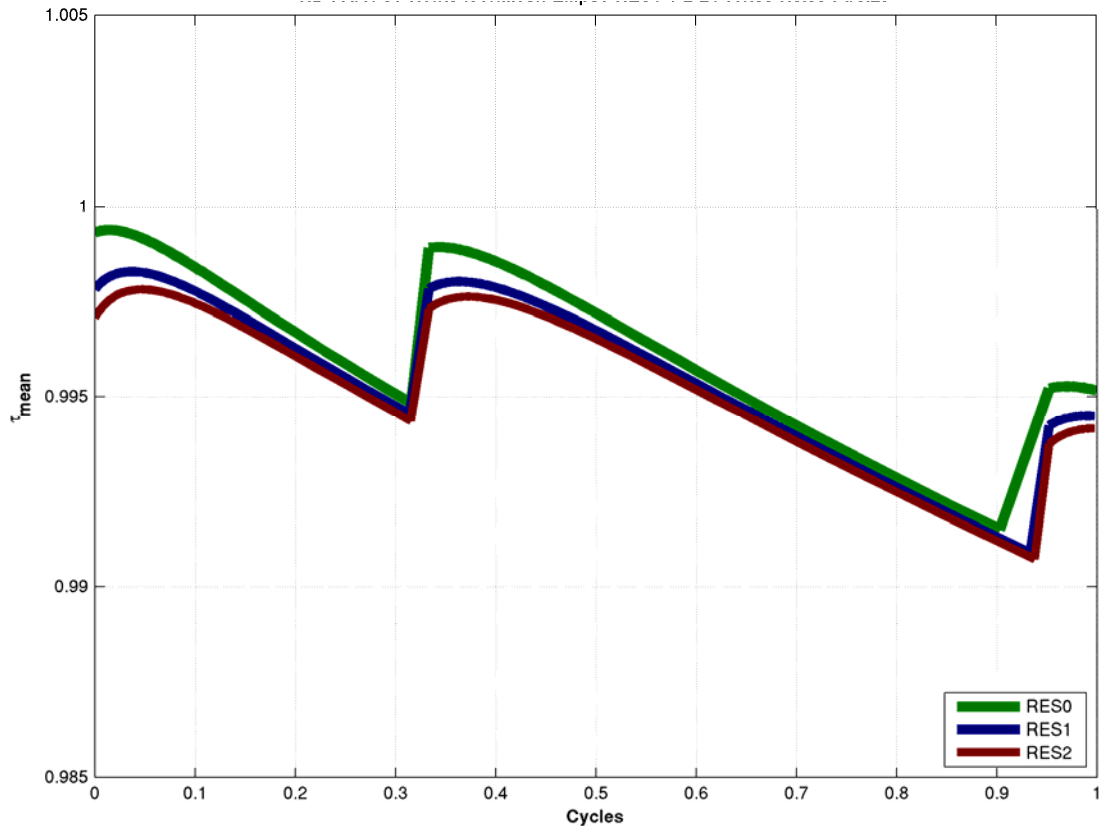


**Figure 5-2.** Convergence of spun-up fault tractions over a full cycle with increasing mesh resolution (RES0 through RES2) around the asperity, for a JT2 mesh (see Section 4.7). Significant improvement is not observed between RES1 and RES2, even though the latter has three-times as many elements in the asperity transition zone compared to the former.

#### 5.4.2 Model spin-up using a synthetic rupture catalog

In order to simulate the multi-asperity problem, we need to start with a realistic catalog of ruptures for spin-up. To build the catalog, we first set the end-time for each asperity's rupture sequence as the time of the most recent rupture on that asperity. We then compute a series of "past" ruptures for each asperity, going backward in time for a sufficiently large number of ruptures. We thus build a synthetic rupture "catalog" that includes all past rupture times for each asperity. We reset the simulation start time to the beginning of the oldest complete characteristic rupture sequence - a sequence consisting of ruptures on all five asperities, in the order of their most recent ruptures - in this catalog. Irrespective of the starting time-shifts,  $T_R$  (Table 5-1), as long as the

characteristic rupture interval,  $\Delta T_R$  for each asperity is fixed, the order of asperity ruptures will be identical after a time,  $T_{CRS}$ , arithmetically equal to the least common multiple of all asperity rupture intervals,  $\Delta T_R$ . For the rupture intervals estimated here (Table 5-1),  $T_{CRS}$  is 600 years. If one of the rupture intervals were off by even one year,  $T_{CRS}$  would be much longer. Here, to avoid unnecessarily extending simulation time, we rounded rupture intervals to the nearest 5 years. So,  $T_{CRS}$  is very sensitive to the actual rupture intervals chosen, which depend not only on the exact asperity size, but also on the mesh resolution used. Therefore,  $T_{CRS}$  does not have any physical meaning. But as shown below, it is a convenient measure for following the evolution of model tractions, once a set of rupture-intervals are chosen for a given asperity configuration, and mesh resolution.

We start each model with zero initial tractions. Although the existing Matlab forward model *EvolveSlip*, has the option to prescribe a pre-stress, for the initial runs at least, we do not specify a pre-stress. Traction induced on the fault surface by repeated asperity ruptures as well as continuous far-field loading by the semi-infinite extensions of the fault (equivalent to backslip) eventually reach an equilibrium value determined by the fault rheology. The time taken to reach equilibrium depends on the dynamic “strength” of the fault, as discussed in Section 5.2. For a given rheology, this steady state traction is that which is required to maintain the relative motion between the hanging- and foot-walls at the loading rate,  $V_0$ . We call this evolution of fault tractions from their initial value to a final steady state, the “spin-up” of fault tractions. Once steady state is attained, the mean value of fault tractions as well as that of the surface displacement field do not change over a time scale equal to that for the characteristic rupture sequence,  $T_{CRS}$ .

Since  $T_{CRS}$  does not have a physical basis and can be a very large number, a practical choice for the reference time-scale,  $T_0$ , over which to compute the evolution of mean tractions is the largest rupture interval of all asperities (75 years, here). Because of ongoing slip associated with ruptures, the mean tractions over the fault surface fluctuate significantly over a single cycle (Figure 5-3). So, we take moving averages of the mean traction vector over time-windows that are multiples of this reference time,  $n.T_0$  (with  $n=$

1, 2, ...). As this averaging time-window gets larger, the moving average of mean tractions gets smoother, and it becomes easier to measure model spin-up. From Figure 5-3, the smallest window for which the spun-up tractions are stable corresponds to the  $T_{CRS}$  (or, cycle =  $T_{CRS}/T_0 = 600/75=8$ ). This is not a surprising result, since  $T_{CRS}$  is an inherent numerical feature of the set of rupture intervals chosen for the simulation. So, in order to measure spin-up, a simulation must be run for the duration of at least  $T_{CRS}$ . The minimum spin-up time estimated for a low-resolution run can be used to significantly reduce computation time for higher resolution runs.

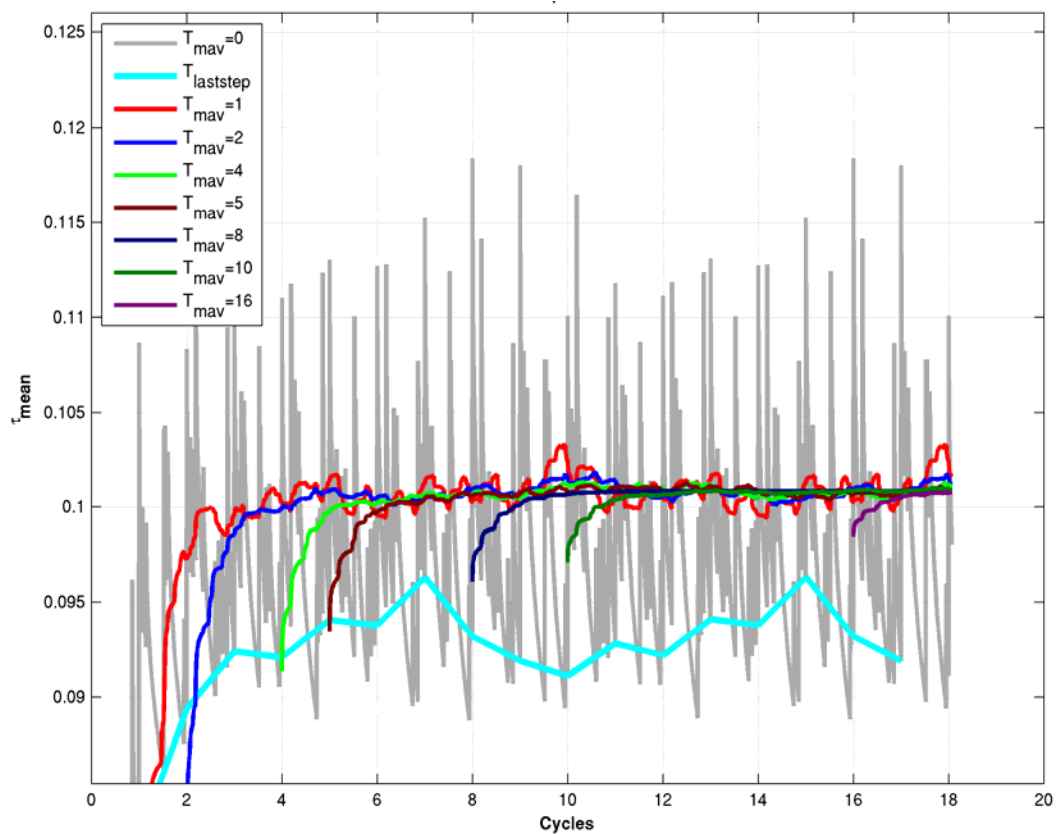


**Figure 5-3.** Spin-up of mean fault tractions, and their moving averages for a linear viscous fault rheology with  $\alpha'=0.1$ . The gray curve represents the mean tractions at every time-step. The light blue curve at the bottom represents a single pick of the grey curve at the end of each cycle of duration equal to the reference time,  $T_0$ . The moving average window,  $T_{mav} = 8$  (dark blue) corresponds to  $T_{CRS}$ . See text for details.

Once the model is spun up, the cumulative slip on the fault surface over the duration of the reference cycle,  $T_0$  (right panels of Figure 5-4), must look identical to the applied variable-rake backslip on the fault surface (Figure 4-6), except for the asperities

themselves, which are in different stages of their cycle. All asperities catch up with the rest of the fault only at the end of a  $T_{CRS}$ -cycle. At the end of a  $T_{CRS}$ -cycle, there should be no difference (except for a scaling factor equal to  $T_{CRS}$ ) between cumulative slip and applied backslip. The use of VTK for visualization allows on the fly spin-up checks such as these to be performed routinely. The dip-slip (top row of Figure 5-4) and strike-slip (bottom row of Figure 5-4) components are visualized separately in order to make sure that any slip-partitioning is being correctly applied. In the left panels of Figure 5-4 displaying slip-rates, the regions of nearly zero-rates surrounding the asperities are the “stress-shadow” zones, which travel passively with the downgoing plate, but are no longer stressed (until the subsequent rupture). The surface velocities on the other hand depend only on the amount of the fault surface that is (nearly) not slipping. Therefore, the larger these stress-shadow zones, the larger, the “apparent locked zone”, and larger the corresponding surface velocities. We would expect dynamically weak rheologies to be able to propagate slip farther over each cycle, thereby producing larger apparently “locked” zones, and thus, larger surface velocities late in the cycle.

Once a model is spun up, the reference cycle of duration  $T_0$  immediately following the last complete  $T_{CRS}$ -cycle contains the “most recent” characteristic rupture sequence (here, the 75 years starting from the oldest rupture in the sequence: Fukushima in 1938). The surface displacement field is extracted over the duration of this most recent rupture sequence, and synthetic surface velocities are estimated over the same time-window as that for the observed GPS velocities.

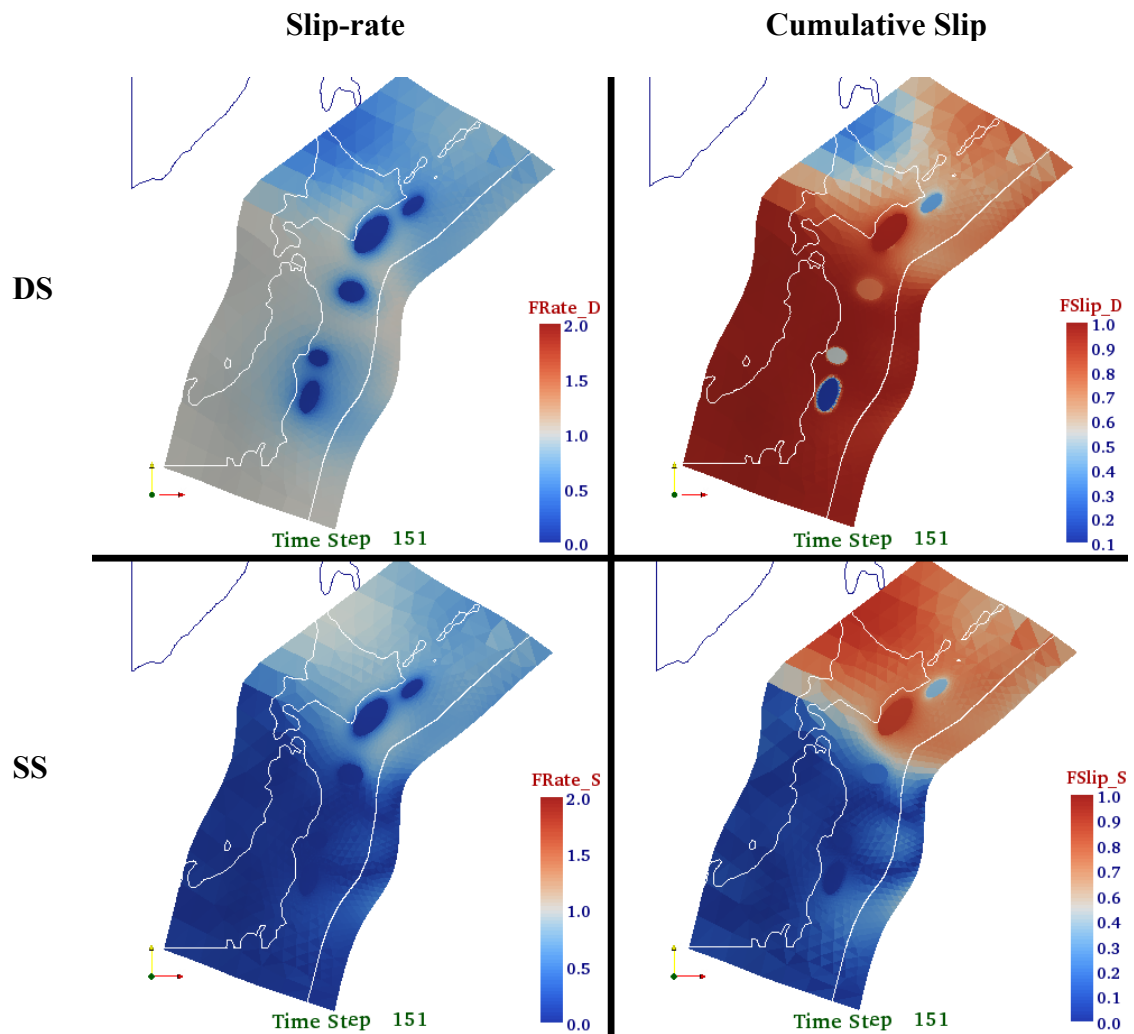


**Figure 5-4.** Plot of slip-rate (left column) and cumulative fault slip (right-column) at the end of the first reference cycle ( $T_\theta$ ), post model spin-up, for the linear viscous rheology used in Figure 5-3. Top rows show the strike-slip component, bottom rows show the dip-slip component. As expected, the right column looks nearly identical to the input backslip velocities (Figure 4-6), except for the asperities themselves, which will match the surrounding fault only at the end of the  $T_{CRS}$ -cycle. See text for details.

## 5.5 Station velocity predictions for northern Japan using a realistic fault rheology

In this section, we demonstrate the methodology discussed in the past couple of chapters by using it to predict synthetic station velocities using realistic rate strengthening frictional rheology parameters inferred for the northern Japan megathrust interface.

Several recent studies inverted post-seismic surface displacements to infer rate-dependent

or rate-state friction parameters for faults in California and Japan [e.g., Johnson *et al.*, 2005; Perfettini and Avouac, 2007; Fukuda *et al.*, 2009]. These studies have inferred that faults seem to be dynamically weak (i.e., low values for the strength parameter,  $\alpha = (a-b)\sigma_0^*$ , of 0.1 to 0.5 MPa). So, for our demonstration run, we pick  $\alpha \approx 0.1$  MPa, and  $\rho \approx 10$ , which yields a dimensionless strength parameter,  $\alpha' \approx 1$  (see section 5.2). Model tractions are mostly spun-up in just over three  $T_{CRS}$  cycles (or 25 reference cycles, Figure 5-5). Note that equilibrium dimensionless stress is ten times larger than for the linear-viscous benchmark presented above (Figure 5-3), while the stress pulses induced by ruptures remains the same as in that case. Therefore, it is hard to see the individual ruptures at the scale of the full convergence test. While the expected steady state tractions are 1.0, the model apparently spins up to a value about 20% higher, which implies that frictional stresses are larger than that expected for the imposed coseismic stresses. The reason for a higher value has to do with which asperity was chosen for the reference asperity dimension,  $D_0$ . This reference dimension not only controls the non-dimensionalization of the mesh (so, larger  $D_0$  implies a smaller non-dimensional mesh domain), but also that of tractions (since  $\tau_0 = \mu S_0/D_0$ ). The dimensionless result presented in Section 5-2 assumes a single characteristic asperity dimension, whereas here we have multiple asperities having a range of sizes.

For the simulation shown below, we picked a single asperity (Fukushima, which is also the second biggest; Figure 5-1) to be the reference for both rupture interval as well as asperity dimension, to be consistent. However, had we chosen the mean asperity size, then  $\tau_0$  would be larger (that is, larger non-dimensional induced stress field), and hence, smaller value of the mean steady state tractions,  $\tau_{mean}$ . In fact a taking the ratio of these two sizes ( $R_{Fukushima}/R_{mean} \approx 1.2$ ), is roughly equal to the observed discrepancy. The resulting stress pulses (Figure 5-6), would be steeper, and hence decay slightly faster, resulting in slightly smaller surface velocity predictions late in the cycle. So, when multiple asperities are present, choosing a single characteristic asperity may be a challenge, especially when the largest asperity may not necessarily rupture with the largest rupture interval, as is the case here.

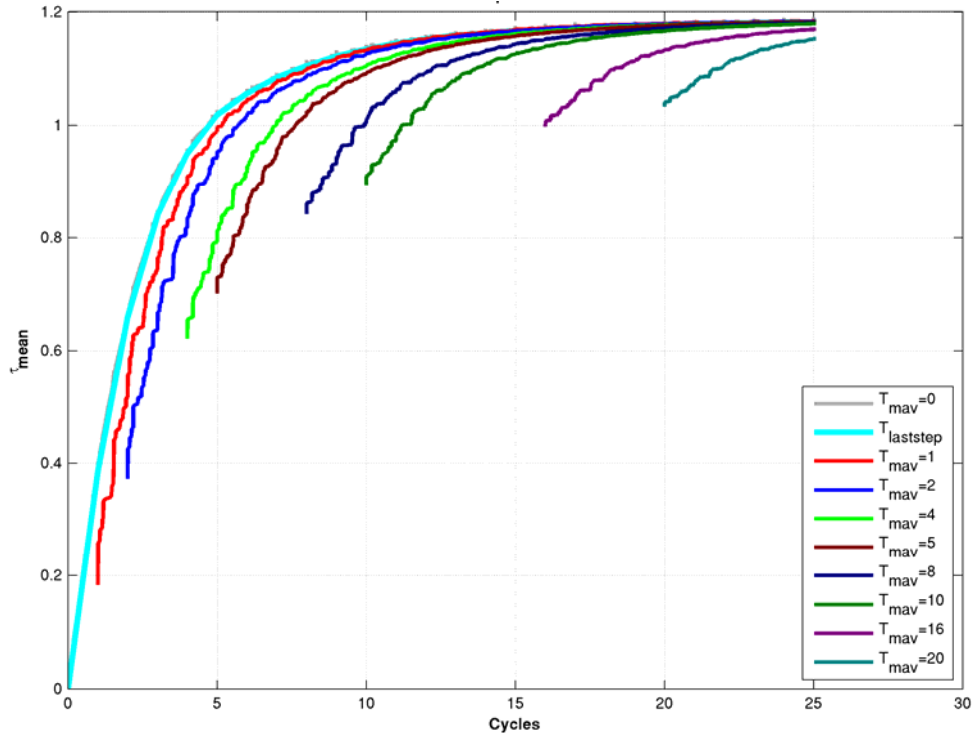


**Figure 5-5.** Spin-up tractions for northern Japan megathrust, for a rate-strengthening frictional rheology, with  $\rho \approx 10$ , and  $\alpha \approx 10^5$  Pa ( $\alpha' \approx 1$ )

The stress change over the 75-year reference cycle right after the third  $T_{CRS}$  cycle — simulating the past 75 years of asperity ruptures — shows the rapid evolution of stress early in the cycle, that is characteristic of frictional rheologies (Figure 5-6). Only the most recent events that occurred prior to the observed GPS velocity estimation window (1996–2000) are labeled for each asperity. The unlabeled stress spike in the middle of that figure is equivalent to the shallow portion of the 1968 Sanriku-oki event, while the last stress spike is equivalent to the 2003 Tokachi-oki event. It is worth noting that the modeled Sanriku-oki event is roughly four years early, because of our assumption regarding the mean rupture interval time. However, our simulations indicate that the 1968 Sanriku-oki event is far enough removed from the GPS velocity window that this slight rupture time-shift may not have a significant impact on velocity predictions, given the same asperity experienced the most recent of these large earthquakes.

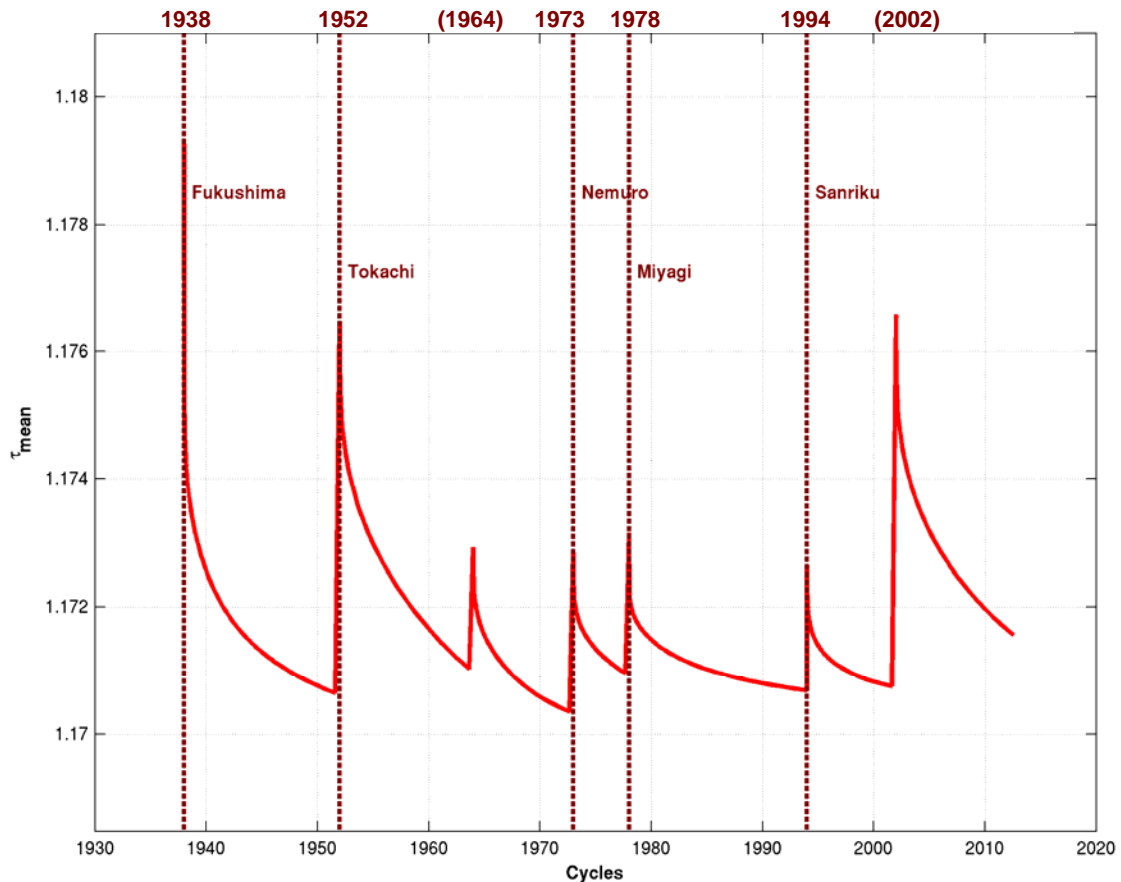


**Figure 5-6.** Evolution of tractions over the “present” reference cycle of 75 yrs. Only the most recent events prior to the end-date of GPS velocity measurements (2000) are identified for each asperity. The two unlabeled events correspond to the 1968 “Tokachi-Oki” event off the Sanriku coast (but occurring in 1964 due to the approximate rupture interval chosen in Section 5.3), and the 2003 M8.2 Tokachi-oki 2003 event (here, occurring in 2002).

In order to check how realistic our input coseismic ruptures are, we compare the synthetic coseismic surface displacements due to characteristic slip on the modeled Tokachi-oik asperity to some recent joint geodetic/seismic inversions of the 2003 Tokachi-oki earthquake [Koketsu et al., 2004]. The overall pattern of surface displacements along southeastern Hokkaido seems to agree well with the observed coseismic surface displacement field (Figure 5-7). The synthetic displacements are scaled relative to the coseismic slip imposed ( $\sim 6.4$  m, see Table 5-1). The maximum scaled synthetic displacements are of the order of 0.07, or 45 cm. In comparison, the peak observed coseismic displacements were roughly 70–80 cm. It is possible that by spreading slip over the entire asperity, we are not able to produce the locally high slip regions (upto 8

m), that were inferred. However, because we impose a characteristic rupture for Tohoku having a significant strike-slip component, our model predicts excessive strike-slip surface coseismic displacements northeast of the Tohoku asperity. This is not seen in Figure 5-7(b), because the 2003 Tokachi-oki rupture was inferred to be predominantly in the dip-slip direction. This discrepancy highlights a limitation of our approach: in reality, the character of coseismic slip changes from rupture to rupture, and is not identical from rupture to rupture. The significant strike-slip partitioning due to the bend in the trench profile between the Sanriku and Tokachi asperities has to be absorbed some other way over the geologic time-scale. One way would be to periodically introduce a purely strike-slip rupture on the Tokachi asperity. However, a more plausible explanation might be that a significant portion of this strike-slip motion is absorbed by the strike-slip fault forming the western boundary of the Kurile sliver plate, which extends almost half way down the eastern Hokkaido coast [e.g., Figure 6 of DeMets, 1992].

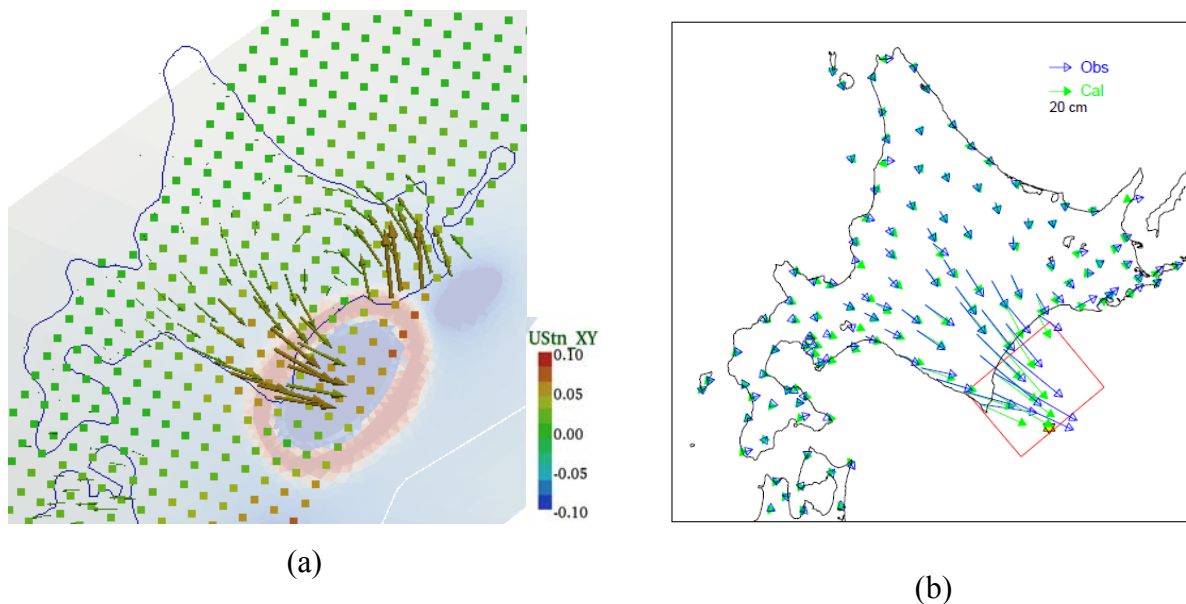


**Figure 5-7.** (a) Synthetic Tokachi-oki coseismic displacements and (b) actual coseismic displacements from 2003  $M_w$  8.2 Tokachi-oki earthquake [Koketsu *et al.*, 2004]. The synthetic displacements are scaled relative to the imposed mean coseismic slip of 6.4 m (Table 5-1).

Sample surface displacements over the last reference cycle also show a rapid post-seismic response for the rheological parameters chosen here (Figure 5-8). It is interesting to note

that both stations displayed here (located along the Sanriku coast) show a different sense of offset in their north (y) component (middle panels of Figure 5-8) for the 1952 Tokachi-oki event and the subsequent 1968 Sanriku-oki event. In our synthetic predictions, this is due to the fact that the applied variable-rake backslip is partitioned into a small northward component (as opposed to being southward over the rest of the fault surface), over a small region around the Sanriku asperity (Figure 4-6), because of the change in orientation of the trench profile relative to the mean plate convergence direction. Such a reversal is also seen between the 1994 Sanriku-oki and 2003 Tokachi-oki events for this station. It will be interesting to check whether this latter reversal is indeed observed in the time-series for this station. A dynamically weaker frictional rheology (smaller  $\alpha'$ ) could result in a more pronounced post-seismic response than that displayed in Figure 5-8.

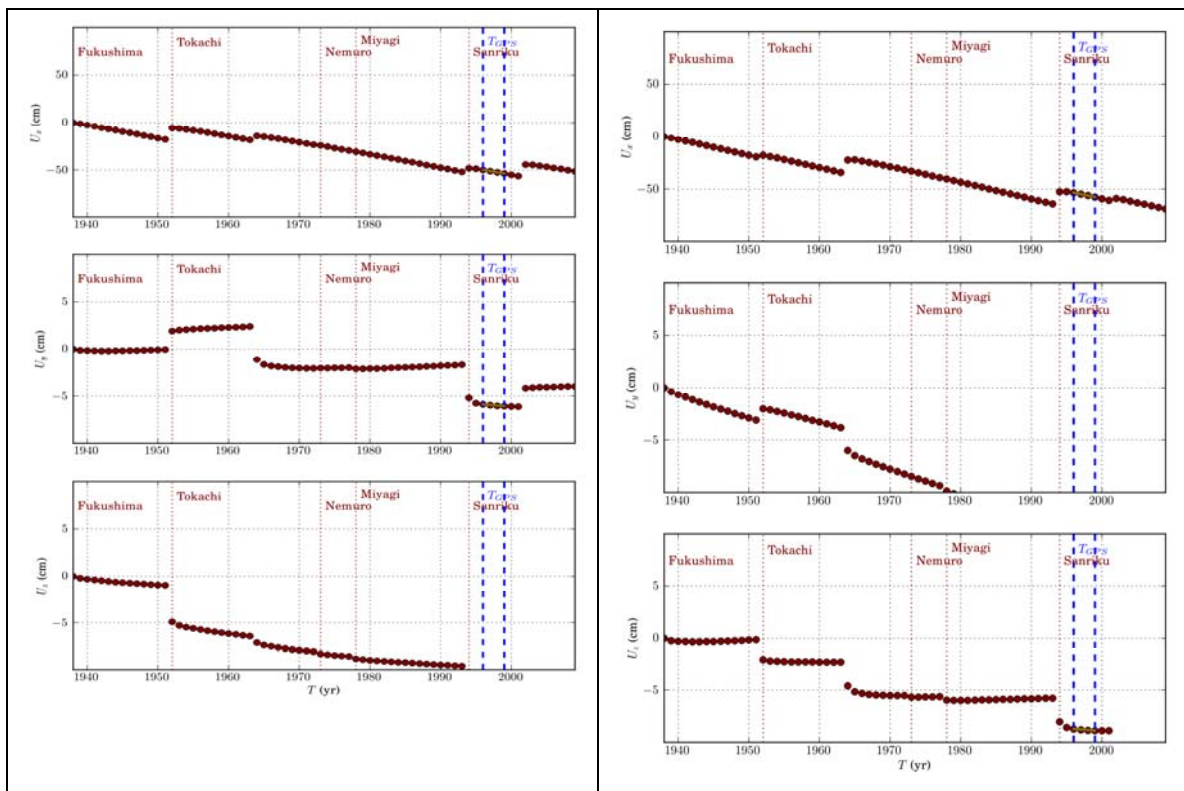


**Figure 5-8.** Sample synthetic surface displacement time-series over the last 75 yr reference cycle for two stations (left: 960533; right: 950156; both located along the Sanriku coast). Blue dashed lines indicate the observed and synthetic GPS velocity estimation window, and the slopes used to infer the velocities are indicated as grey lines within this window.

Finally, we present comparisons between the GPS velocities estimated for the period 1996–2000 [Hashimoto et al., 2009], and the synthetic velocities assuming both a frictionless fault, as well as the rate strengthening rheology discussed above. The observed velocities are relative to the station Adogawa (Geonet #950320), located along the Japan Sea coast, just off the lower left corners of Figure 5-9 and Figure 5-10. In contrast, our model predictions are relative to the far-field of the overriding plate (i.e., Eurasia). Also, we do not model the incipient subduction thought to be occurring along the Japan Sea coast. Therefore, our “raw” model predictions near the Japan Sea coastline are opposite to the above relative velocities. Given that the above reference station is outside the area we can model with motion purely along the Japan Trench megathrust, we pick as the reference station, Geonet #950241, which is northeast of Adogawa along the Japan Sea coast. We confirmed that the observed GPS velocities at this station were negligible. All synthetic velocities presented below are relative to this station. All velocities are scaled relative to the plate velocity of 8.3 cm/yr for the Pacific Plate off Tohoku.

We first compare the predicted horizontal velocity field computed assuming that only the asperities are locked late in the cycle, and the surrounding fault slips aseismically, at the long-term slip-rate equal to the plate velocity (Figure 5-9). This scenario is equivalent to applying backslip over all of the asperities to estimate interseismic velocities. Clearly, this model explains only a small fraction of the observed horizontal field. From a purely backslip perspective, areas between the asperities are also required to be “locked”, or “coupled”, to explain the observed GPS velocities. Alternatively, significant post-seismic slip in the region between the three southernmost asperities, as well as between the two northernmost ones, could also explain the misfit.

We now compare the predicted velocity fields for the frictional rheology assumed above (Figure 5-10). The most interesting observation is that much of the horizontal velocity field in the vicinity of the two largest asperities (Fukushima in the south, and Tokachi in the north) is explained by the extensive post-seismic slip (Figure 5-11) around them after their most recent ruptures. In fact, by including variable-rake backslip, we fit the

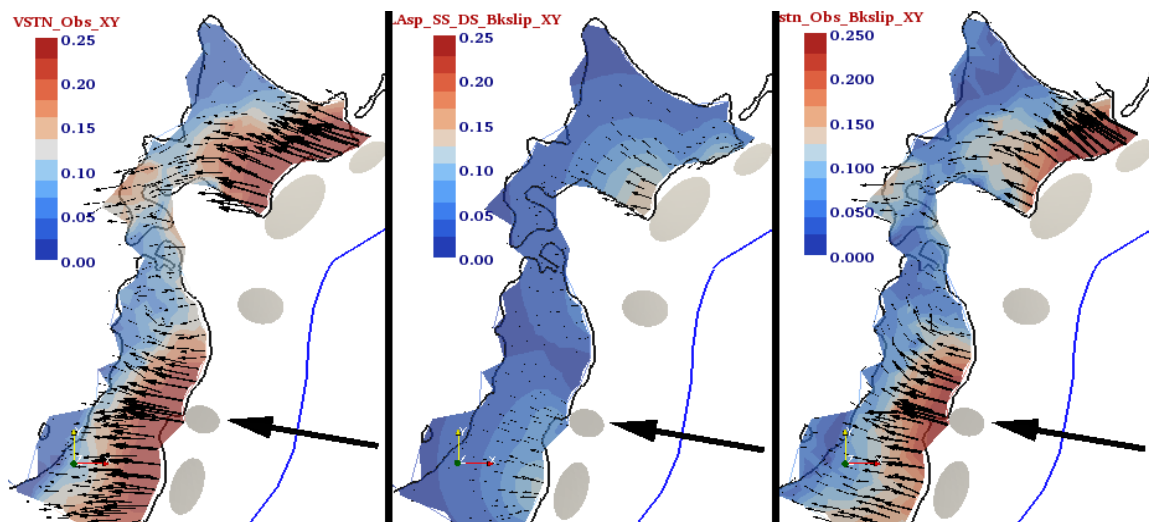


**Figure 5-9.** Observed (left), synthetic-backslip (middle), and residual (right) horizontal GPS velocity fields (relative to a fixed Okhotsk plate) for the period 1996-2000. Synthetics were computed assuming that the fault is locked only at the asperities late in the cycle, and the rest of the fault surface is frictionless. Asperities are shaded in light gray and off-shore of the northern Japan coastline. Thick black arrows indicate the plate convergence direction. Velocities are scaled relative to the plate velocity of 8.3 cm/yr for the Pacific Plate off Tohoku. The color intensity has the same scale in each plot.

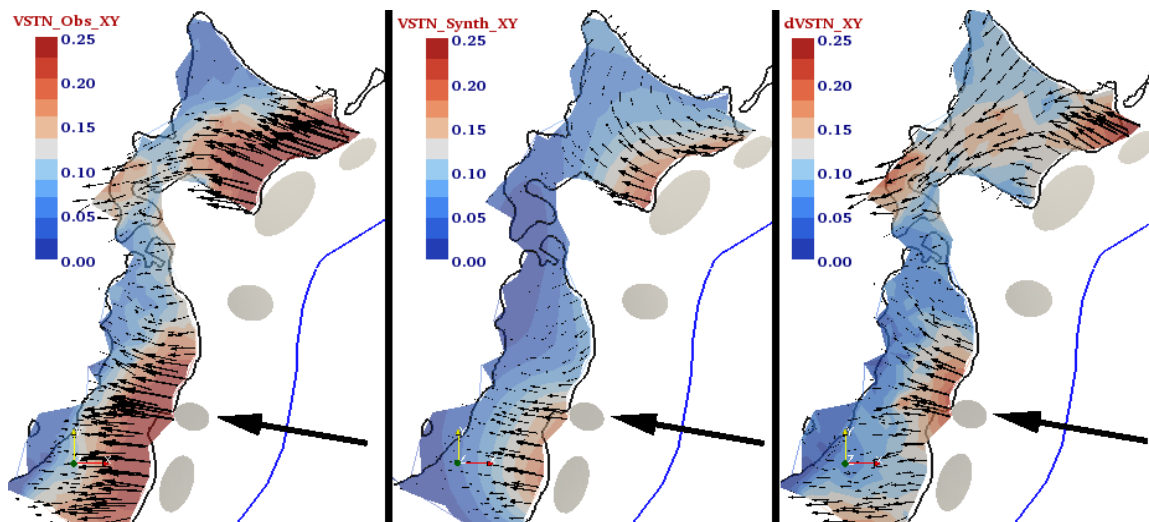


**Figure 5-10.** Observed (left), synthetic-frictional (middle), and residual (right) horizontal GPS velocity fields (relative to a fixed Okhotsk plate) for the period 1996-2000. Synthetics were computed assuming that slip on the fault surface is governed by rate strengthening friction with  $\alpha' \approx 1$ . Asperities are shaded in light gray and off-shore of the northern Japan coastline. Thick black arrows indicate the plate convergence direction. Velocities are scaled relative to the plate velocity of 8.3 cm/yr for the Pacific Plate off Tohoku. The color intensity has the same scale in each plot.

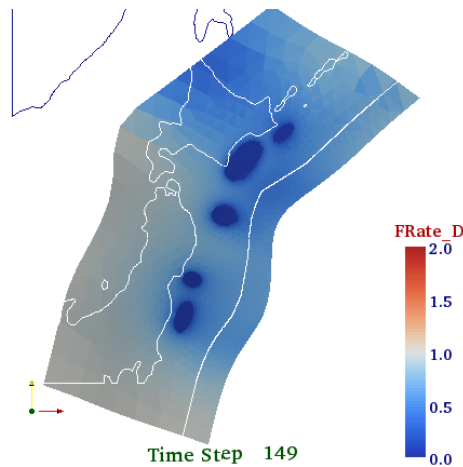


**Figure 5-11.** Slip-rates at the end of the cycle, for a fault surface governed by rate strengthening friction with  $\alpha' \approx 1$ . Notice the much larger areas of near-zero slip-rates compared to the upper-left panel of Figure 5-4.

horizontals much better in southern Hokkaido, compared to recently published horizontal velocity predictions based on a sophisticated inversion scheme that probably did not include this effect [e.g., Supplementary Figure 1, Hashimoto et al., 2009]. However, around both these asperities, a dynamically weaker fault (smaller  $\alpha'$ ) would lead to higher velocities, and perhaps a lower misfit (similar to our conclusion from surface displacement plots above).

However, there are several regions of significant misfits: (a) northeastern Hokkaido, along the Nemuro coastline, (b) along the Japan sea coast of southern Hokkaido, (c) along the eastern coastline of central Tohoku between the Miyagi and Sanriku asperities, and (d) along the Kanto-southern-Tohoku region in central Japan. We now examine each of these regions more closely.

(a) The biggest residuals are in northeastern Hokkaido, along the Nemuro coastline. There are a couple of plausible explanations for this discrepancy. The first has to do with the fact that we have ignored the large 1994 M8.1 Shikotan island earthquake, and perhaps this asperity needs to be included in our simulation to account for the discrepancy. The second has to do with the fact that the original slab geometry created in Gocad has a long-wavelength concave dip starting just downdip of Nemuro asperity. As

a result, there is considerably less downdip component in the variable rake backslip field we impose (blue area in the right column of Figure 4-6). This was confirmed by noting that in the synthetic surface displacement field just prior to the 1973 Nemuro-oki event, there is a significant trench-parallel, but almost no downdip, component (as would be expected late in the cycle, landward of a locked patch). So, correcting this long-wavelength feature (which was missed by the kernel residual checks discussed in Chapter 4) might also help better model the horizontals in this region.

(b) The misfit in southwestern Hokkaido could most likely be from ongoing post-seismic deformation after the 1993  $M_w$  7.8 Hokkaido-Nansei-oki earthquake in Japan Sea [Ueda et al., 2003]. The maximum residuals we obtain for this region are of the order of 0.2 of the plate velocity, or  $\sim 1.7$  cm/yr. In comparison, the best-fit post-seismic relaxation models of Ueda et al. [2003] yield horizontal surface velocities of 1.5 and 2 cm/yr. While there is good agreement between our residuals and their predicted horizontals, we observe a significant counter-clockwise rotation due to the excess strike-slip component in the characteristic rupture imposed on the Tokachi asperity as well as the anomalous strike-slip contribution to the Nemuro asperity (above).

(c) The main characteristic of the misfits in central Tohoku are their trench-perpendicular orientations. This indicates either (i) that a yet to be detected asperity exists between the Miyagi and Sanriku asperities [e.g., Slip deficit region in Fig 6 of Miura et al., 2006], or (ii) this region may be susceptible to episodic aseismic afterslip [Igarashi et al., 2003; Uchida et al., 2004], or (iii) a region that could become “locked” owing to coseismic Coulomb stress changes as observed by Miura et al. [2006]. Although many cases of small but repeating earthquake clusters have also been documented in this region [Igarashi et al., 2003; Uchida et al., 2004], the frequent release of any accumulated strain would not result in an apparent slip-deficit along the megathrust interface here, ruling out the first possibility. Yet another possibility is that the location of the Miyagi asperity centroid may be too deep. The Japanese coastline in this region is located right above a steep change in slab dip, and locating the asperity even a little too landward would also make it deeper, reducing its contribution to the horizontal velocity field.

(d) Recently, Townsend and Zoback [2006] argued for additional permanent horizontal deformation in central Japan — beyond that inferred from deformation due to cyclic subduction zone megathrust ruptures - related to the horizontal motion of the Amurian plate with respect to northeastern Honshu. Their work was based on *Henry et al.* [2001], who estimated net deformation from GPS measurements to be directed west-northwest, ahead of the Izu-Bonin arc collision. Their inferred direction of additional deformation and magnitude of approximately 1.5-2 cm/yr agrees reasonably with the misfit in southern Tohoku.

In spite of the above discrepancies - some of which are due to phenomena we do not model here – to first order, ruptures on existing asperities do seem to explain a significant portion of the horizontal velocities in northeastern Japan. Once the Nemuro asperity is corrected, and the Shikotan rupture is included, we expect the agreement between the observed and predicted horizontal velocity field to be much better even in northeastern Hokkaido.

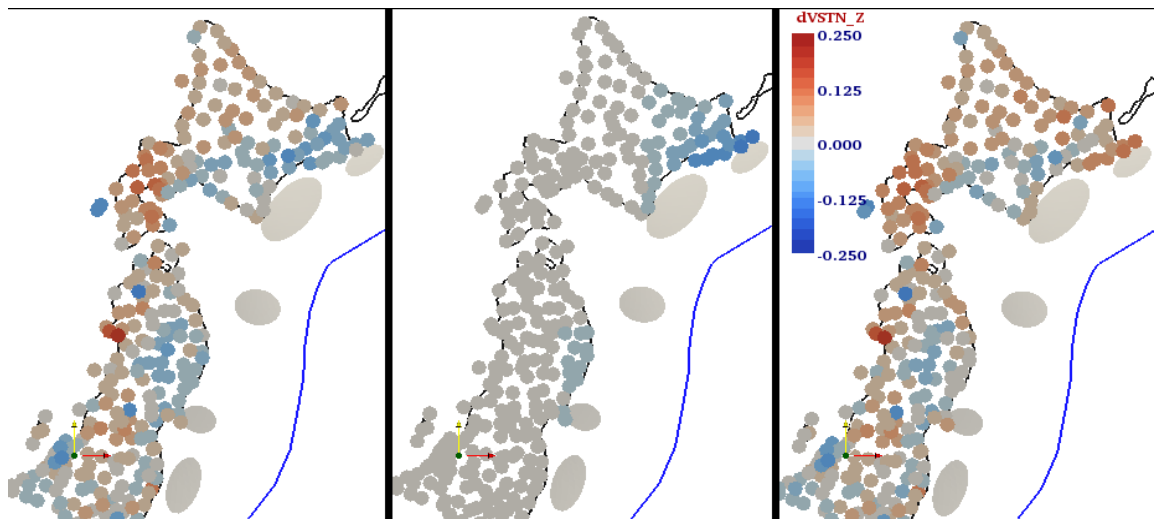


**Figure 5-12.** Observed (left), synthetic-frictional (middle), and residual (right) vertical GPS velocity fields (relative to a fixed Eurasian plate) for the period 1996-2000, for the same frictional rheology as in Figure 5-10.

The observed and predicted vertical velocities as well as their residuals are presented in Figure 5-12. Deep afterslip seems to explain part of the subsidence along the Sanriku, and southeastern Hokkaido coasts. However, most of the vertical signal remains

unexplained. The residuals along the west coast could be due to the fact that we do not model the incipient subduction in Japan Sea. It has long been known that much of the eastern Tohoku coastline has been experiencing persistent subsidence relative to the Eurasian plate. It has been argued that this subsidence is perhaps related to ongoing subduction erosion [Aoki and Scholz, 2003; Heki, 2004; Hashimoto et al., 2008]. We do not consider off-fault processes here, and therefore cannot correctly model the observed vertical geodetic data – even in eastern Tohoku.

## 5.6 Conclusions and future work

The results presented above demonstrate that the procedure developed here provides us with a unique way to probe deformation during the late post-seismic to interseismic time-periods. In a manner similar to the locking of large regions of the megathrust required by interseismic geodetic data inversions [e.g., Suwa et al., 2006], we too require large areas of afterslip (especially downdip) of the inferred asperities to explain current horizontal geodetic velocities. Such large afterslip areas create regions around the asperity having negligible slip-rates late in the seismic cycle, thus mimicking the effects of large slip-deficits required by interseismic geodetic data. Explaining the verticals is a more challenging problem that our single-fault model may not be able to constrain. However, our hypothesis that mechanical coupling on inferred asperities alone is sufficient to explain available geodetic observations along the Japan megathrust seems to be reasonable. More detailed exploration of the frictional rheology parameter space are required to solidify this assertion. Based on the systematic under-prediction by our model, we postulate that perhaps a dynamically weaker rheology might be needed to explain the larger observed late-cycle velocities.

There are some issues related to our model that still need to be resolved. Chief among them is to correct for the slab interface downdip on Nemuro-oki, and add the 1994  $M_w$  8 Shikotan asperity northeast of the Nemuro asperity. Another issue is the exact plate convergence velocity used. The values used in literature range from 9.5 cm/yr [e.g.,

Heki, 2004; Suwa et al., 2006], to 8.3 cm/yr, depending on whether the Eurasian or Okhotsk plates are used as the reference frame. A 10% larger plate velocity will result in synthetic velocities being that much larger, and therefore reduce the misfits further in Fukushima and southeastern Hokkaido. Also, in order to avoid reference frame issues, it may be more appropriate to compare strain rates instead of velocities. Using depth dependent rheological parameters may result in slip being constrained to the shallower portions of the megathrust, leading to stronger horizontal signal from both the shallower dip (on average) as well as by creating a larger zone of apparent locking.

Looking farther into the future, the procedure introduced here can be extended to model the full post-seismic to inter-seismic response of the megathrust to specified ruptures. Including ruptures on other major faults in the region (e.g., those related to incipient subduction in Japan Sea, or the Kurile sliver) can help us understand the current surface deformation field even better. This method can also be applied to other subduction zones where high density geodetic data may become available in the near future (e.g., Sunda Trench off Sumatra, or the Peru-Chile subduction zone). The ability to probe the synthetic velocity field in 3D, and being able to follow the evolution of surface displacements at hundreds of stations simultaneously has potential to provide valuable insights into the behavior of the subduction zones over the seismic cycle.

## References

- Abe, K. (1977), Tectonic implications of the large Shioya-oki earthquakes of 1938, *Tectonophysics*, 41, 269–289.
- ANCORP-Working-Group (2003), Seismic Imaging of a convergent continental margin and plateau in the central Andes (Andean Continental Research Project 1996 (ANCORP'96)), *J. Geophys. Res.*, 108.
- Aoki, Y. and C.H. Scholz (2003), Vertical deformation of the Japanese islands, 1996–1999, *J. Geophys. Res.*, 108, 2257, doi:2210.1029/2002JB002129
- Bird, P. (2003), An updated digital model of plate boundaries, *Geochem Geophys Geosy*, 4, 1027, doi:1010.1029/2001GC000252.
- Blanpied, M., D. Lockner and D. Byerlee (1991), Fault stability at hydrothermal conditions, *Geophys. Res. Lett.*, 18, 609–612.
- Brudzinski, M.R. and W.-P. Chen (2005), Earthquakes and strain in subhorizontal slabs, *J. Geophys. Res.*, 110, B08303.
- Buffett, B.A. (2006), Plate force due to bending at subduction zones, *J. Geophys. Res.*, 111, B09405.
- Bürgmann, R., M. Kogan, V. Levin, G.E. Hilley, G. Steblov and E. Apel (2005), Interseismic coupling and asperity distribution along the Kamchatka subduction zone, *J. Geophys. Res.*, 110, B07405, doi:07410.01029/02005JB003648.
- Chlieh, M., J.-P. Avouac, K. Sieh, D.H. Natawidjaja and J. Galetzka (2008a), Heterogeneous coupling on the Sumatra megathrust constrained from geodetic and paleogeodetic measurements, *J. Geophys. Res.*, 113, B05305.
- Chlieh, M., J.P. Avouac, K. Sieh, D.H. Natawidjaja and J. Galetzka (2008b), Heterogeneous coupling of the Sumatran megathrust constrained by geodetic and paleogeodetic measurements, *J. Geophys. Res.*, 113, B05305, doi:05310.01029/02007JB004981
- Chlieh, M., J.B.d. Chabaliere, J.C. Ruegg, R. Armijo, R. Dmowska, J. Campos and K.L. Feigl (2004), Crustal deformation and fault slip during the seismic cycle in the North Chile subduction zone, from GPS and InSAR observations, *Geophys. J. Int.*, 158, 695–711.
- Cisternas, M., B.F. Atwater, F. Torrejn, Y. Sawai, G. Machuca, M. Lagos, A. Eipert, C. Youlton, I. Salgado, T. Kamataki, M. Shishikura, C.P. Rajendran, J.K. Malik, Y. Rizal and M. Husni (2005), Predecessors of the giant 1960 Chile earthquake, *Nature*, 437, 404–407.

- Cohen, S.C. (1994), Evaluation of the Importance of Model Features For Cyclic Deformation Due to Dip-Slip Faulting, *Geophys. J. Int.*, 119, 831-841.
- Cohen, S.C. (1999), Numerical Models of Crustal Deformation in Seismic Zones, *Adv. Geophys.*, 41, 133-231.
- Conrad, C.P. and B.H. Hager (1999), Effects of plate bending and fault strength at subduction zones on plate dynamics, *J. Geophys. Res.*, 104, 17551-17571.
- DeMets, C. (1992), Oblique Convergence and Deformation Along the Kuril and Japan Trenches, *J. Geophys. Res.*, 97, 17,615–617,625, doi:610.1029/1092JB01306.
- DeShon, H.R., S.Y. Schwartz, A.V. Newman, V. González, M. Protti, L.M. Dorman, T.H. Dixon, D.E. Sampson and E.R. Flueh (2006), Seismogenic zone structure beneath the Nicoya Peninsula, Costa Rica, from three-dimensional local earthquake P- and S-wave tomography, *Geophys. J. Int.*, 164, 109–124.
- Elsasser, W.M. (1971), Sea-floor spreading as thermal convection, *J. Geophys. Res.*, 76, 1101-1112.
- Engdahl, E.R., A. Villasenor, H.R. DeShon and C. Thurber (2007), Teleseismic relocation and assessment of seismicity (1918-2005) in the region of the 2004 Mw 9 Sumatra-Andaman and 2005 M 8.7 Nias great earthquakes, *Bull. Seismol. Soc. Am.*, 97 S43-S61.
- Forsyth, D.W. and s. Uyeda (1975), On the relative importance of the driving forces of plate motion, *Geophys. J. R. Astron. Soc.*, 43, 163-200.
- Fowler, C.M.R. (1990), *The solid earth*, edn, vol., Cambridge University Press, Cambridge.
- Freund, L.B. and D.M. Barnett (1976), A Two-Dimensional Analysis of Surface Deformation due to Dip-slip Faulting, *Bull. Seismol. Soc. Am.*, 66, 667-675.
- Fukahata, Y. and M. Matsu'ura (2006), Quasi-static internal deformation due to a dislocation source in a multilayered elastic/viscoelastic half-space and an equivalence theorem, *Geophys. J. Int.*, 166, 418–434.
- Fukuda, J., K. Johnson, K.M. Larson and S. Miyazaki (2009), Friction parameters inferred from the early stages of afterslip following the 2003 Tokachi-oki earthquake, *J. Geophys. Res.*, 114, B04412, doi:04410.01029/02008JB006166.
- Gagnon, K., C.D. Chadwell and E. Norabuena (2005), Measuring the onset of locking in the Peru–Chile trench with GPS and acoustic measurements, *Nature*, 434, 205–208.
- Gocad, 2010. (<http://www.gocad.org/www/gocad/index.xhtml>) Gocad Research Group.
- Gutscher, M.-A., W. Spakman, H. Bijwaard and E.R. Engdahl (2000), Geodynamics of at subduction: Seismicity and tomographic constraints from the Andean margin, *Tectonics*, 19, 814-833.

- Hacker, B.R., S.M. Peacock, G.A. Abers and S.D. Holloway (2003), Subduction Factory, 2: Are intermediate-depth earthquakes in subducting slabs linked to metamorphic dehydration reactions?, *J. Geophys. Res.*, 108, 2030.
- Hager, B.H. (1984), Subducted slabs and the geoid: constraints on mantle rheology and flow. , *J. Geophys. Res.*, 89, 6003-6015.
- Hamada, N. and Y. Suzuki (2004), Re-examination of aftershocks of the 1952 Tokachi-oki earthquake and a comparison with those of the 2003 Tokachi-oki earthquake, *Earth Planets Space*, 56, 341–345.
- Hashimoto, C., A. Node, T. Sagiya and M. Matsu'ura (2009), Interplate seismogenic zones along the Kuril-Japan trench inferred from GPS data inversion, *Nature Geosci.*, 2, 141-144.
- Hashimoto, C., T. Sato and M. Matsu'ura (2008), 3-D simulation of steady plate subduction with tectonic erosion: Current crustal uplift and free-air gravity anomaly in northeast Japan, *Pure Appl. Geophys.*, 165, 567–583, doi:10.1007/s00024-00008-00321-00020.
- Heki, K. (2004), Space Geodetic Observation of Deep Basal Subduction Erosion in Northeastern Japan, *Earth Planet. Sci. Lett.*, 219, 13-20.
- Henderson, A. (2004), *The Paraview Guide*, 1st edn, vol., Kitware Inc.
- Henry, P., S. Mazzotti and X.L. Pichon (2001), Transient and permanent deformation of central Japan estimated by GPS. 1. Interseismic loading and subduction kinematics, *Earth Planet. Sci. Lett.*, 184, 443-453.
- Hetland, E.A. and M. Simons (2010), Postseismic and interseismic deformation due to fault creep II: Transient creep and interseismic stress shadows on megathrusts. , *Geophys. J. Int.*, 181, 99–112, doi:10.1111/j.1365-1246X.2009.04482.x.
- Hetland, E.A., M. Simons and E.M. Dunham (2010), Postseismic and interseismic deformation due to fault creep I: Model description, *Geophys. J. Int.*, 181, 81–98, doi:10.1111/j.1365-1246X.2010.04522.x.
- Hori, T. (2006), Mechanisms of separation of rupture area and variation in time interval and size of great earthquakes along the Nankai Trough, southwest Japan, *J. Earth Simulator*, 8-19.
- Hsu, Y.-J., M. Simons, J.-P. Avouac, J. Galetzka, K. Sieh, M. Chlieh, D. Natawidjaja, L. Prawirodirdjo and Y. Bock (2006), Frictional Afterslip Following the 2005 Nias-Simeulue Earthquake, Sumatra, *Science*, 312, 1921-1926.
- Hyndman, R.D. and K. Wang (1993), Thermal constraints on the zone of major thrust earthquake failure: The Cascadia subduction zone, *J. Geophys. Res.*, 98, 2039-2060.

- Igarashi, T., T. Matsuzawa and A. Hasegawa (2003), Repeating earthquakes and interplate aseismic slip in the northeastern Japan subduction zone, *J. Geophys. Res.*, 108, 2249, doi:2210.1029/2002JB001920.
- Iio, Y., T. Sagiya and Y. Kobayashi (2004), Origin of the Concentrated Deformation Zone in the Japanese Islands and Stress Accumulation Process of Intraplate earthquakes, *Earth Planets Space*, 56, 831-842.
- Iio, Y., T. Sagiya, Y. Kobayashi and I. Shiozaki (2002), Water-weakened lower crust and its role in the concentrated deformation in the Japanese Islands, *Earth Planet. Sci. Lett.*, 203, 245-253.
- Ito, A., G. Fujie, T. Tsuru, S. Kodaira, A. Nakanishi and Y. Kaneda (2004), Fault plane geometry in the source region of the 1994 Sanriku-oki earthquake *Earth Planet. Sci. Lett.*, 223, 163-175.
- Iwasaki, T., W. Kato, T. Moriya, A. Hasemi, N. Umino, T. Okada, K. Miyashita, T. Mizogami, T. Takeda, S. Seikine, T. Matsushima, K. Tashiro and H. Miyamachi (2001), Extensional structure in northern Honshu arc as inferred from seismic refraction/wide-angle reflection profiling, *Geophys. Res. Lett.*, 28, 2329–2332.
- Johnson, K.M., R. Burgmann and K. Larson (2005), Frictional Properties on the San Andreas Fault near Parkfield, California, Inferred from Models of Afterslip following the 2004 Earthquake, *Bull. Seism. Soc. Am.*, 96, S321-338.
- Kanamori, H. (1971), Focal mechanism of the Tokachi-Oki earthquake of may 16, 1968: Contortion of the lithosphere at a junction of two trenches, *Tectonophysics*, 12, 1-13.
- Kanamori, H. and D.L. Anderson (1975), Theoretical basis of some empirical relations in seismology, *Bull. Seism. Soc. Am.*, 65, 1073-1095.
- Kanda, R.V.S. and M. Simons (2010), An elastic plate model for interseismic deformation in subduction zones, *J. Geophys. Res.*, 115, B03405.
- Kato, N. (2008), Numerical simulation of recurrence of asperity rupture in the Sanriku region, northeastern Japan, *J. Geophys. Res.*, 113, B06302, doi:06310.01029/02007JB005515.
- Khazaradze, G. and J. Klotz (2003), Short and long-term effects of GPS measured crustal deformation rates along the South-Central Andes, *J. Geophys. Res.*, 108, 2289.
- Klotz, J., A. Abolghasem, G. Khazaradze, B. Heinze, T. Vietor, R. Hackney, K. Bataille, R. Maturana, J. Viramonte and R. Perdomo, 2006. Long-term signals in the present-day deformation field of the Central and Southern Andes and Constraints on the viscosity of the Earth's Upper Mantle. . in *The Andes: Active Subduction Orogeny*, *Frontiers in Earth Sciences*, pp. 65–89, eds Oncken, O., Chong, G., Franz, G., Giese, P., Goetze, H., Ramos, V. A., Strecker, M. R. and Wigger, P. Springer Berlin.

- Koketsu, K., K. Hikima, S. Miyazaki and S. Ide (2004), Joint inversion of strong motion and geodetic data for the source process of the 2003 Tokachi-oki, Hokkaido, earthquake, *Earth Planets Space*, 56, 329–334.
- Konca, A.O., J.P. Avouac, A. Sladen, A.J. Meltzner, K. Sieh, P. Fang, Z.H. Li, J. Galetzka, J. Genrich, M. Chlieh, D.H. Natawidjaja, Y. Bock, E.J. Fielding, C. Ji and D.V. Helmberger (2009), Partial rupture of a locked patch of the Sumatra megathrust during the 2007 earthquake sequence, *Nature*, 456, 631-635.
- Lapusta, N. and J. Rice (2003), Nucleation and early seismic propagation of small and large events in a crustal earthquake model, *J. Geophys. Res.*, 108, 2205, doi:2210.1029/2001JB000793.
- Larson, K., P. Bodin and J. Gomberg (2003), Using 1 Hz GPS Data to Measure Permanent and Seismic Deformations Caused by the Denali Fault Earthquake, *Science*, 300, 1421-1424.
- Loveless, J.P. and B.J. Meade (2010), Geodetic imaging of plate motions, slip rates, and partitioning of deformation in Japan, *J. Geophys. Res.*, 115, B02410, doi:02410.01029/02008JB006248.
- Marone, C., C. Scholz and R. Bilham (1991), On the mechanics of earthquake afterslip, *J. geophys. Res.*, 96, 8441–8452.
- Massonnet, D. and K.L. Feigl (1998), Radar interferometry and its application to changes in the earth's surface, *Reviews Geophys.*, 36, 441-500
- Masterlark, T. (2003), Finite element model predictions of static deformation from dislocation sources in a subduction zone: Sensitivities to homogeneous, isotropic, Poisson-solid, and half-space assumptions, *J. Geophys. Res.*, 108 2540.
- Matsu'ura, M. and T. Sato (1989), A dislocation model for the earthquake cycle at convergent plate boundaries, *Geophys. J. Int.*, 96, 23-32.
- Meade, B.J. (2007), Algorithms for the calculation of exact displacements, strains, and stresses for triangular dislocation elements in a uniform elastic half space. , *Comp. Geosci.*, 33, 1064-1075, doi:1010.1016/j.cageo.2006.1012.1003.
- Miura, S., I. Iinuma, S. Yui, N. Uchida, T. Sato, K. Tachibana and A. Hasegawa (2006), Co- and post-seismic slip associated with the 2005 Miyagi-oki earthquake (M7.2) as inferred from GPS data, *Earth Planets Space*, 58, 1567–1572.
- Miura, S., S. Kodaira, A. Nakanishi and T. Tsuru (2003), Structural characteristics controlling the seismicity of southern Japan Trench fore- arc region, revealed by ocean bottom seismographic data, *Tectonophysics*, 363, 79-102.
- Miura, S., N. Takahashi, A. Nakanishi, T. Tsuru, S. Kodaira and Y. Kaneda (2005), Structural characteristics off Miyagi forearc region, the Japan Trench seismogenic zone, deduced from a wide-angle reflection and refraction study, *Tectonophysics*, 407, 165-188.

Miyazaki, S., P. Segall, J. Fukuda and T. Kato, 2004. Space time distribution of afterslip following the 2003 Tokachi-oki earthquake: Implications for variations in fault zone frictional properties. in *Geophys. Res. Lett.*, pp. L06623.

Nakanishi, A., A.J. Smith, S. Miura, T. Tsuru, S. Kodaira, K. Obana, N. Takahashi, P.R. Cummins and Y. Kaneda (2004), Structural factors controlling the coseismic rupture zone of the 1973 Nemuro-Oki earthquake, the southern Kuril Trench seismogenic zone, *J. Geophys. Res.*, 109, B05305, doi: 05310.01029/02003JB002574.

Nakayama, W. and M. Takeo (1997), Slip history of the 1994 Sanriku-Haruka-Oki, Japan, earthquake deduced from strong-motion data, *B. Seismol. Soc. Am.*, 87, 918-931.

Nanayama, F., K. Satake, R. Furukawa, K. Shimokawa, B.F. Atwater, K. Shigeno and S. Yamaki (2003), Unusually large earthquakes inferred from tsunami deposits along the Kuril trench, *Nature*, 424, 660–663.

Nishimura, T., T. Hirasawa, S. Miyazaki, T. Sagiya, T. Tada, S. Miura and K. Tanaka (2004), Temporal change of interplate coupling in northeastern Japan during 1995-2002 estimated from continuous GPS observations, *Geophys. J. Int.*, 157, 901-916.

Nishimura, T., H. Nakahara, H. Sato and M. Ohtake (1996), Source process of the 1994 far east off Sanriku earthquake, Japan, as inferred from a broad-band seismogram, *Tohoku Geophys. J.*, 34, 121–134.

Okada, Y. (1992), Internal deformation due to shear and tensile faults in a half-space, *Bull. Seismol. Soc. Am.*, 82, 1018-1040.

Oleskevich, D.A., R.D. Hyndman and K. Wang (1999), The updip and downdip limits to great subduction earthquakes: thermal and structural models of Cascadia, south Alaska, SW Japan, and Chile, *J. Geophys. Res.*, 104, 14965–14991.

Owen, S.J., 2006. CUBIT 10.2 Documentation, pp. 532, Sandia National Laboratories, Albuquerque, NM, U.S.A.

Park, J.-O., T. Tsuru, S. Kodaira, P.R. Cummins and Y. Kaneda (2002), Splay Fault Branching Along the Nankai Subduction Zone, *Science*, 297, 1157-1160.

Perfettini, H. and J.-P. Ampuero (2008), Dynamics of a velocity strengthening region: implications for slow earthquakes and postseismic slip, *J. Geophys. Res.*, 113, B09411, doi:09410.01029/02007JB005398.

Perfettini, H. and J. Avouac (2004), Postseismic relaxation driven by brittle creep: A possible mechanism to reconcile geodetic measurements and the decay rate of aftershocks, application to the Chi-Chi earthquake, Taiwan, *J. Geophys. Res.*, 109, B02304.

Perfettini, H. and J.P. Avouac (2007), Modeling afterslip and aftershocks following the 1992 Landers earthquake, *J. Geophys. Res.*, 112, B07409, doi: 07410.01029/02006JB004399.

- Rani, S. and S.J. Singh (1992), Static Deformation of a Uniform Half-space due to a Long Dip-slip Fault, *Geophys. J. Int.*, 109, 469-476.
- Rice, J. (1993), Spatio-temporal complexity of slip on a fault, *J. geophys. Res.*, 98, 9885–9907.
- Robinson, D.P. and L.T. Cheung (2003), Source process of the Mw 8.3, 2003 Tokachi-Oki, Japan earthquake and its aftershocks, *Geoph. J. Intl.*, 181, 334-342, DOI: 310.1111/j.1365-1246X.2010.04513.x.
- Ruff, L.J. (1992), Asperity distributions and large earthquake occurrence in subduction zones, *Tectonophysics*, 211, 61-83.
- Rundle, J.B. (1982), Viscoelastic-gravitational deformation by a rectangular thrust fault in a layered Earth, *J. Geophys. Res.*, 87, 7787-7796.
- Satake, K. and B.F. Atwater (2007), Long-term perspectives on giant earthquakes and tsunamis at subduction zones, *Annu. Rev. Earth Planet Sci.*, 35, 349-274.
- Satake, K., K. Hirata, S. Yamaki and Y. Tanioka (2006), Re-estimation of tsunami source of the 1952 Tokachi-oki earthquake, *Earth, Planets and Space*, 58, 535-542.
- Sato, T. and M. Matsu'ura (1988), A kinematic model for deformation of the lithosphere at subduction zones, *J. Geophys. Res.*, 93, 6410–6418.
- Sato, T. and M. Matsu'ura (1992), Cyclic crustal movement, steady uplift of marine terraces, and evolution of the island arc-trench system in southwest Japan, *Geophys. J. Int.*, 111, 617–629.
- Sato, T. and M. Matsu'ura (1993), A kinematic model for evolution of island arc-trench systems, *Geophys. J. Int.*, 114, 512-530.
- Savage, J.C. (1983), A dislocation model of strain accumulation and release at a subduction zone, *J. Geophys. Res.*, 88 4984-4996.
- Savage, J.C. (1995), Interseismic uplift at the Nankai subduction zone, Southwest Japan, 1951–1990, *J. Geophys. Res.*, 100, 6339–6350.
- Savage, J.C. (1996), Comment on "The stress state implied by dislocation models of subduction deformation" by J. J. Douglass and B. A. Buffett, *Geophys. Res. Lett.*, 23, 2709-2710.
- Savage, J.C. (1998), Displacement field for an edge dislocation in a layered half-space, *J. Geophys. Res.*, 103, 2439-2446.
- Scholz, C.H. (1990), *The Mechanics of Earthquakes and Faulting*, edn, vol., pp. 439, Cambridge University Press, New York.
- Schroeder, W., K. Martin and B. Lorenzen (2006), *The Visualization Toolkit An Object-Oriented Approach To 3D Graphics*, 4th edn, vol., Kitware Inc. .

- Seno, T., K. Shimazaki, P. Somerville, K. Sudo and T. Eguchi (1980), Rupture process of the Miyagi-oki, Japan, earthquake of June 12, 1978, *Phys. Earth Planet. Int.*, 23, 39-61.
- Seth, B.R. (1935), Finite Strain in Elastic Problems, *Philosophical Transactions of the Royal Society of London*, 234, 231-264.
- Shimazaki, K. (1974), Nemuro-Oki earthquake of June 17, 1973: A lithospheric rebound at the upper half of the interface, *Phys. Earth. Planet. In.*, 9, 314-327.
- Shimazaki, K. and T. Nakata (1980), Time-predictable recurrence model for large earthquakes, *Geophys. Res. Lett.*, 7, 279-282.
- Sieh, K., D.H. Natawidjaja, A.J. Meltzner, C.-C. Shen, H. Cheng, K.-S. Li, B.W. Suwargadi, J.G. Philibosian and R.L. Edwards (2008), Earthquake supercycles inferred from sea-level changes recorded in the corals of West Sumatra, *Science*, 322, 1674-1678, doi:1610.1126/science.1163589.
- Sieh, K., S.N. Ward, D. Natawidjaja and B.W. Suwargadi (1999), Crustal deformation at the Sumatran subduction zone revealed by coral rings, *Geophys. Res. Lett.*, 26, 3141-3144.
- Simoës, M., J.-P. Avouac, R. Cattin and P. Henry (2004), The Sumatra Subduction Zone: A Case for a Locked Fault Zone Extending into the Mantle, *J. Geophys. Res.*, 109, B10402.
- Simons, M. and P. Rosen, 2007. Interferometric Synthetic Aperture Radar Geodesy. in *Treatise on Geophysics*, pp. 391-446, ed Schubert, G. Elsevier Press.
- Souter, B.J. and B.H. Hager (1997), Fault propagation fold growth during the 1994 Northridge, California, earthquake?, *J. Geophys. Res.*, 102, 11,931-911,942.
- Subarya, C., M. Chlieh, L. Prawirodirdjo, J.P. Avouac, Y. Bock, K. Sieh, A. Meltzner, D. Natawidjaja and R. McCaffrey (2006), Plate-boundary deformation of the great Aceh-Andaman earthquake, *Nature*, 440, 46-51.
- Suppe, J. (1985), *Principles of Structural Geology*, edn, vol., Prentice-Hall.
- Suwa, Y., S. Miura, A. Hasegawa, T. Sato and K. Tachibana (2006), Interplate coupling beneath NE Japan inferred from three-dimensional displacement field, *J. Geophys. Res.*, 111, B04402.
- Takahashi, N., S. Kodaira, T. Tsuru, J.-O. Park, Y. Kaneda, K. Suyehiro, H. Kinoshita, S. Abe, M. Nishino and R. Hino (2004), Seismic structure and seismogenesis off Sanriku region, northeastern Japan, *Geophys. J. Int.*, 159, 129-145.
- Tanioka, Y., 2003a. Rupture area of the 1894 Nemuro-oki earthquake is larger than that of the 1973 Nemurooki earthquake. in *Japan Geoscience Union Meeting*, s208-007, pp. Abstract s208-007.

- Tanioka, Y., 2003b. Source processes of the 1936 and 1978 Miyagi-oki earthquakes from the tsunami waveform analysis. in Japan Geoscience Union Meeting, s052-002, pp. Abstract s052-002.
- Tanioka, Y., L. Ruff and K. Satake (1996), The Sanriku-Oki, Japan, Earthquake of December 28, 1994 (Mw 7.7): Rupture of a different asperity from a previous earthquake, *Geophys. Res. Lett.*, 23, 1465–1468.
- Thatcher, W. and J.B. Rundle (1979), A model for the earthquake cycle in underthrust zones, *J. Geophys. Res.*, 84, 5540-5556.
- Thatcher, W. and J.B. Rundle (1984), A viscoelastic coupling model for the cyclic deformation due to periodically repeated earthquakes at subduction zones, *J. Geophys. Res.*, 89, 7631-7640.
- Tomar, S. and N.K. Dhiman (2003), 2-D Deformation Analysis of a Half-space due to a Long Dip-slip Fault at Finite Depth, *Proc. Indian Acad. Sci. (Earth Planet. Sci.)*, 112, 587-596.
- Townsend, J. and M.D. Zoback (2006), Stress, strain, and mountain building in central Japan, *J. Geophys. Res.*, 111, B03411, doi:03410.01029/02005JB003759.
- Turcotte, D.L. and G. Schubert (2001), *Geodynamics*, 2 edn, vol., Cambridge University Press, New York.
- Twiss, R.J. and E.M. Moores (1992), *Structural Geology*, 1st edn, vol., W. H. Freeman and Company, New York.
- Uchida, N., A. Hasegawa, T. Matsuzawa and T. Igarashi (2004), Pre- and post-seismic slip on the plate boundary off Sanriku, NE Japan associated with three interplate earthquakes as estimated from small repeating earthquake data, *Tectonophysics*, 385, 1–15.
- Ueda, H., M. Ohtake and H. Sato (2003), Postseismic crustal deformation following the 1993 Hokkaido Nansei-oki earthquake, northern Japan: Evidence for a low-viscosity zone in the uppermost mantle, *J. Geophys. Res.*, 108, 2151, doi:2110.1029/2002JB002067.
- Umino, N., T. Kono, T. Okada, J. Nakajima, T. Matsuzawa, N. Uchida, H. A., Y. Tamura and G. Aoki (2006), Revisiting the three Mw7 Miyagioki earthquakes in the 1930s: possible seismogenic slip on asperities that were re-ruptured during the 1978 M=7.4 Miyagi-oki earthquake, *Earth Planets Space*, 58, 1587-1592.
- Vergne, J., R. Cattin and J.P. Avouac (2001), On the use of Dislocations to Model Interseismic Strain and Stress Build-up at Intracontinental Thrust Faults, *Geophys. J. Int.*, 147, 155-162.
- Wang, K. (2007), Elastic and viscoelastic models of crustal deformation in subduction earthquake cycles. in *The Seismogenic Zone of Subduction Thrust Faults*, eds. Dixon, T. and Moore, J. C., pp. 540-575, Columbia University Press, New York.

- Wang, K. and Y. Hu (2006), Accretionary Prisms in Subduction Earthquake Cycles: The Theory of Dynamic Coulomb Wedge, *J. Geophys. Res.*, 111, B06410.
- Wang, K., R. Wells, S. Mazzotti, R.D. Hyndman and T. Sagiya (2003), A revised dislocation model of interseismic deformation of the Cascadia subduction zone, *J. Geophys. Res.*, 108, 2026.
- Wang, R. (2005), The dislocation theory: a consistent way for including the gravity effect in (visco)elastic plane-earth models, *Geophys. J. Int.*, 161, 191-196.
- Williams, C.A. and R. McCaffrey (2001), Stress rates in the central Cascadia subduction zone inferred from an elastic plate model, *Geophys. Res. Lett.*, 28, 2125-2128.
- Yamanaka, Y. and M. Kikuchi (2003), Source processes of the recurrent Tokachi-oki earthquake on September 26, 2003, inferred from teleseismic body waves, *Earth Planet. Sci. Lett.*, 55, e21– e24.
- Yamanaka, Y. and M. Kikuchi (2004), Asperity map along the subduction zone in northeastern Japan inferred from regional seismic data, *J. Geophys. Res.*, 109, B07307, doi:07310.01029/02003JB002683.
- Yoshioka, S., T. Yabuki, T. Sagiya, T. Tada and M. Matsu'ura (1993), Interplate coupling and relative plate motion in the Tokai district, central Japan, deduced from geodetic data inversion using ABIC, *Geophys. J. Int.*, 113, 607-621.
- Zhao, S. and S. Takemoto (2000), Deformation and stress change associated with plate interaction at subduction zones: a kinematic modeling, *Geophys. J. Int.*, 142, 300-318.
- Zweck, C., J.T. Freymueller and S.C. Cohen (2002), Three-dimensional elastic dislocation modeling of the postseismic response to the 1964 Alaska earthquake, *J. Geophys. Res.*, 107, 2064.